FUNCTIONAL EXPANSION TALLIES FOR MONTE CARLO SIMULATIONS

by

David Patrick Griesheimer

A dissertation submitted in partial fulfillment
of the requirements for the degree of
Doctor of Philosophy
(Nuclear Engineering and Radiological Sciences)
in The University of Michigan
2005

Doctoral Committee:

Associate Professor James Paul Holloway Co-Chair
Professor William R. Martin, Co-Chair
Professor Iain D. Boyd
Professor Edward W. Larsen

To my wife Sara
For her love, patience, and understanding

ACKNOWLEDGMENTS

I would like to thank my co-advisors Professors William R. Martin and James Paul Holloway for their support, assistance, and friendship during my time at Michigan. I am especially grateful to both Bill and James for their patience in enduring the many dead-ends that preceded the successful results in this dissertation. I also wish to thank Professors Edward Larsen and Iain Boyd for serving on my doctoral committee and providing valuable feedback on my work.

Special thanks are due to Professor Ziya Akcasu for the many hours that he spent helping me to formulate key parts of my research into a "well-posed" problem that could actually be solved. I am also grateful to Heath Hanshaw and my other colleagues in the fission systems and radiation transport group for the many helpful discussions on my research.

I am extremely grateful for the educational and financial support provided to me by the Naval Nuclear Propulsion Fellowship Program sponsored by the Naval Reactors Division of the U.S. Department of Energy. I would also like to thank my fellowship mentor, Dr. Jonathan Witter and everyone in the Advanced Reactors Project at Knolls Atomic Power Laboratory for their assistance during my laboratory practicum in the summer of 2002.

I would also like to extend my thanks to Chris Becker, Charlie Weger and all of the staff of the former Ford Nuclear Reactor (FNR) for their friendship and assistance

while I was working at the facility. Working at FNR was a valuable experience for me, and I was deeply saddened to see the reactor shut down in 2003.

A special thanks to all of my personal friends, especially John Dasch, Jeff Sanders, and Pat Byrne, for preventing me from spending too much time on my research and going crazy. I also want to acknowledge all of the other unnamed friends, mentors, colleagues, and peers, both at Michigan and Cincinnati, who have given me encouragement, advice and feedback along the way.

Finally, I would like to thank my family for their continued support and encouragement. I will always be indebted to my wife, Sara, for her love, understanding and, above all, patience over these past few years.

TABLE OF CONTENTS

LIST OF TABLES

LIST OF FIGURES

CHAPTER 1

INTRODUCTION

Monte Carlo simulations for particle transport calculations are often used to estimate integral quantities--scalar flux, total current, etc.--averaged over a volume or surface of interest. In cases where a higher level of detail is desired, such as the detailed angular or spatial distribution of the neutron flux in a region, Monte Carlo techniques face several challenges. The traditional approach for obtaining "detailed" solutions with Monte Carlo simulations has been to simply divide the phase space into bins and calculate an average over each bin, resulting in a histogram style distribution. This approach, however, can lead to large uncertainties in the estimated distribution if many bins are used in the histogram.

An alternative, less well-known, approach is to use a Monte Carlo simulation to estimate the functional expansion coefficients of the true distribution with respect to some set of (usually orthogonal) basis functions. The set of estimated expansion coefficients can then be used to construct a continuous functional approximation of the distribution of interest. This technique, referred to as the "functional expansion technique" or "functional expansion tally" (FET) offers several benefits over conventional histogram-style or mesh-style Monte Carlo tallies. The main advantage of this approach is that every score in the region contributes to every expansion coefficient

in that region, yielding information regarding the shape of the phase space quantity as well as its average value that is obtained with simple binning.

This introductory chapter presents an introduction to the Monte Carlo method and various types of traditional tallies that have been developed for Monte Carlo simulations. In addition, a review of previous research in functional expansion tallies is presented along with a detailed overview of the present work.

1.1. The Monte Carlo Method

Monte Carlo simulations are fundamentally nothing more than a stochastic numerical experiment[1]. In order to solve a particular problem with Monte Carlo methods the user must set up and run a simulation of the physical system under consideration. If the simulation accurately recreates the behavior of the system, then the results of the simulation will be an estimate of the expected outcome for the system. However, as with any experiment, a Monte Carlo simulation must be set up correctly to produce meaningful results. A simulation that neglects physical processes or collects insufficient data for statistical analysis will likely produce incorrect or even unphysical results.

One of the greatest benefits of Monte Carlo simulation as compared to other computational methods is the increased level of flexibility that it offers. Users have complete control over how the simulation is set up and run, the level of geometric detail to be included, and even the ability to include physical interactions that may be difficult (or impossible) to formulate analytically.

For these reasons, Monte Carlo methods have become extremely popular for particle transport calculations, especially for reactor and shielding design work in the field of nuclear engineering. The ability to quickly create and analyze detailed models has particular appeal in design groups where engineers may wish to perform calculations on many different designs for scoping and comparative purposes. In these cases Monte Carlo methods have the potential to streamline the multi-step process required when deterministic codes are used.

1.1.1. Monte Carlo for Reactor Analysis and Design

Reactor analysis using deterministic solution methods typically require a series of calculations to be performed in sequence. A series of pin-cell or assembly level transport calculations are necessary to produce group-collapsed homogenized cross sections that can then be input into a nodal diffusion code. Today, this process of generating and using homogenized cross sections is still as much an art form as an exact science. Many reactor analysis groups have even developed their own ad-hoc cross section correction factors to produce better results from the nodal diffusion code. Often these correction factors are not based on first principle derivations, but are rather empirical "fudge factors". In addition to the burden of cross section homogenization routines, deterministic particle transport methods typically require that any design under consideration must be "meshed", or converted from the design drawings into a suitable solution grid for the method being employed. During the "meshing" process many small geometric details that cannot be well represented due to the restrictions of the solution grid (e.g. modeling curved surfaces with a quadrilateral grid) are lost.

Reactor analysis calculations using Monte Carlo methods are much more straightforward. First, the problem geometry is defined in the Monte Carlo code, using as much or as little detail as desired. Many design groups are working to combine their Monte Carlo geometry input routines with existing CAD systems so that Monte Carlo simulations can be run directly from the design drawings. After the geometry has been input into the code and an initial source distribution has been defined, the simulation is ready to run. There is no need to perform auxiliary calculations to collapse cross sections or calculate homogenization constants. Although Monte Carlo calculations generally require more computing time than similarly converged deterministic calculations, the reduced overhead costs for the Monte Carlo geometry input partly compensates for the extra run time. Furthermore, Monte Carlo simulations can be easily divided among multiple processors to expedite large runs. The suitability of Monte Carlo for parallel processing has become more important and relevant as more and more supercomputer facilities have moved towards massively parallel computer clusters rather than traditional vector supercomputers.

In light of the popularity of Monte Carlo among reactor and shielding designers, this thesis will approach Monte Carlo simulations from a particle transport point of view. The applicability of the methods presented, however, are not limited to particle transport and will apply equally well to other types of Monte Carlo simulations.

1.1.2. Particle Transport by Monte Carlo Simulation

The behavior of particles moving freely in a region of space is governed by the Boltzmann equation[2]. Traditionally, particle distributions within a region of interest

have been obtained by numerically solving the linear Boltzmann equation subject to suitable boundary conditions. Most numerical schemes attempt to solve these equations by discretizing the phase space and creating a system of algebraic equations that can be solved iteratively[3].

Monte Carlo methods approach particle transport problems in a completely different way. Instead of writing down and numerically solving an equation for the particle density at all points in the phase space, forward Monte Carlo simulations attempt to recreate a physical system and transport particles through it. The result is a series of stochastic particle trajectories that could occur in the system. Once a statistically significant number of tracks have been generated, it is possible to make inferences about the average number of particles passing through a given region of phase space or the probability of a particle undergoing a certain event. A solution from a Monte Carlo simulation is actually an estimate, based on a finite number of realizations, of the expected behavior for particles in the system. Because these estimates are made from a randomly selected set of particle tracks, their values will change whenever a different set of tracks are chosen. Thus the solutions from a Monte Carlo simulation are stochastic. This result is not surprising, considering that particle transport is itself a stochastic process.

Although Monte Carlo methods can be mathematically derived[4] from the integral or integro-differential forms of the Boltzmann equation, such a tedious approach is not required. Monte Carlo methods can also be derived by treating each particle history as an independent Markov chain[5,6]. In a Markov process, the future behavior of a particle depends only on its present location in phase space[7]. This property greatly simplifies

the computational effort required to track a particle during its random walk. At each simulated event, the exiting state of the particle is determined by randomly sampling a probability density function that describes the relative likelihood of all possible outcomes from the event. After a particle's exiting state has been determined, the distance to the next event is randomly sampled based on the material properties at the particle's current position. The particle is then moved to the next event, and the process is repeated until the particle is absorbed or otherwise removed from the system. As long as each decision in a single history is made from an accurate distribution function, a realistic particle track will be generated.

The preceding discussion demonstrates that a particle history can be replicated by simulating the physics at each interaction, without even referring to the Boltzmann equation. Deriving a Monte Carlo algorithm without using the Boltzmann equation serves to illustrate an important point: Monte Carlo simulations are not a method for directly solving the Boltzmann equation. Monte Carlo methods seek to calculate the expected ensemble particle behavior by calculating averages based on finite sets of particle tracks. The Boltzmann equation, on the other hand, is an analytic description for the expected ensemble particle behavior. The two methods are very closely related (the Boltzmann equation can be derived from the forward Chapman-Kolmogorov equation, which is used in formulating Markov processes[6,7]) and both will eventually converge to the same solution. In practice, however, the two methods give different types of results. A solution to the Boltzmann equation gives the expected particle density for every point in phase space, while Monte Carlo solutions typically give only the average or integral density over a volume of phase space. However, in practice, numerical solutions to the

Boltzmann equation produced with finite difference techniques give average flux values over some solution mesh. Only more advanced solution methods, such as the finite element method (FEM), are able to provide detailed flux resolution within a solution mesh element. In a sense, the motivation for developing the FET for Monte Carlo calculations closely parallels the motivation for developing the FEM for deterministic calculations.

While the Monte Carlo method differs significantly from deterministic methods, all Monte Carlo codes themselves look essentially the same. Monte Carlo transport codes contain three basic components: random sampling routines, particle tracking routines, and tally routines.

The random sampling routines form the basis for the entire Monte Carlo process. These routines are used for generating samples from a given probability distribution. Because particle transport is a complicated physical phenomenon, a typical Monte Carlo code may require the ability to sample from dozens of different probability distributions. For example, isotropic scattering events are represented by a uniform distribution in exiting angle, while the free flight distance for a particle is governed by an exponential distribution. Most random number generators produce samples taken from a uniform distribution on the range [0,1). A mathematical transformation is then required to convert the uniformly distributed samples into samples from the desired distribution. Many different techniques and transformations have been developed to sample from many types of distributions[8].

The particle tracking routines govern the behavior of individual particles during the simulation. For every event in a particle's life these routines must: a) identify the

current location in phase space, b) look up the material properties for that location, and c) determine the next action for the particle based on the material properties and geometry.

Representing the model geometry and determining a particle's current (and future) location in that geometry is the largest part of the particle tracking routines. Most Monte Carlo codes divide the full geometry into subregions called "cells". Each cell is assigned a material composition and a density, and the properties of the cell are typically assumed to be constant throughout. Each time a particle moves in space during the simulation the Monte Carlo code must determine whether the particle will undergo a collision before it exits the current cell. If a model is divided into many small cells the Monte Carlo code will be forced to spend a lot of extra time calculating the distances to cell boundaries. It is therefore preferable to create a model that uses the fewest number of cells possible. For user convenience, many Monte Carlo codes use combinatorial geometry techniques to represent their models[9]. In a combinatorial geometry representation any arbitrary shape is defined as the union or intersection of basic geometric figures (e.g. cubes, spheres, cones). This representation allows curved surfaces to be modeled exactly and, in most cases, provides for simple and straight-forward geometry input.

In addition to the mechanics of storing and accessing the problem geometry, the particle tracking routines must also simulate the behavior of a particle as it interacts with its surroundings. Simulating each interaction is a multi-step process; the code must establish that an interaction has occurred, select which type of reaction occurred, and finally, determine the exiting state of the particle following that reaction. Each of these decisions is made by randomly sampling from a probability distribution function that

characterizes the appropriate physical process. Some of these probability distributions can be derived from theory, but much of the data comes from experimental results collected at physics institutions around the world. Large data sets of these empirical distributions for different types of reactions are widely available (e.g. ENDF/B, JEF). These data sets typically contain reaction probabilities evaluated for a wide range of energies (10^{-5}eV – 20MeV for ENDF/B neutron data[2]). Data of this type is usually referred to as "continuous-energy" data because it has not been collapsed or averaged over coarse energy bins. The ability of Monte Carlo codes to use this raw continuous-energy data is often cited as a major advantage over deterministic codes.

In the purest form of Monte Carlo, analog simulation, individual particles are made to mimic true physical behavior as closely as possible. In fact, analog simulations are the closest realization to an actual numerical transport experiment. Unfortunately, in all but the very smallest problems, direct analog simulation is not feasible. It simply takes too much computer time to run enough particles to obtain good results. In order to achieve satisfactory results in a reasonable amount of computing time, many different non-analog simulation schemes have been developed. In non-analog simulations some non-physical particle behaviors are allowed in order to accelerate statistical convergence of the results. If these schemes are designed properly, then they will be unbiased, meaning that the final results of the non-analog simulation will converge to the same results as a corresponding analog simulation.

The most commonly used non-analog scheme is referred to as "implicit capture." In a simulation using implicit capture each particle is assigned a weight of 1.0 at its birth. At each collision, the code forces the particle to scatter but reduces the particle's weight

by the probability that absorption would have occurred instead at that event. When the weight of a particle drops below a preset threshold then the particle is removed from the system. The benefit of implicit capture is that, by preventing absorption, particles survive longer in the simulation and are able to contribute more information to the tally results. However, the results of the simulation remain valid because the particle weight is adjusted at each collision, making implicit capture an unbiased scheme. Other common non-analog schemes include source biasing, scattering angle biasing, density biasing, Russian Roulette, adjoint biasing, delta scattering, and correlated sampling[10].

The random sampling and particle transport routines in a Monte Carlo code deal with transporting individual particles through the model geometry. The tally routines, on the other hand, collect aggregate data from all of the particle histories to estimate the expected particle behavior. Monte Carlo tallies are fundamentally nothing more than a counting experiment. Every time a particular event (e.g. collision, fission, crossing a surface, etc.) occurs during a particle history a "score" is recorded to a corresponding tally. After the simulation has finished, the probability of each event type can be computed directly as the number of event scores divided by the total number of particles run. Depending on the type of particle event that results in a score, and the value of each score, tallies can be used to estimate many different quantities of interest in particle transport. Common estimators include average flux in a cell, current integrated over a surface, and energy deposition in a cell[9]. Some of these tallies are literally as straightforward as calculating an arithmetic mean, while others require considerable effort to demonstrate that they are an unbiased estimator for the quantity of interest. A

detailed overview and derivation of the most common and useful types of tallies is presented in the next section.

Monte Carlo tallies are statistical estimators[11,12], meaning that each tally is a formula for making an estimate of an unknown quantity based on a random sample of particle tracks. Since tallies represent a statistical estimate of the true answer, it is also possible to calculate the statistical variance or uncertainty of the estimate. The ability to estimate the uncertainty of a solution is another major benefit of Monte Carlo methods. As the number of particles run during a simulation is increased, the variance of the tallies in the problem will decrease, resulting in a more accurate solution. In the limit of an infinite number of particles, an unbiased estimator will converge to the true solution, which is the exact solution of the Boltzmann equation for the system.

The statistical nature of Monte Carlo tallies can also have drawbacks. Complicated systems often require large number of histories to reduce the solution uncertainty to acceptable levels. Furthermore, if any regions of a problem are under-sampled (i.e. not enough particles pass through the region), it is possible to produce biases in the results. As noted previously in this section, a variety of non-analog techniques have been developed to reduce the solution variance while minimizing the number of histories that need to be run.

1.2. Traditional Monte Carlo Tallies

Monte Carlo methods are often touted as being computationally simpler than deterministic methods for particle transport applications[6]. While it is undoubtedly simpler to simulate the physics of individual particles rather than solve the Boltzmann

equation directly, collecting the information from individual particle histories into useful and physically meaningful results can be a challenging task. The development of unbiased Monte Carlo estimators has been ongoing for the past 50 years. In their review of Monte Carlo methods, Carter and Cashwell[6] cite four basic types of estimators: the collision estimator, the last-event estimator, the track length estimator, and the next-event (point-detector) estimator. These four basic types can be further condensed into two classes of estimators: discrete event estimators and track length estimators.

Discrete event estimators, which include collision, last-event, and next-event estimators, only score when a particle undergoes a certain type of event during its random walk. The track length estimator is different because it allows a particle to contribute to the estimator continuously while the particle is in the tally region. These two classes of estimators are related to each other. In 1966, Spanier[13] proved that both collision and track length estimators are limiting forms of a non-analog Monte Carlo technique referred to as delta-scattering.

In this section, a brief review of the mathematical underpinnings of Monte Carlo tallies is presented, along with derivations for several commonly used discrete event and track length estimators.

1.2.1. Notation and General Concepts

The foundations of Monte Carlo methods are based on the theories of random variables and stochastic processes. These fields of mathematics are far too broad to review in detail, so only a brief introduction will be given in this thesis. Specifically, this section will focus on techniques used to derive Monte Carlo tallies and analyze their

mathematical properties. For further information on the general theory and applications of random processes, the text by Papoulis[7] is widely considered to be the definitive reference for the field.

When working with random processes or random variables, it is extremely important to have a consistent and well defined system of notation. Although the underlying concepts are often not difficult, there are many subtleties that can lead to confusion if they are treated in a less-than-rigorous way. Unfortunately, there is no generally accepted notation in the field. In this work, a notation similar to that used by Hammersly and Handscomb[11] has been adopted. In this notation bold, non-italicized, characters (e.g. $\mathbf{x}$) are used to represent random variables. A random variable is a function that associates a real number (or a vector of numbers[11]) to every unique outcome from a random experiment. Each time the random experiment is run, the random variable is "evaluated" and returns a number that describes the outcome. Each value produced in this way is referred to as a "realization" of the random variable, and is represented by the random variable symbol in non-bold, italicized font with a hat symbol above it (e.g. $\hat{x}$ is a realization of the random variable $\mathbf{x}$).

The probability that a single realization of a random variable will take on a specific value (or fall between a range of values in the continuous case) is governed by the parent distribution of the random variable, denoted $p(x)$ for the random variable $\mathbf{x}$. Since the random variable is directly related to a probability density function, it makes sense to talk about the expected value of the random variable,

$$E[\mathbf{x}] = \int_{-\infty}^{\infty} x\, p(x)\, dx. \tag{1.1}$$

The expectation operator is usually expressed as $E[\ ]$, but it is also written as angle brackets $\langle\ \rangle$ in chapter 3 where the E notation becomes too cumbersome. Applying the expectation operator to a random variable yields a single number called the expected value. In this notation the expected value is denoted by the random variable symbol in non-bold, italicized font with a bar symbol above it (e.g. $\bar{x}$ is the expected value of the random variable $\mathbf{x}$).

When dealing with Monte Carlo tallies it is especially important to distinguish between a random variable and a realization of the random variable. A random variable describes a random experiment and all of its possible outcomes; while a realization is an outcome from one trial of that specific experiment. The expectation operator provides a bridge between the two concepts, as discussed later in this section. To help maintain clarity, the above notations for random variables will be used consistently throughout the work. Any other variables or symbols that are introduced into the text will be explained immediately following their first appearance.

With the general random variable notation established, it is possible to introduce some specific notation to describe a particle during its random walk. In this thesis individual particle histories are identified by the index i. Events (collision, absorption, cell boundary encounter, etc.) in a particle's life are identified sequentially by the index c. Values of c can range from 0, the birth event for the particle, to C_i, the event that terminates history i. The phase location of particle i during event c is given by the seven-dimensional vector $\vec{\xi}_{i,c} = (x, y, z, \theta, \varphi, E, t)_{i,c}$. The sequence of events that occur during the life of a single particle is a Markov chain[7], denoted

$$\hat{\xi}_i = \left(\bar{\xi}_{i,C_i}, \bar{\xi}_{i,C_i-1}, \ldots, \bar{\xi}_0\right). \tag{1.2}$$

Every simulated particle history produces a Markov chain $\hat{\xi}$. Each of these chains is an independent realization of the random variable ξ, which is governed by a parent distribution, $p(\xi)$, that describes the relative likelihood of all possible Markov chains[11].

Monte Carlo tallies are functions that operate on a finite set of Markov chain realizations, $\left\{\hat{\xi}_i\right\}_{i=1,N}$, and produce an estimate for some unknown parameter, t, of the distribution $p(\xi)$. All Monte Carlo tallies can be written in the general form

$$\hat{t} = s_t\left(\left\{\hat{\xi}_i\right\}_{i=1,N}\right), \tag{1.3}$$

where $\hat{t}$ is the estimate for t produced by the set of particle histories $\left\{\hat{\xi}_i\right\}_{i=1,N}$, and $s_t(\,)$ is the "tally" or "scoring" function. The scoring function is responsible for extracting selected information from the collection of particle histories. The notion of $\hat{t}$ being an estimate for some unspecified parameter t of the distribution $p(\xi)$ is deliberately left vague. The distribution $p(\xi)$ theoretically describes all particle behaviors that are physically possible in the system. Because it contains all of the relevant information, it is hypothetically possible to express any quantity of interest as a parameter of $p(\xi)$. The difficulty in developing new tallies lies in finding a suitable scoring function that gives an unbiased estimate for the parameter of interest.

The value of $\hat{t}$ in Eq. (1.3) depends on the specific set of particle histories $\left\{\hat{\xi}_i\right\}_{i=1,N}$ used in the calculation. If the simulation is rerun and a different set of independent histories are used then the value of $\hat{t}$ will change. Since its value changes

with every different set of realizations of the random variable ξ, it is clear that $\hat{t}$ is itself a realization of some random variable $\mathbf{t}$. In conventional terminology[12] the random variable $\mathbf{t}$ is referred to as a statistic, and $\hat{t}$ (a single realization of the random variable) is referred to as a point estimate of the parameter t. The statistic $\mathbf{t}$ is said to be an unbiased estimator[12] of t if

$$\bar{t} = E[\mathbf{t}] = t. \tag{1.4}$$

Mathematically proving that an estimator is unbiased allows a user to have confidence in the results generated from a Monte Carlo code.

Equation (1.3) provides a general form that applies to all Monte Carlo tallies. Most estimators, however, are fundamentally based on the arithmetic mean. Each history contributes a score to the tally and, after all histories have been run, the total score is divided by the number of independent histories to yield an average score per particle. Tallies that are based on an arithmetic mean taken over the sample of independent particle histories can be written in the form

$$\hat{t} = \frac{1}{N}\sum_{i=1}^{N} s_{\hat{\xi}}\left(\hat{\xi}_i\right), \tag{1.5}$$

where $\hat{t}$ is the estimator, N is the total number of particles run during the simulation, and $s_{\hat{\xi}}$ is the scoring function. From (1.5) it can be shown that in order for $\hat{t}$ to be an unbiased estimator for a parameter t, the scoring function $s_{\hat{\xi}}\left(\hat{\xi}_i\right)$ must itself be a point estimate of the parameter t due to the random walk of particle i. To prove this, we take the expected value of both sides of Eq. (1.5),

$$E[\hat{t}] = E\left[\frac{1}{N}\sum_{i=1}^{N} s_{\hat{\xi}}\left(\hat{\xi}_i\right)\right]. \tag{1.6}$$

Noting that the expected value of a single realization is the same as the expected value of the associated random variable[12], and using independence of the histories, Eq. (1.6) can be simplified to yield

$$E[\mathbf{t}] = \frac{1}{N}\sum_{i=1}^{N} E\left[s_{\hat{\xi}}(\xi)\right] = E\left[s_{\hat{\xi}}(\xi)\right]. \tag{1.7}$$

Applying the definition of an unbiased estimator from Eq. (1.4) shows that

$$E[\mathbf{t}] = E\left[s_{\hat{\xi}}(\xi)\right] = t. \tag{1.8}$$

This straightforward result implies that for each independent random walk, the evaluated function $s_{\hat{\xi}}(\hat{\xi}_i)$ must be a realization of the parameter t for the single particle i. As an example, we consider a tally $\hat{t}$ that is an estimator for the expected average flux in the system. In this case, Eq. (1.8) implies that the term $s_{\hat{\xi}}(\hat{\xi}_i)$ must be equal to the flux generated by particle i during its random walk. This result greatly simplifies the process of deriving and computing tallies. As long as the histories are statistically independent, the scoring function is simply a point estimator for the parameter of interest due to a single history.

In Eq. (1.5), the general form for a tally was written as the arithmetic mean of a scoring function applied to the complete Markov chains that describe individual particle histories. However, for discrete event estimators the scoring function $s_{\hat{\xi}}(\xi)$ is often a function of only the most recent particle event, and does not depend on any previous events in the chain. In these cases Eq. (1.5) can be written as

$$\hat{t} = \frac{1}{N}\sum_{i=1}^{N}\sum_{c=0}^{C_i} s_{\hat{\xi}}\left(\vec{\xi}_{i,c}\right), \tag{1.9}$$

where the variable c is an index over the sequential events in a particle's history. Note that the inner summation takes into account the fact that a particle can score multiple times to the same tally during its lifetime. Equation (1.9) does not apply to track length tallies or tallies that use cell, surface or source flagging (i.e. tallies that only score contributions from particles that were born in or passed through a predefined region of the problem[9]). These types of tallies all require information about the past behavior of the particle.

The purpose in showing these general forms for Monte Carlo estimators (Eqs. (1.3), (1.5), and (1.9)) is to provide some insight into the development of new tallies. Also, it is possible to prove many general properties of tallies based only on these abstract forms. These properties can then be applied directly to any tally that can be written in the general forms shown above. A few of these general properties are derived in the following subsections.

1.2.2. Tally Variance and the Central Limit Theorem

All effective Monte Carlo tallies combine multiple observations to produce a single estimate for a parameter of interest. Since this estimate is produced from a finite set of random samples, there will be some degree of statistical uncertainty in the results. This uncertainty means that an unbiased estimator $\hat{t}$ will not produce the true value of the parameter t based on a finite number of samples. The magnitude of the statistical uncertainty in an estimate can be approximated by measuring the spread of observed values about the expected result.

The variance of a random variable $\mathbf{x}$, denoted σ_x^2, is the average square-distance of all realizations $\hat{x}$ from the expected value $\bar{x}$. Mathematically, the variance (in one dimension) is defined as

$$\sigma_{\mathbf{x}}^2 = E\left[\left(\mathbf{x}-\bar{x}\right)^2\right]. \tag{1.10}$$

By using the definition for expected value in Eq. (1.1), the variance can also be expressed as an integral over the distribution $p(x)$,

$$\sigma_{\mathbf{x}}^2 = \int_{-\infty}^{\infty}\left(x-\bar{x}\right)^2 p(x)\,dx. \tag{1.11}$$

Equations (1.10) and (1.11) give the true variance for the random variable $\mathbf{x}$, but they require knowledge of the distribution $p(x)$. Unfortunately, the distribution $p(x)$ is an unknown quantity in particle transport applications, and Eq. (1.11) cannot be applied directly to calculate the variance.

In order to estimate the variance of $\mathbf{x}$, an unbiased estimator is needed that can be calculated directly from a set of independent random samples taken from $\mathbf{x}$. This estimator, referred to as the sample variance, is denoted $\hat{\sigma}_{\mathbf{x}}^2$ and is given by the formula

$$\hat{\sigma}_{\mathbf{x}}^2 = \frac{1}{N-1}\sum_{i=1}^{N}\left(\hat{x}_i-\hat{\hat{x}}\right)^2, \tag{1.12}$$

where $\hat{\hat{x}}$ is the estimator for $\bar{x}$,

$$\hat{\hat{x}} = \frac{1}{N}\sum_{i=1}^{N}\hat{x}_i. \tag{1.13}$$

The "double-hat" notation used in Eq. (1.12) and (1.13) is consistent with the notation scheme outlined in the previous section, but it requires some explanation for clarity. We recall that $\hat{x}_i$ is a single realization from the random variable $\mathbf{x}$. With this notation the

quantity $\hat{\hat{x}}$ is a single realization from a random variable $\hat{\mathbf{x}}$, which is defined by Eq. (1.13). The properties of the random variable $\hat{\mathbf{x}}$ will be outlined in detail later. The realizations $\hat{x}$ and $\hat{\hat{x}}$ can be easily confused because both are unbiased estimators for $\bar{x}$. In order to show that they are the same let $N=1$ in Eq. (1.13). The difference between the two realizations is that $\hat{\hat{x}}$ is a better point estimate of $\bar{x}$ than $\hat{x}$.

Returning to the derivation, it can be shown[12] that Eq. (1.12) is an unbiased estimator for $\sigma_{\mathbf{x}}^2$, and therefore, as $N \to \infty$ the estimator $\hat{\sigma}_{\mathbf{x}}^2 \to \sigma_{\mathbf{x}}^2$. The true variance $\sigma_{\mathbf{x}}^2$ measures the spread of realizations of $\mathbf{x}$ about the expected value $\bar{x}$. In Monte Carlo applications, however, the real quantity of interest is the spread of estimates $\hat{\hat{x}}$ around the true parameter $\bar{x}$. This variance, denoted $\sigma_{\hat{\mathbf{x}}}^2$, can be calculated from the true variance of the random variable $\mathbf{x}$.

To demonstrate this, we consider two independent samples $\hat{x}_1$ and $\hat{x}_2$ as estimators for the parameter $\bar{x}$. It is intuitive that the average of these two quantities, $\hat{\hat{x}} = (\hat{x}_1 + \hat{x}_2)/2$, should be a better estimate of $\bar{x}$ than either $\hat{x}_1$ or $\hat{x}_2$ individually. If the average is a better estimate, it should have a smaller variance than that for an individual realization $\left(\sigma_{\hat{\mathbf{x}}}^2 < \sigma_{\mathbf{x}}^2\right)$. Furthermore, as additional samples are included in the average, the variance of $\hat{\hat{x}}$ will continue to decrease. Let us consider an estimator $\hat{x}$ that is the arithmetic mean of N independent samples from the random variable $\mathbf{x}$,

$$\hat{\hat{x}} = \frac{1}{N}\sum_{i=1}^{N} \hat{x}_i \,. \tag{1.14}$$

The sum of independent, identically distributed (iid) random variables is itself a random variable[7,12]. Thus, in Eq. (1.14), the estimator $\hat{\hat{x}}$ is actually a realization from a random variable $\hat{\mathbf{x}}$. By the properties of the Central Limit Theorem[1,4,11,12] it can be shown that, as $N \to \infty$, the distribution $p(\hat{x})$ is normal with mean $\bar{x}$ and variance

$$\sigma_{\hat{\mathbf{x}}}^2 = \sigma_{\mathbf{x}}^2 / N . \tag{1.15}$$

The sample variance $\sigma_{\hat{\mathbf{x}}}^2$ can be calculated by substituting Eq. (1.12) into Eq. (1.15),

$$\hat{\sigma}_{\hat{\mathbf{x}}}^2 = \frac{1}{N(N-1)} \sum_{i=1}^{N} \left(\hat{x}_i - \hat{\hat{x}} \right)^2 . \tag{1.16}$$

We note the similarity between Eq. (1.14) and the general equation for a tally given in Eq. (1.5). It is trivial to apply Eq. (1.16) to this general form to show that the sample variance for a tally can be written,

$$\hat{\sigma}_{\hat{t}}^2 = \frac{1}{N(N-1)} \sum_{i=1}^{N} \left(s_{\hat{\xi}} \left(\hat{\xi}_i \right) - \hat{t} \right)^2 . \tag{1.17}$$

Equation (1.17) is used to estimate the variance in most, if not all, Monte Carlo tallies.

Being able to accurately estimate the variance of Monte Carlo tallies is extremely important for several reasons. First, estimators are not unique. For any physical quantity there can be many scoring functions that give an unbiased estimate. The variance serves as a way to quantitatively compare two different scoring functions and determine which one is more efficient. For instance, the effectiveness of non-analog estimators are judged on their ability to reduce the tally variance, relative to analog estimators, based on a fixed number of particle histories.

The second use of variance in Monte Carlo calculations is determining confidence intervals for the tally results. For an unbiased estimator the confidence is expressed as

Table 1.1. **Probabilities that a normally-distributed estimate falls within a distance I_c from the true solution. Confidence intervals are given in terms of the standard deviation of the estimate.**

Confidence Interval I_c	$p\left(\left\|\hat{t}-t\right\|\right)<I_c$
$\sigma_{\hat{t}}$	68.26%
$2\sigma_{\hat{t}}$	95.44%
$3\sigma_{\hat{t}}$	99.74%

the probability that the true parameter lies within a certain distance of the estimate. As noted earlier, for large sample sizes $(N>30)$[12] realizations of $\hat{t}$ will be normally distributed about the true parameter t with variance $\sigma_{\hat{t}}^2$. The probability of a single sample falling within a given distance from the mean is given in terms of the square root of the variance, $\sigma_{\hat{t}}$, referred to as the standard deviation. These confidence levels are well known for the normal distribution and are shown in Table 1.1.

If the sample size is not large enough for the Central Limit Theorem to be valid, the weaker Chebychev's inequality can be used to estimate the confidence. However, with modern computers it is extremely unusual to run any simulation with a sample size too small for the Central Limit Theorem to apply.

The single value reported as the variance (or standard deviation) of a tally can often be hard to interpret without some standard of comparison. To help with interpretation, many Monte Carlo codes report the accuracy of the tally in terms of the relative standard deviation,

$$R \equiv \frac{\hat{\sigma}_{\hat{t}}}{\hat{t}}. \tag{1.18}$$

Some general guidelines for interpreting the relative standard deviation for a tally[9] are given in Table 1.2.

Table 1.2. Guidelines for interpreting the relative error R

Range of R	Quality of the Tally
> 0.5	Garbage
0.2 to 0.5	Factor of a few
0.1 to 0.2	Questionable
< 0.1	Generally reliable except for point detector
< 0.05	Generally reliable for point detector

Source: Briesmeister, J.F. *MCNP – A General Monte Carlo N-Particle Transport Code.* Los Alamos National Laboratory, Report LA-13709-M, 2000.

1.2.3. Mean Value Theorem

In section 1.1.2 it was noted that Monte Carlo methods are well suited to estimating integral quantities. This property is a result of the Mean Value Theorem[1,14], which relates the average value of a function over a domain to the integral of the function over that domain. To derive this relationship, we consider a function $y = f(x)$ defined over the domain $[a,b]$. If the domain is broken up into N equally spaced partitions, the average value of the function $f(x)$ can be written as the limit,

$$\bar{y} = \lim_{N\to\infty} \frac{1}{N} \sum_{i=1}^{N} f(x_i), \tag{1.19}$$

where x_i is the midpoint of partition i. Because the partitions are equal width they are related to the size of the domain by

$$\Delta x = \frac{(b-a)}{N}. \tag{1.20}$$

Solving for N and substituting into Eq. (1.19) yields

$$\bar{y} = \frac{1}{(b-a)} \lim_{N\to\infty} \sum_{i=1}^{N} f(x_i)\Delta x_i. \tag{1.21}$$

It follows directly, by the definition of a definite integral[14], that

$$\bar{y} = \frac{1}{(b-a)} \int_a^b f(x)\,dx. \tag{1.22}$$

This powerful result forms the basis for many Monte Carlo estimators.

1.2.4. Collision Estimator of Flux

In nuclear engineering applications, the particle flux is defined as the total distance traveled (per unit time) by all particles of energies dE about E in a volume element $d\vec{r}$ about $\vec{r}$ at time t. The energy dependent flux has the units $\left[\text{cm}^{-2} \cdot \text{sec}^{-1}\right]$ and is written mathematically as

$$\phi(\vec{r}, E, t) \equiv v N_p(\vec{r}, E, t), \tag{1.23}$$

where $N_p(\vec{r}, E, t)$ is the density of particles located at the spatial position $d\vec{r}$ about $\vec{r}$ with energies dE about E at time t, and v is the velocity of a particle with energy E. Particle flux is an important quantity because it can be used, in conjunction with macroscopic cross sections, to calculate reaction rate densities. As the name implies, a reaction rate density $R_\chi(\vec{r}, E, t)\,d\vec{r}\,dE$ gives the rate $\left[\text{reactions} \cdot \text{sec}^{-1}\right]$ at which reactions of type χ occur in the volume $d\vec{r}$ about $\vec{r}$, at time t, due to incident particles of energies within dE of E. The reaction rate can be computed as

$$R_\chi(\vec{r}, E, t) = \Sigma_\chi(\vec{r}, E, t)\,\phi(\vec{r}, E, t), \tag{1.24}$$

where Σ_χ is the macroscopic cross section for reaction χ. If Eq. (1.24) is integrated over a phase volume of time, space, and energy, one obtains

$$N_\chi = \int_{\vec{r}} \int_E \int_t \Sigma_\chi(\vec{r}, E, t)\,\phi(\vec{r}, E, t)\,dt\,dE\,d\vec{r}\ , \tag{1.25}$$

which gives the total number of reactions that occur in the volume per particle. Note that, in Eq. (1.25), the flux $\phi(\vec{r},E,t)$ has been normalized by the total number of particles in the system. This normalization is standard for most nuclear engineering applications and will always be assumed unless otherwise specified.

Calculating the average number of reactions in a finite volume is a simple counting experiment that is trivial to perform in a Monte Carlo simulation. It should be clear that, for N independent particle histories, the quantity

$$\hat{N}_\chi \equiv \frac{\text{Total } \chi \text{ reactions in tally volume}}{N} \tag{1.26}$$

is an unbiased estimator for N_χ.

With an estimator for the reaction rate established, attention can be turned towards deriving an estimator for the average flux in the tally volume. The derivation will be presented using two separate methods. The first method is a sketch of the full proof that is valid only for homogenous, energy independent problems. This derivation is intended to provide insight into collision flux estimators and why they work. The second method is a more rigorous, general derivation that will be used throughout the thesis.

The first derivation begins by using the Mean Value Theorem to write the average flux in an arbitrary spatial volume V as

$$\bar{\phi} = \frac{1}{V}\int_V \phi(\vec{r})\,d\vec{r}\,. \tag{1.27}$$

We assume that the total macroscopic cross section Σ_t is constant for all locations, times, and energies in the volume V. We multiply and divide the right hand side of Eq. (1.27) by Σ_t to obtain

$$\bar{\phi} = \frac{1}{V\Sigma_t}\int_V \Sigma_t \phi(\vec{r})\, d\vec{r}\,. \tag{1.28}$$

We notice that the integral term in Eq. (1.28) is identical to Eq. (1.25). Substituting Eq. (1.25) into Eq. (1.28) gives

$$\bar{\phi} = \frac{N_t}{V\Sigma_t}. \tag{1.29}$$

Applying the unbiased estimator for N_t gives

$$\hat{\phi} = \frac{\text{Total \# of reactions in tally volume}}{V\Sigma_t N},$$

or, written in a more conventional tally format (using Eq. (1.9)),

$$\hat{\phi} = \frac{1}{NV\Sigma_t}\sum_{i=1}^{N}\sum_{k=1}^{K_i} w_{i,k}\,, \tag{1.30}$$

where k is a sequential index of collision events for particle i, and $w_{i,k}$ is the weight of particle i prior to collision k. The weights are important only in cases where variance reduction techniques are used; if analog simulation is used then w is always equal to 1. The estimator given in Eq. (1.30) is referred to as a collision estimator because it scores every time a particle undergoes a collision during the simulation. Although the total cross section Σ_t was used in the preceding derivation, it can easily be replaced with any other cross section without affecting the proof. One common alternate to the collision estimator is the absorption (or last event) estimator, in which the macroscopic absorption cross section Σ_a is used and the tally is scored only when the particle is absorbed. Absorption estimators are not commonly used because they accumulate little information (1 event per history) relative to a collision estimator, and therefore have a larger variance[6].

A modified version of the collision estimator can also be used for variance reduction when tallying the reaction rates of unlikely events. Multiplying both sides of Eq. (1.28) by the cross section for reaction χ and following the derivation gives

$$\widehat{\Sigma_\chi \phi} = \frac{\Sigma_\chi}{N V \Sigma_t} \sum_{i=1}^{N} \sum_{k=1}^{K_i} w_{i,k} , \tag{1.31}$$

where $\widehat{\Sigma_\chi \phi}$ is an estimate for the average number of reactions χ occurring throughout volume V. Equation (1.31) tallies the probability that the reaction would have occurred at each collision site. For low probability reactions, this increases the number of effective "events" that are allowed to score and lowers the variance of the tally.

One final type of tally, related to the collision estimator, deserves mentioning: the next-event estimator (or point detector). These tallies are used to estimate the flux at a single point in the system. At every collision point a next-event estimator scores the probability that the incident particle will scatter towards the tally point and travel to that point uncollided. Next-event estimators are widely used, especially in shielding applications, but they can give unreliable and incorrect results if they are not used correctly[1,9].

The above derivation and discussion of collision estimators was predicated on the assumption that the cross sections in the tally volume are independent of time, energy and space. Such an assumption is not physically realistic. For example, the energy dependence of cross sections is known to have an important role in particle transport. By inspection of Eq. (1.30) it seems reasonable to expect that energy and spatial dependence of the cross section must be taken into account by the estimator

$$\hat{\phi} = \frac{1}{NV} \sum_{i=1}^{N} \sum_{k=1}^{K_i} \frac{w_{i,k}}{\Sigma_t\left(\vec{\xi}_{i,k}\right)}, \tag{1.32}$$

where the value of Σ_t is evaluated at the particle phase position $\vec{\xi}$ for every collision. In fact, the anticipated result in Eq. (1.32) is an unbiased estimator, but the traditional proof is less than straightforward[4]. An outline of this proof, taken from a review by Dubi[15] is presented here.

To begin the derivation of the collision estimator, we recall from Eq. (1.5) that a tally for a parameter t can be written as the arithmetic mean over a sample of N independent particle histories,

$$\hat{t} = \frac{1}{N} \sum_{i=1}^{N} s_{\hat{\xi}}\left(\hat{\xi}_i\right). \tag{1.33}$$

It was also established that the scoring function $s_{\hat{\xi}}\left(\hat{\xi}_i\right)$ must be a point estimate of the parameter t due to the random walk of particle i. This was shown by taking the expected value of both sides of Eq. (1.33) to yield

$$E[\mathrm{t}] = E\left[s_{\hat{\xi}}(\xi)\right]. \tag{1.34}$$

In the general case of a collision estimator, the goal is to find a scoring function $s_{\hat{\xi}}\left(\hat{\xi}_i\right)$ such that

$$E\left[s_{\hat{\xi}}(\xi)\right] = \int_{\Gamma} f\left(\vec{\xi}\right)\phi\left(\vec{\xi}\right)d\vec{\xi}. \tag{1.35}$$

We begin by assuming a scoring function of the form

$$s_{\hat{\xi}}\left(\hat{\xi}_i\right) = s_{\hat{\xi}}\left(\vec{\xi}_{i,1}, \ldots, \vec{\xi}_{i,K_i}\right) = \sum_{k=1}^{K_i} f\left(\vec{\xi}_{i,k}\right). \tag{1.36}$$

Taking the expected value of this scoring function with respect to all possible random chains gives,

$$E\left[s_{\hat{\xi}}(\xi)\right]=\sum_{K=1}^{\infty}\int_{\Gamma}\cdots\int_{\Gamma}s_{\hat{\xi}}\left(\vec{\xi}_{i,1},\ldots,\vec{\xi}_{i,K}\right)p\left(\vec{\xi}_{i,1},\ldots,\vec{\xi}_{i,K}\right)d\vec{\xi}_{i,1}\ldots d\vec{\xi}_{i,K}$$

$$=\sum_{K=1}^{\infty}\int_{\Gamma}\cdots\int_{\Gamma}\sum_{k=1}^{K_i}f\left(\vec{\xi}_{i,k}\right)p\left(\vec{\xi}_{i,1},\ldots,\vec{\xi}_{i,K}\right)d\vec{\xi}_{i,1}\ldots d\vec{\xi}_{i,K}\,. \tag{1.37}$$

The probability of a specific chain occurring, $p\left(\vec{\xi}_{i,1},\ldots,\vec{\xi}_{i,K}\right)d\vec{\xi}_{i,1}\ldots d\vec{\xi}_{i,K}$, can be written in terms of the conditional probability functions that govern the random walk,

$$p\left(\vec{\xi}_{i,1},\ldots,\vec{\xi}_{i,K}\right)d\vec{\xi}_1\ldots d\vec{\xi}_K=$$
$$\left(p_s\left(\vec{\xi}_{i,1}\right)d\vec{\xi}_1\,q\left(\vec{\xi}_{i,1}\right)p_c\left(\vec{\xi}_{i,2}\,|\,\vec{\xi}_{i,1}\right)d\vec{\xi}_2\cdots q\left(\vec{\xi}_{i,K-1}\right)p_c\left(\vec{\xi}_{i,K}\,|\,\vec{\xi}_{i,K-1}\right)p_t\left(\vec{\xi}_{i,K}\right)d\vec{\xi}_K\right). \tag{1.38}$$

In Eq. (1.38) the factor $p_s\left(\vec{\xi}_1\right)d\vec{\xi}_1$ is the probability that a source particle will be born within $d\vec{\xi}_1$ of $\vec{\xi}_1$; the quantity $p_c\left(\vec{\xi}_k\,|\,\vec{\xi}_{k-1}\right)d\vec{\xi}_k$ is the probability a particle will undergo its next collision within $d\vec{\xi}_k$ of $\vec{\xi}_k$ given that the last collision occurred at $\vec{\xi}_{k-1}$; the quantity $p_t\left(\vec{\xi}_k\right)$ is the probability that a particle undergoing a collision at $\vec{\xi}_k$ will be absorbed or otherwise terminated during that event; and $q\left(\vec{\xi}_{k-1}\right)=1-p_t\left(\vec{\xi}_{k-1}\right)$ is the probability that a particle undergoing a collision at $\vec{\xi}_k$ will not be terminated during the event. Substituting this definition for the random walk into Eq. (1.37) gives

$$E\left[s_{\hat{\xi}}(\xi)\right]=\sum_{K=1}^{\infty}\int_{\Gamma}\cdots\int_{\Gamma}\sum_{k=1}^{K_i}f\left(\vec{\xi}_k\right)$$
$$\left(p_s\left(\vec{\xi}_1\right)q\left(\vec{\xi}_1\right)p_c\left(\vec{\xi}_2\,|\,\vec{\xi}_1\right)\cdots q\left(\vec{\xi}_{K-1}\right)p_c\left(\vec{\xi}_K\,|\,\vec{\xi}_{K-1}\right)p_t\left(\vec{\xi}_K\right)\right)d\vec{\xi}_1\ldots d\vec{\xi}_K$$

$$E\left[s_{\tilde{\xi}}(\xi)\right]=\sum_{K_i=1}^{\infty}\sum_{k=1}^{K_i}\int_{\Gamma}\cdots\int_{\Gamma}p_s\left(\vec{\xi}_1\right)q\left(\vec{\xi}_1\right)\cdots$$
$$p_c\left(\vec{\xi}_k\mid\vec{\xi}_{k-1}\right)q\left(\vec{\xi}_k\right)f\left(\vec{\xi}_k\right)p_c\left(\vec{\xi}_{k+1}\mid\vec{\xi}_k\right)\cdots \tag{1.39}$$
$$q\left(\vec{\xi}_{K-1}\right)p_c\left(\vec{\xi}_K\mid\vec{\xi}_{K-1}\right)p_t\left(\vec{\xi}_K\right)d\vec{\xi}_1\ldots d\vec{\xi}_K.$$

By expanding the summation over K and collecting terms, Eq. (1.39) can be written as

$$E\left[s_{\tilde{\xi}}(\xi)\right]=\sum_{k=1}^{\infty}\int_{\Gamma}d\vec{\xi}_1\cdots\int_{\Gamma}p_s\left(\vec{\xi}_1\right)q\left(\vec{\xi}_1\right)\cdots q\left(\vec{\xi}_{k-1}\right)p_c\left(\vec{\xi}_k\mid\vec{\xi}_{k-1}\right)f\left(\vec{\xi}_k\right)d\vec{\xi}_k$$
$$\left[p_t\left(\vec{\xi}_k\right)+\int_{\Gamma}q\left(\vec{\xi}_k\right)p_c\left(\vec{\xi}_{k+1}\mid\vec{\xi}_k\right)p_t\left(\vec{\xi}_{k+1}\right)d\vec{\xi}_{k+1}\right.$$
$$+\int_{\Gamma}\int_{\Gamma}q\left(\vec{\xi}_k\right)p_c\left(\vec{\xi}_{k+1}\mid\vec{\xi}_k\right)q\left(\vec{\xi}_{k+1}\right) \tag{1.40}$$
$$p_c\left(\vec{\xi}_{k+2}\mid\vec{\xi}_{k+1}\right)p_t\left(\vec{\xi}_{k+2}\right)d\vec{\xi}_{k+1}\,d\vec{\xi}_{k+2}$$
$$+\ldots+\int_{\Gamma}\cdots\int_{\Gamma}q\left(\vec{\xi}_k\right)p_c\left(\vec{\xi}_{k+1}\mid\vec{\xi}_k\right)\cdots$$
$$\left.\ldots q\left(\vec{\xi}_{K-1}\right)p_c\left(\vec{\xi}_K\mid\vec{\xi}_{k-1}\right)p_t\left(\vec{\xi}_K\right)d\vec{\xi}_{k+1}\ldots d\vec{\xi}_K+\ldots\right].$$

The factor inside the brackets in this expression has a physical interpretation related to the probability that a particle will undergo a given number of collisions during its random walk. If the series in brackets is truncated at some finite value of K, then it gives the probability that a particle will undergo exactly K collisions before being terminated. However, because the series is infinite, it will always be equal to 1 because every particle must eventually be terminated in a realistic Monte Carlo simulation. This observation can be used to reduce Eq. (1.40) to yield a more manageable form

$$E\left[s_{\tilde{\xi}}(\xi)\right]=\sum_{k=1}^{\infty}\int_{\Gamma}\cdots\int_{\Gamma}p_s\left(\vec{\xi}_1\right)q\left(\vec{\xi}_1\right)\cdots q\left(\vec{\xi}_{k-1}\right)p_c\left(\vec{\xi}_k\mid\vec{\xi}_{k-1}\right)f\left(\vec{\xi}_k\right)d\vec{\xi}_1\ldots d\vec{\xi}_k. \tag{1.41}$$

Now that the expected value of the scoring function has been calculated, all that remains is to show that it is equivalent to the right hand side of Eq. (1.35). To demonstrate this, let us consider the integral form of the non-multiplying transport equation for the collision density $N_t\left(\vec{\xi}\right)$ with source term $S\left(\vec{\xi}\right)$ and scattering kernel $K\left(\vec{\xi},\vec{\xi}'\right)$,

$$N_t\left(\vec{\xi}\right)=S\left(\vec{\xi}\right)+\int_\Gamma K\left(\vec{\xi},\vec{\xi}'\right)N_t\left(\vec{\xi}'\right)d\vec{\xi}'. \tag{1.42}$$

It can be shown[4,15] that Eq. (1.42) can be expanded in a Neumann series to yield,

$$N_t\left(\vec{\xi}\right)=\sum_{k=1}^{\infty}\int_\Gamma\cdots\int_\Gamma S\left(\vec{\xi}_1\right)K\left(\vec{\xi}_2,\vec{\xi}_1\right)\cdots K\left(\vec{\xi},\vec{\xi}_{k-1}\right)d\vec{\xi}_1\ldots d\vec{\xi}_{k-1}. \tag{1.43}$$

Multiplying Eq. (1.43) by $f\left(\vec{\xi}\right)$ and integrating over $\vec{\xi}$ gives

$$f\left(\vec{\xi}\right)N_t\left(\vec{\xi}\right)=\sum_{k=1}^{\infty}\int_\Gamma\cdots\int_\Gamma S\left(\vec{\xi}_1\right)K\left(\vec{\xi}_2,\vec{\xi}_1\right)\cdots K\left(\vec{\xi},\vec{\xi}_{k-1}\right)f\left(\vec{\xi}\right)d\vec{\xi}_1\ldots d\vec{\xi}_{k-1},$$

$$\int_\Gamma f\left(\vec{\xi}\right)N_t\left(\vec{\xi}\right)d\vec{\xi}$$

$$=\int_\Gamma\sum_{k=1}^{\infty}\int_\Gamma\cdots\int_\Gamma S\left(\vec{\xi}_1\right)K\left(\vec{\xi}_2,\vec{\xi}_1\right)\cdots K\left(\vec{\xi},\vec{\xi}_{k-1}\right)f\left(\vec{\xi}\right)d\vec{\xi}_1\ldots d\vec{\xi}_{k-1}\,d\vec{\xi},$$

$$\int_\Gamma f\left(\vec{\xi}\right)N_t\left(\vec{\xi}\right)d\vec{\xi}$$

$$=\sum_{k=1}^{\infty}\int_\Gamma\cdots\int_\Gamma S\left(\vec{\xi}_1\right)K\left(\vec{\xi}_2,\vec{\xi}_1\right)\cdots K\left(\vec{\xi}_k,\vec{\xi}_{k-1}\right)f\left(\vec{\xi}_k\right)d\vec{\xi}_1\ldots d\vec{\xi}_k. \tag{1.44}$$

For any random walk process that obeys the integral transport equation given in (1.42), the probability density functions that govern the random walk can be written in terms of parameters found in the transport equation itself. For a non-multiplying particle transport problem it can be shown[15] that the following equalities hold:

$$p_s\left(\vec{\xi}\right)=S\left(\vec{\xi}\right), \qquad \textit{(Normalized Source Distribution)} \tag{1.45}$$

$$p_c\left(\vec{\xi}_k\mid\vec{\xi}_{k-1}\right)=\frac{K\left(\vec{\xi}_k,\vec{\xi}_{k-1}\right)}{q\left(\vec{\xi}_{k-1}\right)}. \qquad \textit{(Normalized Collision Kernel)} \tag{1.46}$$

Substituting these definitions into Eq. (1.44) gives

$$\int_\Gamma f\left(\vec{\xi}\right)N_t\left(\vec{\xi}\right)d\vec{\xi}$$

$$=\sum_{k=1}^{\infty}\int_\Gamma\cdots\int_\Gamma p_s\left(\vec{\xi}_1\right)q\left(\vec{\xi}_1\right)\cdots q\left(\vec{\xi}_{k-1}\right)p_c\left(\vec{\xi}_k\mid\vec{\xi}_{k-1}\right)f\left(\vec{\xi}_k\right)d\vec{\xi}_1\ldots d\vec{\xi}_k. \tag{1.47}$$

By inspection of Eqs. (1.47) and (1.41), it follows directly that

$$\int_{\Gamma} f\left(\vec{\xi}\right) N_t\left(\vec{\xi}\right) d\vec{\xi} = E\left[s_{\hat{\xi}}(\xi)\right], \tag{1.48}$$

thus completing the proof that the scoring function

$$\hat{f}_i = \sum_{k=1}^{K_i} f\left(\vec{\xi}_{i,k}\right) \tag{1.49}$$

is an unbiased point estimator for the parameter

$$\bar{f} \equiv \int_{\Gamma} f\left(\vec{\xi}\right) N_t\left(\vec{\xi}\right) d\vec{\xi}\,. \tag{1.50}$$

If N independent particle histories are simulated, then Eq. (1.33) can be used to produce a lower-variance estimator for $\bar{f}$, given by

$$\hat{f} = \frac{1}{N} \sum_{i=1}^{N} \sum_{k=1}^{K_i} f\left(\vec{\xi}_{i,k}\right). \tag{1.51}$$

Equation (1.51) was derived by assuming an analog particle transport simulation in a non-multiplying medium. These assumptions were used only to simplify the preceding derivation and do not imply a limitation in the estimator itself. Spanier and Gelbard[4] reported a generalized proof that holds in all commonly encountered situations. This general proof can be used to derive the collision estimator for simulations using implicit capture variance reduction and shows that the estimator takes the form

$$\hat{f} = \frac{1}{N} \sum_{i=1}^{N} \sum_{k=1}^{K_i} w_{i,k}\, f\left(\vec{\xi}_{i,k}\right), \tag{1.52}$$

where $w_{i,k}$ is the statistical "weight" of particle i following collision k. We notice that, in the case $w_{i,k} = 1$, the estimator in Eq. (1.52) reduces to the analog estimator in Eq. (1.51), as expected.

Until this point, the term $f(\xi)$ has been left as an arbitrary function. If $f(\xi)$ is defined to take the form

$$f(\xi)=\frac{1}{V\Sigma_t(\xi)}, \tag{1.53}$$

it can be substituted into Eq. (1.50) to yield,

$$\bar{f}=\frac{1}{V}\int_\Gamma \frac{N_t(\vec{\xi})}{\Sigma_t(\vec{\xi})}d\vec{\xi}. \tag{1.54}$$

We note that the definition of $f(\xi)$ is not valid if $\Sigma_t(\vec{\xi})=0$ for any $\vec{\xi}\in\Gamma$. This result confirms the earlier statement that the collision estimator will not work in void regions of a problem. To continue the derivation, recall that the total collision density is defined as

$$N_t(\vec{\xi})=\Sigma_t(\vec{\xi})\phi(\vec{\xi}). \tag{1.55}$$

Substituting this result into Eq. (1.54) gives

$$\bar{f}=\frac{1}{V}\int_\Gamma \phi(\vec{\xi})d\vec{\xi}=\bar{\phi}. \tag{1.56}$$

Equation (1.51) can now be used to develop an unbiased estimator for Eq. (1.56),

$$\hat{\phi}=\frac{1}{NV}\sum_{i=1}^{N}\sum_{k=1}^{K_t}\frac{1}{\Sigma_t(\vec{\xi}_{t,k})}. \tag{1.57}$$

Before continuing, it is important to note that the above derivation can be easily modified to produce estimators for "flux moments" of the form

$$\bar{G}=\int_\Gamma g(\vec{\xi})\phi(\vec{\xi})d\vec{\xi}, \tag{1.58}$$

where $g(\vec{\xi})$ is an arbitrary function. These estimators can be derived by replacing Eq. (1.53) with $f(\xi) = \frac{g(\xi)}{\Sigma_t(\xi)}$ and repeating the derivation to show that

$$\widehat{G} = \frac{1}{N}\sum_{i=1}^{N}\sum_{k=1}^{K_i}\frac{g(\vec{\xi}_{i,k})}{\Sigma_t(\vec{\xi}_{i,k})} \tag{1.59}$$

is an unbiased estimator of $\bar{G}$. Equation (1.59) is very important for estimating integral reaction rates and developing Functional Expansion Tallies, which will be discussed in detail later.

1.2.5. Track Length Estimator of Flux

The accuracy of a collision estimator is directly related to the number of collisions that occur in the tally region. In regions with very small cross sections, these estimators may give unreliable estimates. Also, collision estimators cannot be used to estimate the flux in a vacuum region. These limitations prompted the development of a completely different flux tally: the track length (or path length) estimator.

A heuristic derivation of the track length estimator can be made by simply considering the definition of the scalar flux, given in Eq. (1.23). The speed factor has units $\left[\text{cm}\cdot\text{sec}^{-1}\right]$, which physically corresponds to the distance traveled (or path generated) by a single particle per unit time. The $N_p(\vec{\xi})$ factor is the particle density, which gives the number of particles per unit phase space at the phase location $\vec{\xi}$. When these two factors are multiplied together they give the scalar flux, which can be interpreted as the total path length traveled per unit time and unit phase volume by all

particles passing through $\vec{\xi}$[16]. This interpretation of scalar flux can be written mathematically as

$$\phi\left(\vec{\xi}\right)d\vec{\xi} \equiv \text{Rate at which particles generate path length in d}\vec{\xi} \text{ about } \vec{\xi}\,. \qquad (1.60)$$

Equation (1.60) can be integrated over some arbitrary phase volume Γ to give

$$\int_{\Gamma}\phi\left(\vec{\xi}\right)d\vec{\xi} \equiv \text{Total path length is generated by particles in } \Gamma\,. \qquad (1.61)$$

By dividing both sides by the spatial volume of Γ and applying the Mean Value Theorem, Eq. (1.61) becomes

$$\bar{\phi} = \frac{1}{V}\int_{\Gamma}\phi\left(\vec{\xi}\right)d\vec{\xi} \equiv \frac{\text{Total path length is generated by particles in } \Gamma}{V}\,. \qquad (1.62)$$

The right hand side of Eq. (1.62) is easily estimated in Monte Carlo simulations by simply adding the total distance traveled by each particle in the tally region multiplied by the weight of the particle and dividing by the volume of the tally region,

$$\hat{\phi} = \frac{1}{NV}\sum_{i=1}^{N}\sum_{c=1}^{C_i} w_{i,c}\, d_{i,c,\Gamma} = \frac{\text{Total path length generated by particles in } \Gamma}{\text{per starting particle}}\,, \qquad (1.63)$$

where $d_{i,c,\Gamma}$ is the distance traveled by particle i in phase volume Γ as it moves between events $c-1$ and c. We notice that, as mentioned earlier, the score $d_{i,c,\Gamma}$ is a function of both the present position of the particle $\vec{\xi}_{i,c}$ and the previous position of the particle $\vec{\xi}_{i,c-1}$.

The preceding derivation of the track length estimator is based solely upon observations on the definition of scalar flux. Several sources give more rigorous and detailed proofs[4,13,15] that Eq. (1.63) is an unbiased estimator of Eq. (1.62), but these proofs do not add any new insight into the properties of the track length estimator and will be omitted here.

1.2.6. Surface Crossing Estimators

The final estimator that will be mentioned in this section is the surface crossing estimator for the total particle current through a surface. This estimator is used for calculating the expected number of particles that will pass through some arbitrary surface, S, in the problem geometry. The traditional surface crossing estimator is based on the definition

$$\left|\vec{s}\cdot\vec{j}\left(\vec{\xi}\right)\right|d\vec{\xi} \equiv \begin{array}{c}\text{Expected number of particles crossing surface S}\\ \text{within d}\vec{\xi}\text{ of phase position }\vec{\xi},\end{array} \tag{1.64}$$

where $\vec{s}$ is the unit vector normal to the surface. The vector $\vec{j}\left(\vec{\xi}\right)$ is the angular current density, a quantity that is related to the angular flux by the relationship

$$\vec{j}\left(\vec{\xi}\right)=\vec{\Omega}\phi\left(\vec{\xi}\right), \tag{1.65}$$

where $\vec{\Omega}$ is a unit vector that specifies the direction of the particle. If Eq. (1.64) is integrated over a phase volume Γ_S defined along the surface S, the result becomes

$$\int_{\Gamma_S}\left|\vec{s}\cdot\vec{j}\left(\vec{\xi}\right)\right|d\vec{\xi} \equiv \text{Total number of particles crossing surface S in } \Gamma_S. \tag{1.66}$$

We note that if the absolute value in Eq. (1.66) is removed, the resulting integral gives the net number of particles crossing S in Γ_S. By dividing both sides of Eq. (1.66) by the area of surface S and applying the Mean Value Theorem it is easy to show that

$$\overline{j_S}=\frac{1}{A_S}\int_{\Gamma_S}\left|\vec{s}\cdot\vec{j}\left(\vec{\xi}\right)\right|d\vec{\xi} \equiv \frac{\text{Total number of particles crossing S in } \Gamma_S}{A_S}. \tag{1.67}$$

The right hand side of Eq. (1.67) is now in a form that can be easily tallied during a Monte Carlo simulation. It is straightforward to show that an unbiased estimator for (1.67) can be obtained by adding the total weight (number for analog Monte Carlo) of

surface crossing events that occur within the boundaries of Γ_S and dividing by the total surface area of S and the total number of independent histories. This can be written concisely as

$$\widehat{j}_S = \frac{1}{N A_S} \sum_{i=1}^{N} \sum_{k=1}^{J_i} w_{i,k}, \tag{1.68}$$

where $w_{i,k}$ is the weight of particle i as it crosses surface S for the k^{th} time and J_i is the total number of times particle i crosses surface S. The index k has been deliberately reused here to illustrate the similarities between Eq. (1.68), the surface crossing estimator for current, and Eq. (1.32), the collision estimator for flux. Both are discrete event estimators of the general form shown in Eq. (1.9).

A more formal and general derivation of Eq. (1.68) is presented in a review by Dubi[15] and will be outlined here. This derivation of the surface crossing estimator begins by considering the integral

$$\bar{f} = \int_{\Gamma_S} f\left(\vec{\xi}\right) \phi\left(\vec{\xi}\right) d\vec{\xi} \tag{1.69}$$

taken over a finite arbitrary surface S. Now define a parallel surface S' located a small distance, Δz, away from the original surface. The two surfaces S and S' bound a small volume element, which will be referred to as V_S. For a sufficiently small Δz between the two surfaces it is reasonable to approximate Eq. (1.69) by the volume integral

$$\bar{f} = \bar{f}_V + O[\Delta z] = \frac{1}{V_S} \int_{V_S} f\left(\vec{\xi}\right) \phi\left(\vec{\xi}\right) d\vec{\xi} + O[\Delta z]. \tag{1.70}$$

The volume integral given in Eq. (1.70) is in an ideal form for estimation by a track length estimator. This can be shown by writing $f\left(\vec{\xi}\right) = f\left(\vec{\xi}_S\right) + O[\Delta z]$, where $f\left(\vec{\xi}_S\right)$ is

the function $f\left(\vec{\xi}\right)$ evaluated at the phase location where the particle first crosses at the surface S. Substituting this result into Eq. (1.70) gives

$$\overline{f} = \overline{f}_V + O[\Delta z] = \frac{1}{V_S}\int_{V_S} f\left(\vec{\xi}_S\right)\phi\left(\vec{\xi}\right)d\vec{\xi} + O[\Delta z]. \tag{1.71}$$

The track length estimator derived in Eq. (1.63) can now be applied to give an unbiased estimator for $\overline{f}_V$

$$\hat{f}_V = \frac{1}{NV}\sum_{i=1}^{N}\sum_{k=1}^{J_i} w_{i,k}\, d_{i,k,V}\, f\left(\vec{\xi}_{i,k,S}\right),$$

$$\hat{f}_V = \frac{1}{N A_S}\sum_{i=1}^{N}\sum_{k=1}^{J_i} \frac{d_{i,k,V}}{\Delta z} w_{i,k}\, f\left(\vec{\xi}_{i,k,S}\right), \tag{1.72}$$

where the variable k has been used to index the number of times that a single particle i passes through the volume V. If Δz is chosen to be sufficiently small, no particle will suffer a collision within the volume V and the distance d that a particle travels through V can be expressed using a simple trigonometric relationship

$$d_{i,k,V} = \Delta z \left|\vec{s}_{i,k}\cdot\vec{\Omega}_{i,k}\right|^{-1}. \tag{1.73}$$

Rearranging Eq. (1.73) and substituting into Eq. (1.72) yields

$$\hat{f}_V = \frac{1}{N A_S}\sum_{i=1}^{N}\sum_{k=1}^{J_i} w_{i,k}\, f\left(\vec{\xi}_{i,k,S}\right)\left|\vec{s}_{i,k}\cdot\vec{\Omega}_{i,k}\right|^{-1}. \tag{1.74}$$

Multiplying by A_S and taking the limit as $\Delta z \to 0$ for Eq. (1.71), we obtain

$$\overline{f} = \lim_{\Delta z\to 0}\left[A_s\,\overline{f}_V + O[\Delta z]\right] = \lim_{\Delta z\to 0}\left[\frac{A_S}{V_S}\int_{V_S} f\left(\vec{\xi}_S\right)\phi\left(\vec{\xi}\right)d\vec{\xi} + O[\Delta z]\right],$$

$$\overline{f} = \lim_{\Delta z\to 0}\left[\frac{1}{\Delta z}\int_{\Delta z}\int_{\Gamma_S} f\left(\vec{\xi}\right)\phi\left(\vec{\xi}\right)d\vec{\xi}\,dz\right],$$

$$\overline{f} = \int_{\Gamma_S} f\left(\vec{\xi}\right)\phi\left(\vec{\xi}\right)d\vec{\xi}\,. \tag{1.75}$$

Its estimator Eq. (1.74)

$$\hat{f} = \lim_{\Delta z \to 0} A_S\,\hat{f}_V = \lim_{\Delta z \to 0}\left[\frac{1}{N}\sum_{i=1}^{N}\sum_{k=1}^{J_i} w_{i,k}\, f\left(\vec{\xi}_{i,k,S}\right)\left|\vec{s}_{i,k}\cdot\vec{\Omega}_{i,k}\right|^{-1}\right],$$

$$\hat{f} = \frac{1}{N}\sum_{i=1}^{N}\sum_{k=1}^{J_i} w_{i,k}\, f\left(\vec{\xi}_{i,k,S}\right)\left|\vec{s}_{i,k}\cdot\vec{\Omega}_{i,k}\right|^{-1}, \tag{1.76}$$

completes the derivation of an unbiased estimator for Eq. (1.69).

The function $f(\xi)$ has been deliberately left as an arbitrary function until this point because Eqs. (1.75) and (1.76) are in a very general form that can be used to derive several different estimators. To obtain an estimator for the total current through the surface S, define $f\left(\vec{\xi}\right) = \left|\vec{s}\cdot\vec{\Omega}\right| / A_S$ to yield,

$$\overline{f} = \frac{1}{A_S}\int_{\Gamma_S}\left|\vec{s}\cdot\vec{\Omega}\right|\phi\left(\vec{\xi}\right)d\vec{\xi}$$

$$\overline{j}_S = \overline{f} = \frac{1}{A_S}\int_{\Gamma_S}\left|\vec{s}\cdot\vec{j}\left(\vec{\xi}\right)\right|d\vec{\xi} \tag{1.77}$$

and its associated estimator

$$\hat{f} = \frac{1}{N}\sum_{i=1}^{N}\sum_{k=1}^{J_i} w_{i,k}\,\left|\vec{s}_{i,k}\cdot\vec{\Omega}_{i,k}\right|\left|\vec{s}_{i,k}\cdot\vec{\Omega}_{i,k}\right|^{-1}$$

$$\hat{j}_S = \hat{f} = \frac{1}{N}\sum_{i=1}^{N}\sum_{k=1}^{J_i} w_{i,k}\,. \tag{1.78}$$

It is worth mentioning that the surface crossing estimator can also be modified to tally particle flux on a surface. Unlike the collision and track length estimators, which estimate the average volumetric flux, the surface crossing flux tally gives an estimate for

the average flux over the surface S. This can be shown by defining $f(\xi) = 1/A_S$ in Eqs. (1.75) and (1.76). Making this substitution gives

$$\bar{\phi}_S = \bar{f} = \frac{1}{A_S} \int_{\Gamma_S} \phi(\vec{\xi}) d\vec{\xi}, \tag{1.79}$$

with the estimator

$$\hat{\phi}_S = \hat{f} = \frac{1}{N A_S} \sum_{i=1}^{N} \sum_{k=1}^{J_i} \frac{w_{i,k}}{|\vec{s}_{i,k} \cdot \vec{\Omega}_{i,k}|}$$

$$\hat{\phi}_S = \frac{1}{N A_S} \sum_{i=1}^{N} \sum_{k=1}^{J_i} \frac{w_{i,k}}{\mu_{i,k}}, \tag{1.80}$$

where μ has been defined as the cosine of the angle between the particle direction $\vec{\Omega}$ and the surface normal $\vec{s}$. One common concern with this type of tally is that the estimator in Eq. (1.80) is unbounded, and therefore variance estimates may be unreliable. The score for a single particle event approaches infinity as the particle's direction becomes tangent to the surface, $|\vec{s} \cdot \vec{\Omega}| = 0$. A variety of techniques have been developed to ensure that the resulting estimate is bounded and accurate, except in pathologic cases[1,9].

The usefulness of the preceding derivation lies in the fact that Eq. (1.76) can also be used as an estimator for surface flux and current moments of the forms

$$\bar{G} = \int_{\Gamma_S} g(\vec{\xi}) \phi(\vec{\xi}) d\vec{\xi}, \tag{1.81}$$

$$\bar{H} = \int_{\Gamma_S} h(\vec{\xi}) |\vec{s} \cdot \vec{j}(\vec{\xi})| d\vec{\xi}. \tag{1.82}$$

As noted earlier, these moments are important for the Functional Expansion Tally derivations that are to follow in subsequent chapters.

1.3. The Functional Expansion Tally (FET)

While traditional Monte Carlo tallies work very well for estimating integral quantities, they are limited in their abilities to estimate the distributions of particle flux or current with respect to space, angle, energy or time. This limitation stems from the fact that Monte Carlo is essentially a stochastic numerical integration technique.

There are, however, many applications in which the shape of the flux or current distributions is desired. For such cases, the typical Monte Carlo approach has been to approximate the true distribution by a histogram. These histogram approximations are created by partitioning phase space into "bins" and then using Monte Carlo to tally the integrated flux in each bin, as shown in Figure 1. When normalized by the bin width, the results from these tallies form a step approximation to the true distribution. The resolution and accuracy of the histogram approximation can be increased by partitioning the phase space into finer bins. However, this reduces the number of particles that score in an individual tally bin, causing an increase in the variance of the estimate in each bin. The tradeoff between resolution and increased variance means that very large numbers of histories are required to get detailed distributions that have reasonable statistics when histogram tallying is used.

An alternative approach is to use Monte Carlo to estimate moments of the flux or current distributions with respect to some set of basis functions. We note that, because the moments are actually integral quantities, they are ideal for estimation by Monte Carlo methods. If the basis functions form a complete set, it is possible to represent the shape of the unknown distribution as a series expansion involving the estimated moments. This technique, referred to as the functional expansion tally (FET), provides a continuous

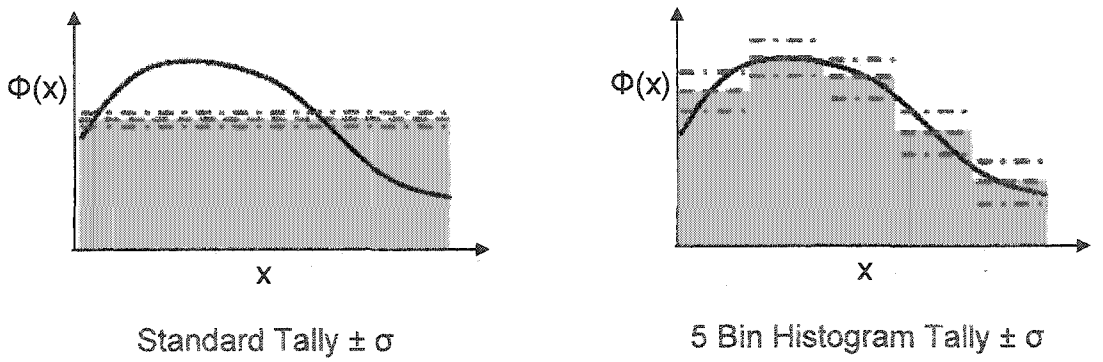

Figure 1.1. Illustration of the differences between a traditional tally and a histogram or "mesh" tally. Dashed lines indicate a hypothetical 1 standard deviation uncertainty band.

analytical representation of the unknown distribution that, in many cases, is a better representation than a comparable histogram approximation.

The concept of using series expansion to approximate the shape of unknown statistical distributions has been known for many years. A good example of an early application occurs in a 1945 paper by Rice[17]. In this paper, the author demonstrates that the random noise current $I(t)$ occurring over an interval of T seconds in an electrical signal can be expressed as a Fourier series expansion,

$$I(t) = \frac{a_0}{2} + \sum_{n=1}^{N} \left(a_n \cos\left(\frac{2\pi nt}{T}\right) + b_n \sin\left(\frac{2\pi nt}{T}\right) \right). \tag{1.83}$$

In the case of truly random noise, the coefficients $\{a_n\}_{n=0}^{N}$ and $\{b_n\}_{n=1}^{N}$ are independent random variables that follow a normal distribution about zero. We note that, in this circumstance, the noise current $I(t)$ is actually just a realization of a random variable I. Although it may seem unusual to consider a function as a realization of a random variable, mathematically this presents no difficulties or ambiguities. Unfortunately, such functional realizations from a random variable can be difficult to write in a closed form or analyze. Often the set of possible realizations will span a large

class of functions (e.g. all piecewise smooth functions). This generality can make it difficult to calculate statistics for the random variable analytically. Rice was among the first to show that these functional realizations could be expressed as a series expansion that includes the more common single-value realization random variables as the coefficients. This expansion makes it much easier to analyze the statistical properties of the original random variable. Although the Monte Carlo method had yet to be mentioned, this paper laid the groundwork for a new class of continuous Monte Carlo estimators.

The earliest known reference to the functional expansion technique (FET) for Monte Carlo occurred in a 1975 paper by Chadsey, Wilson, and Pine[18]. This paper demonstrated that a Monte Carlo simulation can be used to estimate the spherical harmonics expansion coefficients of the angular distribution of x-ray photoemission. The authors noted that the use of a functional expansion representation of the angular distribution had several advantages over a traditional discrete histogram representation. First, the estimated solution was a continuous function, which can be more convenient to treat in post processing analysis. Additionally, the authors stated that "the statistical fluctuations inherent in Monte Carlo calculations can be properly damped out" by use of the FET, and that by selecting an appropriate set of basis functions for the expansion, the FET can offer "substantial variance reduction." No formal proofs or substantive demonstrations for any of these assertions were presented in the paper.

In 1976, a follow up paper by Beers and Pine[19] generalized the FET for any Monte Carlo simulation. The 1976 paper also expanded the FET, and proposed a technique for estimating functional expansion coefficients as particles generate track

length in a given region. The applicability of these methods was demonstrated for electron transport problems using Legendre polynomials and spherical harmonics as basis sets. In this paper five specific advantages of the FET method are cited:

1. "An analytical representation of the data is given; such representations are convenient for the incorporation of the results in further physical calculations."

2. "The problem may reduce to the calculation of only a very few quantities."

3. "Significant variance reduction may occur."

4. "The continuous representation may be the "best possible" for a given number of histories."

5. "Prohibitive multidimensional calculations may become practicable."

The authors state that the examples given in the paper "show these features clearly," although, again, no formal proofs or numerical demonstrations of these assertions were presented.

The first application of the FET for neutron transport Monte Carlo simulations was published by Noel and Wio in 1984[20]. In this paper the FET was used to estimate the angular and spatial distributions of the neutron flux in a 1-D slab shielding problem. The authors used Laguerre polynomials to expand the spatial distribution and Legendre polynomials to expand the angular distribution. This paper was the first to estimate the variance in the functional expansion, which is itself a functional expansion, over the entire expansion domain.

In 1999, Spanier[21] expanded the work of Beers and Pine[19] by developing three types of Monte Carlo estimators for tallying coefficients for a 1-D functional expansion in space: the terminal, collision, and track length estimators. Of these estimators the

track length estimator is the most interesting because it allows a particle to contribute to the estimate of the expansion coefficients over its entire path, not just at discrete points. Spanier's work was primarily aimed at developing Monte Carlo variance reduction techniques that could achieve geometric error convergence rates. Similar research using Monte Carlo functional expansions was published by Booth[22] in 1999, and Lichtenstein and Favorite[23] in 2003.

Recently, several new papers have reported novel applications of the FET. In 2004, Legrady and Hoogenboom presented two papers[24,25] on the use of a Legendre polynomial based FET method for calculating and visualizing the detector response in borehole logging applications. Also in 2004, Rearden[26] published an article on the use of perturbation based sensitivity analysis for reactor safety applications. This article outlines the use of an FET-like methodology for calculating neutron flux moments and angular flux distributions. These distributions, in turn, are used to calculate the scattering terms of the sensitivity coefficients used in the perturbation analysis.

1.4. Description of Work

Although the general methodology and applicability of the FET for Monte Carlo simulations has been widely reported, there has been a lack of work regarding the theoretical properties of the technique. In each paper reviewed in the previous section, the FET was developed and implemented for one specific application. Any general properties of the method were inferred by simply considering empirical results. However, the FET can be more than an ad-hoc method for improving tally performance

in specific instances. In fact, the method is a significant step towards overcoming one of the major limitations that remain in Monte Carlo methods: the lack of continuous tallies.

One of the most touted benefits of Monte Carlo methods has been their continuous nature. Monte Carlo codes can track through arbitrary geometries, and use continuous energy cross sections, whereas deterministic methods require that these variables be discretized before a solution can be obtained. Unfortunately, traditional Monte Carlo tallies give integral, not continuous, results. The FET provides an effective, and easily implemented, method for overcoming this limitation.

Recent work [27-30] has sought to broaden the theoretical understanding of the FET. This thesis will review and expand on previous work in an attempt to develop a theoretical basis for the mathematical properties of the FET. Specifically, this work includes: new derivations for the FET estimators and their associated variances, formal proofs of the convergence properties of the FET estimators, formal demonstration that the FET can provide a better approximation to the shape of an unknown distribution than a comparable histogram approximation, and an overview of other applications of the FET. All of the theoretical results were experimentally verified by implementing and testing the FET in a production level Monte Carlo code. A further review of results contained in this thesis will be broken down by chapter.

Chapter 2 contains updated derivations of the discrete event FET estimators for average particle flux in a volume and average particle current through a surface. Estimators are also derived for the variance of individual expansion coefficients, the variance of the final functional approximation, and the truncation error present in the approximation. A series of one-dimensional test problems are presented to demonstrate

that results from the FET approximation agree with the benchmark histogram approximation to the true distribution.

Chapter 3 presents a detailed mathematical analysis of the convergence properties of the discrete event FET for Monte Carlo calculations. The goal of this chapter is to prove that the FET can provide a better approximation for the shape of an unknown distribution than a traditional histogram (or mesh) tally. To prove this, FET and histogram approximations were considered for the set of all piecewise smooth distributions defined over the expansion domain. To quantify the accuracy of each approximation, the 2-norm of the residual between the approximation and the actual distribution was used. For both the FET and histogram tallies it was found that the accuracy of the final approximation depends on two sources of error: truncation error and statistical error.

Truncation error in the FET arises from approximating a function with a finite series approximation. The magnitude of the truncation error depends only on the order of approximation used and is not affected by the number of histories used in the Monte Carlo simulation. The histogram tally also suffers from truncation error due to approximating a continuous function with a series of flat line segments. Truncation error in a histogram approximation depends on the number of histogram bins used.

Statistical error in both the FET and histogram tallies is due to the stochastic nature of the Monte Carlo simulation. Monte Carlo tallies provide a statistical estimate for the functional expansion coefficients. When these coefficients are used to reconstruct a functional approximation, the uncertainties in each "mode" combine and can cause significant contamination in the final result.

Estimation of expansion coefficients in the FET relies on the Monte Carlo simulation to perform a numerical integration over the individual basis functions. For high order expansion coefficients, the corresponding basis functions can be difficult to integrate numerically, causing increased uncertainty in the estimate. The general trend for expansion coefficients is that statistical uncertainty increases with the order of the coefficient.

Histogram style tallies use the Monte Carlo simulation to numerically evaluate the integral (zeroth moment) of the distribution over each bin. As the number of histogram bins increases, the width of each bin decreases and, as a result fewer histories score in each bin. The smaller number of histories contributing to each bin causes an increase in the variance of the estimates in the bins.

Both the FET and the histogram tallies involve a tradeoff between statistical and truncation errors. Increasing the order of the approximation (or the number of bins, for the histogram) decreases the truncation error of the approximation but increases the statistical uncertainty, and vice versa. In this thesis it is shown that, for a fixed number of histories run, an optimal approximation order exists that minimizes the residual error of the approximation in the 2-norm. It is also shown that the 2-norm error due to the FET approximation is less than the error resulting from a histogram approximation. Numerical results are presented to support these conclusions.

Chapter 4 covers the derivation of track length FET estimators for expansions of spatial flux distributions in 1, 2, and 3 dimensions. Several useful properties of these estimators are also derived, which can help to speed up the calculation of the tallies

during the simulation. Results are shown for 1 and 2 dimensional benchmark problems to demonstrate convergence of the method.

Chapter 5 covers the application of the FET for calculating response functions via Monte Carlo. These response functions, in turn, can be used in a response matrix algorithm to rapidly calculate flux distributions in reactor cores or radiation shields. The result is a hybrid Monte-Carlo/deterministic method that may be a useful tool for accelerating reactor analysis calculations. A simple algorithm for generating response functions with FET is implemented and tested on simple 1-D problems.

Finally, in chapter 6 the results contained in this dissertation are summarized. General conclusions about the development and application of the FET are presented, along with a brief discussion of possible topics for future research.

CHAPTER 2

DISCRETE EVENT FET ESTIMATORS

The first type of FET estimators to be considered is the class of discrete event estimators. As their name implies, these estimators are scored when individual particles undergo certain events. The two most commonly used discrete event estimators are: the collision estimator for average particle flux in a volume, and the surface crossing estimator for average particle current through a surface. Both estimators, Eqs. (1.57) and (1.78), look mathematically very similar, and they follow the general form for a Monte Carlo tally given in Chapter 1, Eq. (1.5). Because of these mathematical similarities, the properties of an FET estimator for one type of tally can easily be generalized to the other tally. As such, this chapter will focus on a detailed derivation of a surface crossing FET estimator and the associated estimators for the variance. A series of computational results are included to provide verification of the theoretical results. In the final sections, the surface crossing estimator results are extended to the collision estimator tally for flux in a volume.

2.1. Derivation of the Surface Crossing Current FET Estimator

Before beginning the derivation, it is useful to consider some of the mathematical properties of the distribution to be approximated by the functional expansion technique. The angular surface crossing current, $\left|\vec{j}(\vec{\xi})\cdot\vec{s}\right|$, is directly related to the particle density function (and angular flux) and can be written:

$$\left|\vec{j}\left(\vec{\xi}\right)\cdot\vec{s}\right| = \left|\vec{\Omega}\cdot\vec{s}\right| v N_p\left(\vec{\xi}\right) = \left|\vec{\Omega}\cdot\vec{s}\right|\phi\left(\vec{\xi}\right). \tag{2.1}$$

Physically, this function corresponds to the expected number of particles passing through an area dA_S on the surface S with energy E in dE, direction $\vec{\Omega}$ in $d\vec{\Omega}$, during time dt about time t.[2] As in the first chapter, the variable $\vec{\xi} = \left(x, y, z, E, \vec{\Omega}, t\right)$ has been used as a general "phase location" variable in order to simplify the notation in the derivations that follow. It is possible to make some general observations and assumptions about common mathematical properties of the function $\left|\vec{j}(\vec{\xi})\cdot\vec{s}\right|$, based on the physics that govern particle transport.

a) *The function* $\left|\vec{j}(\vec{\xi})\cdot\vec{s}\right|$ *is piecewise smooth over its domain.*

This implies that for any closed domain both the function and its first derivative are piecewise continuous. A function is piecewise continuous if, for any closed domain, there exist at most a finite number of discontinuities in the function, and at each point of discontinuity both the left-hand and right-hand limits exist as the discontinuity is approached.

b) *The function* $\left|\vec{j}(\vec{\xi})\cdot\vec{s}\right|$ *has a finite domain and is square-integrable with some weighting function* $\rho\left(\vec{\xi}\right)$ *over that domain.*

This implies that for any bounded domain Γ the following condition holds:

$$\int_{\Gamma} \left| \vec{j}(\vec{\xi}) \cdot \vec{s} \right|^2 \rho\left(\vec{\xi}\right) d\vec{\xi} < \infty . \tag{2.2}$$

With these properties of $\left| \vec{j}(\vec{\xi}) \cdot \vec{s} \right|$ established, it is now possible to consider an expansion of the distribution in terms of a complete set of basis functions. Before proceeding, however, it is important to introduce some concepts from approximation theory for dealing with sets of functions.

To begin, we denote the space of real-valued square-integrable functions with positive weighting function ρ on some finite domain Γ as $L^2_\rho(\Gamma)$. The formal definition of $L^2_\rho(\Gamma)$ is given by

$$L^2_\rho(\Gamma) = \left\{ f : \int_{\Gamma} |f(\vec{x})|^2 \rho(\vec{x}) d\vec{x} < \infty \right\} . \tag{2.3}$$

Note that, by assumption *b)* above, the function $\left| \vec{j}(\vec{\xi}) \cdot \vec{s} \right|$ is an element of $L^2_\rho(\Gamma)$. If the functions f and g are elements of $L^2_\rho(\Gamma)$, then the inner product of f and g is:

$$\langle f, g \rangle = \int_{\Gamma} f(\vec{x}) g(\vec{x}) \rho(\vec{x}) d\vec{x} . \tag{2.4}$$

Likewise, for any function f in $L^2_\rho(\Gamma)$, the L-2-norm of f is:

$$\|f\| = \left(\int_{\Gamma} f(\vec{x})^2 \rho(\vec{x}) d\vec{x} \right)^{1/2} , \tag{2.5}$$

and the square of the L-2 norm is therefore:

$$\|f\|^2 = \int_{\Gamma} f(\vec{x})^2 \rho(\vec{x}) d\vec{x} . \tag{2.6}$$

With these definitions it is possible to consider the expansion of an arbitrary function f with respect to a complete basis set for the space $L^2_\rho(\Gamma)$. To do this. let $\{\psi_n\}_0^\infty$ be a complete orthogonal set with respect to the weighting function ρ in $L^2_\rho(\Gamma)$. For any function $f \in L^2_\rho(\Gamma)$, f can be expanded in terms of $\{\psi_n\}_0^\infty$ as

$$f = \sum_{n=0}^{\infty} \frac{\langle f, \psi_n \rangle}{\|\psi_n\|^2} \psi_n \tag{2.7}$$

For convenience, we define

$$\bar{a}_n \equiv \langle f, \psi_n \rangle = \int_\Gamma f(\vec{x}) \psi_n(\vec{x}) \rho(\vec{x}) d\vec{x} , \tag{2.8}$$

and

$$k_n \equiv \frac{1}{\|\psi_n\|^2} . \tag{2.9}$$

The factors a_n are commonly referred to as expansion coefficients, while k_n is often called the orthonormalization constant. These definitions allow Eq. (2.7) to be written:

$$f = \sum_{n=0}^{\infty} \bar{a}_n k_n \psi_n \tag{2.10}$$

Another related result is Parseval's equation, which relates the square of the 2-norm of the function f to the sum of the squares of the expansion coefficients.

$$\|f\|^2 = \sum_{n=0}^{\infty} \frac{|\langle f, \psi_n \rangle|^2}{\|\psi_n\|^2} = \sum_{n=0}^{\infty} \bar{a}_n^2 k_n . \tag{2.11}$$

Given these results, consider a functional expansion of the angular current. Applying Eq. (2.8) to the surface crossing current yields

$$J(\vec{\xi}) \equiv \left| \vec{j}(\vec{\xi}) \cdot \vec{s} \right| = \sum_{n=0}^{\infty} \bar{a}_n k_n \psi_n(\vec{\xi}), \tag{2.12}$$

where

$$\bar{a}_n = \int_\Gamma \left|\vec{j}\left(\vec{\xi}\right)\cdot\vec{s}\right|\psi_n\left(\vec{\xi}\right)\rho\left(\vec{\xi}\right)d\vec{\xi}\,. \tag{2.13}$$

Equation (2.12) gives a complete expansion of the surface crossing current with respect to the orthogonal basis $\{\psi_n\}_0^\infty$. If the expansion coefficients $\bar{a}_n$ are known, then a functional form of the surface crossing current can be calculated. Fortunately, the expression for evaluating the expansion coefficients is in a convenient integral form that is ideal for estimation by Monte Carlo. In fact, the right hand side of Eq. (2.13) is identical to Eq. (1.81) with $g\left(\vec{\xi}\right)=\psi_n\left(\vec{\xi}\right)\rho\left(\vec{\xi}\right)$. This means that an unbiased estimator for $\bar{a}_n$ can be calculated directly from Eq. (1.76),

$$\hat{a}_n = \frac{1}{N}\sum_{i=1}^{N}\sum_{k=1}^{J_i} w_{i,k,S}\,\psi_n\left(\vec{\xi}_{i,k}\right)\rho\left(\vec{\xi}_{i,k}\right), \tag{2.14}$$

where $w_{i,k,S}$ is the weight of particle i as it crosses the surface S for the k^{th} time. We notice that if a basis set is chosen such that $\psi_0\left(\vec{\xi}\right)\rho\left(\vec{\xi}\right)=1$, then Eq. (2.14) reduces to the traditional surface crossing estimator given in Eq. (1.78). If the basis set also has the property that $\int_\Gamma \psi_n\left(\vec{\xi}\right)\rho\left(\vec{\xi}\right)d\vec{\xi}=0$ for all $n>0$ (a property that holds for orthogonal sets of functions) then it is easy to show that the FET approximation to the angular current distribution will preserve the correct integral value of the current. In these cases the FET is actually extracting higher-order information about the shape of the current distribution from the particle histories, while preserving the low order (integral) information.

In the preceding derivations, we assumed that a basis set was chosen that spans the entire phase volume: $\vec{\xi} \equiv \{x, y, z, E, \mu, \varphi, t\}$. There are, however, many situations where an expansion of the angular current distribution in only one or two phase variables is desired. In these cases, a basis set can be chosen that spans only the phase variables of interest and is independent of other phase variables. Once an appropriate basis set has been chosen, Eq. (2.14) can be used to estimate the functional expansion of the angular current in the phase variables of interest, integrated over the remaining phase variables.

2.2. Uncertainty in the Surface Crossing Current FET Estimator

Since the Monte Carlo method is a stochastic technique, any parameter estimated by the method will have some statistical uncertainty associated with it. The FET expansion coefficients are no exception to this rule. In addition to each coefficient having statistical uncertainty, these coefficients are used together as terms in a series expansion, which has its own statistical uncertainty. Furthermore, the series expansion is only an approximation to the shape of the true distribution, implying that there can be additional uncertainty due to truncation error in the expansion itself. This section will cover these different types of uncertainty and error present in the FET and derive statistical estimators for each type.

2.2.1. Variance of Individual Coefficients

The derivation for the variance of a single expansion coefficient $\bar{a}_n$ begins with the estimator $\hat{a}_n$. For N independent particle histories, the statistic

$$\hat{a}_n = \frac{1}{N}\sum_{i=1}^{N}\sum_{k=1}^{J_i} w_{i,k,S}\,\psi_n\left(\vec{\xi}_{i,k}\right)\rho\left(\vec{\xi}_{i,k}\right) \tag{2.15}$$

is a random variable whose expected value is equal to the true expansion coefficient $\bar{a}_n$ and whose variance is equal to $\sigma^2_{\mathbf{a}_n}/N$. The definition of variance given in Eq. (1.11) can be used to write $\sigma^2_{\mathbf{a}_n}$ in terms of the probability distribution function $p(a_n)$,

$$\sigma^2_{\mathbf{a}_n} = \int_{-\infty}^{\infty}\left(a_n - \bar{a}_n\right)^2 p(a_n)\,da_n . \tag{2.16}$$

Unfortunately, nothing is known about the properties of the function $p(a_n)$ other than the fact that it integrates to 1 over the domain $[-\infty,\infty]$. This property can be used to express Eq. (2.16) in terms of quantities that can be easily estimated. To show this, we begin by expanding the integrand in Eq. (2.16)

$$\sigma^2_{\mathbf{a}_n} = \int_{-\infty}^{\infty}\left(a_n^2 - 2a_n\bar{a}_n + \bar{a}_n^{\,2}\right)p(a_n)\,da_n . \tag{2.17}$$

Continuing on with algebraic simplification gives,

$$\sigma^2_{\mathbf{a}_n} = \int_{-\infty}^{\infty} a_n^2 p(a_n)\,da_n - 2\bar{a}_n\int_{-\infty}^{\infty} a_n p(a_n)\,da_n + \bar{a}_n^{\,2}\int_{-\infty}^{\infty} p(a_n)\,da_n$$

$$\sigma^2_{\mathbf{a}_n} = \int_{-\infty}^{\infty} a_n^2 p(a_n)\,da_n - 2\bar{a}_n\int_{-\infty}^{\infty} a_n p(a_n)\,da_n + \bar{a}_n^{\,2}.$$

By the definition of expected value, Eq. (1.1),

$$\sigma^2_{\mathbf{a}_n} = E\left[\mathbf{a}_n^2\right] - 2\bar{a}_n E\left[\mathbf{a}_n\right] + \bar{a}_n^{\,2}$$

$$\sigma^2_{\mathbf{a}_n} = E\left[\mathbf{a}_n^2\right] - 2\bar{a}_n^2 + \bar{a}_n^{\,2}$$

$$\sigma^2_{\mathbf{a}_n} = E\left[\mathbf{a}_n^2\right] - \bar{a}_n^2 . \tag{2.18}$$

To find an estimator for $E\left[\mathbf{a}_n^2\right]$, we recognize that each independent particle history gives an estimate for the expansion coefficient a_n,

$$\hat{a}_{n,i} = \sum_{k=1}^{J_i} w_{i,k,S}\, \psi_n\left(\vec{\xi}_{i,k}\right) \rho\left(\vec{\xi}_{i,k}\right) . \tag{2.19}$$

Taking the square of Eq. (2.19) gives an estimate for $E\left[\mathbf{a}_n^2\right]$,

$$\widehat{a_{n,i}^2} = \left(\sum_{k=1}^{J_i} w_{i,k,S}\, \psi_n\left(\vec{\xi}_{i,k}\right) \rho\left(\vec{\xi}_{i,k}\right) \right)^2 . \tag{2.20}$$

When taken over N independent histories, Eq. (2.20) becomes

$$\widehat{a_n^2} = \frac{1}{N} \sum_{i=1}^{N} \left(\sum_{k=1}^{J_i} w_{i,k,S}\, \psi_n\left(\vec{\xi}_{i,k}\right) \rho\left(\vec{\xi}_{i,k}\right) \right)^2 . \tag{2.21}$$

The estimator for the second term on the right hand side of Eq. (2.18), $\overline{a}_n^{\,2}$, can be easily derived by taking the square of the estimator $\hat{a}_n$ given in Eq. (2.15):

$$\hat{a}_n^{\,2} = \left(\frac{1}{N} \sum_{i=1}^{N} \sum_{k=1}^{J_i} w_{i,k,S}\, \psi_n\left(\vec{\xi}_{i,k}\right) \rho\left(\vec{\xi}_{i,k}\right) \right)^2 . \tag{2.22}$$

Substituting the results from Eqs. (2.21) and (2.22) into the variance given in Eq. (2.18) yields

$$\begin{aligned} \hat{\sigma}_{\mathbf{a}_n}^2 = & \frac{1}{N} \sum_{i=1}^{N} \left(\sum_{k=1}^{J_i} w_{i,k,S}\, \psi_n\left(\vec{\xi}_{i,k}\right) \rho\left(\vec{\xi}_{i,k}\right) \right)^2 \\ & - \left(\frac{1}{N} \sum_{i=1}^{N} \sum_{k=1}^{J_i} w_{i,k,S}\, \psi_n\left(\vec{\xi}_{i,k}\right) \rho\left(\vec{\xi}_{i,k}\right) \right)^2 . \end{aligned} \tag{2.23}$$

The estimator in Eq. (2.23) is biased because the same set of data was used to calculate the sample mean used in the variance estimator. This bias can be eliminated[12] by multiplying the statistic by $N/N-1$ to give

$$\hat{\sigma}^2_{\bar{a}_n} = \frac{1}{N-1}\sum_{i=1}^{N}\left(\sum_{k=1}^{J_i} w_{i,k,S}\,\psi_n\left(\vec{\xi}_{i,k}\right)\rho\left(\vec{\xi}_{i,k}\right)\right)^2 - \frac{1}{N(N-1)}\left(\sum_{i=1}^{N}\sum_{k=1}^{J_i} w_{i,k,S}\,\psi_n\left(\vec{\xi}_{i,k}\right)\rho\left(\vec{\xi}_{i,k}\right)\right)^2. \tag{2.24}$$

The true variance for an estimate of $\bar{a}_n$ made with N independent trials can now be written as

$$\hat{\sigma}^2_{\bar{a}_n} = \frac{1}{N}\hat{\sigma}^2_{a_n}. \tag{2.25}$$

Substituting Eq. (2.24) into (2.25) provides an unbiased estimator of $\sigma^2_{\hat{a}_n}$,

$$\hat{\sigma}^2_{\hat{a}_n} = \frac{\sum_{i=1}^{N}\left(\sum_{k=1}^{J_i} w_{i,k,S}\,\psi_n\left(\vec{\xi}_{i,k}\right)\rho\left(\vec{\xi}_{i,k}\right)\right)^2 - \frac{1}{N}\left(\sum_{i=1}^{N}\sum_{k=1}^{J_i} w_{i,k,S}\,\psi_n\left(\vec{\xi}_{i,k}\right)\rho\left(\vec{\xi}_{i,k}\right)\right)^2}{N(N-1)}. \tag{2.26}$$

The estimator in Eq. (2.26) gives a measurement of the statistical uncertainty in each individual expansion coefficient.

2.2.2. Variance of the Functional Expansion

It is also possible to derive a more powerful result that gives the pointwise variance of the reconstructed functional estimate instead of the individual coefficients. The derivation begins by considering a truncated functional expansion of the current distribution in some orthogonal basis set of functions,

$$J_M\left(\vec{\xi}\right) \equiv \sum_{n=0}^{M} \bar{a}_n k_n \psi_n\left(\vec{\xi}\right). \tag{2.27}$$

Using the estimator for $\bar{a}_n$ given in Eq. (2.14), any set of N independently observed events can be used to estimate any or all members of the set of expansion

coefficients $\{\bar{a}_n\}_0^\infty$. Even a single history i provides an estimate $\hat{a}_{n,i}$ for every expansion coefficient in the set $\{\bar{a}_{n,i}\}_0^M$, and therefore, by Eq. (2.27), an estimate for the function $J(\vec{\xi})$ itself. It is useful at this point to define a new quantity, $\widehat{J_{M,i}}(\vec{\xi})$, which represents an M^{th} order estimate of the function $J(\vec{\xi})$ resulting from only the i^{th} history,

$$\widehat{J_{M,i}}(\vec{\xi}) = \sum_{n=0}^{M} \hat{\alpha}_{n,i} k_n \psi_n(\vec{\xi}). \tag{2.28}$$

Taking the average of the $\widehat{J_{M,i}}(\vec{\xi})$ over N observations yields an intermediate result,

$$\widehat{J_M}(\vec{\xi}) = \frac{1}{N}\sum_{i=1}^{N} \widehat{J_{M,i}}(\vec{\xi}) = \frac{1}{N}\sum_{i=1}^{N}\sum_{n=0}^{M} \hat{a}_{n,i} k_n \psi_n(\vec{\xi}) \ , \tag{2.29}$$

which can be simplified to yield

$$\widehat{J_M}(\vec{\xi}) = \sum_{n=0}^{M} k_n \psi_n(\vec{\xi}) \left(\frac{1}{N}\sum_{i=1}^{N} \hat{a}_{n,i} \right) = \sum_{n=0}^{M} \hat{a}_n k_n \psi_n(\vec{\xi}). \tag{2.30}$$

Equation (2.30) gives an expected result, in which the mean functional expansion $\widehat{J_M}(\vec{\xi})$ for N independent trials is equal to the functional expansion that uses the sample mean for each expansion coefficient individually. It is also straightforward to apply the sample variance formula to $\widehat{J_M}(\vec{\xi})$,

$$\hat{\sigma}^2_{\widehat{J_M}(\vec{\xi})} = \frac{\sum_{i=1}^{N} \left(\widehat{J_{M,i}}(\vec{\xi}) \right)^2 - N \left(\widehat{J_M}(\vec{\xi}) \right)^2}{N(N-1)}. \tag{2.31}$$

Equation (2.31) can be algebraically manipulated to give the final result,

$$\hat{\sigma}^2_{\widehat{J_M}(\vec{\xi})} = \frac{\sum_{i=1}^{N} \left(\sum_{n=0}^{M} \hat{a}_{n,i} k_n \psi_n(\vec{\xi}) \right)^2 - N \left(\sum_{n=0}^{M} \hat{a}_n k_n \psi_n(\vec{\xi}) \right)^2}{N(N-1)}$$

$$= \frac{1}{N(N-1)} \left(\begin{array}{l} \sum_{i=1}^{N} \left(\sum_{n=0}^{M} \sum_{m=0}^{M} \left(\hat{a}_{n,i} k_n \psi_n \left(\vec{\xi} \right) \right) \left(\hat{a}_{m,i} k_m \psi_m \left(\vec{\xi} \right) \right) \right) \\ \qquad - N \left(\sum_{n=0}^{M} \sum_{m=0}^{M} \left(\hat{a}_n k_n \psi_n \left(\vec{\xi} \right) \right) \left(\hat{a}_m k_m \psi_m \left(\vec{\xi} \right) \right) \right) \end{array} \right)$$

$$= \frac{1}{N-1} \sum_{n=0}^{M} \sum_{m=0}^{M} \left(k_n \psi_n \left(\vec{\xi} \right) \right) \left(k_m \psi_m \left(\vec{\xi} \right) \right) \frac{1}{N} \sum_{i=1}^{N} \left(\hat{a}_{n,i} \hat{a}_{m,i} \right) - \frac{1}{N-1} \left(\sum_{n=0}^{M} \sum_{m=0}^{M} \left(\hat{a}_n \hat{a}_m \right) \left(k_n \psi_n \left(\vec{\xi} \right) \right) \left(k_m \psi_m \left(\vec{\xi} \right) \right) \right)$$

$$= \frac{1}{N-1} \sum_{n=0}^{M} \sum_{m=0}^{M} \left(k_n \psi_n \left(\vec{\xi} \right) \right) \left(k_m \psi_m \left(\vec{\xi} \right) \right) \widehat{a_{n,i} a_{m,i}} - \frac{1}{N-1} \left(\sum_{n=0}^{M} \sum_{m=0}^{M} \left(\hat{a}_n \hat{a}_m \right) \left(k_n \psi_n \left(\vec{\xi} \right) \right) \left(k_m \psi_m \left(\vec{\xi} \right) \right) \right)$$

$$= \frac{1}{N-1} \sum_{n=0}^{M} \sum_{m=0}^{M} \left(\widehat{a_{n,i} a_{m,i}} - \hat{a}_n \hat{a}_m \right) \left(k_n \psi_n \left(\vec{\xi} \right) \right) \left(k_m \psi_m \left(\vec{\xi} \right) \right)$$

$$\hat{\sigma}^2_{\hat{f}_M(\vec{\xi})} = \frac{N}{N-1} \sum_{n=0}^{M} \sum_{m=0}^{M} \hat{\sigma}_{a_n a_m} \left(k_n \psi_n \left(\vec{\xi} \right) \right) \left(k_m \psi_m \left(\vec{\xi} \right) \right) , \tag{2.32}$$

where $\hat{\sigma}_{a_n a_m}$ is, by definition, the sample covariance between estimates of $\hat{a}_n$ and $\hat{a}_m$,

$$\hat{\sigma}_{a_n a_m} = \widehat{a_{n,i} a_{m,i}} - \hat{a}_n \hat{a}_m . \tag{2.33}$$

Equation (2.32) gives the variance (as a function of $\vec{\xi}$) for the estimated functional expansion of the surface crossing current. Unfortunately, this equation requires the covariance between every combination of expansion coefficients to be calculated. Computing the covariance matrix for a large number of expansion coefficients can increase the memory requirements and run time of a Monte Carlo simulation. To prevent this burden on the code, it is useful to consider an estimate for the 2-norm of the variance.

2.2.3. Two-Norm Variance of the Functional Expansion

The derivation of the 2-norm variance estimate begins with the sample variance for $\widehat{J_M}\left(\vec{\xi}\right)$, given in Eq. (2.31). By expanding, integrating both sides over Γ, and using the orthogonal properties of the basis set $\{\psi_n\}_0^M$, Eq. (2.31) yields,

$$\int_\Gamma \hat{\sigma}^2_{\widehat{J_M}(\vec{\xi})}\,\rho\left(\vec{\xi}\right)d\vec{\xi} = \frac{1}{N(N-1)}\left(\begin{array}{l}\int_\Gamma \sum_{i=1}^{N}\left(\sum_{n=0}^{M}\sum_{m=0}^{M}\left(\hat{\alpha}_{n,i}\,k_n\,\psi_n\left(\vec{\xi}\right)\right)\left(\hat{\alpha}_{m,i}\,k_m\,\psi_m\left(\vec{\xi}\right)\right)\right)\rho\left(\vec{\xi}\right) \\ \quad -\int_\Gamma N\left(\sum_{n=0}^{M}\sum_{m=0}^{M}\left(\hat{a}_n\,k_n\,\psi_n\left(\vec{\xi}\right)\right)\left(\hat{a}_m\,k_m\,\psi_m\left(\vec{\xi}\right)\right)\right)\rho\left(\vec{\xi}\right)\end{array}\right)$$

$$= \frac{\sum_{i=1}^{N}\left(\sum_{n=0}^{M}\hat{\alpha}_{n,i}{}^2\,k_n\right) - N\left(\sum_{n=0}^{M}\hat{a}_n^2\,k_n\right)}{N(N-1)}$$

$$= \frac{1}{(N-1)}\sum_{n=0}^{M}\left(\frac{1}{N}\sum_{i=1}^{N}\hat{\alpha}_{n,i}{}^2\,k_n\right) - \frac{1}{N-1}\left(\sum_{n=0}^{M}\hat{a}_n^2\,k_n\right)$$

$$= \frac{1}{(N-1)}\sum_{n=0}^{M}\left(\widehat{\alpha_{n,i}^2} - \hat{a}_n^2\right)k_n,$$

which, upon use of Eq. (2.12), yields the final result,

$$\int_\Gamma \hat{\sigma}^2_{\widehat{J_M}(\vec{\xi})}\,\rho(x)\,dx = \sum_{n=0}^{M}\hat{\sigma}^2_{\hat{a}_n}\,k_n\,. \tag{2.34}$$

Equation (2.34) gives an estimate of the statistical uncertainty in the entire functional expansion based only on the uncertainties in each of the expansion coefficients and not on the covariance of the coefficients.

2.2.4. Truncation Error

In addition to statistical error present in each of the expansion coefficients, the reconstructed functional approximation will also contain truncation error, which arises

from approximating the true distribution with a truncated series expansion. Therefore, the functional expansion for $J\left(\vec{\xi}\right)$ given in Eq. (2.12) is exact only if all terms in the series are included. Clearly, it is not possible to estimate an infinite number of expansion coefficients, and the functional approximation must be truncated at some finite number of terms M:

$$J\left(\vec{\xi}\right) \approx J_M\left(\vec{\xi}\right) = \sum_{n=0}^{M} \bar{a}_n k_n \psi_n\left(\vec{\xi}\right). \tag{2.35}$$

This truncation after M terms introduces an error $E_M\left(\vec{\xi}\right)$ in the estimation of $J\left(\vec{\xi}\right)$, which is equal to the contributions from all expansion terms with $n > M$,

$$E_M\left(\vec{\xi}\right) = \left(J\left(\vec{\xi}\right) - J_M\left(\vec{\xi}\right)\right) = \sum_{n=M+1}^{\infty} \bar{a}_n k_n \psi_n\left(\vec{\xi}\right). \tag{2.36}$$

The detailed convergence properties of functional expansions are well known and widely reported in the literature[31-33].

For the FET, it is desirable to have a measure of how much truncation error is present in a functional approximation of a given order. Unfortunately, this information is not contained in the magnitude of individual expansion coefficients, but rather is related to the rate at which the sequence of coefficients converges towards zero. One commonly used measure of truncation error is the 2-norm. By Parseval's Theorem the 2-norm measure of the truncation error in a finite series approximation is given by the relationship[32]

$$\left\|E_M\right\|^2 = \int J\left(\vec{\xi}\right)^2 \rho\left(\vec{\xi}\right) d\vec{\xi} - \sum_{n=0}^{M} a_n^2 . \tag{2.37}$$

Therefore, as the truncation error goes to zero, the M^{th} partial sum of the expansion coefficients squared will approach a constant value. By examining the partial sum as a function of M, it is possible to estimate the truncation error and the integral of $J\left(\vec{\xi}\right)^2 \rho\left(\vec{\xi}\right)$.

In the preceding sections both the statistical uncertainty and truncation error properties were derived for radiation current expansions only. Similar results can be derived in an analogous way for the flux expansion or any other FET based on a discrete event estimator.

2.2.5. Optimizing the FET Approximation

In the FET, the truncation error and statistical error terms are inversely related. The low order expansion coefficients are the easiest to integrate stochastically and will have smaller statistical uncertainties. However, using too few expansion coefficients will result in a large truncation error and low resolution. Using a higher order series expansion will decrease the truncation error, but higher expansion coefficients will always have larger statistical uncertainties because the basis functions are more difficult to integrate. Keeping too many, or poorly converged, coefficients will result in statistical error "contamination" of the final approximation. To get the maximum effectiveness from the FET, an optimal balance must be found between these two terms that will minimize the total error in the approximation.

Examination of Eqs. (2.34) and (2.37) indicates that for each additional coefficient $\hat{a}_n$ included in the series, the truncation error is reduced by $\hat{a}_n^2$ and the

statistical error is increased by $\hat{\sigma}^2_{\hat{a}_n} k_n$. Taking the ratio of the increase in statistical error to the decrease in truncation error,

$$R_n^2 = \frac{\hat{\sigma}^2_{\hat{a}_n} k_n}{\hat{a}_n^2}, \tag{2.38}$$

gives a relative cost-to-benefit metric associated with adding the n^{th} term to the series. Note that $\sqrt{R_n^2}$ looks similar to the relative standard deviation that is widely used for standard Monte Carlo tallies; the two metrics differ only by a factor of $\sqrt{k_n}$.

The cost-to-benefit ratio provides a convenient test for determining how many expansion coefficients should be used from a given Monte Carlo simulation. Terms with values of $R_n^2 >> 1$ should not be included in a functional approximation because they are not well converged and will not add any useful information to the result. Terms with values of $R_n^2 << 1$, on the other hand should be included in the series approximation because they provide valuable information about the shape of the true function. Terms with $R_n^2 \approx 1$ are near the break even point and should be carefully examined before including any such term in a functional approximation. Some numerical results demonstrating the behavior of the cost-to-benefit ratio will be presented in section 3.3.3.

2.3. Implementation of the Surface Crossing FET Estimator

The previous sections in this chapter have focused on the theoretical and mathematical properties of the surface crossing FET estimators. While these results provide important insights into the estimators, they do not provide any information on how to actually implement the FET into a Monte Carlo particle transport code. This

section will cover many of the important issues surrounding practical implementation of the FET.

2.3.1. Selecting a Set of Basis Functions

Until now, all derivations for the FET have been performed by using an arbitrary set of basis functions $\left\{\psi_n\left(\vec{\xi}\right)\right\}_{n=0}^{\infty}$ that are both complete and orthogonal with respect to some weighting function $\rho\left(\vec{\xi}\right)$. When the method is actually implemented into a Monte Carlo code, it is important to consider which set(s) of basis functions will produce the best functional approximations for the applications of interest. The "best" basis set for a given situation is one that can achieve an acceptably small truncation error with the fewest number of expansion terms (e.g. lowest expansion order).

If any detailed information about the properties or shape of a solution function is known a priori, then a basis set can be chosen to take advantage of this information. Examples of tailoring basis sets to specific applications include the use of Laguerre functions for distributions that are known to be exponential[20], the use of Fourier Sine expansions if symmetry and endpoint information is available, and the use of Bessel or Spherical Harmonics expansions if the distributions are known to have cylindrical or spherical symmetry, respectively. In general, incorporating any available information about the solution into the selection of a basis set will result in a better and more efficient FET approximation.

Unfortunately, it is often the case that no a priori knowledge about the solution function is available, or the information is too weak to be of any real value when

selecting a basis set. The latter is true in the case of surface crossing particle current distributions, where piecewise smoothness is the only property that can be established for the distribution. In such cases it is a good idea to choose a very general set of basis functions, such as the Legendre Polynomials or Chebyshev Polynomials. These polynomial basis sets are widely used for many physics and engineering applications, and their series expansions are known to have fast algebraic convergence for functions that are "nearly" smooth (e.g. containing very few discontinuities in the first and higher derivatives). For functions that are analytically smooth, the performance of the orthogonal polynomial expansions improves, yielding exponential convergence rates.

The generality of these basis sets is itself an advantage. With a basis such as the Legendre polynomials, an FET estimator can be implemented in a code and used for many different purposes, such as expansions in space, time, energy and/or angle. If a basis set were tailored to a specific application, such as an expansion in time, it is likely that the basis would not be well-suited for a different application, such as an expansion in angle.

The polynomial basis functions are very good for expanding analytically smooth distributions, but they can become less effective if they are used to expand functions that contain discontinuities. There are, however, ways to improve the efficiency of the polynomial basis even when they are applied to discontinuous functions. If the locations of discontinuities (i.e. material boundaries) in the function or its derivatives are known, it is then possible to use a piecewise expansion to accelerate the convergence of the functional expansion. In a piecewise expansion, a single tally region with known discontinuities is divided into two or more smaller tallies that are expected to have

continuous solutions. The smaller tallies will have a larger variance than the original because fewer particles score in each tally, but this drawback is usually offset by the benefits of using the FET on a continuous distribution. In certain situations, the use of piecewise tallies can greatly increase the accuracy and efficiency of the FET.

In this dissertation, the discussion of basis sets for use with the FET has thus far been limited to orthogonal sets only. Strictly speaking, there are no theoretical reasons that non-orthogonal basis sets cannot be used with the FET. There are, however, several practical reasons that orthogonal basis sets are preferred. One major reason to choose sets of orthogonal basis functions is convenience. For an expansion in orthogonal functions, the expansion coefficients are equal to the moments of the function with respect to the individual basis elements. For a non-orthogonal basis set, the moments and expansion coefficients are not the same and a linear system must be solved to obtain expansion coefficients from the moments. Fortunately, this linear system needs to be solved only once, during the post-processing of the Monte Carlo simulation, and does not slow down the random walk of individual particles.

The real drawback to using non-orthogonal basis sets lies in the fact that most of the analysis techniques that have been used to estimate the truncation error and convergence rates for the FET are not applicable to non-orthogonal sets of basis functions. In orthogonal sets, the order of a basis function is directly related to its spatial resolution, with higher order functions providing fine spatial detail but being relatively unimportant to the gross shape of the distribution. This ordering makes it easy to estimate the truncation error that will result from terminating an expansion at a given order. This will be shown in Chapter 3. Such an ordering is not, in general, true for non-

orthogonal sets (such as finite element basis sets). This result makes it difficult to estimate the accuracy of an FET with a non-orthogonal basis. Even with these drawbacks, the use of non-orthogonal sets, especially finite element basis sets, may be important for certain types of problems. This topic remains an area of interest and future research.

2.3.2. Scaling the Tally Domain

A basis set is said to be "complete" over a domain if any function defined on the domain can be written as a linear combination of the basis elements. Therefore, when considering different basis sets for use with the FET it is important to consider the expansion domain for the set. There are three general classes of expansion domains: finite, semi-infinite, and infinite. Expansions over finite domains are the most widely used for practical applications of the FET. Examples of 1-dimensional basis sets that are complete over a finite domain include Fourier series, Legendre polynomials, Chebyshev polynomials, Gegenbauer polynomials, and Jacobi polynomials[31]. Most of these basis sets are defined such that the expansion domain lies in the interval $[-1,1]$. The semi-infinite and infinite basis sets can be used in special cases of the FET, but special care must be taken to ensure that the numerical schemes used for evaluation work properly over the entire domain. Examples of 1-D semi-infinite (complete on the interval $[0,\infty)$) and infinite (complete on the interval $(-\infty,\infty)$) basis sets include Bessel functions, Laguerre polynomials (both semi-infinite) and Hermite polynomials (infinite)[31]. Multi-dimensional basis sets can be obtained by taking the product of two (or more) 1-dimensional basis sets. For instance, it can be shown the product set of Legendre

Polynomials $\{P_n(x)P_M(y)\}_{n,m=0}^{\infty}$ is a complete orthogonal basis over the domain $\{(x,y)\,|\,x\in[-1,1], y\in[-1,1]\}$.

It should be clear from the preceding discussion that the choice of a basis set is highly dependent on the size and shape of the tally region. However, it would be unreasonable to expect to find a basis whose expansion domain exactly matches a given tally region. In situations where the tally and expansion domains do not match exactly, a simple change in variables can be used to overcome the problem. Consider a finite 1-dimensional interval $x=[x_{\min}, x_{\max}]$ that is to be approximated by a Legendre polynomial expansion. In order to avoid trying to find a basis that fits $[x_{\min}, x_{\max}]$ exactly, simply define a scaled variable

$$\tilde{x} = 2\left(\frac{x-x_{\min}}{x_{\max}-x_{\min}}\right)-1, \tag{2.39}$$

over the interval $[-1,1]$. When a particle undergoes a surface crossing (or collision) event in the tally region at the position x, the tally will actually score the event at the scaled position $\tilde{x}$. The resulting FET coefficients are then for a functional expansion in the scaled domain.

After the simulation has finished, the expansion can be converted to the original tally domain by substituting Eq. (2.39) into the arguments of the Legendre polynomials,

$$\widetilde{J_M}(x) = \sum_{n=0}^{M} \hat{a}_n k_n P_n(\tilde{x}) \qquad \text{(Scaled Domain)} \tag{2.40}$$

$$\widehat{J_M}(x) = \sum_{n=0}^{M} \hat{a}_n k_n' P_n\left(2\left(\frac{x-x_{\min}}{x_{\max}-x_{\min}}\right)-1\right). \qquad \text{(Original Tally Domain)} \tag{2.41}$$

We notice that in Eq. (2.41), the orthonormalization constant k_n' has changed to a new value. In the case of the Legendre polynomials it is easy to calculate the new constant directly from Eq. (2.9),

$$k_n' \equiv \left(\int_{x_{\min}}^{x_{\max}} P_n^2 \left(2\left(\frac{x - x_{\min}}{x_{\max} - x_{\min}} \right) - 1 \right) dx \right)^{-1} = \frac{2n+1}{x_{\max} - x_{\min}}. \tag{2.42}$$

For multiple dimensions this transformation of variables can be performed independently for each variable.

The simple linear scaling transformation described above works well for Cartesian domains, but breaks down when applied to irregularly shaped domains. In these cases there are more complicated variable transformations available that will make the tally domain match the expansion domain for the basis sets. For discrete event estimators, conformal mapping can be used to expand distributions over irregular (especially curved) domains. However, conformal mapping transformations will not work for track length estimators because the particles do not move in straight lines in the transform space.

2.3.3. Calculation Efficiency

When compared against the entire random walk process, any overhead created from adding a simple 1-D FET estimator is usually fairly small. In fact, the only extra work that is required for an FET surface crossing estimator is the evaluation of the weighting function and basis functions at each tally event. For an M^{th} order functional expansion, the FET estimators require that the first M basis functions be evaluated at each discrete event (surface crossing) that occurs in the tally region. For small values of

M, these calculations can be done quickly and efficiently by a direct evaluation of the function. However, higher order functions are often complicated and require many operations to evaluate directly. Fortunately, many basis sets have recursion relationships that allow higher order functions to be evaluated in terms of several lower order functions. In the case of the Legendre polynomials the recursion relationship is given by

$$\begin{aligned} P_0(x) &= 1 \\ P_1(x) &= x \\ P_n(x) &= \frac{(2n-1)xP_{n-1}(x)-(n-1)P_{n-2}(x)}{n}. \end{aligned} \tag{2.43}$$

Recursion relationships can be used to greatly increase the efficiency of evaluating basis functions for the FET estimators, especially in high order or multidimensional expansions.

Another concern in the numerical evaluation of the FET estimators is the weighting function $\rho(x)$. While most of the weighting functions can be evaluated efficiently, many have singularities that can cause problems for numerical schemes. One such example is the weighting function for the Chebyshev polynomials, $\rho(x)=(1-x^2)^{-1/2}$, which has singularities at the endpoints $x=-1$ and 1. The function is integrable, but integration by Monte Carlo is not guaranteed to produce an accurate result. A random sample of x taken too close to either endpoint can skew the estimate of the integral or result in a numerical overflow error. As a result, special care must be used when implementing a basis function whose weighting function has singularities. Due to this issue, the Legendre polynomials and Fourier series have been found to be especially convenient basis sets because their associated weighting function, $\rho(x)=1$, contains no

singularities. For these reasons the Legendre polynomials are a good choice for a generic FET implementation. Because of this, the Legendre polynomials will be used for the majority of the derivations and results in this dissertation.

2.3.4. Numerical Implementation

Aside from the selection of a basis set, the major consideration for implementing the FET in a Monte Carlo code is where and how the tally should fit into an existing code framework. In the case of the surface crossing estimator the actual implementation is straight forward. For every event that an individual particle undergoes, the code must check whether a) the event is a surface crossing, and if so, b) did it occur within the predefined tally domain? If the answers to both of these questions are yes, then the work of scoring the tally can begin. The first step in determining the score for the event is to scale the event location in the tally domain to fit the expansion domain for the basis set, in this case the Legendre polynomials. This is accomplished by the change of variables defined in Eq. (2.39). The score for a single event is then taken to be the value of the basis function at the scaled event location times the weight of the particle following the event. Therefore, each basis function, up to the user defined truncation order M, must be evaluated at the scaled position. For the Legendre polynomials this evaluation can be done very efficiently using the recursion relationship given in Eq. (2.43). For a single history, the scores from each surface crossing event are added together to give a single estimate for each expansion coefficient $\{\hat{a}_{n,i}\}_{n=0}^{M}$. After N independent histories, these single history estimates (and their square values) can be averaged together using Eqs. (2.15) and (2.23) to yield a single set of estimated expansion coefficients $\{\hat{a}_n\}_{n=0}^{M}$ and

their associated variances $\left\{\sigma^2_{\hat{a}_n}\right\}_{n=0}^{M}$. These expansion coefficients can then be used in the Legendre series expansion, Eq. (2.30), to give a functional approximation to the distribution $\bar{J}\left(\vec{\xi}\right)$ in the scaled domain. This approximation can then be converted to the original domain by the transformation defined in Eqs. (2.41) and (2.42). A detailed overview of this implementation is presented in the flow chart shown in Figure 2.1. For testing purposes, an FET surface crossing estimator has been implemented in the TALLYX subroutine of the production Monte Carlo code MCNP4c[9]. This initial version uses Legendre polynomials to approximate current distributions over quadrilateral tally regions.

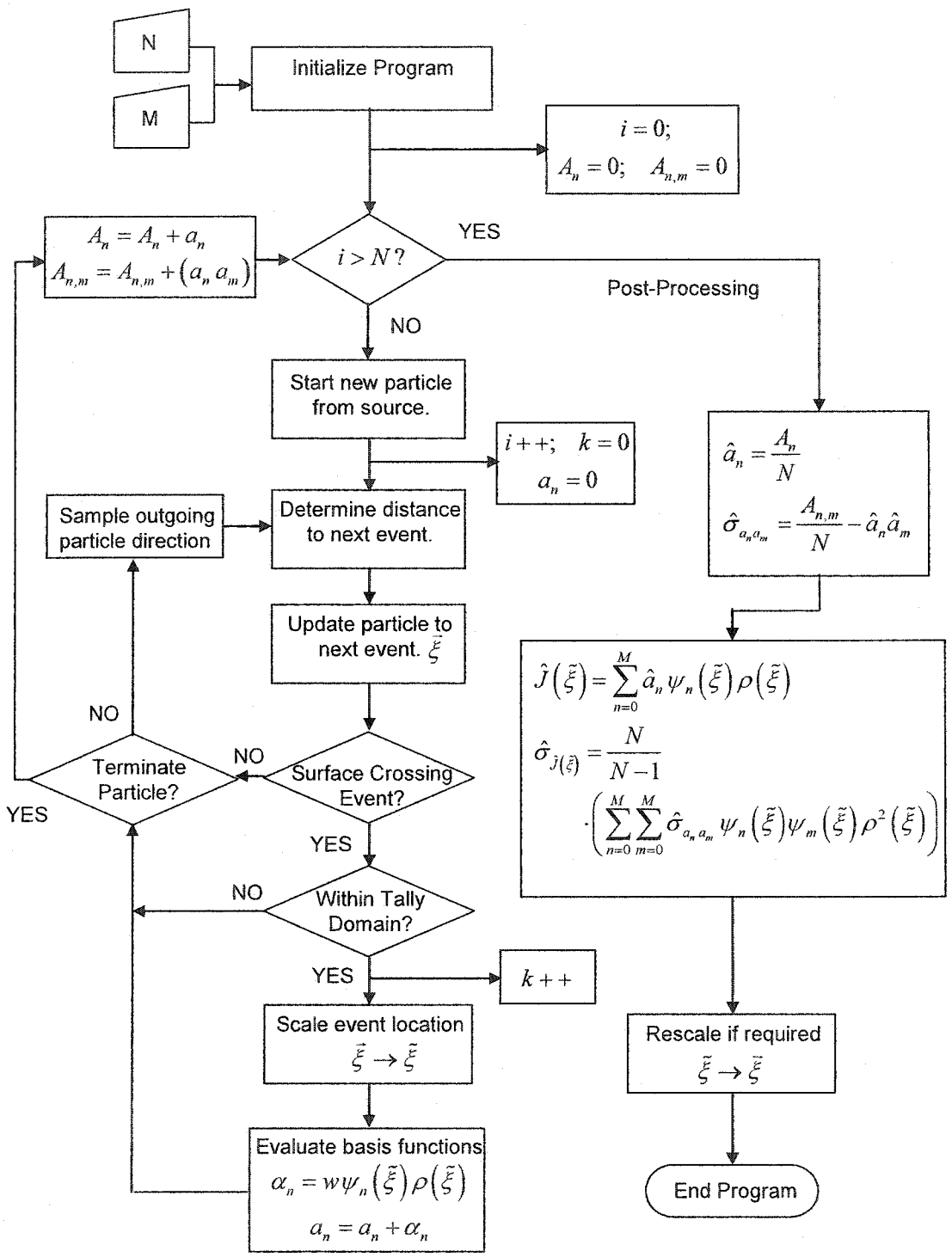

Figure 2.1. Flow chart illustration of surface crossing FET implementation.

2.4. Numerical Results for the FET Surface Crossing Estimator

To verify the theoretical development of the surface crossing FET and its correct implementation in MCNP, the new method was tested against traditional histogram tallies on two benchmark problems. These benchmark results demonstrate that the new FET method agrees with the traditional histogram tally approach and qualitatively indicate that the FET may be more robust and accurate than the histogram. A formal theoretical analysis and quantitative comparison between the two methods will be presented in the next chapter.

2.4.1. Neutron Slowing Down in Hydrogen

The first benchmark problem involves the calculation of the time-spectrum for thermalization of 14 MeV neutrons in hydrogen. This simplified problem is representative of the type of analysis that is required for the design and construction of slowing-down neutron spectrometers. For this benchmark, an MCNP model was created

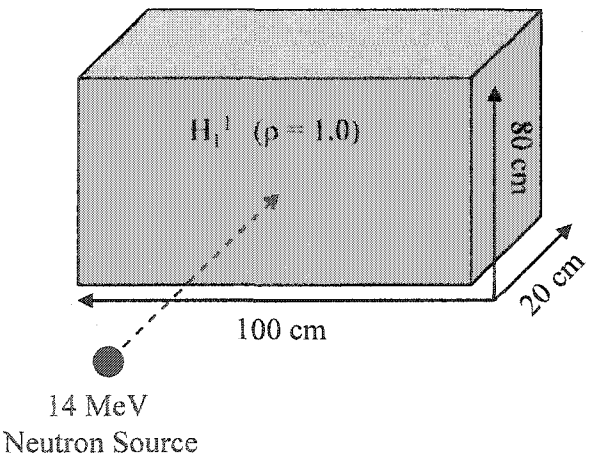

Figure 2.2. MCNP model geometry for the neutron slowing down benchmark.

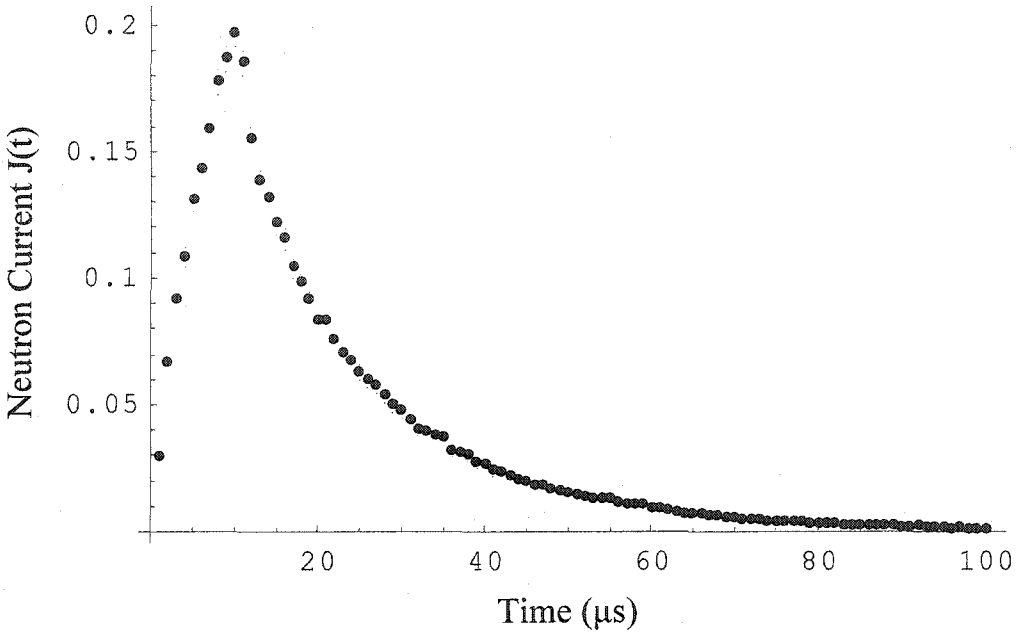

Figure 2.3. Reference time spectrum for neutron slowing down benchmark problem. Reference solution is a 100 bin histogram approximation generated from a 3-million history MCNP simulation. The small points represent a two standard deviation uncertainty band for each data point.

to represent a single neutron source located at the surface of a slab of pure Hydrogen with density ρ=1 gm/cc. The model geometry is shown in Figure 2.2. MCNP was run in fixed source mode to simulate a $10\mu s$ pulse of 14 MeV neutrons directed into the hydrogen. Both histogram and FET tallies were set up to record the times at which neutrons with energies of 1 eV or less (e.g. thermalized neutrons) were emitted from the hydrogen slab. The results provided both a histogram and a functional approximation to the time-spectrum of emitted thermal neutrons.

For comparative purposes, a reference 100-bin histogram approximation was generated using 3 million source particles. A plot of this reference distribution is shown in Figure 2.3. The resulting reference distribution shows a sharp rise in thermal neutron current beginning at 0 μs and peaking at 10 μs. Following this peak, the neutron current appears to fall off exponentially for the next 90 μs. We notice that, for the time scale

selected, the peak in the neutron current is so sharp that it appears as a discontinuity in the first derivative. As noted in the previous section, any "sharp" feature such as this peak can be difficult to resolve with a low order Legendre expansion. In order to temporarily avoid this complication, the first comparison between the histogram and FET approximations was performed on the smooth part of the distribution from 20-100 μs. In this 80 μs interval the first 8 Legendre expansion coefficients for $J(t)$ were estimated by using the FET during a 3 million history simulation. The resulting expansion coefficients are given in Table 2.1 along with their relative uncertainties. We notice that the coefficients all appear to be statistically well converged, both in terms of the relative uncertainty and the cost to benefit metric. We also note that the magnitudes of the coefficients monotonically decrease to 0 (for 4 decimal place precision). This indicates that there should not be a significant amount of truncation error present in the FET approximation. When these coefficients are used to reconstruct a functional approximation, $\hat{J}(t)$, the result (Figure 2.4) shows remarkable agreement with the reference histogram solution.

In order to further compare the histogram and FET approximations, two additional simulations of 30,000 and 3,000 particle histories were run. The results of these simulations are plotted against the reference solution in Figure 2.5 and Figure 2.6, respectively. In the case of the 30,000 history simulation, the FET approximation shows excellent agreement with the histogram benchmark solution. The 30,000 history histogram approximation shows a large amount of variation about the reference result. In this case, the FET appears to give a better approximation to the true shape of the distribution than the corresponding histogram tally. For the 3,000 history simulation,

Table 2.1. FET estimated Legendre expansion coefficients for thermal neutron current distribution in the interval 20-100 μs. The coefficients for a 7th order approximation are presented along with the relative uncertainty and cost-to benefit ratio for each.

Order n	Expansion Coefficient $\hat{a}_n$	Relative Standard Dev. R	Cost to Benefit Ratio R_n^2
0	0.0146	0.003	-
1	-0.0082	0.004	2.40×10^{-5}
2	0.0033	0.008	1.60×10^{-4}
3	-0.0011	0.019	1.26×10^{-3}
4	0.0003	0.055	1.36×10^{-2}
5	-0.0001	0.202	2.24×10^{-1}
6	0.0000*	∞	∞
7	0.0000*	∞	∞

*Indicates a value less than the minimum precision reported in the table. Relative standard deviation and cost-to-benefit ratios cannot be calculated when the estimate is zero.

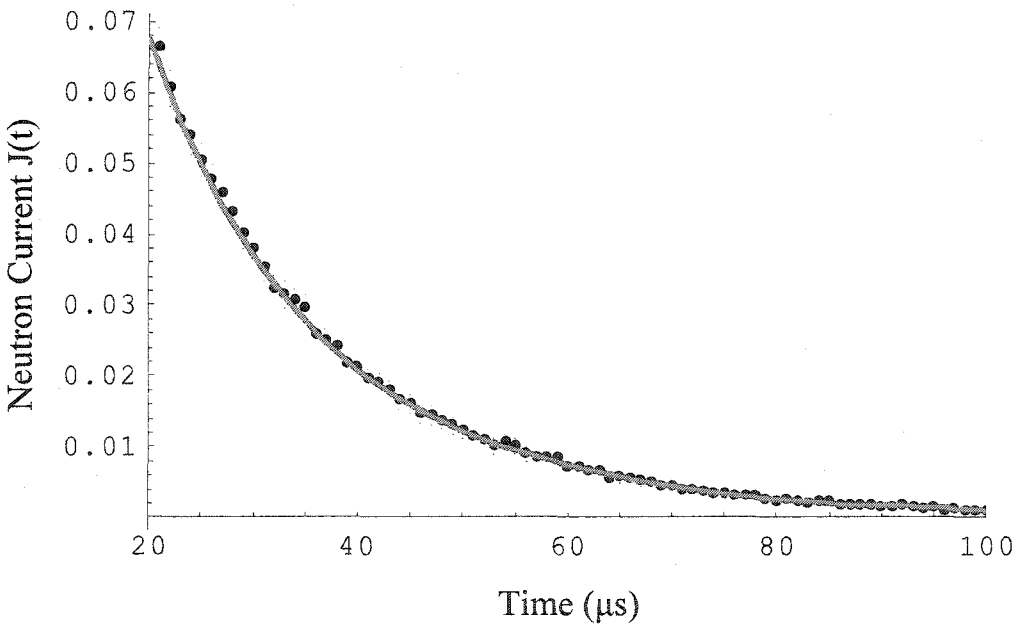

Figure 2.4. Seventh order Legendre FET approximation to thermal neutron time spectrum from 20-100 μs. FET coefficients were generated using a 3-million history MCNP simulation. The dots represent the 3-million history reference histogram approximation.

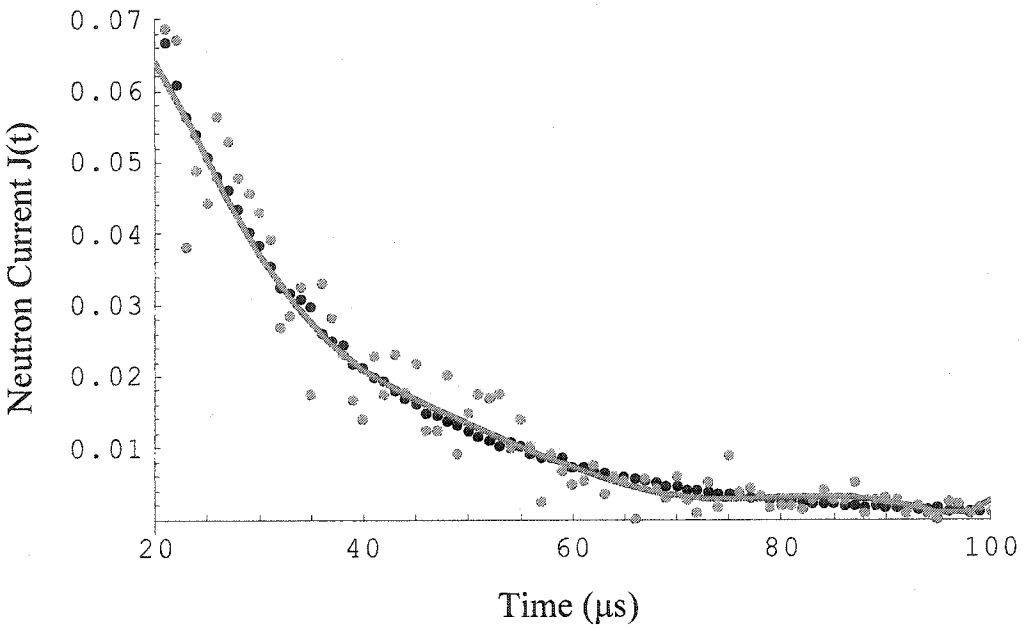

Figure 2.5. Comparison of FET and histogram approximations produced from a 30,000 history MCNP simulation. The black dots represent the 3-million history reference histogram approximation.

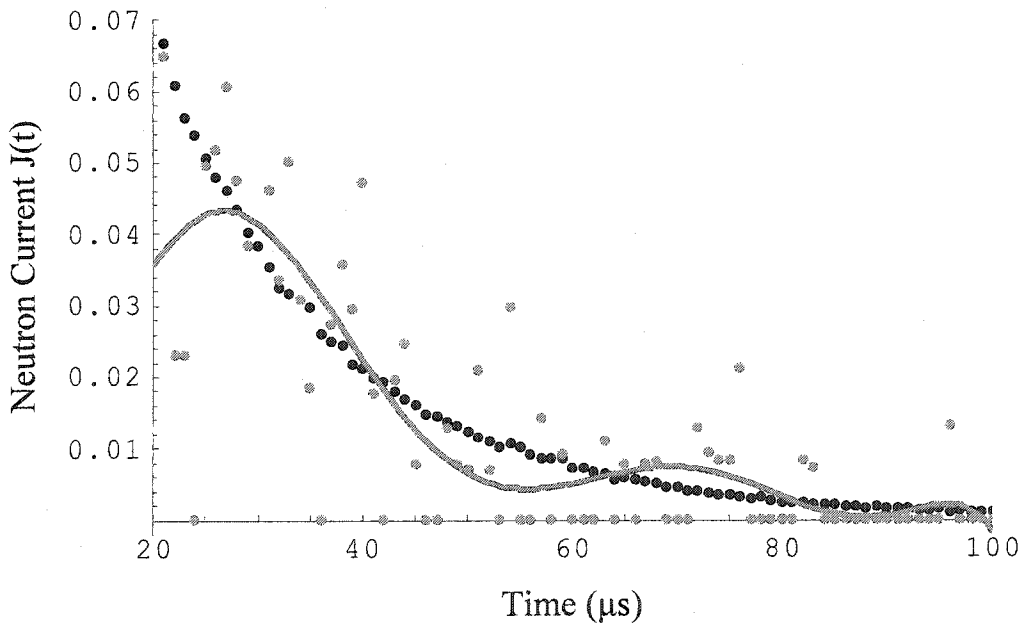

Figure 2.6. Comparison of FET and histogram approximations produced from a 3,000 history MCNP simulation. The black dots represent the 3-million history reference histogram approximation.

neither method is able to give an accurate approximation of the true distribution. In this simulation only 107 of the 3,000 initial particles were scored by the tallies. With only 107 scoring particles, there is too little information available to make a statistically significant approximation using any method.

The results shown above demonstrate that the FET can be used to create an accurate functional approximation for smooth, "well-behaved," distributions. However, the effectiveness of the FET for distributions that are not well-behaved remains to be shown. To address this issue, the neutron slowing down benchmark was repeated; this time using the FET to approximate the entire time spectrum from 0-100 μs. The full-range expansion coefficients were generated during a single 3-million history MCNP simulation, and are given in Table 2.2. Again the coefficients all appear to be statistically well converged, with relative uncertainties and cost-to-benefit ratios well within acceptable limits. We notice, however, that the magnitudes of the coefficients do not monotonically decrease to 0. The coefficients $\hat{a}_5, \hat{a}_6, \hat{a}_7$ all have magnitudes that are relatively large (5-10% of the magnitude of $\hat{a}_0$). The large magnitudes of these coefficients indicate that the Legendre series is not near convergence and that a 7^{th} order expansion may contain significant truncation error. A comparison between the 7^{th} order FET approximation and the reference histogram approximation (Figure 2.7) confirms this fact. The FET approximation does not accurately represent the sharp peak in neutron current that occurs at about 10 μs. It is important to restate that this inaccuracy is due to truncation error caused by not estimating enough expansion coefficients. It is not a result of statistical error, and, therefore, the accuracy of the approximation can not be improved

Table 2.2. FET estimated Legendre expansion coefficients for thermal neutron current distribution in the interval 0-100 μs. The coefficients for a 7th order approximation are presented along with the relative uncertainty and cost-to benefit ratio for each.

Order n	Expansion Coefficient $\hat{a}_n$	Relative Standard Dev. R	Cost to Benefit Ratio R_n^2
0	0.0398	0.002	-
1	-0.0238	0.003	1.35×10^{-5}
2	0.0082	0.006	9.00×10^{-5}
3	0.0005	0.073	1.87×10^{-2}
4	-0.0037	0.008	2.88×10^{-4}
5	0.0040	0.007	2.70×10^{-4}
6	-0.0031	0.009	5.27×10^{-4}
7	0.0019	0.014	1.47×10^{-3}

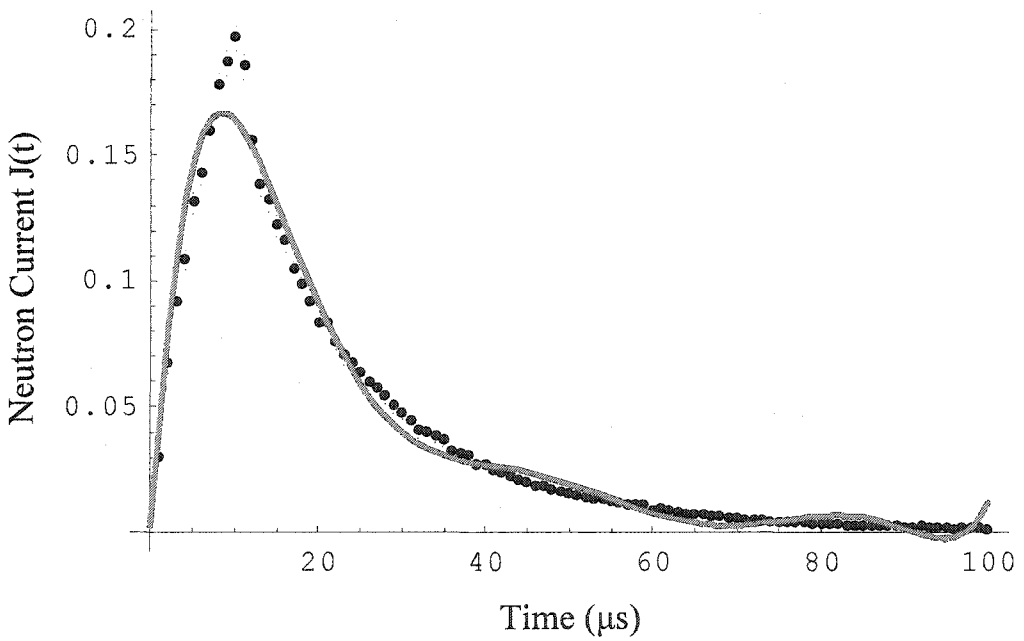

Figure 2.7. Seventh order Legendre FET approximation to thermal neutron time spectrum from 0-100 μs. FET coefficients were generated using a 3-million history MCNP simulation. The dots represent the 3-million history reference histogram approximation.

by running more particle histories during the simulation. The relationship between truncation error and statistical error in the FET will be examined in detail in the next chapter.

Another method for improving the accuracy of the FET approximation in this case is the use of a piecewise tally. In a piecewise tally, the entire tally domain is broken into several smaller tallies, in an effort to eliminate singularities that may be present in the solution function. For the neutron slowing-down benchmark problem, a two region piecewise tally could produce significant improvement. If the tally domain were divided at t=10 μs, then the true distribution in each piecewise tally bin would be well approximated by a low order Legendre expansion. Even if the true location of the neutron current peak is not known exactly, a piecewise tally can be used to stretch and smooth the distribution in this vicinity, possibly resulting in better resolution of the peak.

2.4.2. Active Neutron Interrogation of Subterranean Water

As a second benchmark, the modified version of MCNP was tested on a fixed-source neutron interrogation problem that mimics a search for subterranean water. The problem is modeled as a uniformly distributed 14 MeV neutron source located 5 cm above a 20 cm × 20 cm area of the ground surface. The ground consists of sand (SiO_2) at a density of 1.55 g/cc with a 11 cm × 13 cm × 1.2 cm pocket of water located 15 cm below the surface. A diagram of the model geometry is given in Figure 2.8. All source neutrons are started at time zero with an initial direction normal to the surface. A surface crossing estimator located at the ground surface is used to tally thermalized neutrons that

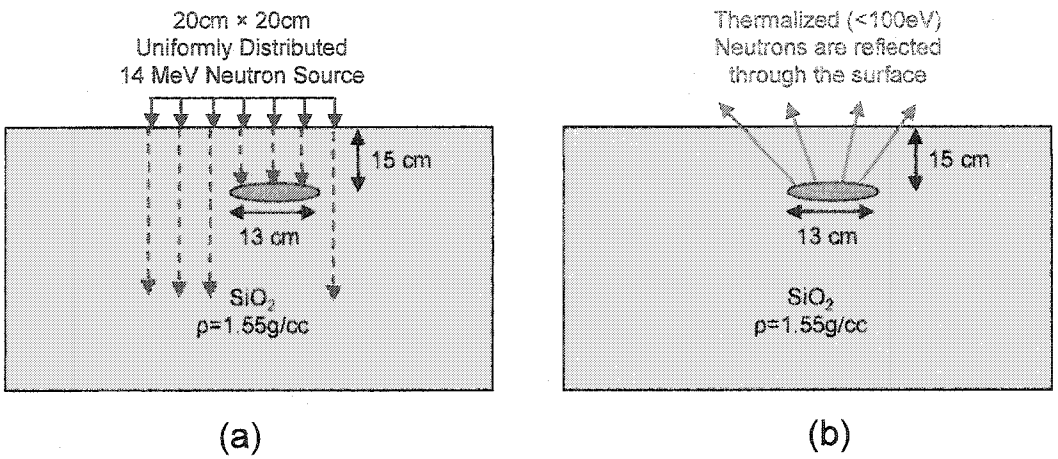

Figure 2.8. MCNP Model geometry for the active neutron interrogation benchmark problem. A uniformly distributed source of 14 MeV neutrons is directed into sandy soil containing a pocket of water located 15 cm below the surface (a). Neutrons entering the water pocket are themalized and reflected back towards the ground surface (b).

exit the soil. The time spectrum of these reflected thermal neutrons can be used to diagnose the presence of subsurface water.

For a reference solution, the time domain from 0-25 μs was divided into 100 bins, and a 100-million history fixed source MCNP calculation was used to tally the exiting thermal neutron current in each bin. This results in a histogram approximation to the true thermal neutron time spectrum. The same problem was then run using the surface crossing FET to estimate the first 20 Legendre expansion coefficients of the time spectrum between t=0 and 25 μs. The expansion coefficients, along with their relative cost-to-benefit ratios are given in Table 2.3. Inspection of the results shows that all but one of the expansion coefficients have an R_n value of less than one, indicating that they are statistically well converged and should be included in the series expansion. Table 2.3 also includes the partial sums of the $\hat{a}_n^2$ terms. These sums can be used to verify that the

Table 2.3. The first 20 Legendre expansion coefficients for active neutron interrogation benchmark problem. All coefficients were produced from a 100-million history MCNP simulation.

Order M	Expansion Coefficient $\hat{a}_M$	Cost-to-Benefit Ratio R_M^2	$\sum_{n=0}^{M} \hat{a}_n^2$
0	7.551×10^{-4}	-	2.281×10^{-10}
1	-1.876×10^{-4}	7.206×10^{-5}	2.703×10^{-10}
2	-2.204×10^{-5}	4.108×10^{-3}	2.713×10^{-10}
3	6.921×10^{-5}	3.974×10^{-4}	2.847×10^{-10}
4	-6.167×10^{-5}	5.654×10^{-4}	2.984×10^{-10}
5	4.596×10^{-5}	1.126×10^{-3}	3.077×10^{-10}
6	-2.808×10^{-5}	3.053×10^{-3}	3.118×10^{-10}
7	8.538×10^{-6}	3.202×10^{-2}	3.122×10^{-10}
8	6.704×10^{-6}	4.979×10^{-2}	3.125×10^{-10}
9	-1.577×10^{-5}	8.852×10^{-3}	3.144×10^{-10}
10	1.610×10^{-5}	8.594×10^{-3}	3.166×10^{-10}
11	-1.264×10^{-5}	1.412×10^{-2}	3.181×10^{-10}
12	7.310×10^{-6}	4.321×10^{-2}	3.186×10^{-10}
13	-2.413×10^{-6}	3.964×10^{-1}	3.187×10^{-10}
14	-5.742×10^{-7}	6.916	3.187×10^{-10}
15	3.702×10^{-6}	1.653×10^{-1}	3.189×10^{-10}
16	-5.042×10^{-6}	8.850×10^{-2}	3.192×10^{-10}
17	5.156×10^{-6}	8.431×10^{-2}	3.196×10^{-10}
18	-3.888×10^{-6}	1.503×10^{-1}	3.198×10^{-10}
19	2.663×10^{-6}	3.223×10^{-1}	3.199×10^{-10}

truncation error in the approximation is acceptably small. Inspection of the partial sums (Figure 2.10) shows convergence to a constant value as predicted by Parseval's theorem.

These results also demonstrate that, for this problem, an expansion with as few as 7-10 terms may be a suitable approximation. In addition to the expansion coefficients, the MCNP simulation also provided sample estimates for the covariance between every combination of coefficients. These covariance results were then used in Eq. (2.32) to produce an estimate for the uncertainty in the functional expansion.

The previous benchmark problem focused on examining the behavior of a fixed order FET approximation as the numbers of particle histories were varied. For this

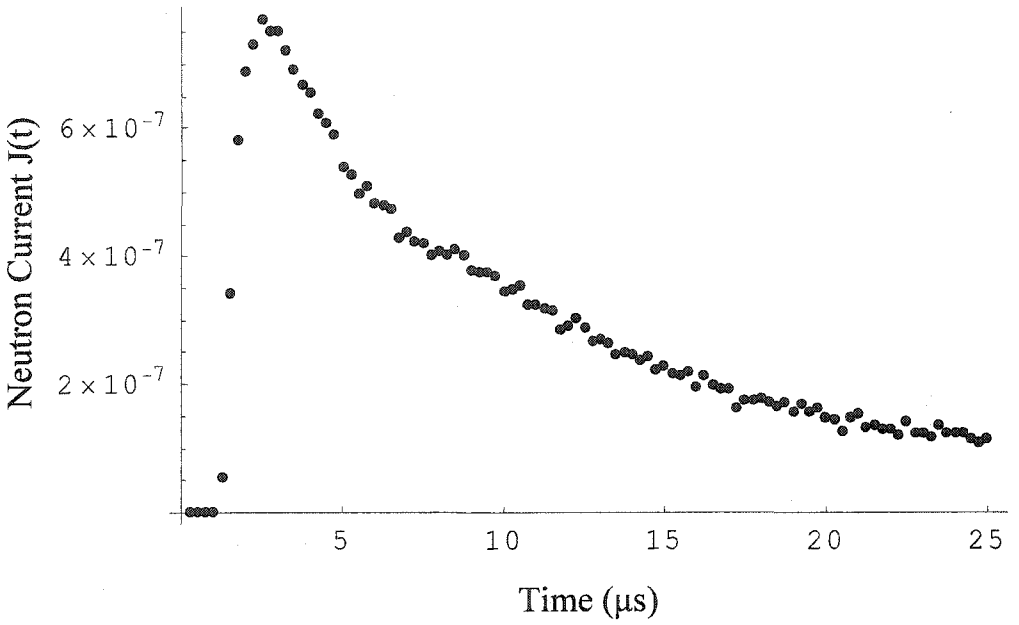

Figure 2.9. Reference time spectrum for the active neutron interrogation benchmark problem. Reference solution is a 100 bin histogram approximation generated from a 100-million history MCNP simulation.

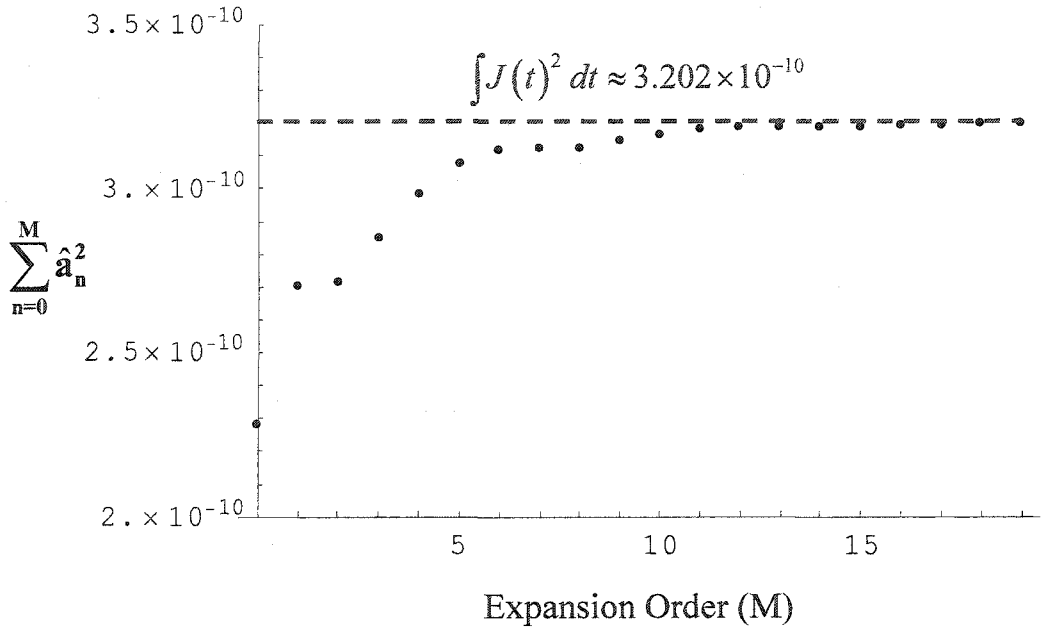

Figure 2.10. Partial sums of the Legendre expansion coefficients squared for the active neutron interrogation benchmark. By Parseval's theorem these sums should converge to the two-norm of the true distribution as the truncation error goes to zero. The dashed line shows an estimate of the 2-norm calculated from the reference histogram distribution.

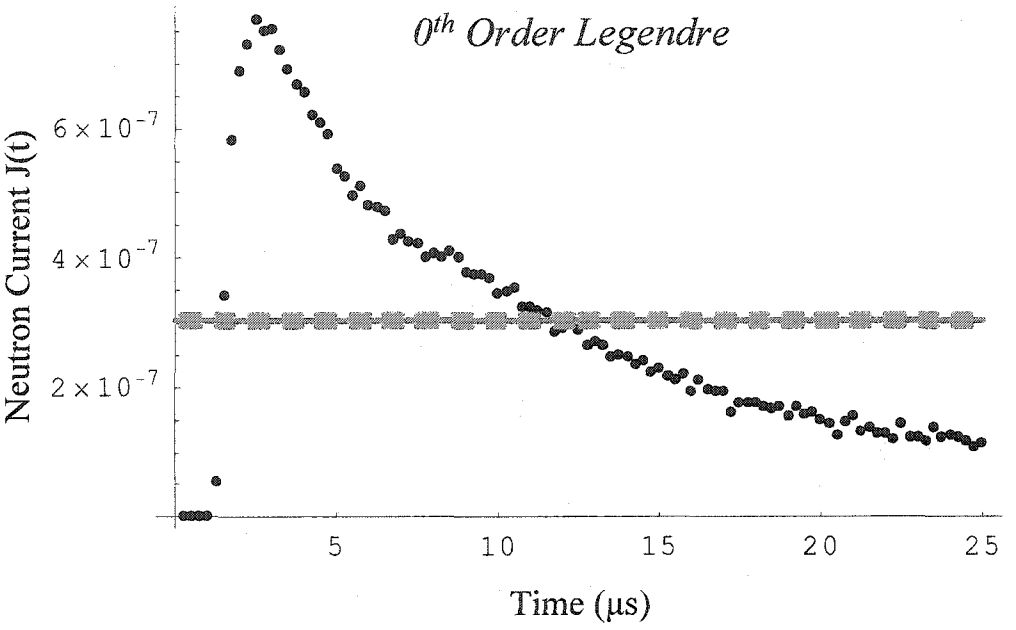

Figure 2.11. Zeroth order Legendre approximation to thermal neutron time distribution from 0-25 μs. FET coefficients were generated using a 100-million history MCNP simulation. The dashed lines represent a two standard deviation uncertainty band around the functional approximation.

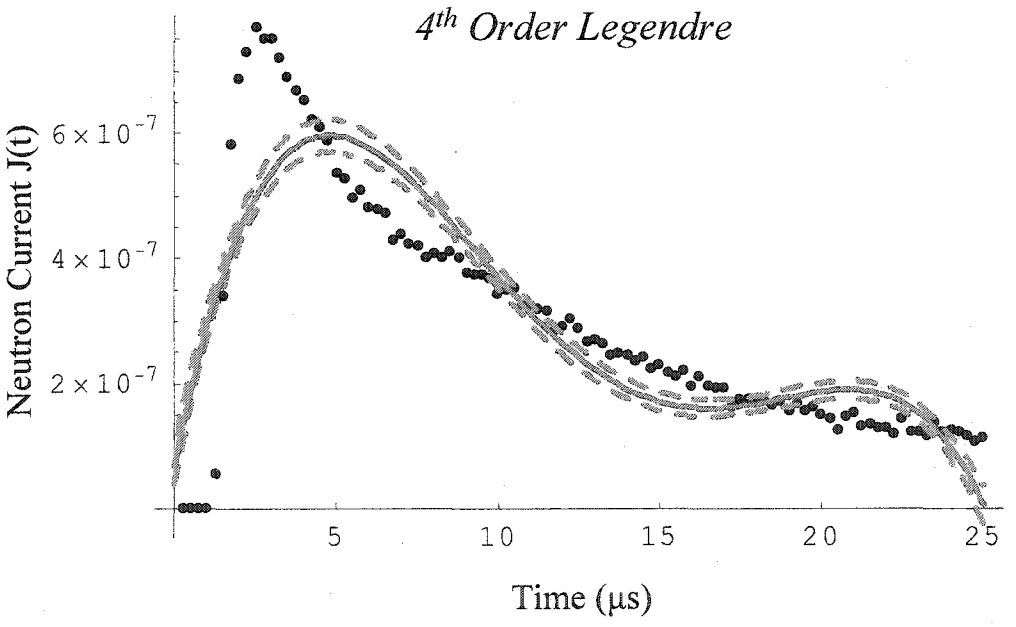

Figure 2.12. Fourth order Legendre approximation to thermal neutron time distribution from 0-25 μs. FET coefficients were generated using a 100-million history MCNP simulation. The dashed lines represent a two standard deviation uncertainty band around the functional approximation.

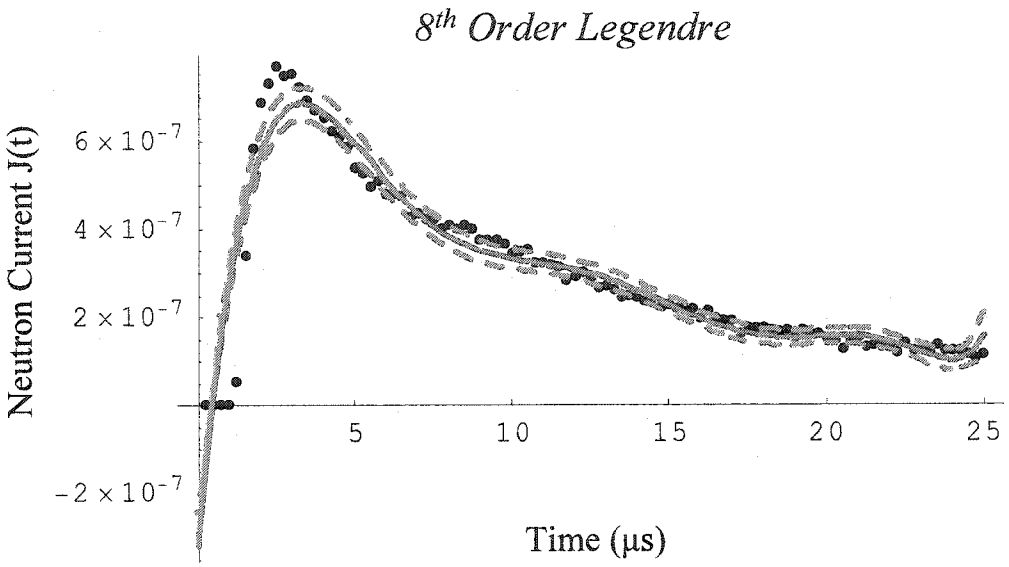

Figure 2.13. Eighth order Legendre approximation to thermal neutron time distribution from 0-25 μs. FET coefficients were generated using a 100-million history MCNP simulation. The dashed lines represent a two standard deviation uncertainty band around the functional approximation.

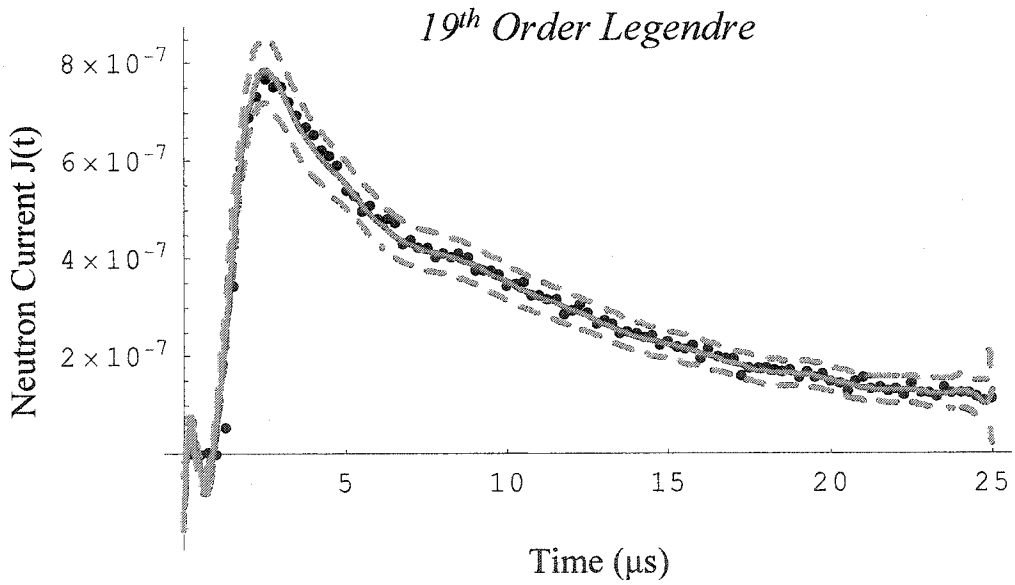

Figure 2.14. Ninteenth order Legendre approximation to thermal neutron time distribution from 0-25 μs. FET coefficients were generated using a 100-million history MCNP simulation. The dashed lines represent a two standard deviation uncertainty band around the functional approximation.

benchmark the number of particle histories will remain fixed at 100-million, while the expansion order of the FET will be varied. These tests will provide additional insight into the role of truncation error in the FET. Using the expansion coefficients given in Table 2.3, four separate Legendre approximations (with truncation orders of 0, 4, 8, and 19) were constructed. These Legendre approximations are shown plotted against the reference solution in Figure 2.11 through Figure 2.14.

The 0^{th} order expansion (Figure 2.11) is equivalent to a single bin histogram taken over the tally domain. This approximation gives the average current over the domain, and preserves the integral of the distribution (as do all of the higher order approximations). Notice that the statistical uncertainty (dashed lines) for the functional expansion is very small, but the approximation is unable to resolve any temporal features of the true distribution.

The 4^{th} order expansion (Figure 2.12) adds some gross temporal resolution to the approximation but is not able to resolve important features of the distribution correctly. This low-order approximation correctly describes the asymmetry of the distribution but fails to correctly reconstruct the sharp rise and peak in neutron current or the exponential decay that follows.

The 8^{th} order expansion (Figure 2.13) does a much better job at resolving the sharp rise in neutron current and the location of the peak, but it still underpredicts the height of the peak. Furthermore, this approximation shows an unphysical negative current for the first microsecond of the problem.

Finally, the 19^{th} order expansion, shown in Figure 2.14, demonstrates excellent agreement with the reference histogram solution. The majority of histogram data points

fall within one ensemble standard deviation of the 19th order Legendre approximation, indicating agreement within the limits of statistical uncertainty. The functional approximation is able to accurately model the important features of the spectrum, including the occurrence of the leading edge at ~1 μs, the sharp rise to the peak of the spectrum at ~3 μs, and the subsequent exponential decay following the peak. The functional approximation does not do well in the short period (0-1 μs) before the first thermal neutrons are observed exiting from the surface of the ground. During this time the functional approximation again shows a non-physical negative total current. This arises due to the discontinuity in the derivative of the current distribution that occurs at the leading edge. This problem is inherent to functional expansions near discontinuities in the function or its derivatives. It is important to note, however, that the problem is localized near the discontinuity and does not have a significant effect on the rest of the approximation.

Another noticeable feature of the 19th order approximation occurs near the right endpoint, at t=25 μs. Here, the standard deviation of the functional approximation shows a sudden increase, indicating more statistical uncertainty at the endpoint. Close examination of the raw data used to produce Figure 2.14 reveals that there is also a sharp increase in the standard deviation of the functional approximation near the left endpoint, as well. These sudden increases in the standard deviation are a consequence of using the Legendre polynomials as the basis set for the expansion. All Legendre polynomials are normalized so that their endpoints evaluate to ±1. Away from the endpoints, however, high-order Legendre polynomials have values close to zero. Therefore, high-order Legendre terms contribute the most near the two endpoints of an expansion. Because the

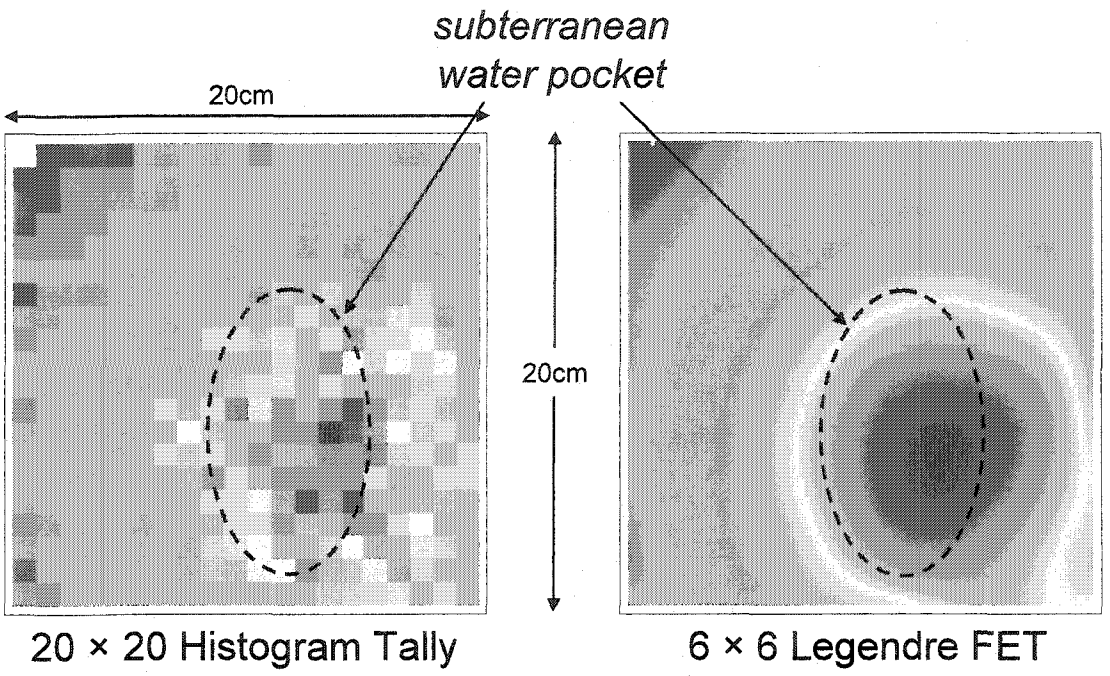

Figure 2.15. Histogram and Legendre approximations to the surface distribution of thermal neutrons exiting soil surface. The red indicates a high intensity of reflected thermal neutrons directly above the water pocket (dashed line) located 15 cm below the ground surface.

highest order terms also have the most statistical uncertainty, it follows that the resulting functional expansion will have a greater variance near the endpoints.

As a final component of this benchmark, the FET was used to produce a 2-D approximation for the spatial distribution (in the X-Y plane) of thermal neutrons reflected back through the soil surface. In practice, measurements like this could be used to estimate the location and shape of underground water deposits. A 2-D product set of Legendre polynomials, $P_{m,n}(x,y) = P_m(x)P_n(y)$, was used for the expansion basis. A 100-million history MCNP simulation was run to estimate 36 expansion coefficients (a 6×6 expansion) with respect to this basis set. An additional 100-million history simulation was run to produce a 20×20 bin histogram solution. The results of these simulations, shown in Figure 2.15, demonstrate that both methods produce results that

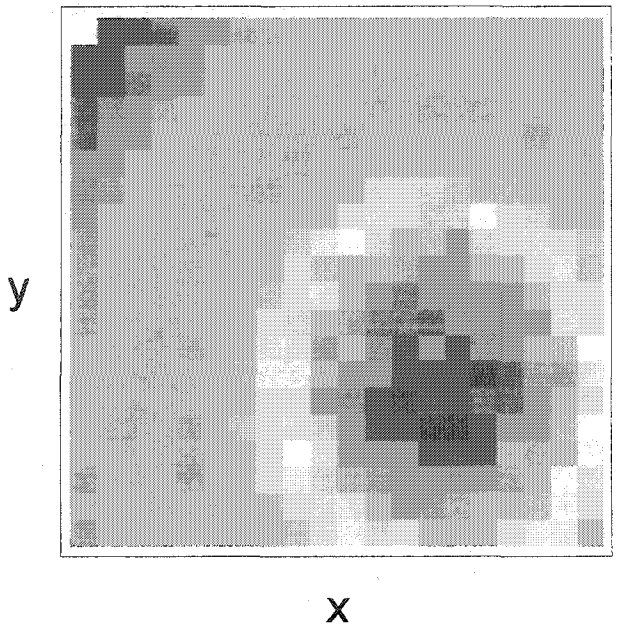

Figure 2.16. Reference histogram solution for the surface distribution of thermal neutrons exiting the soil surface. The red indicates a high intensity of reflected thermal neutrons directly above the water pocket located 15 cm below the ground surface. The reference solution was generated by a 1-billion history fixed source calculation in MCNP4c. Each bin in the solution has a relative standard deviation less than 2%.

clearly show the location of the underground water pocket (dashed line). The two results appear qualitatively very similar, indicating agreement between the two. The FET approximation, however, produces a much smoother solution than the histogram.

In order to quantitatively compare these two results, a 1-billion history simulation was run to provide a reference 20×20 bin histogram solution. The relative statistical uncertainty for every bin of this reference histogram solution was estimated to be has less than 2%. A plot of the reference solution is shown in Figure 2.16. A direct comparison between the 100-million history and 1-billion history histogram approximations was made by calculating the relative difference between the individual bins of the two approximations. This comparison (Figure 2.17a) shows reasonable agreement between

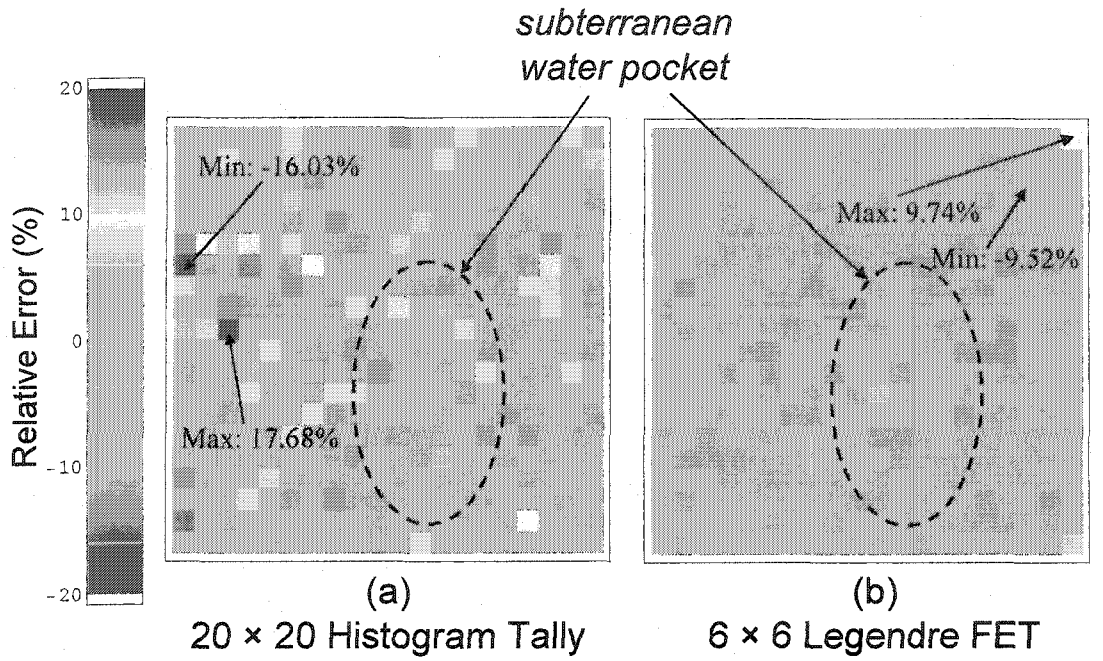

Figure 2.17. Approximation errors for the 100-million history histogram (a) and FET (b) approximations for the spatial distribution of thermal neutrons reflected through the soil surface. Errors shown are relative to the 1-billion history reference solution. The histogram approximation has a maximum single-bin error of 17.68%, and an average error (over all bins) of 4.48%. The FET approximation has a maximum single-bin error of 9.74%, and an average error of 2.07%.

the two approximations, with a maximum bin difference of 17.68%, and an average difference of 4.48%, when taken over all 400 bins.

A direct comparison of the FET and reference histogram approximations is more difficult. The FET approximation is a continuous function over the entire expansion domain, while the histogram approximation is an array of current values, each averaged over a small tally area. In order to obtain a fair comparison between these two results, the FET approximation was converted into a histogram. This was done by integrating the functional expansion over small segments of the surface that correspond with individual bins in the histogram approximation. A more thorough explanation of this FET-to-histogram technique is provided in section 4.5.1. After the FET solution was converted

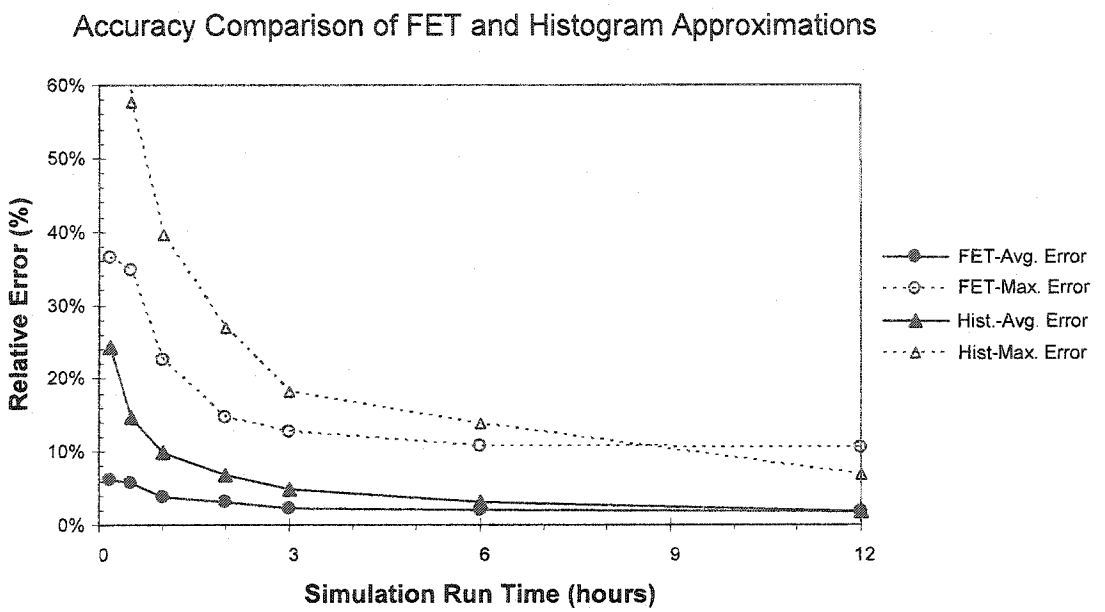

Figure 2.18. Relative accuracy comparison of the FET and histogram approximations for the 2D spatial surface current benchmark problem. The maximum single-bin and average bin errors (relative to a 1-billion history reference histogram) for both approximations are shown as a function of computer run-time for each simulation.

into a histogram, it could be compared with the reference solution by calculating the relative difference between the individual bins of the two approximations. This comparison (Figure 2.17b) shows that the FET solution is actually a closer approximation to the reference histogram than the 100-million history histogram, with a maximum bin difference of 9.74%, and an average difference of 2.07%, when taken over all 400 bins. However, this increased accuracy comes with a computational cost. On average, the FET simulations were found to run ~6-8% longer than simulations with histogram tallies. This extra run time is due to the fact that the code must evaluate a series of Legendre polynomials each time a particle scores the tally.

In order to assess the relative benefit of the FET, a series of fixed run-time simulations were run using the 2D spatial surface crossing current benchmark problem. In each trial, two identical simulations were run for a fixed amount of computer time on a

Dell Precision 520 workstation with two 1.70 GHz Intel Xeon processors and 2 gigabytes of RAM. One simulation used FET to estimate 20 functional expansion coefficients, while the other simulation used a 20×20 bin histogram tally. After the simulations finished, the two approximations were compared against the 1-billion history reference result, using the methodology described above. The relative errors of the fixed-time approximations for each trial were computed and plotted against run time, as shown in Figure 2.18. For the same amount of work, the results show that the FET is able to produce a more accurate approximation than the histogram tally. This increase in accuracy is especially pronounced for shorter run-times (30 minutes- 2 hours).

2.5. FET Collision Estimators for Particle Flux

The derivations and numerical examples presented so far in this chapter have dealt only with surface crossing FET estimators. All of these results, however, are actually much more general and apply to any discrete event FET estimator. One such estimator of particular interest is the collision estimator, used to tally flux in a volume. The collision estimator is so widely used in Monte Carlo simulations that some comments on the application of the FET to this estimator are required for the sake of completeness.

2.5.1. Derivation of the FET Collision Estimators and their Variance

The derivation of the FET collision estimators for approximating volumetric flux distributions $\phi(\vec{\xi})$ mimics the derivation for the surface crossing current distributions

presented in section 2.1. Following the same line of logic, the volumetric flux distribution can be written as a series expansion in an arbitrary set of basis functions $\left\{\psi_n\left(\vec{\xi}\right)\right\}_{n=0}^{\infty}$ that are orthogonal with respect to a weighting function $\rho\left(\vec{\xi}\right)$,

$$\phi\left(\vec{\xi}\right)=\sum_{n=0}^{\infty}\bar{b}_n\psi_n\left(\vec{\xi}\right)\rho\left(\vec{\xi}\right). \tag{2.44}$$

Expressions for the expansion coefficients $\bar{b}_n$ can be derived immediately from the orthogonality property of the basis functions,

$$\bar{b}_n=\int_{\Gamma}\phi\left(\vec{\xi}\right)\psi_n\left(\vec{\xi}\right)\rho\left(\vec{\xi}\right)d\vec{\xi}\ . \tag{2.45}$$

The expression for $\bar{b}_n$ is in an integral form that can be easily evaluated by Monte Carlo. By taking $g\left(\vec{\xi}\right)=\psi_n\left(\vec{\xi}\right)\rho\left(\vec{\xi}\right)$ in Eq. (1.59), it follows that

$$\hat{b}_n=\frac{1}{N}\sum_{i=1}^{N}\sum_{k=1}^{K_i}\frac{\psi_n\left(\vec{\xi}_{i,k}\right)\rho\left(\vec{\xi}_{i,k}\right)}{\Sigma_t\left(\vec{\xi}_{i,k}\right)} \tag{2.46}$$

is an unbiased estimator for the expansion coefficient $\bar{b}_n$. It can also be shown (using the derivations outlined earlier in the chapter) that the statistic

$$\begin{aligned}\hat{\sigma}^2_{\bar{b}_n}=&\frac{1}{N(N-1)}\sum_{i=1}^{N}\left(\sum_{k=1}^{J_i}\frac{w_{i,k,S}}{\Sigma_t\left(\vec{\xi}_{i,k}\right)}\psi_n\left(\vec{\xi}_{i,k}\right)\rho\left(\vec{\xi}_{i,k}\right)\right)^2\\&-\frac{1}{N-1}\left(\frac{1}{N}\sum_{i=1}^{N}\sum_{k=1}^{J_i}\frac{w_{i,k,S}}{\Sigma_t\left(\vec{\xi}_{i,k}\right)}\psi_n\left(\vec{\xi}_{i,k}\right)\rho\left(\vec{\xi}_{i,k}\right)\right)^2\end{aligned} \tag{2.47}$$

is an unbiased estimator for the variance of an individual expansion coefficient, $\sigma^2_{\bar{b}_n}$. All of the other results shown in sections 2.1 and 2.2 (e.g. variance of the functional

expansion, two-norm of the functional expansion variance, truncation error estimates, and cost-to-benefit ratio) are identical for the collision estimator.

2.5.2. Implementation of the FET Collision Estimator

Most of the issues surrounding the numerical implementation of an FET collision estimator are identical to those for a surface crossing estimator, which were covered in section 2.3. In fact, the only difference between the implementations of the two methods is when a given particle scores. For the surface crossing estimator, a particle scores when it crosses the tally surface within the specified domain. For the collision estimator, a particle scores when it undergoes a collision within the tally domain. This difference is reflected on the implementation flow chart shown in Figure 2.19.

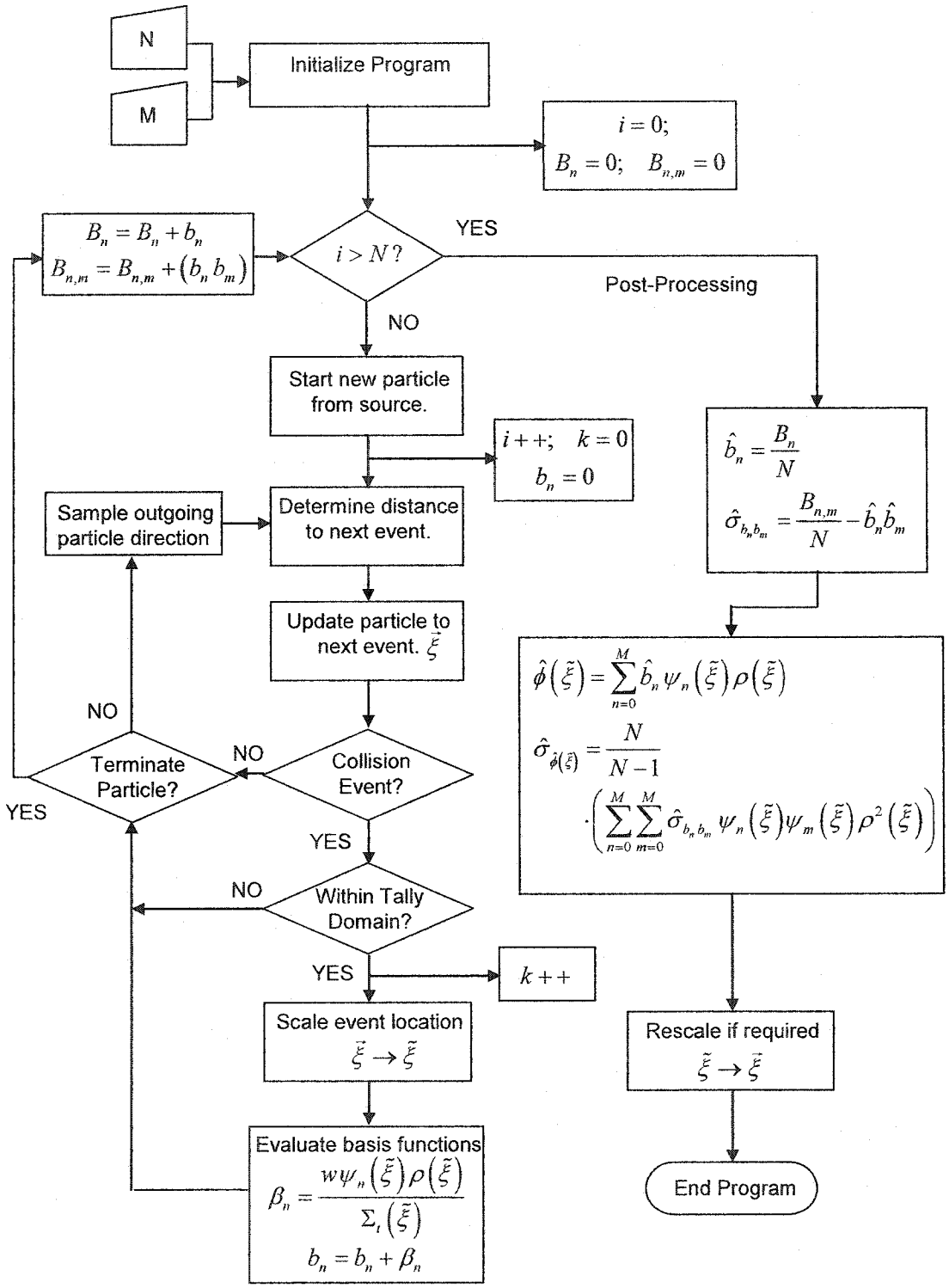

Figure 2.19. Flow chart illustration of FET collision estimator implementation.

CHAPTER 3

FET CONVERGENCE PROPERTIES

In two of the earliest papers on the FET[18,19], claims were made that the method can offer "substantial variance reduction" over traditional tallies. These statements were based on the insight of the authors coupled with a few supporting examples. Indeed, the conclusion of variance reduction seems both reasonable and plausible. Even the results in the previous chapter seem to indicate that a well-converged, properly executed FET expansion can provide a more accurate approximation than a histogram produced from the same data. However, all of these conclusions are based on individual experiments. No quantitative comparison between the two approximation techniques has ever been reported in the literature.

In this chapter a detailed theoretical analysis of the convergence properties of the FET and histogram approximations is presented. These convergence properties can then be used to directly compare the two methods and establish under what conditions the FET can offer variance reduction.

3.1. Comparison of Generic FET and Histogram Estimators

The analysis begins by considering an accurate Monte Carlo algorithm that produces independent realizations of a random variable x. It is assumed that the probability density function $P(x)$ associated with this random variable is not known a priori and that the end-user wishes to infer the shape of $P(x)$ from a set of independent realizations produced by a Monte Carlo simulation. The traditional approach to obtaining such information is to divide the domain of the random variable into "bins", $b = \{1,2,\ldots,M\}$, and then count the number of events that occur in each bin, N_b, during the simulation. The total score in a bin, N_b, divided by the number of independent trials, N, is an unbiased estimator for the probability that a given realization will fall within the bin, or

$$E\left[\frac{N_b}{N}\right] = P\left(x_{b-1} \le x < x_b\right), \tag{3.1}$$

where x_{b-1} and x_b denote the bounds of bin b. When this process is repeated for all of the bins the result is a histogram approximation to the actual probability density function,

$$P(x) = \sum_{b=1}^{M}\left(\overline{P_{M,b}^{hist}}(x) + O\left[\Delta x_b\right]\right), \tag{3.2}$$

where

$$\overline{P_{M,b}^{hist}}(x) = \frac{P(x_{b-1} \le x < x_b)}{\Delta x_b}, \tag{3.3}$$

Δx_b is the width of bin b, and $\overline{P_{M,b}^{hist}}(x)$ is the true value of the histogram in bin b. As the number of bins, M, is increased the truncation error decreases and the histogram approximation converges to the continuous distribution.

In the FET, the unknown pdf $P(x)$ is represented as a series expansion in a complete set of basis functions, and the set of independent samples is used to estimate the expansion coefficients for the expansion. If $\{\psi_n\}_0^\infty$ is a complete orthogonal set with respect to the weighting function ρ in $L_\rho^2(\Gamma)$, the space of all square integrable functions over some bounded domain Γ, then any $P(x) \in L_\rho^2(\Gamma)$ can be written as

$$P(x) = \sum_{n=0}^{\infty} \overline{a}_n k_n \psi_n(x). \tag{3.4}$$

In Eq. (3.4) $\overline{a}_n$ is the true n^{th} expansion coefficient defined by the inner-product,

$$\overline{a}_n = \int_\Gamma \psi_n(x)\rho(x)P(x)dx, \tag{3.5}$$

and k_n is the normalization constant for the n^{th} basis function [32],

$$k_n = \frac{1}{\|\psi_n\|^2}. \tag{3.6}$$

In order to calculate a functional approximation to $P(x)$, the expansion coefficients $\overline{a}_n$ must be determined. Fortunately, Eq. (3.5) can be easily estimated by Monte Carlo by using the sample statistic

$$\hat{a}_n = \frac{1}{N}\sum_{i=1}^{N} \psi_n(x_i)\rho(x_i), \tag{3.7}$$

which is an unbiased estimator for the true expansion coefficient $\overline{a}_n$. We notice that Eq. (3.7) is very similar to the discrete event FET estimators given in Eq. (2.14) and (2.46).

In fact, Eq. (3.7) is a simplified version of the estimators derived in the previous chapter. In this simplified formulation, only one independent sample is taken from the distribution per history, as opposed to the series of correlated samples that result from a true random walk. Still, Eq. (3.7) captures the essence of the FET, and the analysis of the convergence properties becomes much easier without having to worry about the statistical dependence between samples. Furthermore, even though the results and analysis presented in this chapter are given for a simplified version of the FET, they can be easily extended to apply to any of the specific FET estimators.

By comparing Eq. (3.5) with the definition for an expected value (Eq. (1.1)), it becomes clear that the true expansion coefficient $\bar{a}_n$ is actually the expected value of the function $a_n(x) = \psi_n(x)\rho(x)$ over the random variable $\mathbf{x}$,

$$\bar{a}_n = E\left[\psi_n(\mathbf{x})\rho(\mathbf{x})\right] = \int_\Gamma \psi_n(x)\rho(x)P(x)dx \,. \tag{3.8}$$

From Eq. (3.8), it is straightforward to calculate the variance of $a_n(\mathbf{x})$,

$$\begin{aligned} \sigma^2_{a_n} &= E\left[\left(\psi_n(\mathbf{x})\rho(\mathbf{x})\right)^2\right] - E\left[\psi_n(\mathbf{x})\rho(\mathbf{x})\right]^2 \\ &= \int_\Gamma \left(\psi_n(x)\rho(x)\right)^2 P(x)\, dx - \bar{a}_n{}^2 . \end{aligned} \tag{3.9}$$

The variance for an estimate of the mean $\bar{a}_n$ made with N independent trials can now be written in terms of the true variance given in Eq. (3.9):

$$\sigma^2_{\hat{a}_n} = \frac{1}{N}\sigma^2_{a_n} \,. \tag{3.10}$$

Equations (3.9) and (3.10) give an analytic form for the true variance of expansion coefficients estimated by the Monte Carlo calculation. The sample variance of Eq. (3.10) provides an unbiased estimator of $\sigma^2_{\hat{a}_n}$ and can be calculated in the usual way,

$$\hat{\sigma}^2_{\hat{a}_n} = \frac{\sum_{i=1}^{N}\left(\psi_n(x_i)\rho(x_i)\right)^2 - \frac{1}{N}\left(\sum_{i=1}^{N}\psi_n(x_i)\rho(x_i)\right)^2}{N(N-1)}. \tag{3.11}$$

Equation (3.11) gives a measurement of the statistical uncertainty in each individual expansion coefficient. We notice that the result is similar to the variance for the discrete event FET estimators derived in section 2.2.1. In fact, the same methodology that was used in section 2.2.2 can be applied in this case to derive the sample variance for the functional expansion,

$$\hat{\sigma}^2_{\widehat{P_M}(x)} = \frac{N}{N-1}\sum_{n=0}^{M}\sum_{m=0}^{M}\hat{\sigma}_{a_n a_m}\left(k_n\psi_n(x)\right)\left(k_m\psi_m(x)\right), \tag{3.12}$$

and its 2-norm,

$$\int_{\Gamma}\hat{\sigma}^2_{\widehat{P_M}}(x)\rho(x)\,dx = \sum_{n=0}^{M}\hat{\sigma}^2_{\hat{a}_n}k_n. \tag{3.13}$$

In Eqs. (3.12) and (3.13) the notation $\widehat{P_M}(x)$ has been used to represent the M^{th} order functional approximation to the true function $P(x)$.

3.2. Theoretical Convergence Properties of the FET

Having established that Monte Carlo can be used to calculate a functional approximation to an unknown probability distribution, we now examine the accuracy of such an approach.

3.2.1. Truncation Error in the FET

The functional expansion for $P(x)$ given in Eq. (3.4) is exact only if all terms in the series are included. Clearly, it is not possible with Monte Carlo to estimate an infinite number of expansion coefficients, and the functional approximation must be truncated at some finite number of terms M,

$$P(x) \approx P_M(x) = \sum_{n=0}^{M} \bar{a}_n k_n \psi_n(x) . \tag{3.14}$$

This truncation introduces an error $E_M(x)$ in the estimation of $P(x)$, which is equal to the contributions from all expansion terms with $n > M$,

$$E_M(x) = \left| P(x) - P_M(x) \right| = \left| \sum_{n=M+1}^{\infty} \bar{a}_n k_n \psi_n(x) \right| . \tag{3.15}$$

The theory behind calculating (or estimating) the truncation error in a finite series approximation of a general function has been an important area of research in mathematics for over a century. Many books devoted to the subject have been written, and the collected volume of the work is much too large to be presented in detail here. While a full review is not warranted, the derivation of several relevant results will help to provide insight into the FET. In particular, the derivations included here will focus specifically on the Legendre, Chebyshev, and Fourier basis sets. Further information on the convergence properties of series expansions in arbitrary sets of basis functions is widely available in many textbooks[31-33].

The truncation error for a given expansion depends largely on the properties of the function being approximated. Unfortunately, in the FET very little (if any) information concerning the shape of the true distribution is available a priori. However,

even without any detailed information it is possible to derive an upper bound for the truncation error that will hold for most (non-pathological) functions. The derivation of this bound begins with the definition of truncation error given in Eq. (2.36), and uses only weak inequality relationships;

$$\begin{aligned} E_M(x) &= \left|P(x) - P_M(x)\right| = \left|\sum_{n=M+1}^{\infty} \bar{a}_n k_n \psi_n(x)\right| \\ &\leq \sum_{n=M+1}^{\infty} \left|\bar{a}_n k_n \psi_n(x)\right| \\ &\leq \sum_{n=M+1}^{\infty} \left|\bar{a}_n k_n\right| Max\left[\left|\psi_n(x)\right|\right]. \end{aligned}$$

If the basis functions are normalized such that $Max\left[\left|\psi_n(x)\right|\right] = 1$, which is true for the Legendre, Chebyshev, and Fourier basis sets, then the following relationship will hold for any function $P(x)$,

$$E_M(x) \leq \sum_{n=M+1}^{\infty} \left|\bar{a}_n k_n\right|. \tag{3.16}$$

Equation (3.16) demonstrates that it is possible to put an upper limit on the truncation error by considering only the magnitudes of the neglected expansion coefficients and normalization constants. Now the focus must shift to finding an analytical estimate for the rate at which the sequence of expansion coefficients converges as $n \to \infty$.

One technique for determining the convergence rate for the expansion coefficients is to use integration by parts. To demonstrate this technique, consider the expansion of an arbitrary function $f(x)$ in Legendre polynomials. The expansion coefficients can be written exactly as

$$\bar{a}_n = \int_{-1}^{1} f(x) P_n(x) dx. \tag{3.17}$$

Using integration by parts it is possible to rewrite Eq. (3.17) as

$$\begin{aligned}\bar{a}_n &= \int_{-1}^{1} f(x)\,P_n(x)\,dx \\ &= f(x)\int_{-1}^{x} P_n(x')\,dx'\Big|_{-1}^{1} - \int_{-1}^{1} f'(x)\int_{-1}^{x} P_n(x')\,dx'\,dx.\end{aligned} \tag{3.18}$$

To evaluate the first term on the right hand side of Eq. (3.18), we recall the following identities for the Legendre polynomials

$$\begin{aligned}&\text{If } n=0 \quad \int_{-1}^{1} P_0(x)\,dx = 2 \\ &\text{If } n\neq 0 \quad \int_{-1}^{1} P_n(x)\,dx = 0,\end{aligned} \tag{3.19}$$

along with the trivial integral identity,

$$\int_a^a f(x)\,dx = 0 \quad \forall\ f(x). \tag{3.20}$$

Evaluating Eq. (3.18) for $n \neq 0$ using the identities in Eq. (3.19) and (3.20) gives

$$a_n = \int_{-1}^{1} f'(x)\int_{-1}^{x} P_n(x')\,dx'\,dx. \tag{3.21}$$

The inner integral in Eq. (3.21) can be simplified by using a recurrence relationship of the Legendre polynomials to derive the following integral relationship

$$\int_a^b P_n(x)\,dx = \frac{1}{(2n+1)}\left[P_{n+1}(b) - P_{n+1}(a) - P_{n-1}(b) + P_{n-1}(a)\right]. \tag{3.22}$$

This result will be formally derived in section 4.2. Equation (3.22) can be applied directly to Eq. (3.21) to yield

$$\bar{a}_n = \int_{-1}^{1} \frac{f'(x)}{(2n+1)}\left[P_{n+1}(x) - P_{n-1}(x) + P_{n-1}(-1) - P_{n+1}(-1)\right]dx. \tag{3.23}$$

The Legendre polynomials are all normalized with the condition $P_n(1) = 1$. In addition, it is easy to show that $P_n(x)$ is an even function of x for n even, and an odd function of x for n odd. These results imply the following:

$$P_n(x) = P_n(-x) \Rightarrow P_n(-1) = P_n(1) = 1 \qquad \textit{for } n \textit{ even}$$
$$P_n(x) = -P_n(-x) \Rightarrow P_n(-1) = -P_n(1) = -1 \quad \textit{for } n \textit{ odd}. \tag{3.24}$$

Because $P_{n+2}(x)$ must have the same parity as $P_n(x)$ it follows from Eq. (3.24) that

$$P_{n-1}(-1) = P_{n+1}(-1) \Rightarrow P_{n-1}(-1) - P_{n+1}(-1) = 0. \tag{3.25}$$

This result allows Eq. (3.23) to be simplified as

$$\bar{a}_n = \int_{-1}^{1} \frac{f'(x)}{(2n+1)}\left[P_{n+1}(x) - P_{n-1}(x)\right]dx$$

$$\bar{a}_n = \frac{1}{(2n+1)}\left[\int_{-1}^{1} f'(x)P_{n+1}(x)dx - \int_{-1}^{1} f'(x)P_{n-1}(x)dx\right]. \tag{3.26}$$

An upper bound on $\bar{a}_n$ can be obtained by using a weak inequality to rewrite Eq. (3.26) as

$$|\bar{a}_n| \le \frac{1}{(2n+1)}\left[\left|\int_{-1}^{1} f'(x)P_{n+1}(x)dx\right| + \left|\int_{-1}^{1} f'(x)P_{n-1}(x)dx\right|\right]. \tag{3.27}$$

For any integral of two functions the general inequality

$$\left|\int_a^b f(x)g(x)dx\right| \le \int_a^b |f(x)||g(x)|dx \le (b-a)Max\left[|f(x)|\right]Max\left[|g(x)|\right] \tag{3.28}$$

holds. Applying this inequality to Eq. (3.27) and recalling that $Max\left[|P_n(x)|\right] = 1$ yields

$$|\bar{a}_n| \le \frac{4\,Max\left[|f'(x)|\right]}{(2n+1)}. \tag{3.29}$$

The term $4\,Max\left[|f'(x)|\right]$ is constant with respect to n, and thus it has been shown that the upper bound on the convergence rate of $\bar{a}_n$ is at least

$$|\bar{a}_n| \sim O\left[\frac{1}{n}\right]. \tag{3.30}$$

Also, we recognize that Eq. (3.26) is in a form where it may be possible to integrate by parts again. If possible, integrating Eq. (3.26) by parts would yield

$$\bar{a}_n = \frac{1}{(2n+1)}\left[\frac{1}{(2n+3)}\left[\int_{-1}^{1} f''(x)P_{n+2}(x)dx - \int_{-1}^{1} f''(x)P_n(x)dx\right] - \frac{1}{(2n-1)}\left[\int_{-1}^{1} f''(x)P_n(x)dx - \int_{-1}^{1} f''(x)P_{n-2}(x)dx\right]\right]. \tag{3.31}$$

Applying the inequalities in Eq. (3.27) and (3.28) gives a tighter upper bound on $\bar{a}_n$

$$|\bar{a}_n| \le \frac{4\,Max\left[\left|f''(x)\right|\right]}{4n^2+8n+3} + \frac{4\,Max\left[\left|f''(x)\right|\right]}{4n^2-1}. \tag{3.32}$$

The new result, after two applications of integration by parts, shows that the coefficients converge at least as fast as

$$|\bar{a}_n| \sim O\left[\frac{1}{n^2}\right]. \tag{3.33}$$

Obviously this process can continue until further integration by parts is no longer possible. In order to estimate an upper bound convergence rate, it is, therefore, necessary to understand what conditions prevent further integration by parts.

The first limiting condition that would prevent an equation of the form in Eq. (3.17) from being further integrated by parts occurs when any of the functions $f(x)$, $f'(x)$, or $P_n(x)$ are not integrable. By definition, the functions $P_n(x)$ are always integrable, but this condition does not hold for the arbitrary function $f(x)$. For each successive application of integration by parts, the function $f(x)$ is replaced by the next higher derivative of the function: $f'(x)$. Thus, to apply integration by parts κ times to an arbitrary function, $f(x)$, requires that the κ^{th} derivative of the function $f^{(\kappa)}(x)$ must

be integrable. In his text, Boyd[31] provides the following condition for the integrability of $f^{(\kappa)}(x)$:

"The integrability of $f^{(\kappa)}(x)$ requires that $f(x), f^{(1)}(x), \ldots, f^{(\kappa-2)}(x)$ must all be continuous".

Another condition that can prevent further integration by parts occurs when the boundary term $\left[f(x)g(x)\right]\Big|_a^b$ does not vanish. Equation (3.19) demonstrates that the boundary term will go to zero if $n \neq 0$. Inspection of Eq. (3.31) shows that integrating by parts κ times introduces the Legendre polynomial $P_{n-\kappa}(x)$ into the equation. Therefore, for an arbitrary $f(x)$ it is possible to integrate by parts κ times before obtaining a $P_0(x)$ term that will result in a nonzero boundary term on the next integration. Notice, however, that this is not an issue if the function $f(x)$ is periodic over the expansion domain $[a,b]$ and $f(a) = f(b)$. In this case the boundary term will always vanish, as can be seen from evaluating Eq. (3.18) with a periodic function for any n.

The result of this derivation is an integration by parts coefficient bound for Legendre polynomials that states:

For a functional expansion of an arbitrary function $f(x)$ in Legendre polynomials the upper bounds of the expansion coefficients $\bar{a}_n$ are given by $|\bar{a}_n| \leq F\left(\sum_{j=0}^{\kappa} c_j n^j\right)^{-1}$ for some sufficiently large F and constants $\{c_0, c_1, \ldots, c_\kappa\}$ if the following conditions hold: (i) $f^{(\kappa)}(x)$ is integrable and (ii) $\kappa \leq n$ unless the function is periodic over $[-1,1]$ (i.e. $f(-1) = f(1)$). (3.34)

The same procedure can be used to produce analogous results for any of the standard sets of basis functions (Fourier series, Chebyshev polynomials, Hermite

functions, spherical harmonics, etc). By applying this methodology, it is easy to show that the convergence rate (and conditions) for a generalized Fourier series is given by[31]:

For a functional expansion of an arbitrary function $f(x)$ *in a generalized Fourier series the upper bounds of the expansion coefficients* $\bar{a}_n$ *(Cosine) and* $\bar{b}_n$ *(Sine) are given by* $|\bar{a}_n| \leq F n^{-\kappa}$ *and* $|\bar{b}_n| \leq F n^{-\kappa}$ *for some sufficiently large F if the following conditions hold: (i)* $f^{(\kappa)}(x)$ *is integrable and (ii) the function and its first κ-2 derivatives are periodic over* $[-\pi, \pi]$

(i.e. $f(-\pi) = f(\pi), f^{(1)}(-\pi) = f^{(1)}(\pi), \ldots, f^{(\kappa-2)}(-\pi) = f^{(\kappa-2)}(\pi)$ *).* (3.35)

The text by Boyd[31] also notes that the Chebyshev series coefficients converge at the same rate as the Fourier series coefficients, except that convergence of the Chebyshev coefficients do not require the function to be periodic over the expansion domain[31]. This powerful result is a reason why Chebyshev polynomials are so widely used.

For the three basis sets considered, Eqs. (3.34) and (3.35) indicate that the dominant rate of convergence is:

$$|\bar{a}_n| \sim O\left[\frac{1}{n^{\kappa}}\right], \tag{3.36}$$

where κ is the largest derivative of $f(x)$ that is still integrable. When the expansion coefficients converge according to Eq. (3.34), the constant κ is referred to as the algebraic index of convergence.

It is also important to note that there are very large classes of functions that have an unlimited number of integrable derivatives and/or are periodic with a period equal to the expansion domain. For these functions, the integration by parts technique can be repeated indefinitely, suggesting that $\kappa \to \infty$ (i.e the coefficients are converging faster than any finite power of n). In these cases it is possible to show that the coefficients are converging exponentially with the form

$$\left|a_n\right| \sim O\left[e^{-\varepsilon n}\right]. \tag{3.37}$$

The rate of exponential convergence ε cannot be estimated by the integration by parts technique, but various other methods exist for bounding this quantity.

While the convergence results shown in Eqs. (3.36) and (3.37) are very general, they still require that the index of convergence for the function being approximated be known. Fortunately, the index of convergence for a class of functions can be deduced from very general information about the class. It was asserted in Chapter 2 that the angular current distribution in particle transport problems, $\left|\vec{j}(\vec{\xi})\cdot\vec{s}\right|$, is typically piecewise smooth over its domain, meaning that both the distribution and its first derivative are at least piecewise continuous. By using the same reasoning applied in section 2.1, it can be asserted that the particle density distribution $N_p\left(\vec{\xi}\right)$ is also piecewise smooth for most problems of interest. If the particle density is piecewise smooth, then it follows that functions of the particle density (e.g. flux, current, reaction rates) will also be piecewise smooth. For a class of functions $f\left(x\right)$ that are piecewise smooth it holds by definition (see section 2.1) that $f(x)$, $f'(x)$ and $f''(x)$ are all integrable. Thus, the algebraic index of convergence for these functions is at least $\kappa = 2$. Therefore, by Eq. (3.36), expansion coefficients in either the Legendre or Chebyshev polynomials will converge at least as fast as

$$\left|\overline{a}_n\right| \sim O\left[\frac{1}{n^2}\right]. \tag{3.38}$$

The resulting coefficient convergence behavior given in Eq. (3.38) can now be used to complete the derivation for an upper bound on the truncation error. We recall from Eq. (3.16) that the truncation error of the expansion is bounded by the inequality

$$E_M(x) \leq \sum_{n=M+1}^{\infty} |\bar{a}_n k_n| = \sum_{n=M+1}^{\infty} |\bar{a}_n||k_n|. \tag{3.16}$$

Substituting Eq. (3.38) into (3.16) gives, for some sufficiently large C,

$$E_M(x) \leq \sum_{n=M+1}^{\infty} \frac{C|k_n|}{n^2}. \tag{3.39}$$

For the case of Legendre Polynomials,

$$k_n = \frac{(2n+1)}{2}. \tag{3.40}$$

Substituting this factor into Eq. (3.39) gives

$$E_M(x) \leq \sum_{n=M+1}^{\infty} \frac{C}{n} + \frac{C}{2n^2}. \tag{3.41}$$

The harmonic series in Eq. (3.41) does not converge. This means that, for the Legendre polynomials, it is not possible to put an upper bound on the truncation error in the infinity norm.

It is, however, possible to develop a bound for a basis set that has a constant normalization factor k_n, such as the Chebyshev polynomials. To show this, begin with Eq. (3.39) evaluated with the normalization factor for the Chebyshev polynomials, $k_n = \pi/2$,

$$E_M(x) \leq \sum_{n=M+1}^{\infty} \frac{C\pi}{2n^2}. \tag{3.42}$$

It has been shown[34], for $M >> 1$,

$$\sum_{n=M+1}^{\infty} \frac{1}{n^p} \approx \frac{1}{(p-1)M^{p-1}}. \tag{3.43}$$

Using approximation (3.43), Eq. (3.42) can be simplified to yield

$$E_M(x) \leq \frac{C\pi}{2M}. \tag{3.44}$$

Equation (3.44) gives an upper bound on the convergence rate of the truncation error for an M^{th} order expansion. However, this result only holds for basis sets that have a constant orthonormalization factor. Equation (3.44) can be rewritten (using Eq. (3.38)) to give a common rule of thumb for estimating the magnitude of the truncation error,

$$E_M(x) \sim O\left[M\left|\bar{a}_M\right|\right], \qquad \textit{for Chebyshev polynomials} \tag{3.45}$$

where $\bar{a}_M$ is the last expansion coefficient retained before truncation. Thus, for Chebyshev polynomials, it is easy to estimate the truncation error based on the magnitude of the last expansion coefficient estimated.

Having now established the upper bound (or lack, thereof) of the truncation error for a large class of piecewise smooth functions that are found in solutions to the particle transport equations, let us consider how the upper bound of the truncation error will behave if the function being expanded is analytical and has an arbitrary number of integrable derivatives. In this case (for Chebyshev polynomials), Eq. (3.39) becomes

$$E_M(x) \leq \sum_{n=M+1}^{\infty} Ce^{-\varepsilon n}\left|k_n\right|. \tag{3.46}$$

Using the general result,

$$\sum_{n=M+1}^{\infty} p^n = \frac{p^{M+1}}{(1-p)}, \tag{3.47}$$

Eq. (3.46) becomes

$$E_M(x) \leq C\left| k_n \right| e^{-\varepsilon(M+1)} = C\left| k_n \right| e^{-\varepsilon(M)}\, e^{-\varepsilon}. \tag{3.48}$$

Applying Eq. (3.37) allows this to be written, to leading order, as

$$E_M(x) \sim O\left[\left|\overline{a}_M\right| \right], \tag{3.49}$$

for analytically smooth $f(x)$.

The results in this section have demonstrated key properties about the upper bound of the truncation error in the infinity norm that result from approximating a function $f(x)$ by a finite expansion in an orthogonal set of basis functions. These results, while providing some methods for bounding truncation error for a given case, are still too weak to allow a comparison of the Monte Carlo FET to conventional histogram tallies. In order to make this comparison it is necessary to consider the bounding properties of the truncation error in the 2-norm.

3.2.2. 2-Norm Truncation Error in the FET

The previous section sought to establish an upper bound (in the infinity norm) on the truncation error due to approximating a piecewise smooth distribution $P(x)$ with a finite series expansion in an orthogonal set of functions $\{\psi_n(\xi)\}_0^\infty$. For the Chebyshev polynomials, we showed that the magnitude of the truncation error is bounded by the magnitude of the last retained expansion coefficient. Unfortunately, this result does not hold for all basis sets (in particular the Legendre polynomials), and so a more general condition on the truncation error is sought.

The 2-norm of the truncation error is defined as

$$\begin{aligned}\|E_M\| &= \| P(x) - P_M(x) \| \\ &= \left(\int_a^b \left(P(x) - P_M(x) \right)^2 \rho(x)\, dx \right)^{1/2},\end{aligned} \tag{3.50}$$

where $P(x)$ is the true function and $P_M(x)$ is the M^{th} order functional expansion approximation to $P(x)$. By expanding Eq. (3.50), it is easy to show

$$\begin{aligned}\|E_M\|^2 &= \int_a^b \left(P(x) - P_M(x) \right)^2 \rho(x)\, dx \\ &= \int_a^b \left(P(x)^2 - 2P(x)P_M(x) + P_M(x)^2 \right) \rho(x)\, dx \\ &= \int_a^b \left(P(x)^2 - 2\left(\sum_{n=0}^{\infty} \bar{a}_n k_n \psi_n(x) \right)\left(\sum_{n=0}^{M} \bar{a}_n k_n \psi_n(x) \right) + \left(\sum_{n=0}^{M} \bar{a}_n k_n \psi_n(x) \right)^2 \right) \rho(x)\, dx \\ &= \int_a^b P(x)^2 \rho(x)\, dx - 2\int_a^b \left(\sum_{n=0}^{\infty} \bar{a}_n k_n \psi_n(x) \right)\left(\sum_{n=0}^{M} \bar{a}_n k_n \psi_n(x) \right) \rho(x)\, dx \\ &\quad + \int_a^b \left(\sum_{n=0}^{M} \bar{a}_n k_n \psi_n(x) \right)^2 \rho(x)\, dx \\ &= \|P(x)\|^2 - 2\sum_{n=0}^{M} \bar{a}_n^2 k_n + \sum_{n=0}^{M} \bar{a}_n^2 k_n\end{aligned}$$

$$\|E_M\|^2 = \|P(x)\|^2 - \sum_{n=0}^{M} \bar{a}_n^2 k_n \,. \tag{3.51}$$

Using Parseval's theorem[31,32,35],

$$\|P(x)\|^2 = \sum_{n=0}^{\infty} \bar{a}_n^2 k_n \,, \tag{3.52}$$

allows Eq. (3.51) to be simplified,

$$\|E_M\|^2 = \sum_{n=M+1}^{\infty} \bar{a}_n^2 k_n \,. \tag{3.53}$$

Substituting the approximation for the expansion coefficients given in Eq. (3.36) gives an upper bound on the truncation error in the 2-norm

$$\|E_M\|^2 \leq \sum_{n=M+1}^{\infty} \frac{C k_n}{n^4}. \tag{3.54}$$

Again, the upper bound depends on the basis set chosen, and in particular the orthonormalization constants k_n for each term. In the previous section, reliable upper convergence bounds in the infinity norm could not be made for expansions in the set of Legendre polynomials because $k_n \sim O[n]$. In the 2-norm, the upper bound can be estimated, even for basis sets that have linearly increasing normalization constants in n. For the case of the Legendre polynomials (i.e. $k_n \sim O[n]$), Eq. (3.53) becomes

$$\|E_M\|^2 \leq \sum_{n=M+1}^{\infty} \frac{C}{n^3}. \tag{3.55}$$

Approximation (3.43) can now be used to evaluate Eq. (3.55) and to show the final result

$$\|E_M\| \sim O\left[\frac{1}{M}\right]. \tag{3.56}$$

At last, Eq. (3.56) gives an upper bound for the truncation error in the 2-norm for an expansion in Legendre polynomials. It is then trivial to show that the analogous result to Eq. (3.56) for the Chebyshev polynomials is

$$\|E_M\| \sim O\left[\frac{1}{M^{3/2}}\right]. \tag{3.57}$$

Now that an upper bound for truncation error has been established, it is possible to directly compare histogram and FET approximations.

3.2.3. Statistical Error in the FET

Another source of error in the FET arises from statistical uncertainty in the expansion coefficients. The 2-norm can be used to measure the total error between the stochastic FET approximation and the true function,

$$\left\|\hat{E}_M\right\| = \left\|P(x) - \hat{P}_{M,N}(x)\right\| = \sqrt{\int_\Gamma \left(P(x) - \hat{P}_{M,N}(x)\right)^2 \rho(x)\,dx}\ , \tag{3.58}$$

where $\hat{P}_{M,N}(x)$ is the Monte Carlo estimate of the M^{th} order functional expansion approximation to $P(x)$ calculated using N independent particle histories. Equation (3.58) can be rewritten as

$$\begin{aligned}\left\|\hat{E}_M\right\|^2 &= \int_\Gamma \left(\sum_{n=0}^{\infty} k_n \bar{a}_n \psi_n(x) - \sum_{n=0}^{M} k_n \hat{a}_n \psi_n(x)\right)^2 \rho(x)\,dx \\ &= \int_\Gamma \left(\sum_{n=M+1}^{\infty} k_n \bar{a}_n \psi_n(x) + \sum_{n=0}^{M} k_n \left(\bar{a}_n - \hat{a}_n\right)\psi_n(x)\right)^2 \rho(x)\,dx\,. \end{aligned} \tag{3.59}$$

The right hand side of Eq. (3.59) can be expanded to yield

$$\begin{aligned}\left\|\hat{E}_M\right\|^2 = &\int_\Gamma \left(\sum_{n=M+1}^{\infty}\sum_{m=M+1}^{\infty} k_n k_m \bar{a}_n \bar{a}_m \psi_n(x)\psi_m(x)\right)\rho(x)\,dx \\ &+ \int_\Gamma \left(\sum_{n=0}^{M}\sum_{m=0}^{M} k_n k_m \left(\bar{a}_n - \hat{a}_n\right)\left(\bar{a}_m - \hat{a}_m\right)\psi_n(x)\psi_m(x)\right)\rho(x)\,dx \\ &+ \int_\Gamma 2\left(\sum_{n=M+1}^{\infty}\sum_{m=0}^{M} k_n k_m \bar{a}_n \left(\bar{a}_m - \hat{a}_m\right)\psi_n(x)\psi_m(x)\right)\rho(x)\,dx.\end{aligned} \tag{3.60}$$

Using the orthogonality property of the basis functions, the integrals in Eq. (3.60) can be reduced to

$$\left\|\hat{E}_M\right\| = \sqrt{\left(\sum_{n=M+1}^{\infty} \bar{a}_n^{\,2} k_n\right) + \left(\sum_{n=0}^{M} \left(\bar{a}_n - \hat{a}_n\right)^2 k_n\right)}\,. \tag{3.61}$$

By inspection (see Eq. (3.53)), the first term under the radical in Eq. (3.61) is the truncation error due to approximating a continuous function with a finite series expansion. The second term gives the contribution to the total error due to statistical uncertainty in the expansion coefficients.

Equation (3.61) demonstrates that the FET contains sources of both statistical error and truncation error. The presence of statistical uncertainty in Eq. (3.61) means that $\left\|\hat{E}_M\right\|$ is itself a random variable. Therefore, in order to analyze the convergence behavior of the FET we should consider the root-mean-square (RMS) error for simulations using N independent histories. The RMS error can be calculated directly from Eq. (3.61),

$$\sqrt{\left\langle \left\|\hat{E}_M\right\|^2 \right\rangle} = \sqrt{\left(\sum_{n=M+1}^{\infty} \bar{a}_n^{\,2} k_n \right) + \left\langle \sum_{n=0}^{M} \left(\bar{a}_n - \hat{a}_n\right)^2 k_n \right\rangle}, \tag{3.62}$$

where angle brackets $\langle\ \rangle$ have been used to denote the expected value of a statistical quantity.

The first task is to evaluate the statistical uncertainty term. Algebraically expanding and applying the expectation operator to each term in the summation yields

$$\left\langle \sum_{n=0}^{M} \left(\bar{a}_n - \hat{a}_n\right)^2 k_n \right\rangle = \left(\sum_{n=0}^{M} \left\langle \hat{a}_n^2 \right\rangle k_n - \bar{a}_n^2 k_n \right). \tag{3.63}$$

By the definition of the variance of $\hat{a}_n$,

$$\left\langle \hat{a}_n^2 \right\rangle = \sigma_{\hat{a}_n}^2 + \bar{a}_n^2 . \tag{3.64}$$

Substituting Eq. (3.64) into Eq. (3.63) shows that the statistical error in the functional approximation is related to the sum of the variances of the individual expansion coefficients,

$$\left\langle \sum_{n=0}^{M} \left(\bar{a}_n - \hat{a}_n\right)^2 k_n \right\rangle = \sum_{n=0}^{M} k_n \sigma_{\hat{a}_n}^2 \,. \tag{3.65}$$

Using Eq. (3.9) and (3.65) the statistical uncertainty term can be written as

$$\left\langle \sum_{n=0}^{M} \left(\bar{a}_n - \hat{a}_n\right)^2 k_n \right\rangle = \sum_{n=0}^{M} \frac{k_n}{N} \left(\int_{\Gamma} \left(\psi_n(x)\rho(x)\right)^2 P(x)\, dx - \bar{a}_n^{\,2} \right), \tag{3.66}$$

and so

$$\left\langle \sum_{n=0}^{M} \left(\bar{a}_n - \hat{a}_n\right)^2 k_n \right\rangle \le \sum_{n=0}^{M} \frac{k_n}{N} \left(\underset{\Gamma}{Max}\left(\left|\rho(x)P(x)\right|\right) \int_{\Gamma} \psi_n^2(x)\rho(x)\, dx - \bar{a}_n^{\,2} \right). \tag{3.67}$$

It should be noted that Eq. (3.67) is only valid if the function $\left|\rho(x)P(x)\right|$ is finite over the domain Γ. In cases where $\left|\rho(x)P(x)\right|$ is unbounded, special attention must be paid to ensure that the approximation is converging as expected.

Using the definition of k_n from Eq. (3.6) in Eq.(3.67) yields

$$\left\langle \sum_{n=0}^{M} \left(\bar{a}_n - \hat{a}_n\right)^2 k_n \right\rangle \le \frac{1}{N} \sum_{n=0}^{M} \left[\underset{\Gamma}{Max}\left(\left|\rho(x)P(x)\right|\right) - \bar{a}_n^{\,2} k_n \right],$$

and so

$$\left\langle \sum_{n=0}^{M} \left(\bar{a}_n - \hat{a}_n\right)^2 k_n \right\rangle \le \frac{M}{N} \underset{\Gamma}{Max}\left(\left|\rho(x)P(x)\right|\right) - \frac{1}{N} \sum_{n=0}^{M} \bar{a}_n^{\,2} k_n \,. \tag{3.68}$$

Further inspection of Eq. (3.68) reveals that the second term on the right hand side is always negative and can therefore be omitted without affecting the inequality. With this simplification, Eq. (3.68) can be written

$$\left\langle \sum_{n=0}^{M} \left(\bar{a}_n - \hat{a}_n\right)^2 k_n \right\rangle \le \frac{M}{N} \underset{\Gamma}{Max}\left(\left|\rho(x)P(x)\right|\right). \quad \textit{(expected statistical error)} \tag{3.69}$$

Next, the truncation error term from Eq. (3.61) is evaluated using the convergence rate of the expansion coefficients given in Eq. (3.38),

$$\sum_{n=M+1}^{\infty} \bar{a}_n^{\,2} k_n = \sum_{n=M+1}^{\infty} O\left[\frac{1}{n^{2\kappa}}\right] k_n . \qquad \textit{(truncation error)} \tag{3.70}$$

Finally, the results from Eq. (3.69) and (3.70) can then be used to rewrite Eq. (3.61) as

$$\sqrt{\left\langle \left\| \hat{E}_M \right\|^2 \right\rangle} \le \sqrt{\frac{M}{N} \underset{\Gamma}{Max}\left(\left|\rho(x)\, P(x)\right|\right) + \sum_{n=M+1}^{\infty} O\left[\frac{1}{n^{2\kappa}}\right] k_n} . \tag{3.71}$$

The detailed convergence behavior of Eq. (3.71) depends on both κ for the function $P(x)$ and the behavior of the series $\{k_n\}$.

The expression for the total (statistical + truncation) error can be written, to leading orders, as,

$$\sqrt{\left\langle \left\| \hat{E}_M \right\|^2 \right\rangle} \le \sqrt{O\left[\frac{M}{N}\right] + \sum_{n=M+1}^{\infty} O\left[\frac{1}{n^{2\kappa}}\right] k_n} . \tag{3.72}$$

Equation (3.72) demonstrates that the rate of convergence is determined not only by the smoothness of the function $P(x)$, but also by the ratio of the expansion order M to the number of histories run N. This divergent term indicates that, for a fixed number of histories N, the total error in the approximation will eventually begin to grow as more expansion orders are added.

3.3. Numerical Verification of FET Convergence

In order to verify the theoretical convergence rates derived in the previous section, a series of numerical experiments were conducted. In these experiments, Monte Carlo simulations were used to estimate Legendre functional approximations for a reference distribution $P(x)$. The 2-norm of the residual error between the functional approximation and the exact distribution of $P(x)$ was then calculated for different

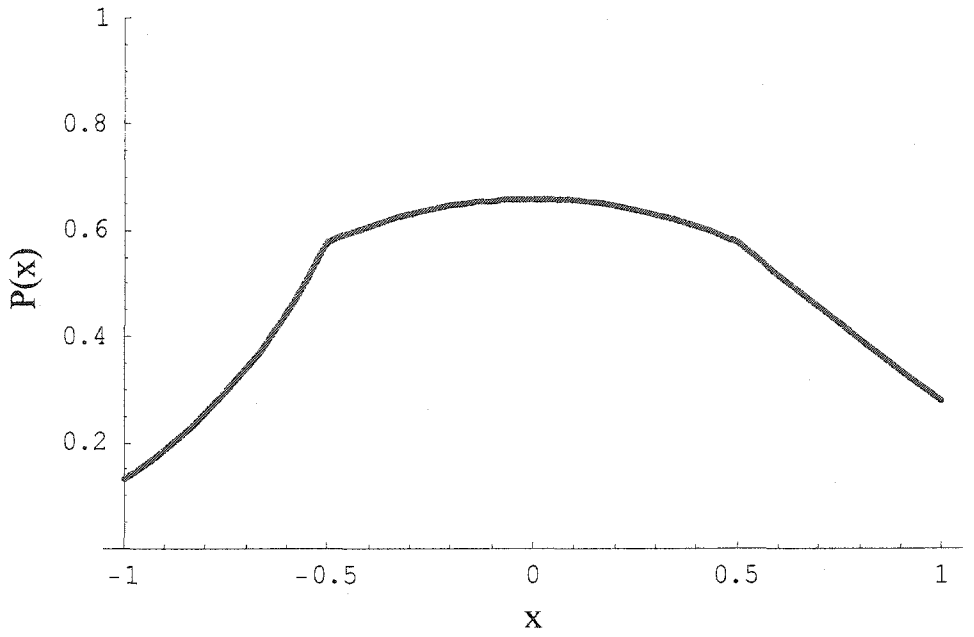

Figure 3.1. Plot of reference distribution of P(x) used for numerical verification of theoretical convergence results for the FET.

expansion orders and numbers of histories. The same reference distribution for $P(x)$ was used in each numerical experiment,

$$P(x)=\frac{1}{1.51985}\begin{cases}\cos(x)e^{2x+1} & x\in[-1,-1/2]\\ \cos(x) & x\in[-1/2,1/2]\\ \cos(x)e^{-x/2+1/4} & x\in[1/2,1]\end{cases}. \tag{3.73}$$

The distribution in Eq. (3.73) was specifically chosen to simulate many features of distributions encountered during Monte Carlo particle transport simulations. The distribution is continuous over the domain $(-1,1)$ and piecewise smooth with discontinuities in the first derivative of the distribution occurring at $x=\pm 1/2$. Because $P(x)$ is piecewise smooth it has two integrable derivatives and, therefore, an algebraic index of convergence $\kappa=2$. A plot of the reference distribution is shown in Figure 3.1.

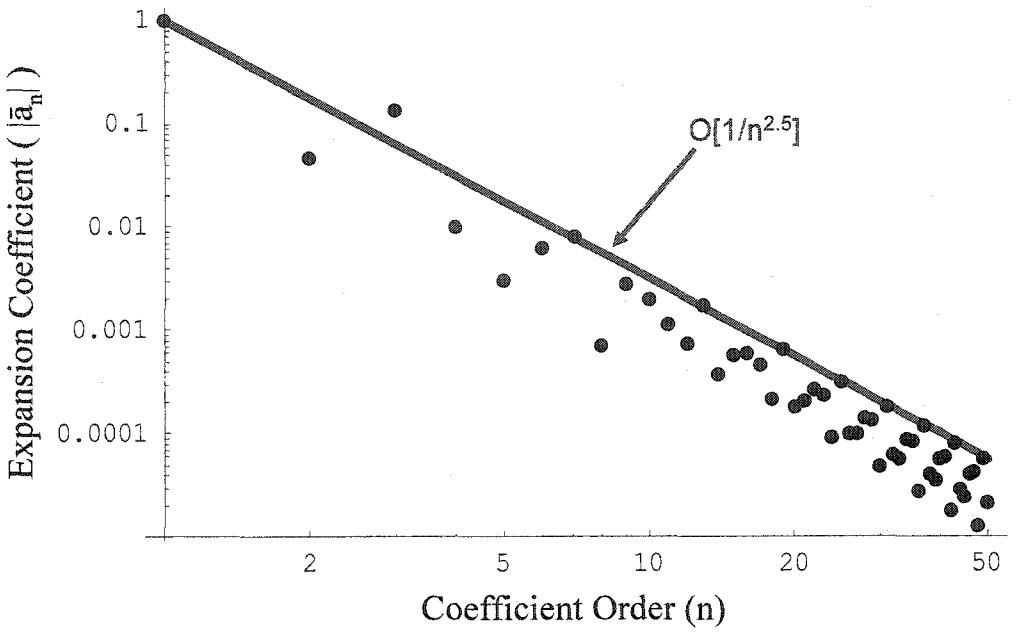

Figure 3.2. Exact Legendre expansion coefficients for P(x) plotted against Legendre expansion order. A $1/n^{2.5}$ trend line is shown for comparative purposes, indicating the convergence rate of the expansion coefficients.

3.3.1. Analytical FET Approximation Results

For testing purposes, functional approximations of $P(x)$ in the set of Legendre polynomials were considered. The Legendre polynomials are a complete set of basis functions that are orthogonal over the range $[-1,1]$ with respect to the weighting function $\rho(x) = 1$. The normalization constants for the Legendre polynomials are

$$k_n = \frac{2n+1}{2}. \tag{3.74}$$

For comparative purposes the exact Legendre expansion coefficients for $P(x)$ were calculated using Eq. (3.5). A plot of the absolute values of the first 50 exact expansion coefficients is shown in Figure 3.2. In the derivation of the convergence properties of the

FET, it was established in Eq. (3.38) that the expansion coefficients should converge algebraically with an asymptotic bound of $O[n^{-\kappa}]$. Numerical results, shown in Figure 3.2, indicate that the index of convergence for $P(x)$ is $\kappa \approx 2.5$, slightly faster than the $\kappa = 2$ bound for a piecewise smooth function.

It was also established that the truncation error for a finite Legendre series approximation will converge as the expansion coefficients tend to zero. Using the result given in Eq. (3.70), the truncation error can be written concisely as

$$\|E_M\| = \sqrt{\sum_{n=M+1}^{\infty} \bar{a}_n^{\,2} k_n} = \sqrt{\sum_{n=M+1}^{\infty} O\left[\frac{1}{n^{2\kappa}}\right] k_n} \,. \tag{3.75}$$

For the reference distribution of $P(x)$ in the set of Legendre polynomials, Eq. (3.75) predicts that the truncation error should converge at least as fast as

$$\|E_M\| = \sqrt{\sum_{n=M+1}^{\infty} O\left[\frac{1}{n^5}\right] \frac{2n+1}{2}} \le O\left[\frac{1}{\sqrt{M^3}}\right]. \tag{3.76}$$

To demonstrate this convergence behavior, the exact Legendre expansion coefficients were used to construct functional approximations to $P(x)$ for values of M ranging from 0 to 49. For each order of exact functional approximation, the 2-norm truncation error was calculated directly by

$$\|E_M\| = \sqrt{\int_{-1}^{1} \left(P(x) - P_M(x)\right)^2 dx} \,. \tag{3.77}$$

The results, Figure 3.3, show that the truncation error converges at the rate $O\left[1/\sqrt{M^3}\right]$, as expected. These results verify that a Legendre expansion of the reference distribution has the convergence properties predicted by the classical results for such expansions and provides a measured value for the algebraic index of convergence κ.

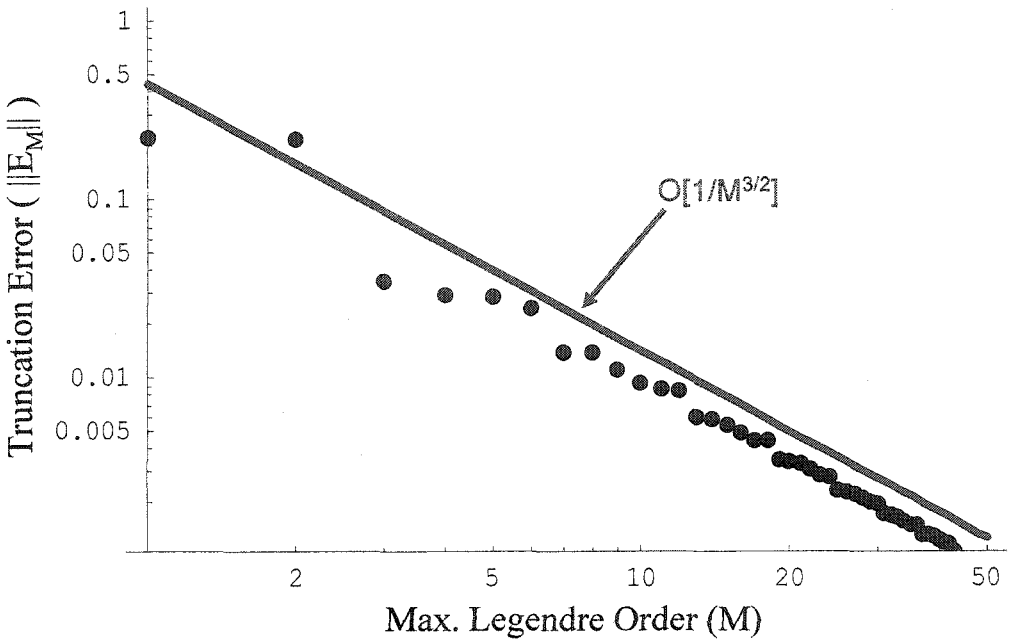

Figure 3.3. Two norm measure of truncation error for a Legendre expansion approximation of P(x) plotted against Legendre truncation order. A $1/M^{3/2}$ trend line is shown for comparative purposes, indicating the approximate convergence rate.

3.3.2. Stochastic FET Approximation Results

Additional studies were conducted to study the convergence properties of a Legendre approximation to $P(x)$ that uses stochastically estimated expansion coefficients. For these studies, random samples were taken (via rejection sampling) from the distribution $P(x)$. These samples were then used in Eq. (3.7) to estimate the Legendre expansion coefficients for $P(x)$. In the previous section it was shown, Eq. (3.64), that the expected statistical error in a Monte Carlo estimate of an expansion coefficient is proportional to the true variance of $\hat{a}_n$, or

$$\left\langle \left| \hat{a}_n - \bar{a}_n \right| \right\rangle = \sqrt{\frac{1}{N}\left(\int_\Gamma \left(\psi_n(x)\rho(x) \right)^2 P(x)\, dx - \bar{a}_n^{\,2} \right)}. \tag{3.78}$$

Equation (3.78) can be further simplified by using Eq. (3.67) to yield

$$\left\langle \left| \hat{a}_n - \bar{a}_n \right| \right\rangle \le \sqrt{\frac{1}{N}\left(\frac{Max_{\Gamma}\left(\left| \rho(x) P(x) \right| \right)}{k_n} - \bar{a}_n^{\,2} \right)}. \tag{3.79}$$

For the trial distribution of $P(x)$ and the basis set of Legendre polynomials, Eq. (3.79) can be evaluated directly,

$$\left\langle \left| \hat{a}_n - \bar{a}_n \right| \right\rangle \le \sqrt{\frac{1}{N}\left(\frac{1.3159}{2n+1} - \bar{a}_n^{\,2} \right)}. \tag{3.80}$$

For a fixed sample size N and large values of n, Eq. (3.80) behaves, to leading order, as

$$\left\langle \left| \hat{a}_n - \bar{a}_n \right| \right\rangle \le O\left[\sqrt{\frac{1}{2n+1}} \right]. \tag{3.81}$$

It was previously established in Eq. (3.36) that the true expansion coefficients $|\bar{a}_n|$ will converge with order $O\left[1/n^{2.5} \right]$. Thus, for large n, the true expansion coefficients $\bar{a}_n$ will be very close to zero, and statistical error will dominate the convergence rate of the stochastically estimated expansion coefficients. Substituting the approximation $\bar{a}_n = 0$ (for large n) into Eq. (3.81) gives

$$\left\langle \left| \hat{a}_n \right| \right\rangle \le O\left[\sqrt{\frac{1}{2n+1}} \right] \tag{3.82}$$

as the convergence rate for stochastically estimated coefficients. To test this convergence rate the first 1,000 expansion coefficients for $P(x)$ were estimated in a 10,000 history Monte Carlo simulation. The results, given in Figure 3.4, show that the absolute value of the statistical error in the expansion coefficients converges as $O\left[1/\sqrt{2n+1} \right]$. This agrees with the predicted behavior given in Eq. (3.82).

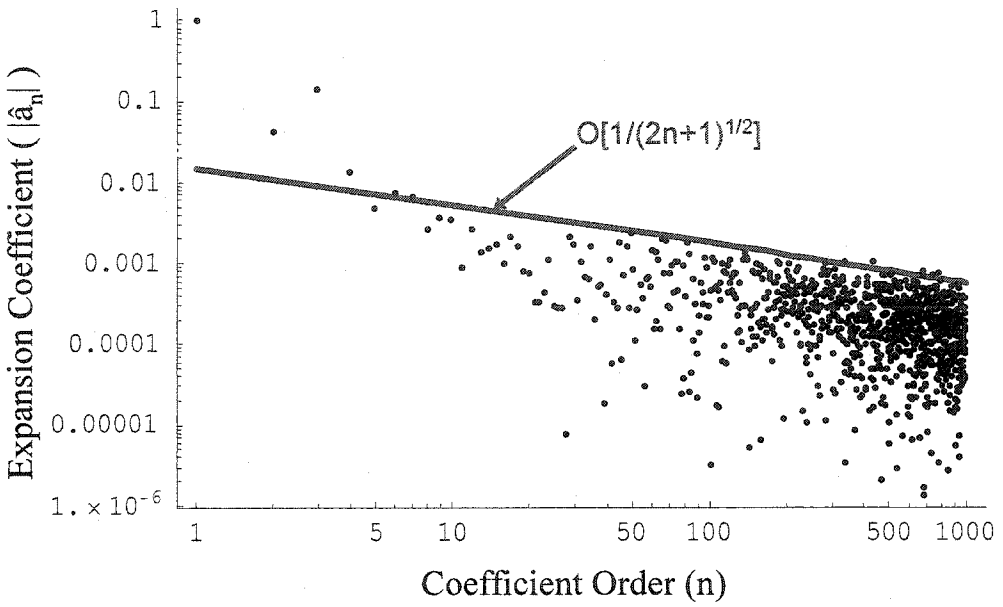

Figure 3.4. Monte Carlo estimated Legendre expansion coefficients for P(x) plotted against Legendre expansion order. Each expansion coefficient was estimated using the same 10,000 history random walk process. A $1/(2n+1)^{1/2}$ trend line is shown for comparative purposes, indicating the theoretical convergence rate.

Theoretical results also predict that the total error in a stochastic FET approximation to $P(x)$ will behave as the sum of two independent terms: the truncation error, which will converge as the expansion order increases; and the statistical error, which is divergent with increasing expansion order for a constant sample size. The general form for the 2-norm measure of residual error was given in Eq. (3.72). For the trial distribution of $P(x)$, the expected convergence rate can be evaluated using Eq. (3.76)

$$\sqrt{\left\langle \left\| \hat{E}_M \right\|^2 \right\rangle} = \sqrt{O\left[\frac{M}{N}\right] + O\left[\frac{1}{\sqrt{M^3}}\right]}. \tag{3.83}$$

In order to verify this convergence behavior, a 10,000 history Monte Carlo simulation was used to estimate the first 1,000 Legendre expansion coefficients. These expansion coefficients were then used to construct functional approximations with orders

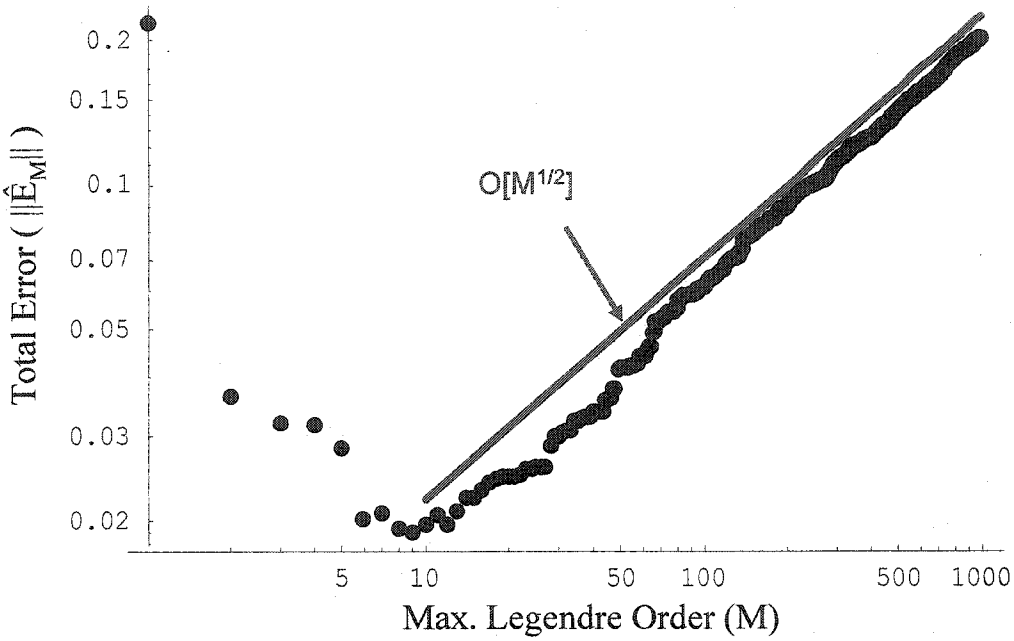

Figure 3.5. Two norm measure of total error for a stochastic Legendre expansion approximation to plotted P(x) against Legendre truncation order. Each expansion coefficient was estimated using the same N=10,000 history random walk process.

0-1000. For each order approximation the exact 2-norm error was calculated directly from Eq. (3.77).

The results, given in Figure 3.5, show that there is an optimal expansion order that minimizes the residual error of the approximation. This optimal order, which is about 10 for this test problem, is the point where the statistical uncertainty in the expansion coefficients begins to contaminate the approximation. Below this optimal order, each added expansion term improves the functional approximation by reducing the truncation error of the series expansion. Above the optimal expansion order, the residual error begins to diverge at the $O[M/N]$ rate predicted by Eq. (3.83) (or the equivalent Eq. (3.72)). The optimal expansion order also depends on the number of histories used in the Monte Carlo simulation. As more histories are used, the uncertainty associated with all

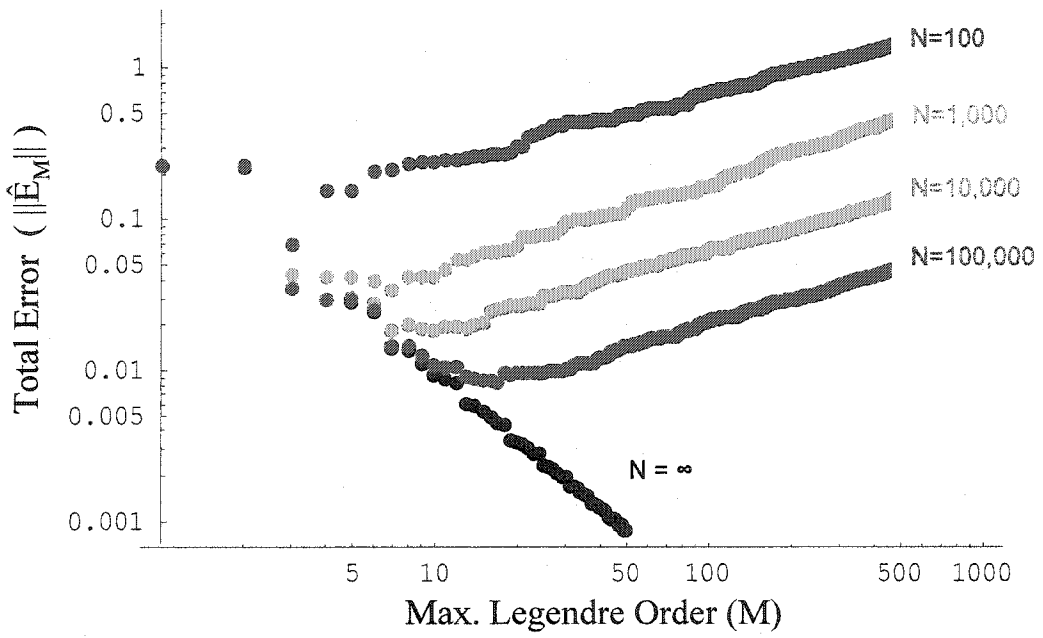

Figure 3.6. Two norm measure of approximation error for stochastic Legendre expansion approximations to P(x) plotted for different sample sizes N. The N=∞ results give the error for the exact M^{th} order Legendre expansion. As the number of histories increases, higher order coefficients can be included in the functional approximation without contaminating the approximation with statistical error.

of the coefficients is reduced, allowing more terms to be included in an expansion without contaminating the overall solution.

Thus, as the number of histories in the simulation is increased, the optimal value will begin to shift towards larger values, and the minimum total error will decrease. This behavior is illustrated in Figure 3.6.

3.3.3. Estimating the Optimal Expansion Order

The results shown in Figure 3.6 demonstrate that for every simulation there exists an optimal order FET expansion that gives the highest accuracy (in the 2-norm) approximation. In the benchmark problem considered it is easy to identify this minimum by calculating the exact error for different order expansions and then finding the

minimum. In a practical application, however, such an approach is obviously not possible. What is needed is a metric that would allow the user to decide which coefficients should be used in an expansion and which should be discarded. Such a metric was derived in section 2.2.5. This metric, referred to as the cost to benefit ratio R_n^2, is defined to be the statistical error "cost" divided by the truncation error "benefit" due to a single coefficient. This provides a computationally simple method to assess whether a given coefficient will provide an increase in accuracy if it is included in the functional expansion.

Theoretically, any coefficient with $R_n^2 \leq 1$ should be included in an expansion, while those with $R_n^2 >> 1$ should be excluded. For the benchmark problem described above, the cost to benefit ratio was calculated for each expansion coefficient. The results are shown in Figure 3.7. We notice that many of the expansion coefficients with order < 9 have values of $R_n^2 < 10$, while the higher order coefficients have ratios > 10. Unfortunately, because the cost to benefit ratio involves stochastic quantities, it cannot be used to exactly identify the optimal expansion order, but it does provide valuable information about the optimal order. One possible use of the cost to benefit ratio is to use it as a filter to automatically select which coefficients will be included in the final approximation. This could be implemented by defining an R_n^2 threshold value in the Monte Carlo code. During post-processing any coefficients that had a value of R_n^2 greater than the threshold would then be discarded.

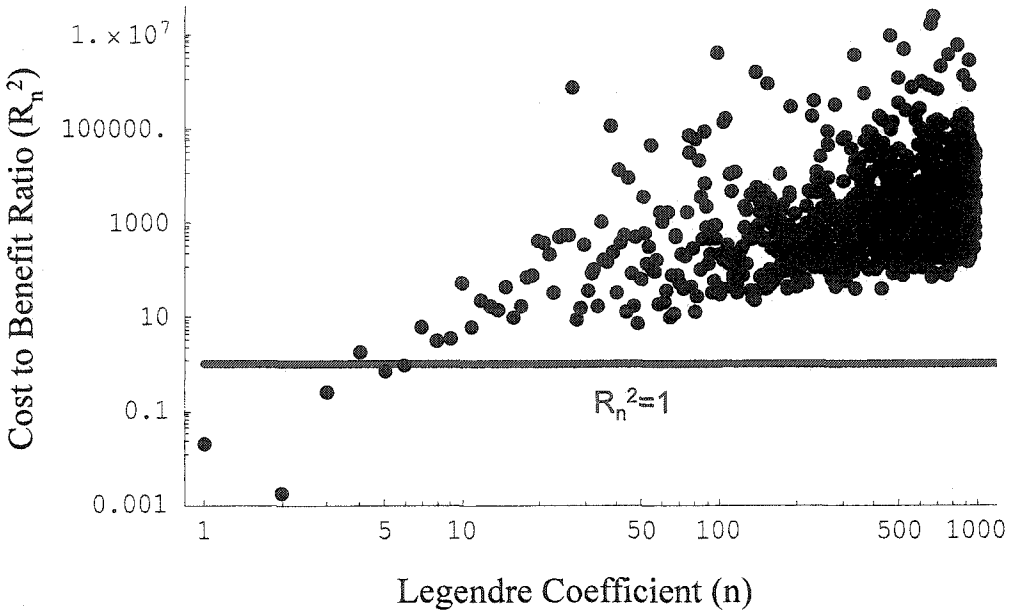

Figure 3.7. Cost to Benefit Ratio for estimated Legendre expansion coefficients for P(x) plotted against coefficient order. Each expansion coefficient was estimated using the same 10,000 history random walk process.

To test this approach a filtering algorithm was implemented in the test version of MCNP4c and used to produce a filtered FET approximation for the benchmark problem. The resulting approximation (generated with an R_n^2 threshold of 2.0) does a very good job of minimizing the total 2-norm error, as shown in Figure 3.8. Notice, however, that the filtered approximation is truncated at 6th order, where the "best" approximation should be 9th order, according to Figure 3.5. Still, the filtered approximation comes within 0.002 of the minimum error for the unfiltered approximation. This is an outstanding result, considering that no prior knowledge of the true solution shape is required. In practice, the FET can be configured to always estimate a large number of coefficients, and then filtering can be used to ensure a good approximation for the number of histories run. Conversely, an expansion order can be specified by the user and

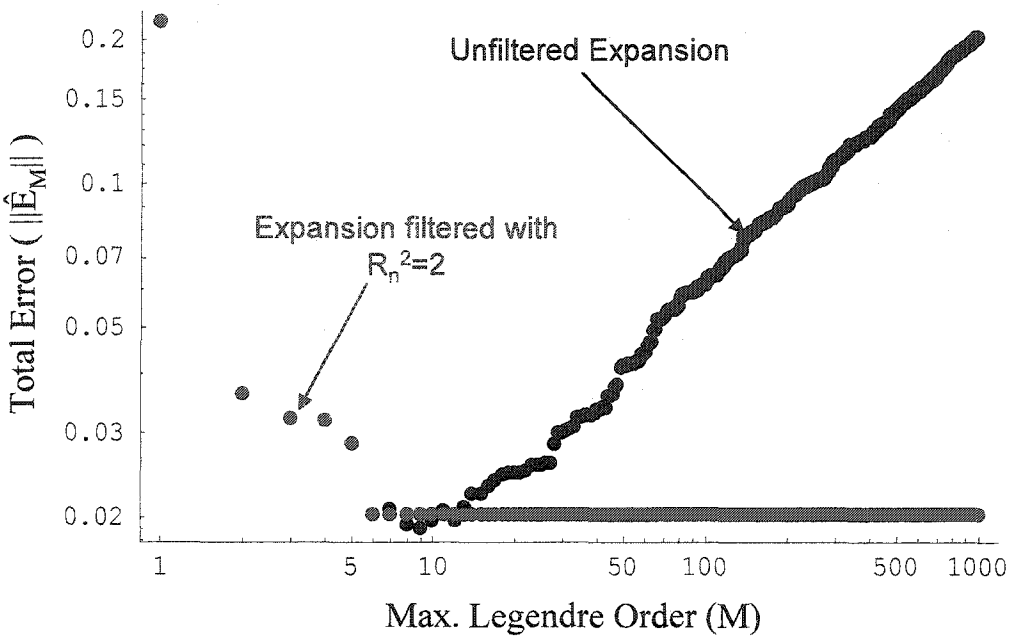

Figure 3.8. Total approximation error for filtered and unfiltered Legendre approximations plotted against truncation order. Filtered Legendre approximation was produced by discarding all expansion coefficients with $R_n^2 > 2$.

then the simulation can be left to run until all coefficients below that order meet the R_n^2 threshold. While the results of filtering can be adjusted slightly by changing the R_n^2 threshold value, the method appears to be relatively insensitive to values below 10. Repeated trials have shown that threshold values between 1 and 3 usually produce the best results.

3.4. Theoretical Convergence of the Histogram Approximation

3.4.1. Truncation Error in the Histogram

With the convergence properties of the FET established, it is time to examine the convergence of the traditional histogram approximation. With conventional Monte

Carlo, if one wants more information regarding the shape of the unknown distribution, the variable of interest is divided into bins and the random walk process is used to estimate the quantity integrated over each bin. This process results in an estimate of the histogram-style approximation to the function $P(x)$ that has the piecewise form (in 1-dimension)

$$\overline{P_M^{hist}}(x) = \frac{1}{x_b - x_{b-1}} \int_{x_{b-1}}^{x_b} P(x)\,dx \qquad \forall\ x \in [x_{b-1}, x_b]. \tag{3.84}$$

In Eq. (3.84), the set $\{x_0, x_1, \ldots, x_{M-1}, x_M\}$ represents the bin boundaries for an M bin histogram, assuming 1-D for convenience. In order to simplify the following analysis, we assume that each bin of the histogram is of equal width Δx. The 2-norm measure of the residual error between the true function and the best-fit histogram approximation can be written

$$\left\| E_M^{hist} \right\| = \left\| P(x) - \overline{P_M^{hist}}(x) \right\| = \sqrt{\int_{x_0}^{x_M} \left(P(x) - \overline{P_M^{hist}}(x) \right)^2 \rho(x)\,dx}\,. \tag{3.85}$$

Because the histogram approximation is constant over each bin, it is convenient to write the integral on the right hand side of Eq. (3.85) as

$$\left\| E_M^{hist} \right\| = \sqrt{\sum_{b=1}^{M} \int_{x_{b-1}}^{x_b} \left(P(x) - \overline{P_{M,b}^{hist}} \right)^2 dx}\,, \tag{3.86}$$

where $\overline{P_{M,b}^{hist}}$ is the value of the b^{th} histogram bin. By Taylor expanding $P(x)$ about the midpoint of each bin and simplifying, Eq. (3.86) yields, to leading order,

$$\left\| E_M^{hist} \right\| = \sqrt{\sum_{b=1}^{M} O[\Delta x^3]}\,. \tag{3.87}$$

Equation (3.87) gives the truncation error of the approximation as a function of the bin width instead of the total number of bins. For a bounded interval of length L divided into M equal bins, Δx is inversely proportional to the number of bins,

$$\Delta x = \frac{L}{M}. \tag{3.88}$$

With this assumption, Eq. (3.87) can be rewritten in terms of the number of histogram bins used,

$$\left\| E_M^{hist} \right\| = \sqrt{\sum_{b=1}^{M} O\left[\frac{1}{M^3}\right]}. \tag{3.89}$$

Since there are M bins, each with error $O\left[1/M^3\right]$ it follows immediately that the total truncation error is

$$\left\| E_M^{hist} \right\| = \sqrt{O\left[\frac{1}{M^2}\right]} = O\left[\frac{1}{M}\right]. \qquad \textit{(truncation error)} \tag{3.90}$$

A comparison of the FET and histogram truncation error convergence rates, Eq. (3.70) and (3.90), demonstrates that the FET will asymptotically converge to the correct distribution faster than a histogram approximation in cases where

$$\sqrt{\sum_{n=M+1}^{\infty} O\left[\frac{k_n}{n^{2\kappa}}\right]} < O\left[\frac{1}{M}\right]. \tag{3.91}$$

Evaluating the infinite series in the first term for $M >> 1$ shows that Eq. (3.91) will hold as long as

$$\frac{k_n}{n^{2\kappa}} < o\left[\frac{1}{n^3}\right]. \tag{3.92}$$

The terms k_n and κ in Eq. (3.91) and (3.92) illustrate that the convergence properties of the FET depend on both the smoothness of the function $P(x)$ as well as the set of basis

functions chosen for the expansion. For the case of a Legendre polynomial expansion of a probability distribution with $\kappa = 2.5$, such as the example shown in section 3.3, Eq. (3.92) gives

$$\frac{k_n}{n^{2\kappa}} = \frac{2n+1}{2n^5} = \frac{1}{n^4} + \frac{1}{2n^5} < o\left[\frac{1}{n^3}\right]. \tag{3.93}$$

Equation (3.93) shows that the FET approximation should converge to the true distribution faster than a histogram approximation. This implies that a functional expansion tally of order M may provide a more accurate estimate of the true distribution than a histogram approximation with M bins.

It is important to note that Eq. (3.92) applies only to the asymptotic truncation error convergence rates for the FET and histogram approximations. Convergence properties at low approximation orders do not necessarily follow these asymptotic limits. Therefore, Eq. (3.92) should only be used as a rough guide for selecting a tally method, to be used when only a minimal amount of a priori information, such as continuity or smoothness, is available for the unknown distribution. If more detailed information about the distribution is known, then it may be possible to tailor an optimal tally, by either selecting a more suitable set of orthogonal basis functions, in the case of the FET, or choosing a non-uniform set of bin widths in the histogram method. Obviously the best possible result is to choose a basis set that fits the unknown distribution exactly with the minimum number of terms.

3.4.2. Statistical Error in the Histogram

When a histogram is created from a Monte Carlo calculation, each estimated bin height has some degree of statistical uncertainty. The variance of each bin estimate is directly related to the number of histories that score in that particular bin. This uncertainty can be accounted for in the analysis by including a random noise term ε in each bin of the histogram definition, Eq. (3.84),

$$\widehat{P_{M,b}^{hist}} = \frac{1}{\Delta x}\int_{x_{b-1}}^{x_b} P(x)\,dx + \varepsilon_b \qquad \forall\ x \in [x_{b-1}, x_b]. \tag{3.94}$$

The ε term is a zero-mean random variable[7] that describes the distribution of statistical error in the estimate of $\overline{P_M^{hist}}(x)$. Although the notation is slightly different, this analysis of statistical error is identical to that used for the FET. A Taylor expansion of $P(x)$ about the midpoint $x_{b-1/2}$ of a bin in Eq. (3.94) yields

$$\left(P(x) - \widehat{P_{M,b}^{hist}}\right) = \varepsilon_b - \frac{P''(x_{b-1/2})}{6}\Delta x^2 + O[\Delta x^4]. \tag{3.95}$$

The total error for the histogram approximation, including statistical uncertainty, can be written

$$\left\|\hat{E}_M^{hist}\right\| = \sqrt{\sum_{b=1}^{M}\int_{x_{b-1}}^{x_b}\left(P(x) - \widehat{P_{M,b}^{hist}}\right)^2 dx}\ . \tag{3.96}$$

Substituting Eq. (3.95) into Eq. (3.96) gives

$$\left\|\hat{E}_M^{hist}\right\| = \sqrt{\sum_{b=1}^{M}\int_{x_{b-1}}^{x_b}\left(\varepsilon_b - \frac{P''(x_{b-1/2})}{6}\Delta x^2 + O[\Delta x^4] + P'(x_{b-1/2})\,x + \frac{P''(x_{b-1/2})}{2}x^2 + O[x^3]\right)^2 dx}\ . \tag{3.97}$$

Expanding Eq. (3.97) and integrating,

$$\left\|\hat{E}_M^{hist}\right\| = \sqrt{\sum_{b=1}^{M} \varepsilon_b^2 \Delta x + \frac{P'(x_{b-1/2})^2 \Delta x^3}{3} + O[\Delta x^5]}\,. \tag{3.98}$$

Equation (3.98) gives the 2-norm of the residual error in terms of ε_b, the statistical uncertainty in the estimate of $\widehat{P_{M,b}^{hist}}$. According to the Central Limit Theorem, this random variable will be normally distributed with mean zero and variance $\sigma^2_{\widehat{P_{M,b}^{hist}}}$. As with the FET analysis, the presence of statistical uncertainty in Eq. (3.98) means that $\left\|\hat{E}_M^{hist}\right\|$ is a random variable. To proceed, we consider the RMS expected value of $\left\|\hat{E}_M^{hist}\right\|$,

$$\sqrt{\left\langle \left\|\hat{E}_M^{hist}\right\|^2 \right\rangle} = \sqrt{\sum_{b=1}^{M} \left\langle \varepsilon_b^2 \right\rangle \Delta x + \frac{P'(x_{b+1/2})^2 \Delta x^3}{3} + O[\Delta x^5]}\,. \tag{3.99}$$

Using the definition of $\sigma^2_{\widehat{P_{M,b}^{hist}}}$ for a random variable with a mean of zero, it is possible to express the expected value of the statistical error squared as

$$\left\langle \varepsilon_b^2 \right\rangle = \sigma^2_{\widehat{P_{M,b}^{hist}}}\,. \tag{3.100}$$

Using Eq. (3.100) in Eq. (3.99) yields an intermediate form for the expected 2-norm error of the histogram approximation, which contains the bin variance $\sigma^2_{\widehat{P_{M,b}^{hist}}}$ instead of a random noise term ε_b,

$$\sqrt{\left\langle \left\|\hat{E}_M^{hist}\right\|^2 \right\rangle} = \sqrt{\sum_{b=1}^{M} \sigma^2_{\widehat{P_{M,b}^{hist}}} \Delta x + \frac{P'(x_{b-1/2})^2 \Delta x^3}{3} + O[\Delta x^5]}\,. \tag{3.101}$$

The bin variance can be derived by recognizing that the estimator for $\widehat{P_{M,b}^{hist}}$ is simply the number of histories that score in bin b, denoted N_b. For such a case it is easy to show that the relative uncertainty in each bin obeys traditional counting statistics,

$$\frac{\sigma_{\widehat{P^{hist}_{M,b}}}}{\widehat{P^{hist}_{M,b}}} = \frac{1}{\sqrt{N_b}}. \tag{3.102}$$

The expected number of counts in each bin is equal to the ratio of the integral over the bin to the integral over all bins,

$$\langle N_b \rangle = \frac{\int_{x_{b-1}}^{x_b} P(x)\,dx}{\int_{x_0}^{x_M} P(x)\,dx} N. \tag{3.103}$$

Using Eq. (3.102) and (3.103) to solve for $\left\langle \sigma_{\widehat{P^{hist}_{M,b}}} \right\rangle$ yields,

$$\left\langle \sigma_{\widehat{P^{hist}_{M,b}}} \right\rangle = \frac{\overline{P^{hist}_{M,b}} \sqrt{\int_{x_0}^{x_M} P(x)\,dx}}{\sqrt{N \int_{x_{b-1}}^{x_b} P(x)\,dx}} = \frac{\overline{P^{hist}_{M,b}}}{\sqrt{N \int_{x_{b-1}}^{x_b} P(x)\,dx}}, \tag{3.104}$$

which simplifies by using Eq. (3.84),

$$\left\langle \sigma_{\widehat{P^{hist}_{M,b}}} \right\rangle = \frac{\sqrt{\overline{P^{hist}_{M,b}}}}{\sqrt{\Delta x\, N}}. \tag{3.105}$$

Finally, Eq. (3.88) can be used to write the standard deviation in terms of the total number of histogram bins,

$$\left\langle \sigma_{\widehat{P^{hist}_{M,b}}} \right\rangle = \sqrt{\frac{M\,\overline{P^{hist}_{M,b}}}{N}}. \tag{3.106}$$

Equation (3.106) and (3.84) can be used to simplify Eq. (3.101) as

$$\sqrt{\left\langle \left\| \hat{E}^{hist}_{M} \right\|^2 \right\rangle} = \sqrt{\frac{M}{N} \sum_{b=1}^{M} \int_{x_{b-1}}^{x_b} P(x)\,dx + \sum_{b=1}^{M} \frac{P'(x_{b-1/2})^2}{3M^3} + O\left[\frac{1}{M^5}\right]}. \tag{3.107}$$

The summation over all bins in the first term under the radical produces an integral over the entire distribution and evaluates to 1,

$$\sqrt{\left\langle \left\| \hat{E}_M^{hist} \right\|^2 \right\rangle} = \sqrt{\frac{M}{N} + \sum_{b=1}^{M} \frac{P'(x_{b-1/2})^2}{3M^3} + O\left[\frac{1}{M^5}\right]}. \tag{3.108}$$

Equation (3.108) can then be written to leading order as

$$\sqrt{\left\langle \left\| \hat{E}_M^{hist} \right\|^2 \right\rangle} = \sqrt{O\left[\frac{M}{N}\right] + O\left[\frac{1}{M^2}\right]}. \tag{3.109}$$

Comparing Eq. (3.109) and (3.72) shows that statistical uncertainty has the same effect on both the FET and the histogram tally, causing the 2-norm of the total error to diverge as order $\sqrt{M/N}$ for large values of M. This important result indicates that both methods behave qualitatively in a similar way with respect to M. For any number of histories, N, there is an optimal value of M that allows the most information about the functional shape to be obtained. Using a value of M that is larger than the optimal value will result in the functional approximation becoming contaminated by modes (or bins) that are not well converged.

The preceding derivations have assumed that all of the bins in the histogram approximation have equal width. With this equal width assumption, the 2-norm convergence for truncation error in the histogram tally is $1/M$ for functions with a nonzero first derivative.

3.5. Numerical Results for Histogram Convergence

Using the test distribution for $P(x)$ given in Eq. (3.73), verification studies of the theoretical histogram tally convergence rates were conducted. These studies examined the convergence rate of the 2-norm residual error for histogram approximations using exact bin heights and different numbers of bins. For each histogram bin, values were

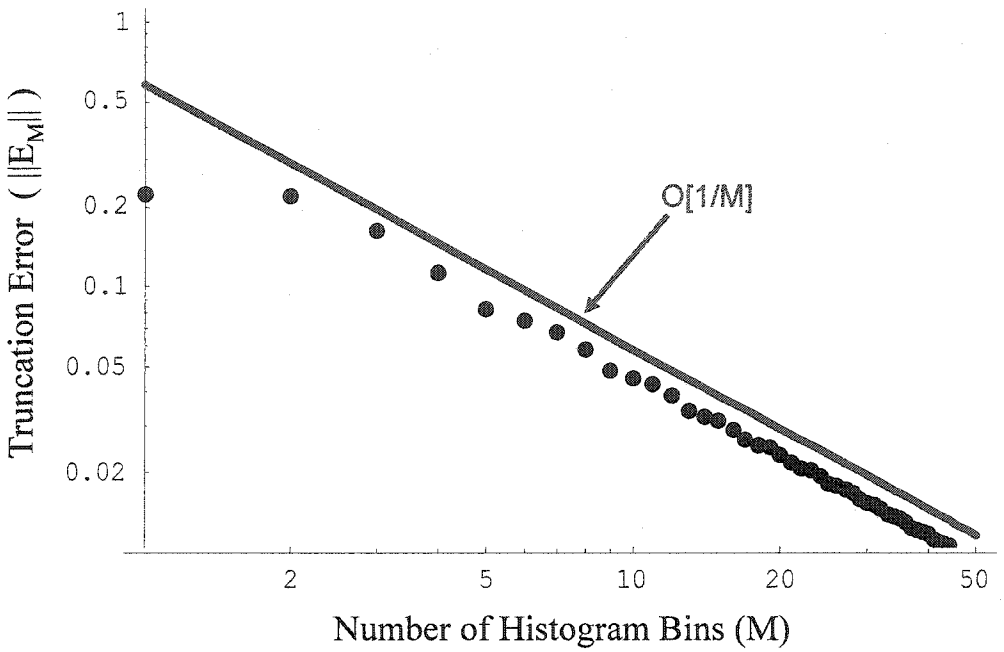

Figure 3.9. Two norm measure of residual error for a histogram approximation to P(x) plotted against the number of histogram bins. A 1/M trend line is shown for comparative purposes, indicating the convergence rate.

calculated with Eq. (3.84) and the residual errors were calculated with Eq. (3.86). The result of this study, shown in Figure 3.9, demonstrate that for $M \geq 2$, the residual error in the histogram approximation converges as $O[1/M]$, the exact rate predicted in Eq. (3.90).

The effects of statistical uncertainty on the convergence rate of the histogram approximation were then included in the study. Instead of calculating bin values directly, random samples were taken from the test distribution of $P(x)$ and tallied in the appropriate histogram bin. Bin values were then estimated by dividing the number of samples scoring in each bin by the total number of samples times the bin width. The residual error between the Monte Carlo histogram approximation and true distribution was calculated directly with Eq. (3.86).

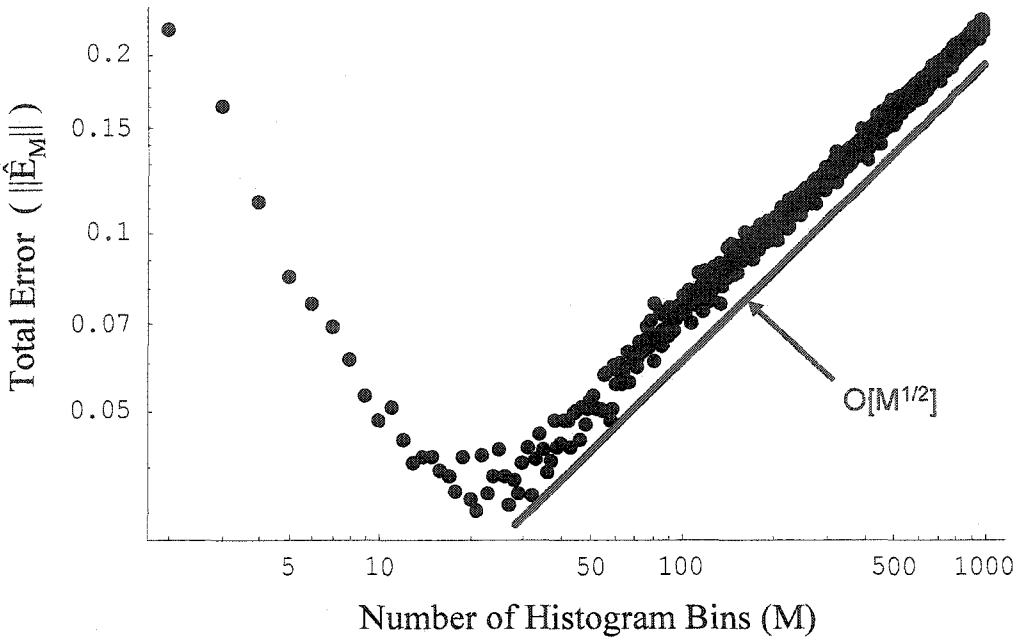

Figure 3.10. Two norm measure of residual error for a stochastic histogram approximation to P(x) plotted against the number of histogram bins used. Each histogram approximation was created using the same N=10,000 samples from P(x).

The results, shown in Figure 3.10, demonstrate that the convergence behavior of the truncation error behaves qualitatively as predicted in Eq. (3.109). Like the FET, for fixed N, the histogram has an optimal number of bins that will minimize the total residual error of the approximation. The optimal number of bins is approximately 20 for the test distribution considered. For a histogram approximation using more than the optimal number of bins, the residual error begins to increase as more bins are used.

3.6. Discussion and Comparison of Results

This chapter has sought to demonstrate, theoretically and numerically, that the FET and histogram approximations converge to the true distribution in qualitatively the same way as the approximation order is increased. To compare the FET and histogram

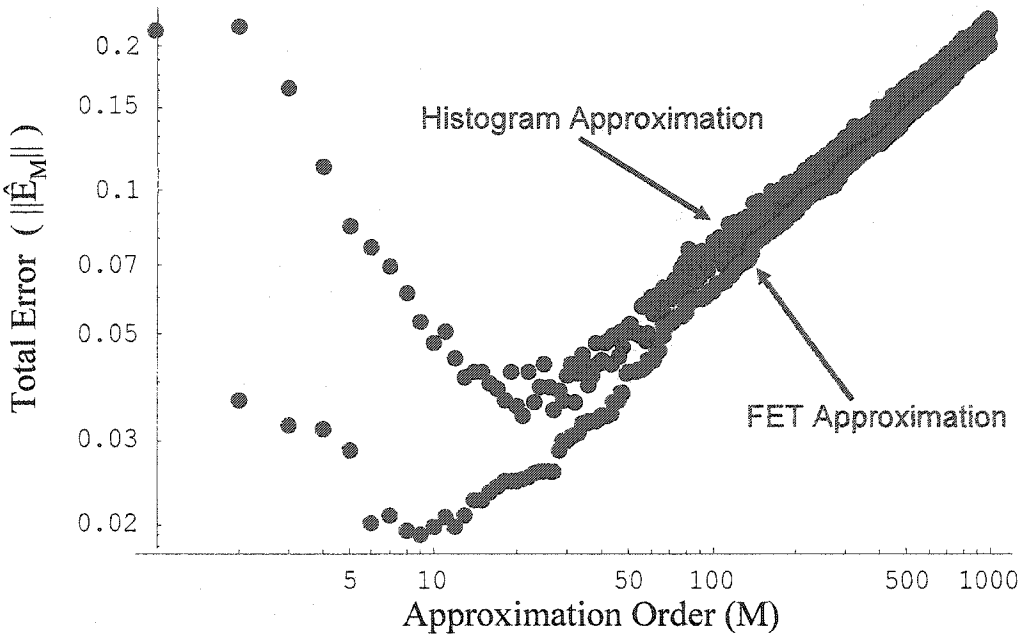

Figure 3.11. Comparison of residual errors due to the stochastic histogram and FET approximations to P(x). Each approximation was created using the same 10,000 samples from P(x).

residual errors, Figure 3.5 and Figure 3.10 are shown plotted together in Figure 3.11; this figure demonstrates that the FET and histogram approximations have roughly the same convergence behavior with respect to the approximation order M. Both methods show a reduction in residual error with increasing order before reaching the optimal value of M as $M \to \infty$. Below the optimal value, the convergence is dominated by the truncation error inherent in each of the approximations. For approximation orders greater than the optimal value, the residual error begins to increase due to statistical noise in the system. The FET error is always less than the histogram error as $M \to \infty$.

Figure 3.11 illustrates that, for the trial distribution of $P(x)$ selected, the FET is superior to the histogram tally. The FET can achieve a smaller residual error, for a 10,000 history calculation, than a histogram for any order of approximation. Furthermore, the results show that a 4^{th} or 5^{th} order Legendre approximation to $P(x)$

outperforms even the optimal histogram approximation. In this case, the FET can clearly extract more information about the distribution $P(x)$ than a histogram tally.

Although the FET is superior to the histogram tally for this specific example, it is not possible to claim that this will hold in general because the accuracy of the final fit depends on the approximation technique that best matches the shape and properties of the unknown function. The best approach for a given distribution is the one that has the fastest truncation error convergence rate. For example, the histogram approximation is best suited for discontinuous distributions or those with very sharp gradients.

On the other hand, estimating higher moments within these histogram bins may yield substantial improvement in the results, allowing piecewise FET to do very well in situations where the analyst has prior knowledge regarding the location of discontinuities, such as at material boundaries[27]. For homogeneous systems, or any case where smoothly varying distributions are expected, a Legendre or Chebyshev FET approximation will most likely show large improvements over a histogram tally.

CHAPTER 4

TRACK LENGTH FET ESTIMATORS

Chapters 2 and 3 covered the derivation of the FET for discrete event estimators. The derivation and implementation of the FET in this class of estimators proved to be relatively straightforward, requiring only a minor modification to the original scoring functions. While discrete event estimators are still used for tallying surface crossing quantities, most modern Monte Carlo codes rely on track length estimators for tallying volumetric fluxes. This is due to the fact that a track length estimator will, in most cases, give a lower variance for flux estimates than a collision estimator. Furthermore, track length estimators give reliable estimates even in void regions where collision estimators fail. Given the importance of track length estimators in particle transport Monte Carlo codes, it would clearly be beneficial to develop a version of the FET for track length estimators. This chapter offers detailed derivations for the track length FET estimators in both 1 and 3 dimensions. Additionally, some thoughts and comments on the numerical implementation of these estimators are provided, along with numerical results to demonstrate the effectiveness of the tally.

4.1. Derivation of the 1-D Track Length FET Estimator

In order to estimate the spatial flux distribution over the 1-dimensional region $x \in [x_{\min}, x_{\max}]$, the flux in this region is assumed to be expandable in terms of a complete set of basis functions $\{\psi_n\}_{n=0}^{\infty}$ that are orthogonal with respect to the weighting function $\rho(x)$. The spatial distribution of the scalar flux can now be expanded in terms of the basis functions by the series expansion

$$\phi(x) = \sum_{n=0}^{\infty} \bar{a}_n k_n \psi_n(x). \tag{4.1}$$

Using the orthogonal property of the basis functions allows the expansion coefficients to be evaluated as

$$\bar{a}_n = \int_{x_{\min}}^{x_{\max}} \phi(x)\psi_n(x)\rho(x)dx. \tag{4.2}$$

Now, by partitioning the tally region into P equally spaced slices, Eq. (4.2) can be written as

$$\bar{a}_n = \sum_{p=1}^{P} \int_{x_p}^{x_{p+1}} \phi(x)\psi_n(x)\rho(x)dx \tag{4.3}$$

If the width of each partition Δx_p is small, the value of the function $\psi_n(x)\rho(x)$ within a partition can be approximated by its value at the midpoint of the partition

$$\psi_n(x)\,\rho(x) = \psi_n(x_{p+1/2})\rho(x_{p+1/2}) + O(\Delta x_p) \quad \text{for} \quad x \in [x_p, x_{p+1}]. \tag{4.4}$$

Using this approximation, Eq. (4.3) gives

$$\bar{a}_n = \sum_{p=1}^{P} \int_{x_p}^{x_{p+1}} \left(\psi_n(x_{p+1/2})\rho(x_{p+1/2}) + O(\Delta x_p)\right)\phi(x)dx$$

$$= \sum_{p=1}^{P} \left(\int_{x_p}^{x_{p+1}} \psi_n\left(x_{p+1/2}\right) \rho\left(x_{p+1/2}\right) \phi(x)\, dx + \int_{x_p}^{x_{p+1}} \phi(x) O\left(\Delta x_p\right) dx \right)$$

$$\bar{a}_n = \sum_{p=1}^{P} \left(\psi_n\left(x_{p+1/2}\right) \rho\left(x_{p+1/2}\right) \int_{x_p}^{x_{p+1}} \phi(x)\, dx + O\left(\Delta x_p^2\right) \right). \tag{4.5}$$

We notice that the last term in Eq. (4.5) is the integrated flux over the p^{th} partition in the x-direction. This quantity can also be interpreted as the total amount of track length, D_p, generated by all neutrons passing through the partition[16],

$$\int_{x_p}^{x_{p+1}} \phi(x)\, dx = D_p . \tag{4.6}$$

Using Eq. (1.63), it is easy to show that the statistic

$$\hat{D}_p = \frac{1}{N} \sum_{i=1}^{N} d_{i,p} , \tag{4.7}$$

where N is the total number of particles started and $d_{i,p}$ is the path length generated in partition p by particle i during its life, is an unbiased estimator for Eq. (4.6).

In order to develop an expression for the total amount of track length generated by a particle in the p^{th} partition, consider an arbitrary particle i as it travels through the system. During the random walk process, the particle will travel in a straight line between events. At each event the particle may change direction (i.e. scatter) or continue along the path it was on. The path length generated by a single particle over its life can therefore be written as the sum of the distances traveled between events

$$d_i = \sum_{c=1}^{C_i} w_{i,c}\, d_{i,c} = \sum_{p=1}^{P} \sum_{c=1}^{C_i} w_{i,c}\, d_{i,c,p} , \tag{4.8}$$

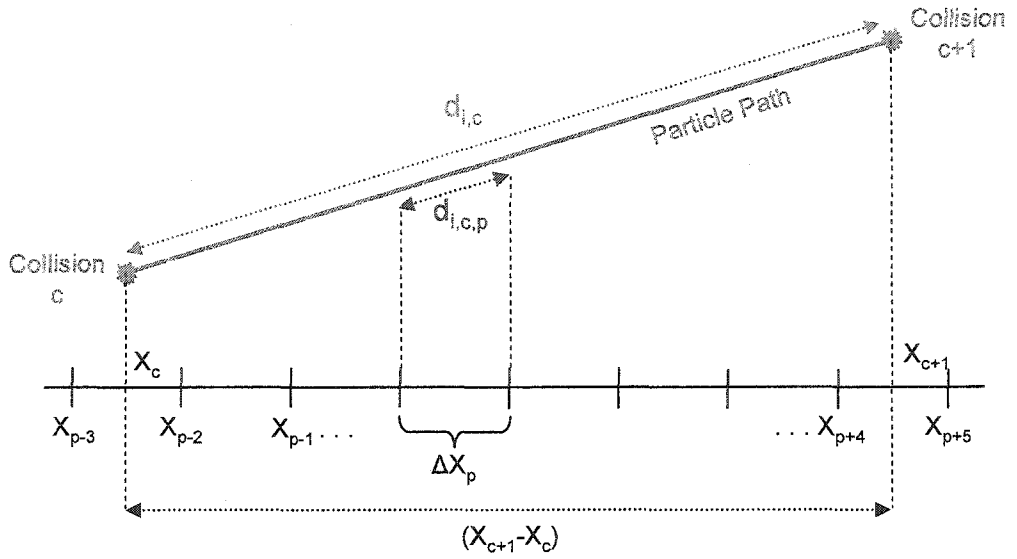

Figure 4.1. Illustration of a particle traveling between consecutive events c and c+1. The total distance traveled by the particle is $d_{i,c}$, and the starting and ending positions of the particle are given by the points x_c and x_{c+1}, respectively. Using simple trigonometry it is easy to show that the particle travels a distance $(d_{i,c}\Delta x_p)/(x_c - x_{c+1})$ in each interior cell.

where $d_{i,k,p}$ is the path length generated by particle i in partition p as it travels from event c to event $c+1$. Furthermore, let the locations of the c^{th} and $(c+1)^{st}$ events be denoted as x_c and x_{c+1}, respectively. The path of a particle between two consecutive events is illustrated in Figure 4.1. Because a particle travels in a straight line between events, simple trigonometry can be used to determine the total path length generated in each partition. Inspection of the particle flight path shown in Figure 4.1 shows that the particle travels a distance

$$d_{i,c,p} = \frac{d_{i,c}}{\left(x_{i,c+1} - x_{i,c}\right)} \Delta x_p \tag{4.9}$$

in partitions $p-2$ through $p+3$. Equation (4.9) is not exact in the partitions where the particle begins or ends its free-flight (partitions $p-1$ and $p+4$, respectively). In these partitions, Eq. (4.9) overestimates the path traveled in the partition, but is still accurate to

$O(\Delta x_p)$. Therefore, for a generalized 1-D path of a particle beginning in partition p' and ending in partition p'', the total distance traveled in each partition is given by

$$d_{i,c,p} = \begin{cases} \dfrac{d_{i,c}}{(x_{i,c+1} - x_{i,c})} \Delta x_p & \forall \; p \in (p', p'') \\ \dfrac{d_{i,c}}{(x_{i,c+1} - x_{i,c})} \Delta x_p - O(\Delta x_p) & p = p' \;\; or \;\; p = p'' \\ 0 & otherwise. \end{cases} \tag{4.10}$$

Equations (4.8) can now be used to rewrite Eq. (4.7) as

$$\hat{D}_p = \frac{1}{N} \sum_{i=1}^{N} \sum_{c=1}^{C_i} w_{n,c} \, d_{n,c,p} \tag{4.11}$$

Substituting Eq. (4.11) into Eq. (4.5) gives

$$\hat{a}_n = \sum_{p=1}^{P} \left(\psi_n(x_{p+1/2}) \rho(x_{p+1/2}) \left(\frac{1}{N} \sum_{i=1}^{N} \sum_{c=1}^{C_i} w_{i,c} \, d_{i,c,p} \right) + O(\Delta x_p^2) \right), \tag{4.12}$$

which is an unbiased estimator for $\bar{a}_n$. Rearranging the order of summation and applying the definition of $d_{i,c,p}$ given in Eq. (4.10) gives

$$\begin{aligned} \hat{a}_n = \frac{1}{N} \sum_{i=1}^{N} \sum_{c=1}^{C_i} w_{i,c} \sum_{p=p'+1}^{p''-1} & \left(\psi_n(x_{p+1/2}) \rho(x_{p+1/2}) \left(\frac{d_{i,c} \Delta x_p}{(x_{i,c+1} - x_{i,c})} \right) + O(\Delta x_p^2) \right) \\ & + \psi_n(x_{p'+1/2}) \rho(x_{p'+1/2}) \left(\frac{d_{i,c} \Delta x_p}{(x_{i,c+1} - x_{i,c})} - O(\Delta x_p) \right) + O(\Delta x_p^2) \\ & + \psi_n(x_{p''+1/2}) \rho(x_{p'+1/2}) \left(\frac{d_{i,c} \Delta x_p}{(x_{i,c+1} - x_{i,c})} - O(\Delta x_p) \right) + O(\Delta x_p^2) \end{aligned}$$

$$\hat{a}_n = \frac{1}{N}\sum_{i=1}^{N}\sum_{c=1}^{C_i} w_{i,c} \sum_{p=p'+1}^{p''-1}\left(\psi_n\left(x_{p+1/2}\right)\rho\left(x_{p+1/2}\right)\left(\frac{d_{i,c}\,\Delta x_p}{\left(x_{i,c+1}-x_{i,c}\right)}\right)+O\left(\Delta x_p^2\right)\right)$$
$$+\psi_n\left(x_{p'+1/2}\right)\rho\left(x_{p'+1/2}\right)O\left(\Delta x_p\right)+\psi_n\left(x_{p''+1/2}\right)\rho\left(x_{p''+1/2}\right)O\left(\Delta x_p\right) \qquad (4.13)$$
$$+O\left(\Delta x_p^2\right).$$

Expanding the terms inside of the partition summation gives

$$\hat{a}_n = \frac{1}{N}\sum_{i=1}^{N}\sum_{c=1}^{C_i} w_{i,c} \sum_{p=p'+1}^{p''-1}\left(\psi_n\left(x_{p+1/2}\right)\rho\left(x_{p+1/2}\right)\left(\frac{d_{i,c}\,\Delta x_p}{\left(x_{i,c+1}-x_{i,c}\right)}\right)+O(\Delta x_p{}^2)\right) \qquad (4.14)$$
$$+\left(\psi_n\left(x_{p'+1/2}\right)\rho\left(x_{p'+1/2}\right)+\psi_n\left(x_{p''+1/2}\right)\rho\left(x_{p'+1/2}\right)\right)O(\Delta x_p)+O\left(\Delta x_p^2\right).$$

Finally, taking the limit as $P\to\infty$ (or $\Delta x_p\to 0$) yields

$$\hat{a}_n = \frac{1}{N}\sum_{i=1}^{N}\sum_{c=1}^{C_i}\frac{w_{i,c}\,d_{i,c}}{\left(x_{i,c+1}-x_{i,c}\right)}\int_{x_c}^{x_{c+1}}\psi_n(x)\,\rho(x)\,dx. \qquad (4.15)$$

Note that Eq. (4.15) is singular if $x_c = x_{c+1}$, which physically corresponds to a particle moving perpendicular to the x-axis. In this special case, a separate form of the estimator must be derived to handle the singularity. Starting with Eq. (4.15), the fundamental theorem of calculus can be used to evaluate the definite integral in terms of the antiderivatives $\Psi_n(x)$ of the integrand $\psi_n(x)\rho(x)$,

$$\hat{a}_n = \frac{1}{N}\sum_{i=1}^{N}\sum_{c=1}^{C_i}\frac{w_{i,c}\,d_{i,c}}{\left(x_{i,c+1}-x_{i,c}\right)}\left[\Psi_n\left(x_{n,c+1}\right)-\Psi_n\left(x_{n,c}\right)\right]. \qquad (4.16)$$

Taking the limit of Eq. (4.16) as $x_{n,c+1}\to x_{n,c}$ gives

$$\hat{a}_n = \lim_{x_{n,c+1}\to x_{n,c}}\frac{1}{N}\sum_{i=1}^{N}\sum_{c=1}^{C_i}\frac{w_{i,c}\,d_{i,c}}{\left(x_{i,c+1}-x_{i,c}\right)}\left[\Psi_n\left(x_{n,c+1}\right)-\Psi_n\left(x_{n,c}\right)\right]$$

$$=\frac{1}{N}\sum_{i=1}^{N}\sum_{c=1}^{C_i} w_{i,c}\,d_{i,c}\lim_{x_{n,c+1}\to x_{n,c}}\frac{\Psi_n\left(x_{n,c+1}\right)-\Psi_n\left(x_{n,c}\right)}{\left(x_{i,c+1}-x_{i,c}\right)}$$

$$= \frac{1}{N} \sum_{i=1}^{N} \sum_{c=1}^{C_i} w_{i,c}\, d_{i,c}\, \Psi'_n\left(x_{n,c}\right)$$

$$\hat{a}_n = \frac{1}{N} \sum_{i=1}^{N} \sum_{c=1}^{C_i} w_{i,c}\, d_{i,c}\, \psi_n\left(x_{n,c}\right) \rho\left(x_{n,c}\right). \tag{4.17}$$

Equations (4.15) and (4.17) together form the 1-D track length FET estimator,

$$\hat{a}_n = \frac{1}{N} \sum_{i=1}^{N} \sum_{c=1}^{C_i} S_{n,i,c}\left(w_{i,c}, d_{i,c}, x_{i,c+1}, x_{i,c}\right)$$

$$S_{n,i,c} = \begin{cases} \dfrac{w_{i,c}\, d_{i,c}}{\left(x_{i,c+1} - x_{i,c}\right)} \displaystyle\int_{x_c}^{x_{c+1}} \psi_n(x)\, \rho(x)\, dx & \text{if } x_{i,c} \neq x_{i,c+1} \\ w_{i,c}\, d_{i,c}\, \psi_n\left(x_{n,c}\right) \rho\left(x_{n,c}\right) & \text{if } x_{i,c} = x_{i,c+1}. \end{cases} \tag{4.18}$$

4.2. Implementation of 1-D Track Length FET Estimators

The numerical implementation of the 1-D track length estimator poses many of the same challenges as the implementation of the discrete event estimator (section 2.3). In addition to the previously discussed issues of basis selection and variable scaling, the track length estimator presents a new computational challenge. While the discrete event FET estimators required that each basis function be evaluated at a series of discrete points, the track length estimator requires an integral of each basis function to be evaluated. The calculation of this integral for each particle flight can potentially become a major source of computational overhead in the code. A variety of numerical schemes, such as Gaussian quadrature, can be used to evaluate the integral relatively efficiently. For the basis set of Legendre polynomials it is actually possible to derive a recursion relationship for the integral in Eq. (4.18).

The derivation of this Legendre integral recursion relationship begins with the Rodrigues representation for a Legendre polynomial[35,36]

$$P_n(x)=\frac{1}{2^n n!}\frac{d^n}{dx^n}\left(x^2-1\right)^n. \tag{4.19}$$

Taking the derivative of Eq. (4.19) with respect to x gives

$$P_n'(x)=\frac{1}{2^n n!}\frac{d^{n+1}}{dx^{n+1}}\left(x^2-1\right)^n. \tag{4.20}$$

Equation (4.20) can now be used to show the following relationship

$$\begin{aligned}P_{n+1}'(x)-P_{n-1}'(x)=&\frac{1}{2^{n+1}(n+1)!}\frac{d^{n+2}}{dx^{n+2}}\left(x^2-1\right)^{n+1}\\&-\frac{1}{2^{n-1}(n-1)!}\frac{d^n}{dx^n}\left(x^2-1\right)^{n-1}.\end{aligned} \tag{4.21}$$

Algebraic manipulation of the right hand side of Eq. (4.21) gives

$$P_{n+1}'(x)-P_{n-1}'(x)=\frac{1}{2^{n+1}}\left[\frac{1}{(n+1)!}\frac{d^{n+2}}{dx^{n+2}}\left(x^2-1\right)^{n+1}-\frac{4}{(n-1)!}\frac{d^n}{dx^n}\left(x^2-1\right)^{n-1}\right]$$

$$=\frac{1}{2^{n+1}}\left[\frac{1}{(n+1)!}\frac{d^n}{dx^n}\left[\frac{d^2}{dx^2}\left(x^2-1\right)^{n+1}\right]-\frac{4}{(n-1)!}\frac{d^n}{dx^n}\left(x^2-1\right)^{n-1}\right]$$

$$=\frac{1}{2^{n+1}n!(n+1)}\frac{d^n}{dx^n}\left[4n(n+1)x^2\left(x^2-1\right)^{n-1}+2(n+1)\left(x^2-1\right)^n\right]$$

$$-\frac{4}{2^{n+1}(n-1)!}\frac{d^n}{dx^n}\left(x^2-1\right)^{n-1}$$

$$=\frac{1}{2^{n+1}}\left[\frac{1}{n!}\frac{d^n}{dx^n}\left[4nx^2\left(x^2-1\right)^{n-1}+2\left(x^2-1\right)^n\right]-\frac{4n}{n!}\frac{d^n}{dx^n}\left(x^2-1\right)^{n-1}\right]$$

$$=\frac{1}{2^{n+1}n!}\left[\frac{d^n}{dx^n}\left[2\left(x^2-1\right)^n\right]+\frac{d^n}{dx^n}\left[4nx^2\left(x^2-1\right)^{n-1}-4n\left(x^2-1\right)^{n-1}\right]\right]$$

$$= \frac{1}{2^{n+1} n!}\left[\frac{d^n}{dx^n}\left[2\left(x^2-1\right)^n\right] + \frac{d^n}{dx^n}\left[4n\left(x^2-1\right)\left(x^2-1\right)^{n-1}\right]\right]$$

$$= \frac{1}{2^{n+1} n!}\left[\frac{d^n}{dx^n}\left[2\left(x^2-1\right)^n + 4n\left(x^2-1\right)^n\right]\right]$$

$$= \frac{1}{2^{n+1} n!}\left[\frac{d^n}{dx^n}(4n+2)\left(x^2-1\right)^n\right]$$

$$P'_{n+1}(x) - P'_{n-1}(x) = \frac{(2n+1)}{2^n n!}\left[\frac{d^n}{dx^n}\left(x^2-1\right)^n\right]. \tag{4.22}$$

Using Eq. (4.19), this relationship can be written as

$$P'_{n+1}(x) - P'_{n-1}(x) = (2n+1)P_n(x). \tag{4.23}$$

Rearranging Eq. (4.23) to solve for $P_n(x)$,

$$P_n(x) = \frac{1}{(2n+1)}\left(P'_{n+1}(x) - P'_{n-1}(x)\right), \tag{4.24}$$

and integrating over x gives

$$\int_a^b P_n(x)\,dx = \frac{1}{(2n+1)}\left[\int_a^b P'_{n+1}(x)\,dx - \int_a^b P'_{n-1}(x)\,dx\right]. \tag{4.25}$$

By the Fundamental Theorem of Calculus, Eq. (4.25) becomes

$$\int_a^b P_n(x)\,dx = \frac{1}{(2n+1)}\left[P_{n+1}(b) - P_{n+1}(a) - P_{n-1}(b) + P_{n-1}(a)\right]. \tag{4.26}$$

Equation (4.26) shows that a definite integral of a Legendre polynomial can be easily calculated by simply evaluating the higher and lower order polynomials at the endpoints of the integral. In fact, with this relationship, evaluating the 1-D track length FET estimator is just as efficient as evaluating a discrete event FET estimator. The only difference is that the Monte Carlo code must store both the current event location as well

as the location of the previous event. Aside from the evaluation of the path length integral, the implementation of the track length FET estimator is virtually identical to the implementation for the discrete event estimators.

4.3. Numerical Results for 1-D Track Length FET

4.3.1. Pressurized Water Reactor (Single Pin) Benchmark Problem

The track length FET estimator given in Eq. (4.18) was implemented in a modified version of MCNP4c to tally spatial flux distributions in one dimension. The modified code was then tested on eigenvalue calculations for infinite lattices of low-enriched (< 2%) UO_2 fuel pins. The fuel pins were loosely modeled on actual fuel rods used in a Westinghouse design pressurized water reactor (PWR). Each fuel pin has a diameter of 1cm, 0.04 cm air gap, 0.04 cm clad thickness, and a square pitch of 2 cm. The 1-D pins are infinite in the y- and z-directions. An illustration of the reference fuel pin is shown in Figure 4.2.

For a reference solution, the pin cell was subdivided into 50 sub-cells in the x-direction and a standard track length tally was taken for thermal neutrons in each cell during a continuous-energy k-code calculation using 120 cycles (20 inactive) and 1000 histories per cycle. The results of this reference calculation are shown in Figure 4.3. The relative standard deviation for the benchmark flux estimate in each cell ranged from 0.0035-0.0044. Notice in this reference solution that the flux distribution appears to have "kinks," or discontinuities in the first derivative, near the positions $x = 0.5$ cm and 1.5 cm. These discontinuities occur at each of the material interfaces.

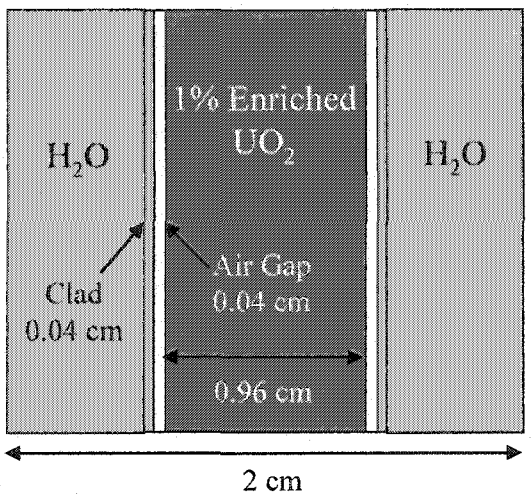

Figure 4.2. One-dimensional representation of a PWR fuel pin used for benchmark testing. The pin contains a zirconium clad slab of 1% enriched UO_2 surrounded by water at standard temperature and pressure. Reflecting boundary conditions were applied to all sides of the cell in order to simulate a repeating lattice of infinitely long fuel pins. The calculated eigenvalue for this infinite lattice was 1.05.

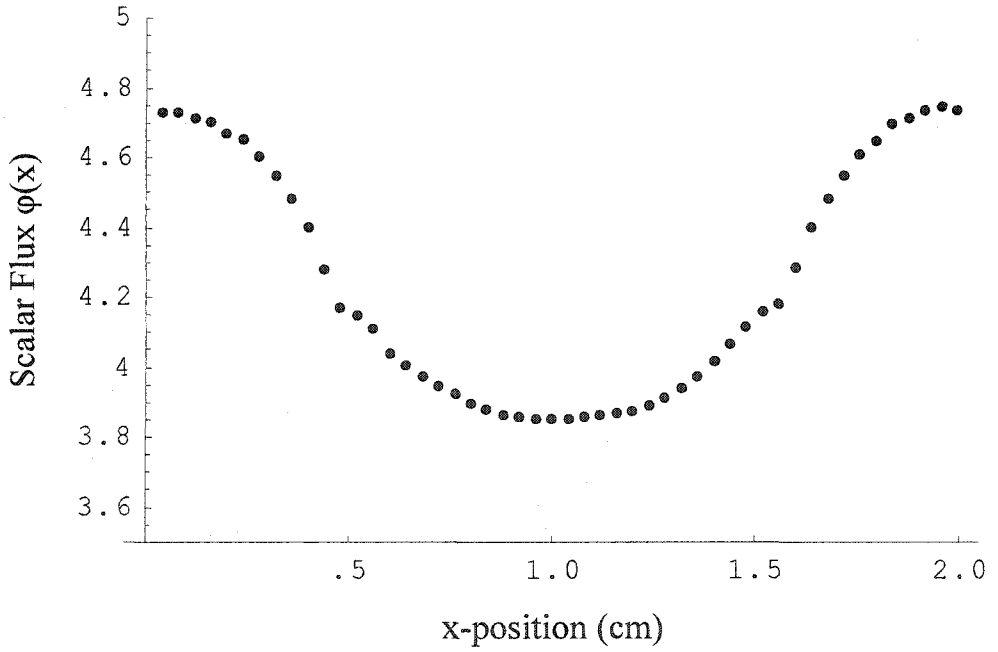

Figure 4.3. Reference 50-bin histogram approximation of the thermal flux distribution across the 1-D PWR fuel pin. This data was collected from a single 100,000 history eigenvalue calculation run in MCNP4c. Note the "kinks" in the flux distribution that occur near x = 0.5 and x = 1.5. These kinks are due to the water/clad/gap/fuel material interfaces located in these regions.

Following the reference calculation, the benchmark problem was then run twice using the modified track length tally to estimate the first 10 Legendre expansion coefficients. In the first trial, a total of 2,000 active neutron histories were run to produce estimates for the expansion coefficients. In the second trial, the number of active neutron histories was increased to 100,000. The resulting functional approximations from the two trials are shown in Figure 4.4 and Figure 4.5, respectively.

Both FET approximations agree, within statistical uncertainty, with the reference solution over most of the tally domain. The results in Figure 4.4 indicate that the 9^{th} order Legendre approximation produced using 2,000 active neutron histories contains a large amount of statistical uncertainty. However, even with this uncertainty, the approximation is able to capture the gross shape of the distribution and is accurate to within 2 standard deviations of the reference solution. The 100,000 history Legendre approximation does a much better job of resolving the true flux distribution. Correspondingly, the statistical uncertainty in this approximation is much lower than the 2,000 history approximation. Even with this reduced statistical uncertainty, the 100,000 history FET approximation still appears to have difficulties resolving the flux shape near material interfaces in the problem. The FET approximation appears to smooth-over the kinks in the flux that occur at these interfaces. We recall from Chapter 3 that the FET is most effective when approximating distributions that are analytically smooth. If there are any discontinuities in the distribution or its higher derivatives, then the FET will converge more slowly near those discontinuities. As noted earlier, the material interfaces in this problem create discontinuities in the first derivative of the flux.

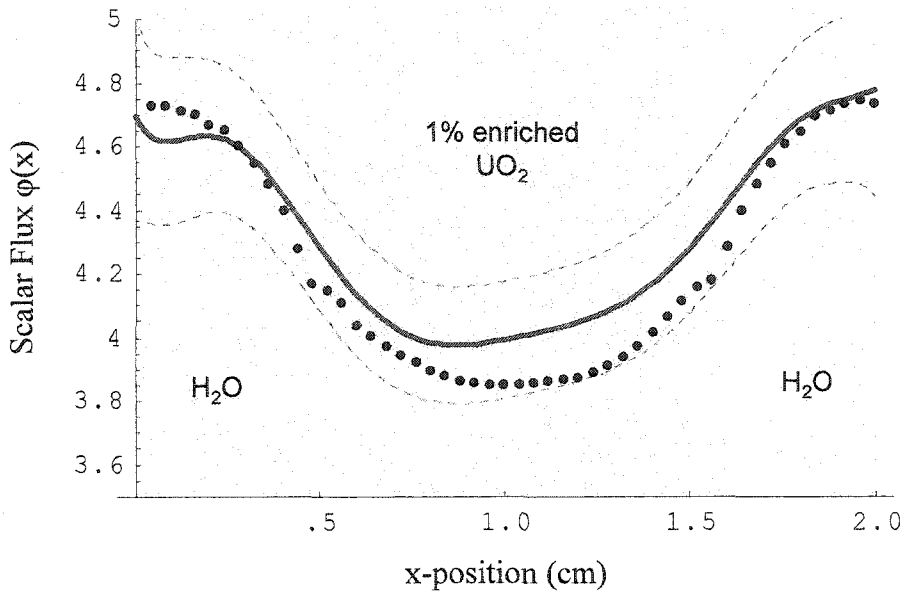

Figure 4.4. Results from the 2,000 history simulation showing the ninth order Legendre FET approximation to the thermal flux distribution across a 1-D PWR fuel pin. The black dots represent the benchmark histogram solution. Each histogram point lies within the two standard deviation uncertainty band (dashed curves) of the FET solution. The different material regions in the unit cell are shown superimposed on top of the plot to illustrate the locations of material interfaces.

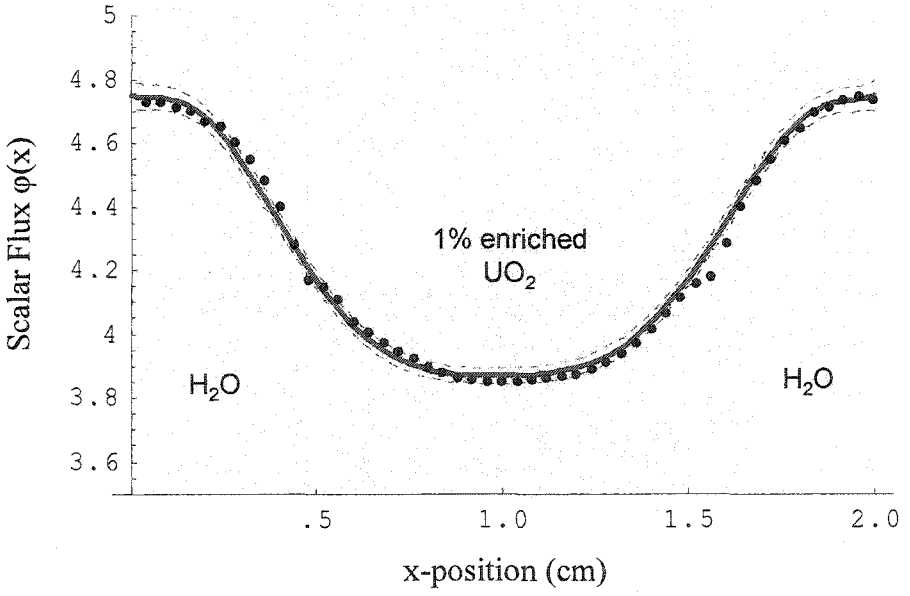

Figure 4.5. Results from the 100,000 history simulation showing the ninth order Legendre FET approximation to the thermal flux distribution across a 1-D PWR fuel pin. The FET shows excellent agreement with the reference histogram solution for all points except near the material interfaces. The relatively small two-sigma uncertainty band (dashed lines) indicates that the FET approximation is statistically well converged.

Therefore, while a low order Legendre approximation works well for the smooth parts of the flux distribution, it cannot resolve the distribution near the material interfaces. Resolving the flux in these regions would require either a higher order approximation or a piecewise approximation. An example of a piecewise approximation is given in the next benchmark problem.

4.3.2. Pressurized Water Reactor (Lattice) Benchmark Problem

The previous benchmark demonstrated the effectiveness of the FET for approximating the spatial distribution of thermal flux within a single fuel pin in an infinite lattice. Realistic problems, however, do not resemble an infinite lattice of fuel pins. A standard reactor design will contain poison rods, instrumentation tubes, water channels, and structural elements, all interspersed with the fuel pins. The resulting flux distribution in a single fuel pin depends heavily on the location of any non-fuel elements nearby. In order to test the effectiveness of the FET in realistic reactor problems, a second 1-D benchmark problem was developed consisting of six low-enriched fuel pins and one poison pin arranged in a repeating lattice. The problem geometry is illustrated in Figure 4.6. The poison pin contains boron-10, a strong thermal neutron absorber, at a density of 0.022 g/cc. The presence of this poison element results in a sharp drop in thermal neutron flux near the boron rod. Correctly predicting the shape of this flux depression near strong absorbers has long been a challenge for neutron transport codes[37], both deterministic and stochastic.

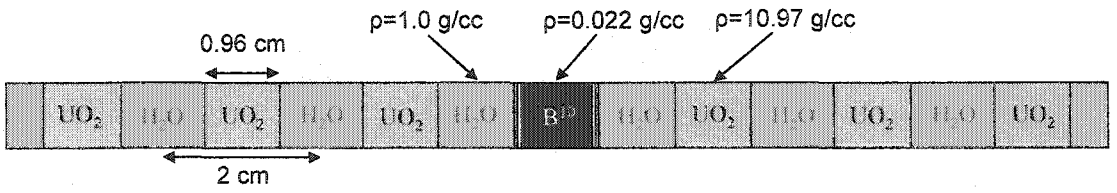

Figure 4.6. One-dimensional representation of a PWR fuel lattice containing a boron control pin. Each fuel pin contains a slab of 1.95% enriched UO_2 surrounded by water at standard temperature and pressure. The center cell contains a zirconium clad boron-10 poison pin. Reflecting boundary conditions were applied to all sides of the geometry in order to simulate a repeating lattice of infinitely long pins. The measured eigenvalue for this infinite system was 0.96218.

In the benchmark model, the pin cladding and air gap were modeled explicitly only for the poison pin. For the fuel pins, the cladding and air gap were simply homogenized into the fuel region. Even with this simplification, the model still contains eighteen material boundaries. Given the performance of the FET in the previous benchmark problem, it is unreasonable to expect that a global low-order functional expansion will produce a good approximation across all of those material boundaries. Instead, a series of piecewise FET approximations were used instead of a single global solution. Since the locations of the material boundaries are known from the problem geometry, a separate tally region was created for each homogeneous region. During each simulation, the 1-D track length FET estimator was used to produce an estimate for the first 10 Legendre coefficients in each homogeneous region.

In the first test, a 100,000 history simulation was used to produce both a 50-bin histogram approximation and a three region piecewise FET approximation (9^{th} order) to the thermal flux distribution across the boron pin. A comparison of the results, Figure 4.7, shows that the piecewise FET approximation agrees very well with the histogram solution. With the piecewise approach, the low order FET approximation is even able to resolve the kinks in the scalar flux that occur at the material boundaries. This results in a

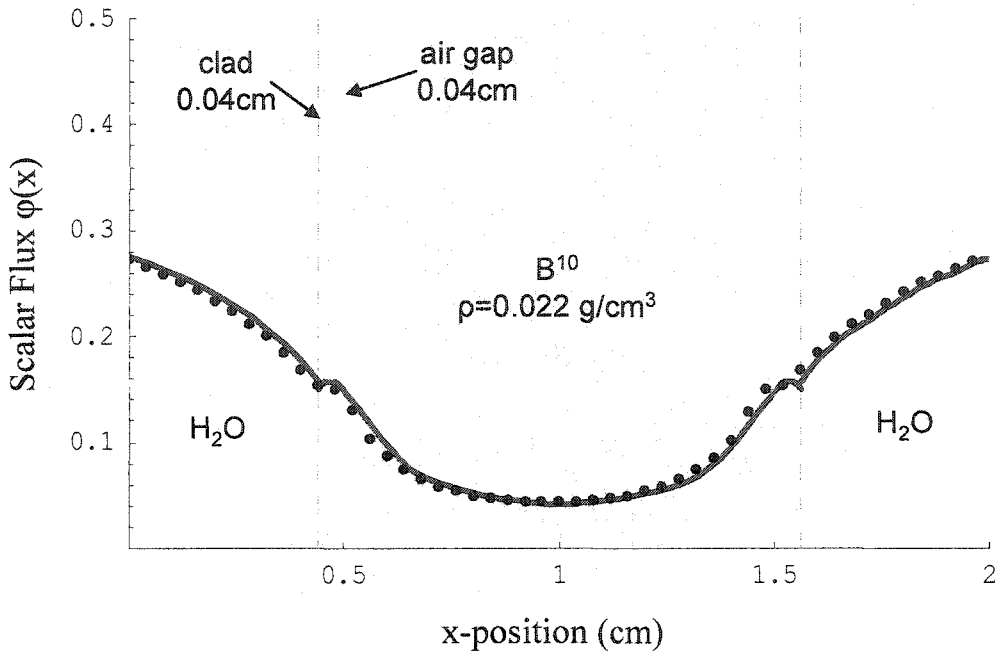

Figure 4.7. Results from a 100,000 history simulation showing a three region piecewise Legendre FET approximation to the thermal flux distribution across a 1-D boron pin. The black dots represent a 50-bin reference histogram solution produced from the same simulation. The dashed lines located near x = 0.5 cm and x=1.5 cm show the domain boundaries for the piecewise tallies. The results show that the piecewise FET is able to accurately approximate the kinks that occur in the flux near the material boundaries.

more accurate approximation than would be possible with a single, global, expansion. There is, however, a drawback to using piecewise FET.

Although the piecewise FET approximation shown in Figure 4.7 appears to be continuous, it is not. Closer examination reveals that there are discontinuities in the functional approximations at both of the tally boundaries. These discontinuities arise because the piecewise approach produces a completely independent functional approximation for each tally region. There has, to date, been no attempt to impose any boundary or continuity conditions on the independent tallies. Even though the independent tallies are mathematically discontinuous at the tally edges, for well converged FET approximations the tallies often "appear" to be continuous, as in Figure

4.7. This "natural" continuity arises because each tally gives a good approximation to the true flux distribution in each tally region. Because the true flux is continuous across tally bins, it follows that the functional approximations should nearly match at the boundaries. This line of reasoning, however, only holds if the FET approximations in each tally region are accurate (i.e. small statistical and truncation errors). If the individual functional approximations are poorly converged, then the resulting piecewise approximation will appear noisy and discontinuous. This fact can be used as a rough gage of the quality and accuracy of a piecewise fit. Any approximation that appears continuous at the tally boundaries is probably well-converged, while those that are noticeably discontinuous require more particle histories, a higher expansion order, or both.

In order to demonstrate this informal test for convergence, piecewise Legendre approximations for the thermal flux distribution over the entire lattice were generated using Monte Carlo k-code simulations of 2,000 and 100,000 neutron histories. The resulting approximations are shown in Figure 4.8 and Figure 4.9, respectively. For the 100,000 history simulation, Figure 4.9, the resulting approximation appears to be continuous across all of the tally boundaries. This approximation appears to be an accurate estimate of the flux across the lattice, a fact confirmed in the boron pin by Figure 4.7. The piecewise approximation from the 2,000 history simulation (Figure 4.8), on the other hand, does not appear to be continuous across tally boundaries. While the approximation gets the general shape of the flux correct, there appears to be a significant amount of statistical noise. In this case it is clear that more particles are needed to produce an accurate estimate of the true flux distribution.

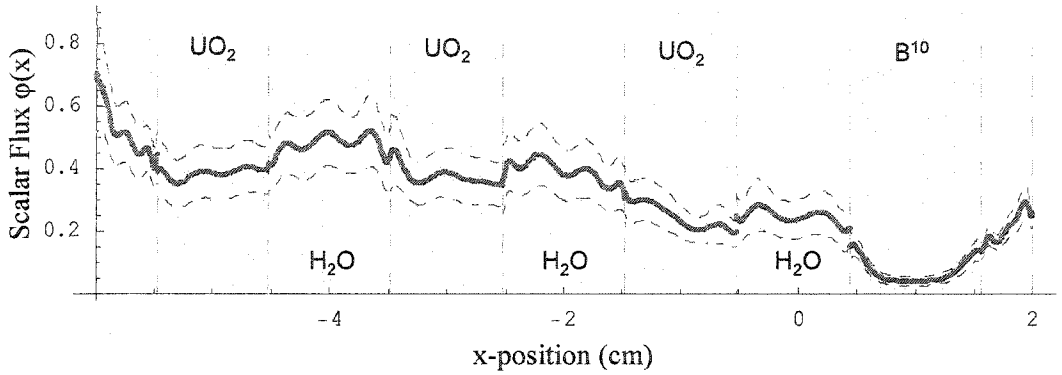

Figure 4.8. Results from a 2,000 history simulation showing a nine region piecewise Legendre FET approximation to the thermal flux distribution across a 1-D fuel/poison lattice. The vertical dashed lines show the domain boundaries for the piecewise tallies. The unphysical, higher-mode oscillations in each tally region indicate significant statistical error in the final solution. The FET approximation also exhibits obvious discontinuities near some of the tally boundaries.

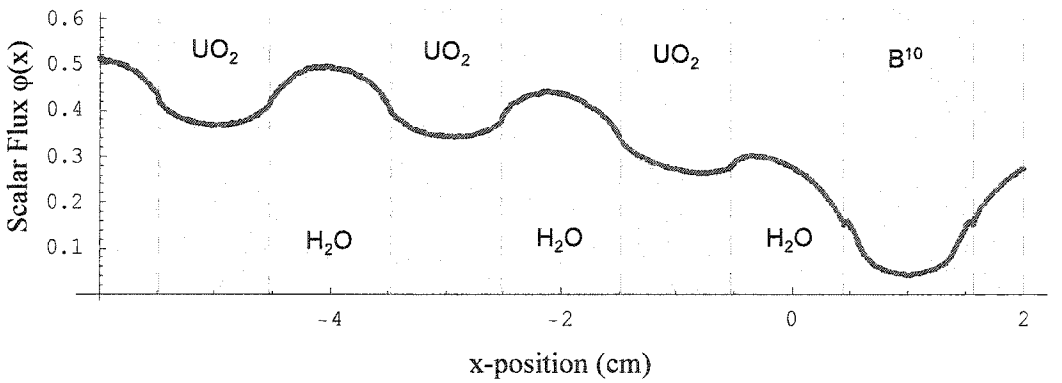

Figure 4.9. Results from a 100,000 history simulation showing a nine region piecewise Legendre FET approximation to the thermal flux distribution across a 1-D fuel/poison lattice. The vertical dashed lines show the domain boundaries for the piecewise tallies. In this case the piecewise FET approximations appear nearly continuous across tally boundaries, indicating that the result is statistically well converged.

4.4. Derivation of 2-D and 3-D Track Length FET Estimators

The derivations for the two- and three-dimensional track length FET estimators are similar to the derivation for the 1-D estimator. In fact, the one-, two-, and three-dimensional estimators all look very similar. Unfortunately, the higher dimension estimators require significantly more work than the 1-D estimator. This added work stems from the fact that multi-dimensional expansions contain many more expansion coefficients, and each of these coefficients becomes computationally more expensive to estimate in higher dimensions.

4.4.1. Multi-Dimension Orthogonal Basis Sets

As always, the derivation of the FET estimators begins with the selection of an orthogonal set of basis functions that are complete over the phase volume of the tally. Most multi-dimensional sets of orthogonal basis functions are created by taking product sets of 1-D orthogonal basis functions. The use of product basis sets simplifies the derivation and implementation of the multi-dimensional FET estimators by allowing theoretical results and algorithms developed for 1-D basis functions to be reused.

Consider three sets of orthogonal functions, $\{\psi_l(x)\}_{l=0}^{\infty}$, $\{\psi_m(y)\}_{m=0}^{\infty}$, and $\{\psi_n(z)\}_{n=0}^{\infty}$, that are complete over the x, y, and z spatial dimensions, respectively. It follows that the product set, $\{\psi_l(x)\psi_m(y)\psi_n(z)\}_{l,m,n=0}^{\infty}$, is complete over $\mathbb{R}^3$ and that each member is orthogonal to all of the other functions in the set. Since this set is

complete over $\mathbb{R}^3$, it is possible to expand any function $f(x,y,z)$ in this space in terms of a series expansion,

$$f(x,y,z) = \sum_{l=0}^{\infty}\sum_{m=0}^{\infty}\sum_{n=0}^{\infty} \bar{a}_{l,m,n}\, k_{l,m,n}\, \psi_l(x)\psi_m(y)\psi_n(z). \tag{4.27}$$

As in 1-D, the orthogonality of the functions can be used to solve for the expansion coefficients,

$$\bar{a}_{l,m,n} = \int_{\Gamma_x}\int_{\Gamma_y}\int_{\Gamma_z} f(x,y,z)\psi_l(x)\psi_m(y)\psi_n(z)\,dx\,dy\,dz. \tag{4.28}$$

In order to simplify the notation, we have assumed that the functions in each basis set are orthogonal with respect to the weighting function $\rho(\cdot)=1$. All of the results that follow can be generalized to hold for basis sets that are orthogonal with respect to an arbitrary weighting function, but this generalization clutters the derivations without adding any useful information.

By far, the largest challenge in implementing and using multidimensional FET is calculating and storing the large number of terms required for each tally region. The amount of information that must be stored becomes large in higher dimensions because the number of expansion coefficients (for a given order expansion) grows exponentially with the dimensionality of the problem. It has previously been shown that, in 1-D, a 9th order Legendre expansion is usually sufficient to produce an accurate approximation. The 9th order approximation itself requires the calculation of 10 expansion coefficients, while a functional variance estimate requires the calculation of an additional 100 covariance terms. While keeping track of 110 terms per tally region is manageable, the number of terms increases to 10,100 terms in two-dimensions, and 10,010,000 terms for a full 3-D expansion. Fortunately, these numbers can be reduced considerably if the 2-

norm measure of the variance (Eq. (2.34)) is used instead of the full functional variance (20 terms for 1-D, 200 terms for 2-D, and 2000 terms for 3-D). The 2-norm of the variance provides an accurate measure of the aggregate amount of statistical uncertainty in an FET approximation, but it does not provide any information about the uncertainty at a single point within the tally region. Even if the 2-norm variance estimate is used, a fully coupled 3-D functional approximation will still require about 2000 terms to be stored for each tally region. This is still a lot of information to store per tally, but there is no way to reduce the number of stored terms further without risking a potential loss in accuracy.

4.4.2. Separable FET Expansions in 2-and 3-D

Before considering the fully coupled FET estimators, it is worth mentioning that there are certain classes of 2- and 3-dimensional problems that do not require a fully coupled, multi-dimensional expansion. In cases where the solution function $\phi(x,y,z)$ is separable,

$$\phi(x,y,z) = f(x)g(y)h(z), \tag{4.29}$$

a functional approximation can be constructed from three separate 1-D approximations rather than a single, fully coupled 3-D approximation. The advantage of this separable FET method is a significant reduction in the number of expansion coefficients required per tally (~30 coefficients for the separable FET versus 1,000 for the fully coupled). While there are some problems in particle transport that have a separable spatial flux distribution (e.g. certain purely absorbing problems), most realistic problems do not have separable solutions. However, numerical experiments have shown that the separable FET

appears to give a rough approximation for non-separable distributions, and does so for a fraction of the computational cost of the fully coupled solution. It is therefore likely that the separable FET has some merit, so a short derivation and explanation of the method will be included here.

The derivation begins by considering a two-dimensional flux distribution defined over a tally region $\{(x,y)\,|\,x\in[x_0,x_1],\,y\in[y_0,y_1]\}$. Furthermore, we assume that the flux distribution is separable and can be written as

$$\phi(x,y)=f(x)g(y). \tag{4.30}$$

From Eq. (4.27) it follows that the flux distribution can be approximated by a finite expansion in a suitable set of orthogonal basis functions,

$$\phi(x,y,z)\approx\sum_{m=0}^{M}\sum_{n=0}^{M'}\overline{a}_{m,n}\,k_{m,n}\,\psi_m(x)\psi_n(y). \tag{4.31}$$

Now, define two additional functions $F(x)$ and $G(y)$ as the transverse integrated one-dimensional fluxes

$$\begin{aligned} F(x)&=\int_{y_0}^{y_1}\phi(x,y)\,dy=f(x)\int_{y_0}^{y_1}g(y)\,dy\\ G(y)&=\int_{x_0}^{x_1}\phi(x,y)\,dx=g(y)\int_{x_0}^{x_1}f(x)\,dx. \end{aligned} \tag{4.32}$$

Because the functions $F(x)$ and $G(y)$ are continuous, well-behaved, functions they can also be expanded in terms of the orthogonal basis functions,

$$\begin{aligned} F(x)&=\sum_{m=0}^{M}\overline{a}_{x,m}\,k_m\,\psi_m(x)\\ G(y)&=\sum_{n=0}^{M'}\overline{a}_{y,n}\,k_n\,\psi_n(y). \end{aligned} \tag{4.33}$$

The coefficients $\overline{a}_{x,m}$ and $\overline{a}_{y,n}$ can be estimated using the 1-D track length estimator given in Eq. (4.18). In order to relate the transverse integrated flux expansions (Eq. (4.33)) to the 2-dimensional expansion (Eq. (4.31)), we start by multiplying $F(x)$ and $G(y)$ together

$$F(x)G(y) = \left(f(x)\int_{y_0}^{y_1} g(y)\,dy\right)\left(g(y)\int_{x_0}^{x_1} f(x)\,dx\right). \tag{4.34}$$

By the definition of the flux distribution, Eq. (4.30), it follows that

$$\begin{aligned} F(x)G(y) &= f(x)g(y)\left(\int_{y_0}^{y_1} g(y)\,dy\right)\left(\int_{x_0}^{x_1} f(x)\,dx\right) \\ &= \phi(x,y)\left(\int_{x_0}^{x_1}\int_{y_0}^{y_1} f(x)g(y)\,dy\,dx\right). \end{aligned} \tag{4.35}$$

Rearranging Eq. (4.35) to solve for $\phi(x,y)$ gives

$$\phi(x,y) \approx \frac{F(x)G(y)}{\int_{x_0}^{x_1}\int_{y_0}^{y_1} f(x)g(y)\,dy\,dx}. \tag{4.36}$$

If the basis sets are normalized such that $\psi_0(x) = \psi_0(y) = 1$, then Eq. (4.36) can simplify further to yield

$$\phi(x,y) \approx \frac{F(x)G(y)}{\overline{a}_{0,0}}. \tag{4.37}$$

Substituting the series expansions (Eqs. (4.33)) in for $F(x)$ and $G(y)$ gives

$$\phi(x,y) \approx \frac{\left(\sum_{m=0}^{M} \overline{a}_{x,m} k_m \psi_m(x)\right)\left(\sum_{n=0}^{M'} \overline{a}_{y,n} k_n \psi_n(y)\right)}{\overline{a}_{0,0}},$$

$$\phi(x,y) \approx \frac{\sum_{m=0}^{M}\sum_{n=0}^{M'} \overline{a}_{x,m}\overline{a}_{y,n} k_n k_m \psi_m(x)\psi_n(y)}{\overline{a}_{0,0}}. \tag{4.38}$$

By inspection of Eqs. (4.38) and (4.31) it is trivial to see that

$$\begin{aligned} \bar{a}_{m,n} &= \bar{a}_{x,m}\,\bar{a}_{y,n} \\ k_{m,n} &= \frac{k_n\,k_m}{\bar{a}_{0,0}}, \end{aligned} \tag{4.39}$$

in the original expansion. It was established previously that the coefficients $\bar{a}_{x,m}$ and $\bar{a}_{y,n}$ can be estimated by the 1-D track length estimators, denoted $\hat{a}_{x,m}$ and $\hat{a}_{y,n}$. Substituting these estimated coefficients directly into Eq. (4.39) gives the separable FET estimator for the expansion coefficients

$$\begin{aligned} \hat{a}_{m,n} &= \hat{a}_{x,m}\,\hat{a}_{y,n} \\ k_{m,n} &= \frac{k_n\,k_m}{\hat{a}_{0,0}}. \end{aligned} \tag{4.40}$$

Notice that by assuming separability in the solution function, only $M+M'$ terms need to be estimated during the simulation, as compared to the $M\times M'$ terms required for the fully coupled two-dimensional expansion.

To be completely thorough, it must be noted that the coefficient estimator given in Eq. (4.40) will be unbiased only if the estimates $\hat{a}_{x,m}$ and $\hat{a}_{y,n}$ are statistically independent. If these estimates are produced from a single simulation, then they are not statistically independent and the correlation between the estimates must be taken into account. In this case the "corrected" separable FET coefficient estimators are given by

$$\begin{aligned} \hat{a}_{m,n} &= \hat{a}_{x,m}\,\hat{a}_{y,n} + \hat{\sigma}_{\hat{a}_{x,m}\hat{a}_{y,n}} \\ k_{m,n} &= \frac{k_n\,k_m}{\hat{a}_{0,0}}, \end{aligned} \tag{4.41}$$

where $\hat{\sigma}_{\hat{a}_{x,m}\hat{a}_{y,n}}$ is the sample covariance between the estimates $\hat{a}_{x,m}$ and $\hat{a}_{y,n}$. Unfortunately, this correction requires the estimation of the covariance for each pair of

estimated coefficients. Evaluating this covariance matrix would require the calculation and storage of an additional $M \times M'$ terms; exactly the number of terms that the separable FET method was seeking to eliminate. Therefore, for distributions that are known to be non-separable, a fully coupled FET approximation should be used instead of attempting to correct the separable FET for statistical correlation.

4.4.3. Coupled FET Expansions in Multiple Dimensions

In cases where a separable FET approximation is not sufficient, a fully coupled multi-dimensional FET approximation is required. In order to derive the coupled FET estimators, we begin by considering a three-dimensional tally volume defined over the space

$$\left\{(x,y,z) \mid x \in [x_0, x_1], y \in [y_0, y_1], z \in [z_0, z_1]\right\}. \tag{4.42}$$

It follows from Eqs. (4.27) and (4.28) that any function defined over this space (in this case the scalar flux) can be expanded in terms of an orthogonal set of basis functions

$$\phi(x,y,z) = \sum_{l=0}^{\infty}\sum_{m=0}^{\infty}\sum_{n=0}^{\infty} \bar{a}_{l,m,n}\, k_{l,m,n}\, \psi_l(x)\psi_m(y)\psi_n(z), \tag{4.43}$$

where the expansion coefficients are given by

$$\bar{a}_{l,m,n} = \int_{\Gamma_x}\int_{\Gamma_y}\int_{\Gamma_z} \phi(x,y,z)\psi_l(x)\psi_m(y)\psi_n(z)\,dx\,dy\,dz. \tag{4.44}$$

To proceed, we conceptually divide the tally domain into P, Q, and R equally spaced partitions in the x, y, and z directions, respectively. With these partitions, Eq. (4.44) can then be written

$$\bar{a}_{l,m,n} = \sum_{p=1}^{P}\int_{x_p}^{x_{p+1}}\sum_{q=1}^{Q}\int_{y_q}^{y_{q+1}}\sum_{r=1}^{R}\int_{y_r}^{y_{r+1}} \phi(x,y,z)\psi_l(x)\psi_m(y)\psi_n(z)\,dy\,dx\,dz,$$

$$\bar{a}_{l,m,n} = \sum_{p=1}^{P}\sum_{q=1}^{Q}\sum_{r=1}^{R}\int_{x_p}^{x_{p+1}}\int_{y_q}^{y_{q+1}}\int_{y_r}^{y_{r+1}}\phi(x,y,z)\psi_l(x)\psi_m(y)\psi_n(z)\,dy\,dx\,dz\,. \tag{4.45}$$

If the widths of the partitions, Δx_p, Δy_q, and Δz_r are small, then it is reasonable to approximate the value of each basis function in a partition by the value of the function evaluated at the midpoint of the cell,

$$\psi_l(x) = \psi_l(x_{p+1/2}) + O(\Delta x_p) \text{ for } x \in [x_p, x_{p+1}]. \tag{4.46}$$

Substituting Eq. (4.46) into Eq. (4.45) gives

$$\begin{aligned}\bar{a}_{l,m,n} = \sum_{p=1}^{P}\sum_{q=1}^{Q}\sum_{r=1}^{R}\Big[&\psi_l(x_{p+1/2})\psi_m(y_{q+1/2})\psi_n(z_{r+1/2}) \\ &\times\int_{x_p}^{x_{p+1}}\int_{y_q}^{y_{q+1}}\int_{z_r}^{z_{r+1}}\phi(x,y,z)\,dy\,dx\,dz \\ &+O(\Delta x_p^2)+O(\Delta y_q^2)+O(\Delta z_r^2)+\ldots\Big]\end{aligned} \tag{4.47}$$

The higher order terms in Eq. (4.47) can all be omitted, because they will all become zero when the limits Δx_p, Δy_q, and $\Delta z_r \to 0$ are applied,

$$\begin{aligned}\bar{a}_{l,m,n} = \sum_{p=1}^{P}\sum_{q=1}^{Q}\sum_{r=1}^{R}\Big[&\psi_l(x_{p+1/2})\psi_m(y_{q+1/2})\psi_n(z_{r+1/2}) \\ &\times\int_{x_p}^{x_{p+1}}\int_{y_q}^{y_{q+1}}\int_{z_r}^{z_{r+1}}\phi(x,y,z)\,dy\,dx\,dz\Big].\end{aligned} \tag{4.48}$$

The last term in Eq. (4.48) is the integrated scalar flux taken over the (p,q,r) partition volume. By Eq. (1.61), this quantity can also be interpreted as the total amount of track length generated by all particles passing through this small volume element, D_{pqr},

$$D_{pqr} = \int_{x_p}^{x_{p+1}}\int_{y_q}^{y_{q+1}}\int_{z_r}^{z_{r+1}}\phi(x,y,z)\,dy\,dx\,dz\,. \tag{4.49}$$

It was shown previously (Eq. (1.63)) that an unbiased estimator for D_{pqr} exists and is given by the statistic

$$\hat{D}_{p,q,r} = \frac{1}{N}\sum_{i=1}^{N}\sum_{c=1}^{C_i} d_{i,c,p,q,r}\, w_{i,c}\,, \tag{4.50}$$

where N is the total number of particles started, C_i is the total number of events (collision, surface crossing, etc) where the i^{th} particle can change direction, $w_{i,c}$ is the weight of the particle and $d_{i,c,p,q,r}$ is the path length traveled in element (p,q,r) by particle i as it travels between events c and $c+1$. Substituting Eq. (4.50) into (4.47) yields an estimator for the coefficient $\overline{a}_{l,m,n}$,

$$\hat{a}_{l,m,n} = \sum_{p=1}^{P}\sum_{q=1}^{Q}\sum_{r=1}^{R}\Big[\psi_l\left(x_{p+1/2}\right)\psi_m\left(y_{q+1/2}\right)\psi_n\left(z_{r+1/2}\right) \times\frac{1}{N}\sum_{i=1}^{N}\sum_{c=1}^{C_i} d_{i,c,p,q,r}\, w_{i,c}\Big]. \tag{4.51}$$

Equation (4.51) can be rearranged to yield

$$\hat{a}_{l,m,n} = \frac{1}{N}\sum_{i=1}^{N}\sum_{c=1}^{C_i} w_{i,c}\sum_{p=1}^{P}\sum_{q=1}^{Q}\sum_{r=1}^{R}\Big[\psi_l\left(x_{p+1/2}\right)\psi_m\left(y_{q+1/2}\right)\psi_n\left(z_{r+1/2}\right) d_{i,c,p,q,r}\Big]. \tag{4.52}$$

Taking the limit of the right hand side of Eq. (4.52) as Δx_p, Δy_q and $\Delta z_r \to 0$ gives

$$\hat{a}_{lmn} = \frac{1}{N}\sum_{i=1}^{N}\sum_{c=1}^{C_i} w_{i,c}\int_{d_{i,c}} \psi_l(x)\psi_m(y)\psi_n(z)\,ds\,, \tag{4.53}$$

where the integral term is a line integral taken along the path $S_{i,c}$ taken by particle i as it moves between events c and $c+1$. The variable s in the integral, therefore, can have values $\left[0, d_{i,c}\right]$, where $d_{i,c}$ is the total distance between events c to $c+1$. The path integral in Eq. (4.53) can be evaluated by parameterizing x, y, and z in terms of the variable s,

$$\hat{a}_{lmn} = \frac{1}{N}\sum_{i=1}^{N}\sum_{c=1}^{C_i} w_{i,c} \times \int_0^{d_{i,c}} \psi_l\left(x(s)\right)\psi_m\left(y(s)\right)\psi_n\left(z(s)\right)\sqrt{\left(\frac{dx}{ds}\right)^2+\left(\frac{dy}{ds}\right)^2+\left(\frac{dz}{ds}\right)^2}\, ds. \tag{4.54}$$

Because a particle can only change direction at an event c, the path a particle follows between events c and $c+1$ is a straight line between the points $\left(x_{i,c}, y_{i,c}, z_{i,c}\right) = \left(x(0), y(0), z(0)\right)$ and $\left(x_{i,c+1}, y_{i,c+1}, z_{i,c+1}\right) = \left(x(d_{i,c}), y(d_{i,c}), z(d_{i,c})\right)$. As the particle travels, it has direction $\Omega_{i,c} = \left(\mu, \varphi, \rho\right)_{i,c}$, where $\mu_{i,c}$, $\varphi_{i,c}$, and $\rho_{i,c}$ are the directional cosines in the x, y, and z directions, respectively.

Because the particle path between events is linear, it is possible to further parameterize two of the spatial variables in terms of the third. For example, the variables y and z can both be written as a function of x:

$$\begin{aligned} y &= \frac{\varphi_{i,c}}{\mu_{i,c}}\left(x - x_{i,c}\right) + y_{i,c}, \\ dy &= \frac{\varphi_{i,c}}{\mu_{i,c}}\, dx, \end{aligned} \tag{4.55}$$

and

$$\begin{aligned} z &= \frac{\varphi_{i,c}}{\rho_{i,c}}\left(x - x_{i,c}\right) + z_{i,c}, \\ dz &= \frac{\varphi_{i,c}}{\rho_{i,c}}\, dx. \end{aligned} \tag{4.56}$$

Using this parameterization, Eq. (4.54) can be rewritten as

$$\hat{a}_{l,m,n} = \frac{1}{N}\sum_{i=1}^{N}\sum_{c=1}^{C_i} w_{i,c} \int_0^{d_{i,c}} \psi_l\left(x(s)\right)\psi_m\left(\frac{\varphi_{i,c}}{\mu_{i,c}}\left(x(s) - x_{i,c}\right) + y_{i,c}\right) \times \psi_n\left(\frac{\varphi_{i,c}}{\rho_{i,c}}\left(x(s) - x_{i,c}\right) + z_{i,c}\right)\sqrt{\left(\frac{dx}{ds}\right)^2+\left(\frac{\varphi_{i,c}}{\mu_{i,c}}\frac{dx}{ds}\right)^2+\left(\frac{\varphi_{i,c}}{\rho_{i,c}}\frac{dx}{ds}\right)^2}\, ds,$$

$$\hat{a}_{l,m,n} = \frac{1}{N}\sum_{i=1}^{N}\sum_{c=1}^{C_i} w_{i,c}\int_0^{d_{i,c}} \psi_l\left(x(s)\right)\psi_m\left(\frac{\varphi_{i,c}}{\mu_{i,c}}\left(x(s)-x_{i,c}\right)+y_{i,c}\right) \times\psi_n\left(\frac{\varphi_{i,c}}{\rho_{i,c}}\left(x(s)-x_{i,c}\right)+z_{i,c}\right)\sqrt{1+\left(\frac{\varphi_{i,c}}{\mu_{i,c}}\right)^2+\left(\frac{\varphi_{i,c}}{\rho_{i,c}}\right)^2}\,\frac{dx}{ds}\,ds. \tag{4.57}$$

Equation (4.57) now depends only on x, and following a change in the limits of integration can be simplified to yield

$$\hat{a}_{lmn} = \frac{1}{N}\sum_{i=1}^{N}\sum_{c=1}^{C_i} w_{i,c}\sqrt{1+\left(\frac{\varphi_{i,c}}{\mu_{i,c}}\right)^2+\left(\frac{\varphi_{i,c}}{\rho_{i,c}}\right)^2} \times\int_{x_{i,c}}^{x_{i,c+1}}\psi_l\left(x\right)\psi_m\left(\frac{\varphi_{i,c}}{\mu_{i,c}}\left(x-x_{i,c}\right)+y_{i,c}\right)\psi_n\left(\frac{\varphi_{i,c}}{\rho_{i,c}}\left(x-x_{i,c}\right)+z_{i,c}\right)dx. \tag{4.58}$$

While it is possible to evaluate Eq. (4.58) directly, it is convenient to simplify the radical factor in front of the integral through some algebraic manipulations. These simplifications begin by multiplying and dividing the factor by the constant $d_{n,k}\left(x_{n,k+1}-x_{n,k}\right)$,

$$\sqrt{1+\left(\frac{\varphi_{i,c}}{\mu_{i,c}}\right)^2+\left(\frac{\varphi_{i,c}}{\rho_{i,c}}\right)^2} = \frac{d_{n,k}\left(x_{n,k+1}-x_{n,k}\right)}{d_{n,k}\left(x_{n,k+1}-x_{n,k}\right)}\sqrt{1+\left(\frac{\varphi_{i,c}}{\mu_{i,c}}\right)^2+\left(\frac{\varphi_{i,c}}{\rho_{i,c}}\right)^2}$$

$$= \frac{d_{i,c}}{\left(x_{i,c+1}-x_{i,c}\right)} \times\sqrt{\left(\frac{\left(x_{i,c+1}-x_{i,c}\right)}{d_{i,c}}\right)^2+\left(\frac{\left(x_{i,c+1}-x_{i,c}\right)}{d_{i,c}}\frac{\varphi_{i,c}}{\mu_{i,c}}\right)^2+\left(\frac{\left(x_{i,c+1}-x_{i,c}\right)}{d_{i,c}}\frac{\rho_{i,c}}{\mu_{i,c}}\right)^2}. \tag{4.59}$$

From basic trigonometry it is easy to show

$$\mu_{i,c} = \left(\frac{\left(x_{i,c+1}-x_{i,c}\right)}{d_{i,c}}\right). \tag{4.60}$$

Substituting Eq. (4.60) into Eq. (4.59) yields

$$\sqrt{1+\left(\frac{\varphi_{i,c}}{\mu_{i,c}}\right)^2+\left(\frac{\varphi_{i,c}}{\rho_{i,c}}\right)^2}=\frac{d_{i,c}}{\left(x_{i,c+1}-x_{i,c}\right)}\sqrt{\left(\mu_{i,c}\right)^2+\left(\varphi_{i,c}\right)^2+\left(\rho_{i,c}\right)^2},$$

$$\sqrt{1+\left(\frac{\varphi_{i,c}}{\mu_{i,c}}\right)^2+\left(\frac{\varphi_{i,c}}{\rho_{i,c}}\right)^2}=\frac{d_{i,c}}{\left(x_{i,c+1}-x_{i,c}\right)}\left\|\Omega_{i,c}\right\|,$$

$$\sqrt{1+\left(\frac{\varphi_{i,c}}{\mu_{i,c}}\right)^2+\left(\frac{\varphi_{i,c}}{\rho_{i,c}}\right)^2}=\frac{d_{i,c}}{\left(x_{i,c+1}-x_{i,c}\right)}. \tag{4.61}$$

Finally, substituting Eq. (4.61) into Eq. (4.58) gives a final result for the 2-D track length FET estimator

$$\hat{a}_{l,m,n}=\frac{1}{N}\sum_{i=1}^{N}\sum_{c=1}^{C_i}\frac{w_{i,c}\,d_{i,c}}{\left(x_{i,c+1}-x_{i,c}\right)}\times\int_{x_{i,c}}^{x_{i,c+1}}\psi_l\left(x\right)\psi_m\left(\frac{\varphi_{i,c}}{\mu_{i,c}}\left(x-x_{i,c}\right)+y_{i,c}\right)\psi_n\left(\frac{\varphi_{i,c}}{\rho_{i,c}}\left(x-x_{i,c}\right)+z_{i,c}\right)dx. \tag{4.62}$$

This estimator was derived by parameterizing both the y and z directions. There are two other possible parameterizations that could have been used in place of Eqs. (4.55) and (4.56). If the path length is parameterized in terms of y or z, the corresponding estimators are given by

$$\hat{a}_{l,m,n}=\frac{1}{N}\sum_{i=1}^{N}\sum_{c=1}^{C_i}\frac{w_{i,c}\,d_{i,c}}{\left(y_{i,c+1}-y_{i,c}\right)}\times\int_{y_{i,c}}^{y_{i,c+1}}\psi_l\left(\frac{\mu_{i,c}}{\varphi_{i,c}}\left(y-y_{i,c}\right)+x_{i,c}\right)\psi_m\left(y\right)\psi_n\left(\frac{\mu_{i,c}}{\rho_{i,c}}\left(y-y_{i,c}\right)+z_{i,c}\right)dy, \tag{4.63}$$

and

$$\hat{a}_{l,m,n} = \frac{1}{N}\sum_{i=1}^{N}\sum_{c=1}^{C_i}\frac{w_{i,c}\,d_{i,c}}{\left(z_{i,c+1}-z_{i,c}\right)} \times \int_{z_{i,c}}^{z_{i,c+1}} \psi_l\left(\frac{\rho_{i,c}}{\varphi_{i,c}}\left(z-z_{i,c}\right)+x_{i,c}\right)\psi_m\left(\frac{\rho_{i,c}}{\mu_{i,c}}\left(z-z_{i,c}\right)+y_{i,c}\right)\psi_n(z)\,dz, \tag{4.64}$$

respectively. Any of these estimators will produce an unbiased estimate for the expansion coefficient. As a general rule of thumb, it is useful to select a parameterization based on the dominant direction of particle motion for each path in the particle's lifetime. For example, if a particle moving between two successive events travels further in the y direction than in either the x or z directions, then it is best to choose Eq. (4.63) as the estimator for that path length. This rule of thumb prevents the denominator in the estimator from ever becoming zero as long as $d_{i,c}$ is non zero.

The 3-D estimators derived above can also be used for one- and two-dimensional functional expansions as well. In order to obtain the two-dimensional estimators, we simply recognize that a 2-D basis set $\{\psi_l(x)\psi_m(y)\}_{m,n=0}^{\infty}$ can be written in terms of an incomplete 3-D basis set,

$$\{\psi_l(x)\psi_m(y)\}_{m,n=0}^{\infty} = \{\psi_l(x)\psi_m(y)\psi_0(z)\}_{m,n=0}^{\infty}. \tag{4.65}$$

Substituting $\psi_n(z)=\psi_0(z)$ into Eq. (4.62) gives the two-dimensional estimator

$$\hat{a}_{l,m} = \frac{1}{N}\sum_{i=1}^{N}\sum_{c=1}^{C_i}\frac{w_{i,c}\,d_{i,c}}{\left(x_{i,c+1}-x_{i,c}\right)} \times \int_{x_{i,c}}^{x_{i,c+1}} \psi_l(x)\psi_m\left(\frac{\varphi_{i,c}}{\mu_{i,c}}\left(x-x_{i,c}\right)+y_{i,c}\right)dx. \tag{4.66}$$

When the coefficients calculated with Eq. (4.66) are used in a series expansion, the result is a 2-D functional approximation for the transverse integrated scalar flux,

$$\hat{\phi}(x,y) = \int_{\Gamma_z} \hat{\phi}(x,y,z)\,dz = \sum_{l=0}^{M}\sum_{m=0}^{M'} \hat{a}_{l,m}\, k_{l,m}\, \psi_l(x)\psi_m(y). \tag{4.67}$$

If this process is repeated for another dimension by letting $\psi_m(y) = \psi_0(y)$, the result is a 1-D estimator,

$$\hat{a}_l = \frac{1}{N}\sum_{i=1}^{N}\sum_{c=1}^{C_i} \frac{w_{i,c}\, d_{i,c}}{\left(x_{i,c+1} - x_{i,c}\right)} \int_{x_{i,c}}^{x_{i,c+1}} \psi_l(x)\,dx, \tag{4.68}$$

which is identical to the result derived in section 4.1. For convenience all of the different track length estimators for one-, two-, and three-dimensions have been listed in Table 4.1, along with some guidelines on when each estimator should be applied.

4.4.4. Implementing the Multidimensional Track Length FET Estimators

By far, the most difficult aspect of implementing the multidimensional track length FET is evaluating the path integrals for the scoring functions. Although these integrals are one-dimensional, they are not in a form that is convenient for numerical evaluation. The integrands found in the scoring functions are usually high order polynomials that are highly-oscillatory, making numerical evaluation of the definite integral impractical. In the case of the 1-D track length estimator a recursion relationship was derived that provided an extremely efficient method for evaluating the integral. Unfortunately, despite repeated attempts, no such recursion relationship was found for the integrals in the multidimensional estimators. The only remaining solution is to use a numerical integration technique to solve the integrals along each path length. The drawback to this approach is that numerical integration schemes are generally computationally expensive, and numerically evaluating an integral each time a particle

Table 4.1. Track Length FET scoring functions for one- two- and three-dimensions. Also included are rules for selecting the appropriate scoring function based on the current direction of a scoring particle. The variables μ, ρ, and φ represent the directional cosines of particle motion in the x-, y-, and z-directions, respectively.

Track Length FET Estimator

$$\hat{a}_{l,m,n} = \frac{1}{N}\sum_{i=1}^{N}\sum_{c=1}^{C_i} S_{i,c,l,m,n}\left(w_{i,c}, d_{i,c}, x_c, x_{c+1}, y_c, y_{c+1}, z_c, z_{c+1}\right)$$

Scoring Functions $S_{i,c,l,m,n}\left(w_{i,c}, d_{i,c}, x_c, x_{c+1}, y_c, y_{c+1}, z_c, z_{c+1}\right) =$	When to Use
Three Dimensional Approximation	
$\frac{w_{i,c}\, d_{i,c}}{\left(x_{i,c+1} - x_{i,c}\right)} \int_{x_{i,c}}^{x_{i,c+1}} \psi_l(x)\psi_m\left(\frac{\varphi_{i,c}}{\mu_{i,c}}\left(x - x_{i,c}\right) + y_{i,c}\right)\psi_n\left(\frac{\varphi_{i,c}}{\rho_{i,c}}\left(x - x_{i,c}\right) + z_{i,c}\right)dx$	$\mu_{i,c} \geq \varphi_{i,c}$ $\mu_{i,c} \geq \rho_{i,c}$
$\frac{w_{i,c}\, d_{i,c}}{\left(y_{i,c+1} - y_{i,c}\right)} \int_{y_{i,c}}^{y_{i,c+1}} \psi_l\left(\frac{\mu_{i,c}}{\varphi_{i,c}}\left(y - y_{i,c}\right) + x_{i,c}\right)\psi_m(y)\psi_n\left(\frac{\mu_{i,c}}{\rho_{i,c}}\left(y - y_{i,c}\right) + z_{i,c}\right)dy$	$\varphi_{i,c} > \mu_{i,c}$ $\varphi_{i,c} \geq \rho_{i,c}$
$\frac{w_{i,c}\, d_{i,c}}{\left(z_{i,c+1} - z_{i,c}\right)} \int_{z_{i,c}}^{z_{i,c+1}} \psi_l\left(\frac{\rho_{i,c}}{\varphi_{i,c}}\left(z - z_{i,c}\right) + x_{i,c}\right)\psi_m\left(\frac{\rho_{i,c}}{\mu_{i,c}}\left(z - z_{i,c}\right) + y_{i,c}\right)\psi_n(z)dz$	$\rho_{i,c} > \mu_{i,c}$ $\rho_{i,c} > \varphi_{i,c}$
Two Dimensional Approximation	
$\frac{w_{i,c}\, d_{i,c}}{\left(x_{i,c+1} - x_{i,c}\right)} \int_{x_{i,c}}^{x_{i,c+1}} \psi_l(x)\psi_m\left(\frac{\varphi_{i,c}}{\mu_{i,c}}\left(x - x_{i,c}\right) + y_{i,c}\right)dx$	$\mu_{i,c} \geq \varphi_{i,c} > 0$
$\frac{w_{i,c}\, d_{i,c}}{\left(y_{i,c+1} - y_{i,c}\right)} \int_{y_{i,c}}^{y_{i,c+1}} \psi_l\left(\frac{\mu_{i,c}}{\varphi_{i,c}}\left(y - y_{i,c}\right) + x_{i,c}\right)\psi_m(y)dy$	$\varphi_{i,c} > \mu_{i,c} > 0$
$w_{i,c}\, d_{i,c}\, \psi_l(x)\psi_m(y)$	$\mu_{i,c} = \varphi_{i,c} = 0$
One Dimensional Approximation	
$\frac{w_{i,c}\, d_{i,c}}{\left(x_{i,c+1} - x_{i,c}\right)} \int_{x_{i,c}}^{x_{i,c+1}} \psi_l(x)dx$	$\mu_{i,k} > 0$
$w_{i,c}\, d_{i,c}\, \psi_l(x)$	$\mu_{i,k} = 0$

moves between events can significantly increase the run time for a transport simulation. However, unless a recursion relationship for the integral is found, it appears that numerical evaluation is the only option.

After research into several types of numerical integration schemes, integration by Gaussian quadrature appears to be the most efficient and reliable technique available. Evaluation by Gaussian quadrature has several benefits when used with the FET scoring function. First, Gaussian quadrature can be used to give exact results for the integration of polynomials, which are commonly used as basis functions in the FET. In fact, specific quadrature sets can be derived easily from many of the commonly used basis sets (e.g. Legendre, Chebyshev, Hermite, Laguerre). The size of the quadrature set can be specifically tailored to the FET expansion order to ensure that the integrals are evaluated with the fewest number of calculations possible. Also, the Gaussian quadrature scheme, when coupled with recursion relationships for evaluating basis functions, has proven to be extremely fast when implemented.

The fundamental principle of Gaussian quadrature is that the integral of a function over some domain is equal to a weighted sum of the function evaluated at specific abscissa points within that domain. The Gauss quadrature formula is usually written as[10]

$$\int_{-1}^{1} f(x)\,dx = \sum_{i=1}^{I} w_i f(x_i), \tag{4.69}$$

where w_i are the weights and x_i are the abscissa points. The locations of the abscissa points and the corresponding weights are referred to as a quadrature set. The limits of integration in Eq. (4.69) are shown to be -1 and 1, the standard values. The formula can be generalized to any limits of integration by using the transformation[10]

$$\tilde{x} = \frac{2x - x_{\min} - x_{\max}}{x_{\max} - x_{\min}}. \tag{4.70}$$

As noted previously, Gaussian quadrature is most effective when used to evaluate integrals over polynomials. An I point quadrature set will give the exact integral for any polynomial of order $2I$ or less. Examination of Eqs. (4.66) and (4.62) reveals that the 2- and 3-D estimators contain integrals over polynomials of order $M+M'$, and $M+M'+M''$, respectively. Assuming M, M', and M'' are all taken to be 10 (a reasonable value for most applications), this gives a polynomial order of 20 for 2-D and 30 for 3-D. These orders of approximation would therefore require a 10 and 15 point quadrature set, respectively. In the three dimensional case, this means that each basis polynomial must be evaluated at 15 different locations along every flight path that a particle takes. Although this seems like a large number of calculations, testing has shown that the run times for simulations using the FET with Gaussian quadrature are comparable to those using traditional mesh tallies.

4.5. Numerical Results for the Multidimensional Track Length FET

In order to verify the multidimensional track length FET estimators, a version of the 2-D estimators were implemented in MCNP4c using Legendre polynomials as the expansion basis set. Because the Legendre polynomials are defined only on the domain $[-1,1]$, the code was designed to scale the spatial expansion domain to fit the Legendre domain. The scalar flux distribution over the scaled 2-D region can then be expanded in terms of Legendre polynomials,

$$\hat{\phi}(\tilde{x},\tilde{y}) = \sum_{m=0}^{M}\sum_{n=0}^{M'} \frac{(2m+1)(2n+1)}{4} \hat{a}_{m,n} \psi_m(\tilde{x}) \psi_n(\tilde{y}), \tag{4.71}$$

where $\tilde{x}$ and $\tilde{y}$ are the scaled spatial variables. Once the expansion domain has been appropriately scaled, expansion coefficients can be estimated by scoring the 2-D estimators (given in Table 4.1) during the random walk simulation. The Monte Carlo code evaluates the function $S_{i,k,l,m,n}$ after every particle transport operation and stores the cumulative sum over all histories. After the simulation has finished, this sum is normalized by the number of starting particles to give the final estimate. A 10 point Gauss-Legendre quadrature set was used to evaluate the integral in the function S. This order quadrature allows the code to estimate expansion coefficients up to, and including, $\hat{a}_{9,9}$. The benchmark problem used was a two-dimensional infinite lattice of simulated PWR fuel pins. Each pin cell (Figure 4.10) was modeled as a 1.5% enriched 0.603 cm radius UO_2 pellet surrounded by water. The pin cells were modeled as infinitely long and arranged in a square lattice with a pitch of 1.875cm.

For testing purposes the track length FET estimators were used to create both separable and coupled 2-D functional approximations to the steady-state thermal flux distribution across the face of a pin. For comparison, a 2 million history MCNP5 benchmark eigenvalue calculation was performed using 400 mesh tally regions (20 in the x-direction, 20 in the y-direction) to obtain a direct estimate of the thermal flux distribution over the x-y plane of the pin cell. The results of this simulation are shown in Figure 4.11.

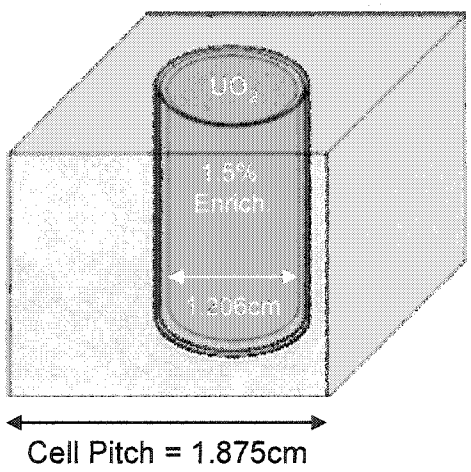

Figure 4.10. Two-dimensional representation of a PWR fuel pin used for benchmark testing. The pin contains a zirconium clad cylinder of 1.5% enriched UO_2 surrounded by water at standard temperature and pressure. Reflecting boundary conditions were applied to all sides of the cell in order to simulate a repeating lattice of infinitely long fuel pins. The calculated eigenvalue for this infinite lattice was 1.026.

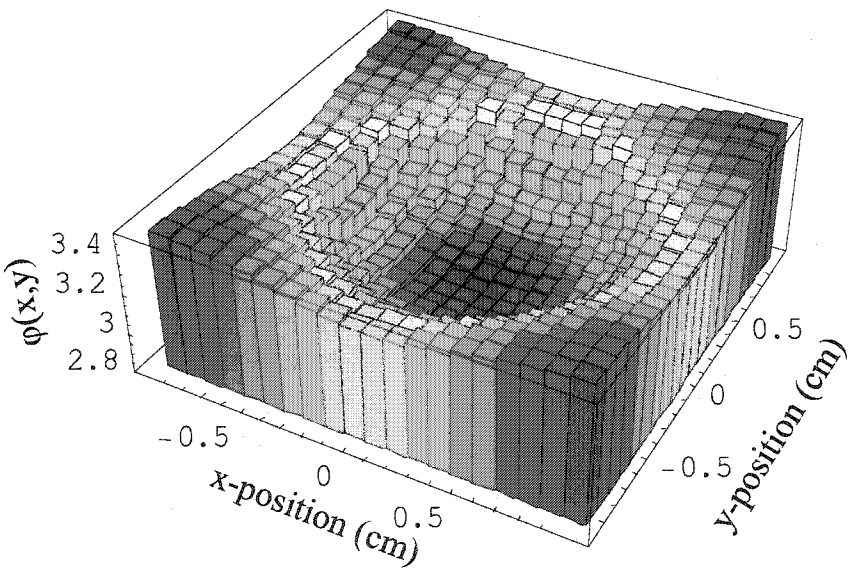

Figure 4.11. Benchmark two-dimensional thermal flux distribution across the face of a PWR fuel pin. Results were generated during a two-million history eigenvalue simulation in MCNP5. A 20×20 bin mesh tally was used to tally the data.

4.5.1. Separable FET Approximation for Thermal Flux Across a PWR Fuel Pin

The first benchmark test used one-dimensional track length estimators to produce ten flux expansion coefficients in the x and y directions during a 2-million history simulation. These 19 one-dimensional coefficients were then used in Eq. (4.40) to produce a complete set of two-dimensional expansion coefficients. These two-dimensional coefficients, in turn, were then used to construct a functional approximation to the thermal flux distribution. The resulting functional approximation is shown in Figure 4.12, along with a mathematically smoothed version of the mesh tally reference distribution. The separable FET approximation is surprisingly good, considering that the flux distribution is not a separable function, and the effect of cross-correlation between the coefficient estimates was neglected. Although the separable expansion captures the general shape of the distribution, there are clearly differences between the FET and reference distributions. The FET approximation overestimates the flux at the corners of the cell and underestimates the flux in the centers of the cell faces. While these qualitative differences are illustrative, a quantitative measure was required in order to directly compare the two methods. However, a direct comparison is difficult because the reference distribution contains discrete data points (histogram approximation), while the FET approximation is a continuous function. In order to obtain a meaningful and qualitative comparison between them, the continuous FET approximation was converted into a histogram by superimposing the MCNP mesh tally grid and then averaging the functional approximation over each mesh tally cell. The results of this FET-to-histogram process are illustrated in Figure 4.14.

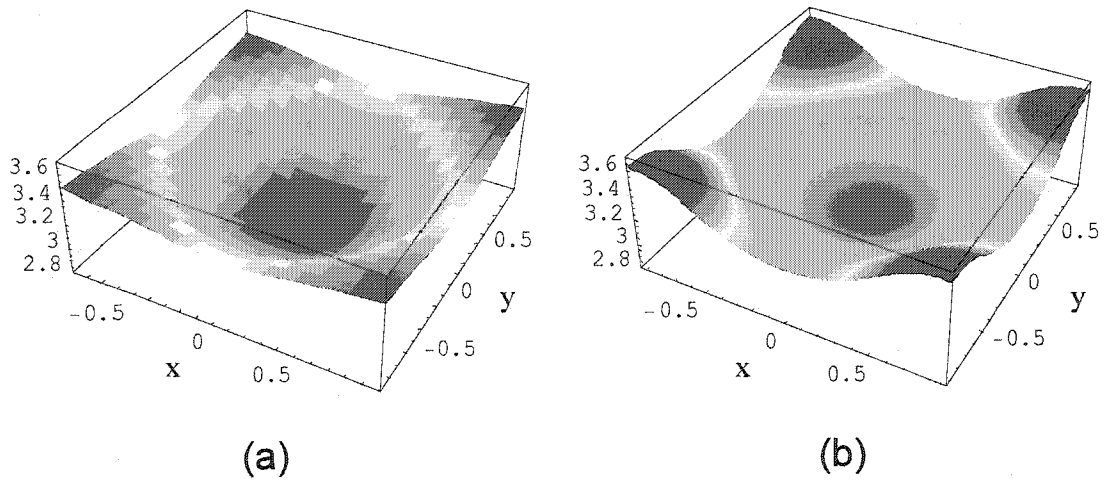

Figure 4.12. Comparison between mesh tally (a) and separable FET (b) approximations to 2-D thermal flux distribution across the face of a PWR fuel pin. The separable FET approximation uses 1-D, 9th order, Legendre expansions in the x- and y- directions to approximate the full 2-D distribution. All 19 FET expansion coefficients were produced in a single 2-million history Monte Carlo simulation. Note that the mesh tally approximation in (a) has been smoothed to allow for a better visual comparison with the continuous FET approximation.

Once the FET approximation was converted into a histogram a direct comparison can be made by calculating the relative difference between cells in the reference and FET solutions. The results of this comparison are shown in Figure 4.14. As the initial observations had indicated, the FET approximation overestimates the flux in the cell corners by nearly 4% and underestimates the flux at in the cell faces by nearly 3%. All of the mesh regions show a relative error of less than 4%, with an average error of 1.62%. The average error was calculated by computing the absolute value of the relative error in each mesh region, and then taking the mean over all 400 regions. These results are surprisingly good for a separable approximation. However, Figure 4.14 shows that there is definitely a structure to the relative error across the pin face. This error indicates that the separable solution is not providing accurate approximations for some of the cross-term expansion coefficients. In order to correct these errors, a coupled FET approximation will be required.

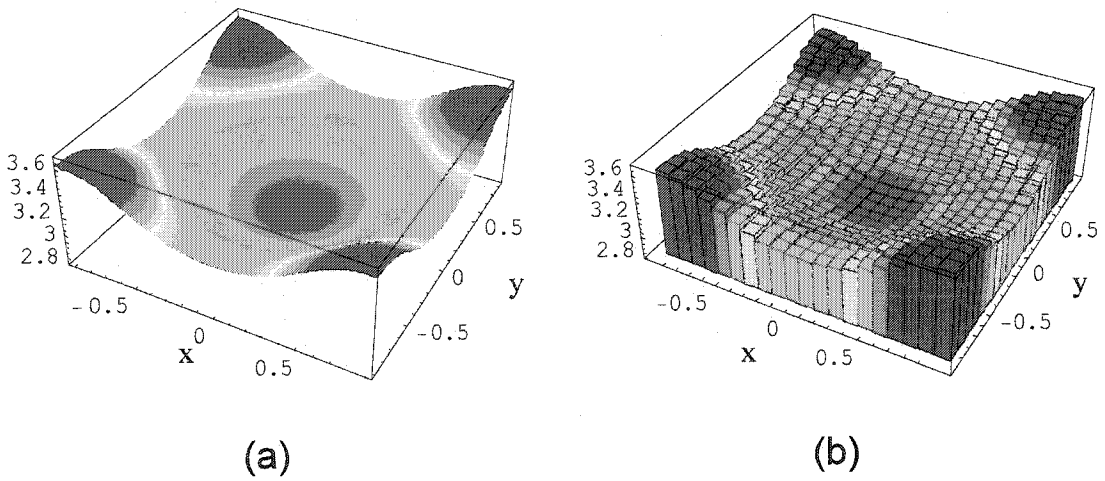

Figure 4.13. Comparison of the 9×9 Legendre FET approximation as a continuous function (a) and after being converted into a histogram. After being converted to a histogram the FET approximation can be directly compared with the reference mesh tally flux distribution shown in Figure 4.11.

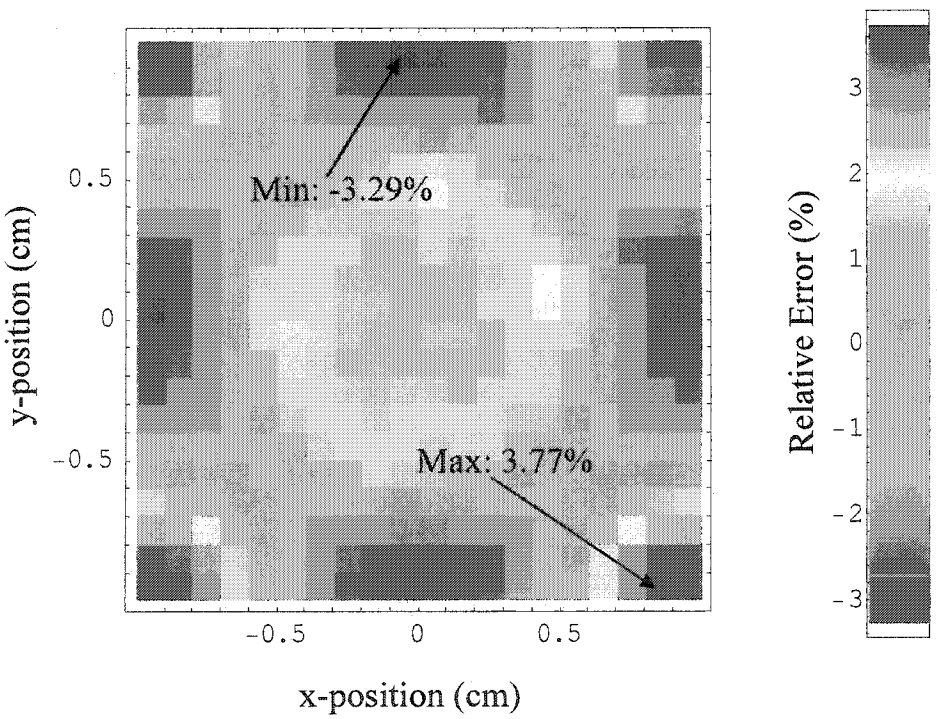

Figure 4.14. Density plot of the error between the separable FET and the reference mesh tally approximations to the spatial flux across the pin face. The average magnitude of error over all of the mesh regions was calculated to be 1.62%. The largest magnitude error is 3.77% and occurs near the center of a water channel.

4.5.2. Coupled FET Approximation for Thermal Flux Across a PWR Fuel Pin

In this test the modified version of MCNP4c was used during a 200-million history simulation to estimate all 100 of the coupled Legendre moments required for a 9×9^{th} order functional expansion across the PWR fuel pin face. These coefficients were then used to construct the fully coupled functional expansion of the thermal flux in the pin cell, shown in Figure 4.15. Once again, by averaging the functional expansion over each of the mesh tally regions defined in the MCNP5 reference solution, a quantitative comparison of the two methods was obtained. Figure 4.16 shows a density plot of the relative difference between the FET and mesh tally approximations across the x-y plane of the fuel pin. These results show that the coupled FET produces a much more accurate solution than the separable approximation. The fully coupled approximation agrees well with the reference solution in the centers of both the fuel region and the coolant channels. The only noticeable error present in this approximation is the slight ~1% disagreement in the behavior of the flux near the fuel-water material interface. This disagreement is due to truncation error, which results from approximating a piecewise smooth function by a finite series Legendre expansion. This is the same behavior that was seen in the 1-D approximations in Figure 4.5. In the one-dimensional case, the solution for overcoming this truncation error was to use a separate piecewise tally in each of the material regions. Unfortunately, due to the shapes of the material regions in this 2-D problem (a circular fuel cell surrounded by a square water cell) it is very difficult to imagine finding a complete set of basis functions for either material.

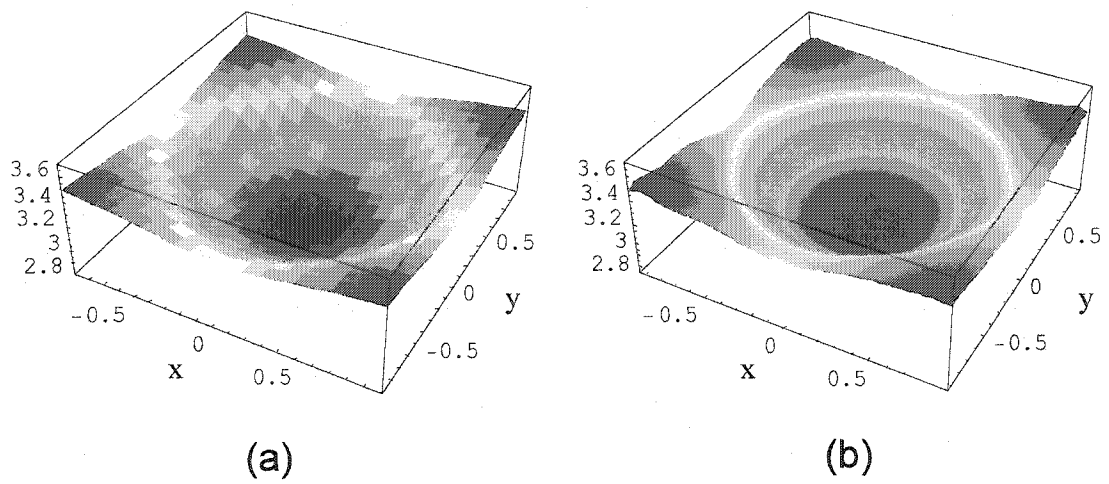

Figure 4.15. Comparison between mesh tally (a) and coupled FET (b) approximations to 2-D thermal flux distribution across the face of a PWR fuel pin. The FET approximation uses coupled 2-D, 9×9 order, Legendre expansions in the x-y plane. All 100 FET expansion coefficients were produced in a single 2-million history Monte Carlo simulation. Note that the mesh tally approximation in (a) has been smoothed to allow for a better visual comparison with the continuous FET approximation.

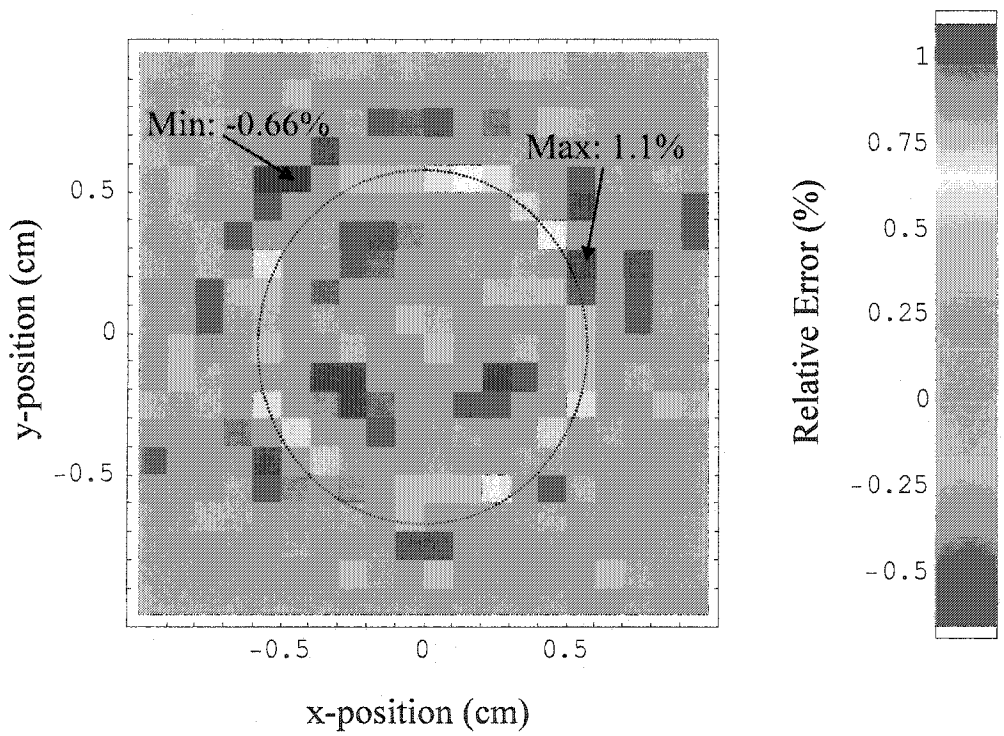

Figure 4.16. Density plot of the error between the coupled FET and the reference mesh tally approximations to the spatial flux across the pin face. The average magnitude of error over all of the mesh regions was calculated to be 0.23%.

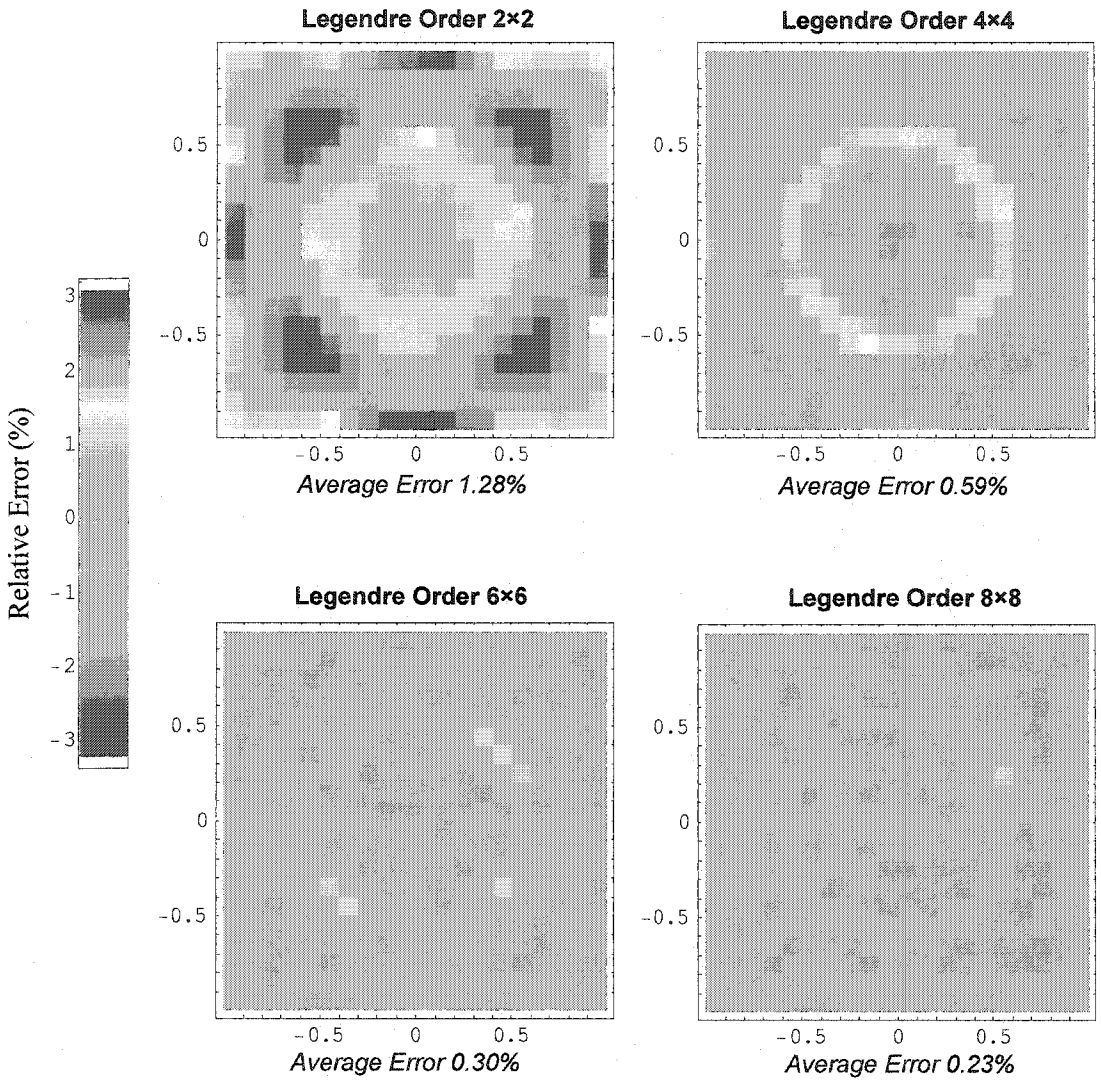

Figure 4.17. Density plots of the error between the coupled FET and the reference mesh tally approximations for different Legendre expansion orders. These results show the convergence of the FET approximation to the reference solution as the expansion order is increased.

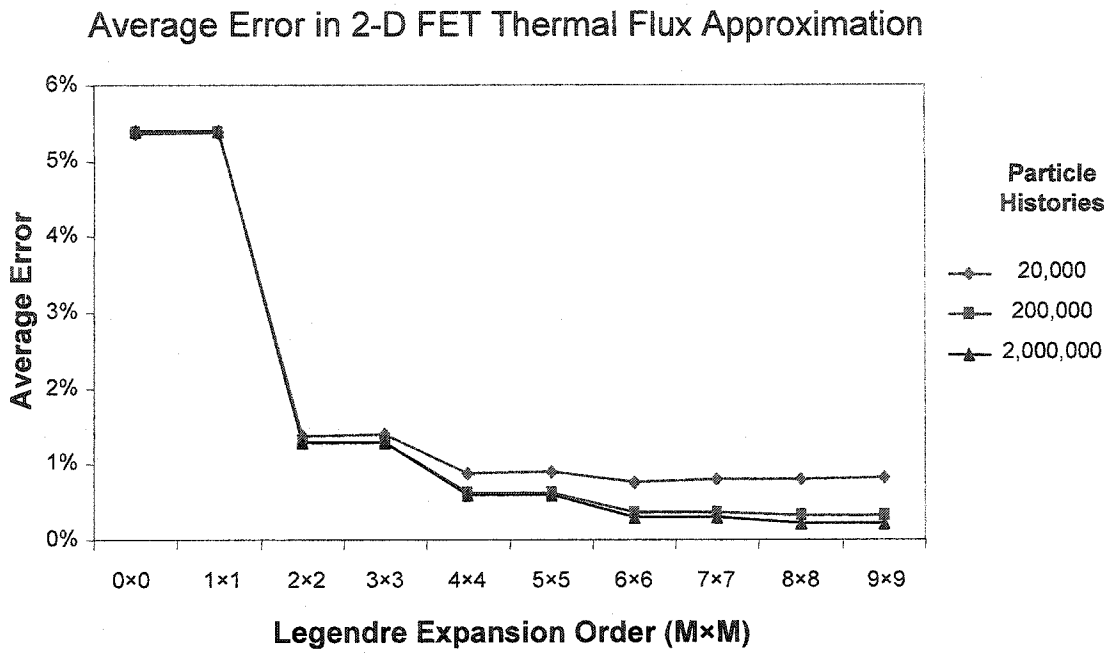

Figure 4.18. Average error in a Legendre FET approximation to the spatial flux distribution across the face of a 2-D PWR fuel pin. Results are shown for three Monte Carlo simulations, each run with a different number of particle histories.

To order to better assess the effect of truncation error on the track length FET, a series of tests was run to measure the average relative error of the FET (as compared to the MCNP5 benchmark solution) as a function of both Legendre expansion order and number of starting particles. The results of these tests, shown in Figure 4.17 and Figure 4.18, demonstrate that the functional expansion of the flux converges towards the benchmark solution as the number of histories and the number of terms in the Legendre expansion becomes larger. The observed convergence with increasing Legendre order for a fixed number of histories again confirms that both statistical and truncation errors need to be considered with any Monte Carlo functional expansion technique. Simply increasing the number of histories used in a simulation will only reduce the statistical error associated with the estimation of each expansion coefficient. In order to obtain an accurate pointwise scalar flux estimate over the entire spatial domain, it is necessary to

Table 4.2. Comparison of run times between a 9th order coupled Legendre FET and an MCNP5 20×20 mesh tally for estimating the 2-D spatial distribution of thermal flux over a PWR fuel pin.

Run Time Comparison (minutes)		
Particle Histories	**MCNP4c Coupled FET**	**MCNP5 Mesh Tally**
20,000	0.77	0.87
200,000	6.53	8.23
2,000,000	64.83	75.84

increase the number of terms in the Legendre expansion and thereby reduce the truncation error associated with approximating a function by a finite series of polynomials. Finally, a comparison of run times between the 2-D coupled FET and the MCNP5 mesh tally approximation methods for a 200-million history simulation is given in Table 4.2. These results show that estimating a functional expansion of the flux is slightly faster than using a mesh tally approach. Mesh tally algorithms require the addition of extra tally surfaces to the problem geometry. Tracking particles through these extra surfaces can add a significant amount of run-time to the simulation. While the coupled 2-D estimators also require additional calculations during particle transport, the results indicate that these calculations are more efficient than those associated with the mesh tally.

4.5.3. PWR Quarter Assembly Benchmark Problem

In order to provide a more challenging test of the capabilities of the 2-D track length FET, a benchmark problem was developed to simulate a realistic PWR fuel assembly. A fuel assembly is a square bundle of fuel and poison rods surrounded by

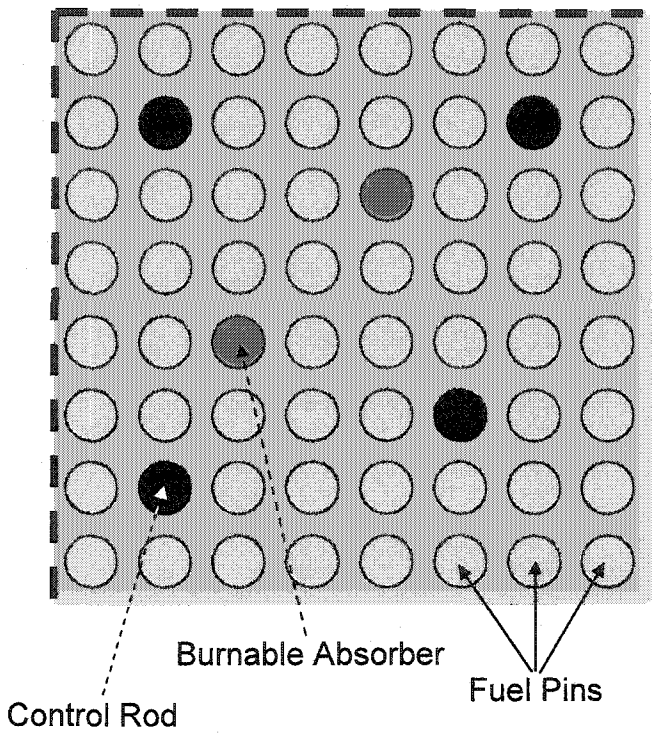

Figure 4.19. Two-dimensional representation of a PWR fuel assembly used for benchmark testing. The assembly contains three types of elements. Fuel pins contain 1.5% enriched UO_2. Burnable absorber pins and control rods both contain boron-10 at a density of 0.03 g/cc. All pins are surrounded by water at standard temperature and pressure. Reflecting boundary conditions were applied to all sides of the cell in order to simulate a repeating lattice of assemblies. The dashed lines show the quarter symmetry planes for the assembly.

structural material. A typical PWR assembly contains anywhere from a 14×14 to a 18×18 array of rods, usually with quarter- or eighth-assembly symmetry. A two-dimensional representation of one-fourth of a hypothetical 16×16 assembly is shown in Figure 4.19. This assembly is loosely based on assemblies designed for the Westinghouse AP600 reactor, but it is not intended to be an exact replica of any particular design.

The fuel assembly shown in Figure 4.19 contains two types of neutron poison elements. The burnable absorber rods, shown in dark grey, contain pure boron-10 with a density of 0.03 g/cc. These rods are fixed in place and are always present in the

assembly. The control rods, shown in black, have the same composition as the burnable absorber rods, but they are moveable. These control rods can be either withdrawn from the assembly or inserted into the assembly to control the reactivity of the assembly. The movement of these rods has a dramatic effect on the flux distribution within an assembly.

The quarter assembly illustrated in Figure 4.19 contains 64 individual fuel and poison elements. With this many elements, it should be expected that a global FET approximation over the entire problem will not produce acceptable results. Instead, a piecewise FET approximation should be used to increase the approximation accuracy. For this test, the quarter assembly was divided into 64 tally regions; one over each individual pin cell. The track length FET was then used to estimate a 9×9 set of Legendre expansion coefficients in each cell during a Monte Carlo eigenvalue calculation. Two simulations of 10-million histories each were run in order to simulate the assembly with control rods inserted and withdrawn. The FET flux approximations from these simulations are shown in Figure 4.20 and Figure 4.21. These results clearly illustrate the change in flux distribution that occurs when the control rod positions are changed. In Figure 4.20 the control rods are withdrawn and the guide channels are filled with water. These large concentrations of water allow for increased neutron thermalization, and a resulting peak in the thermal flux within each water-filled tube. When the control rods are inserted, Figure 4.21, the added neutron poisons eliminate the thermal neutrons nearby causing sharp flux depressions. The added effect of these poisons pushes the thermal flux peak to the lower right corner of the assembly, as far away from the poison elements as possible. In both cases, the FET produces a consistent

physically intuitive approximation for the flux distribution. Both approximations appear nearly continuous across all of the tally boundaries, indicating a well-converged solution.

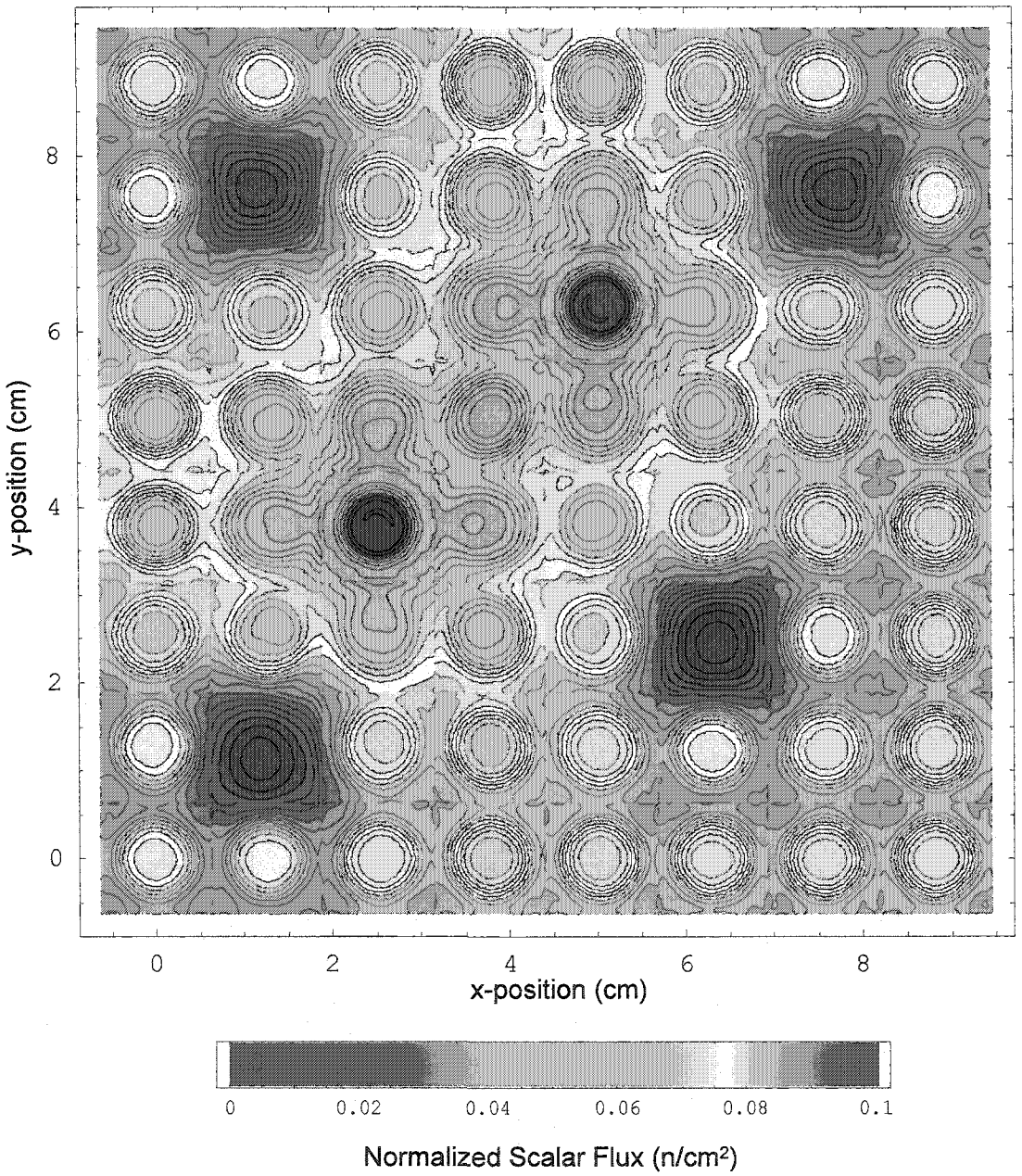

Figure 4.20. Two-dimensional density plot of the thermal flux across the face of the fuel assembly with control rods withdrawn. Each pin cell was approximated by a separate 9×9 order Legendre expansion. All expansion coefficients were produced using coupled track length FET estimators during a 2-million history Monte Carlo eigenvalue calculation. The resulting scalar flux values have been normalized by the number of particle histories run. The eigenvalue for the infinite system with control rods withdrawn was calculated to be 1.1630.

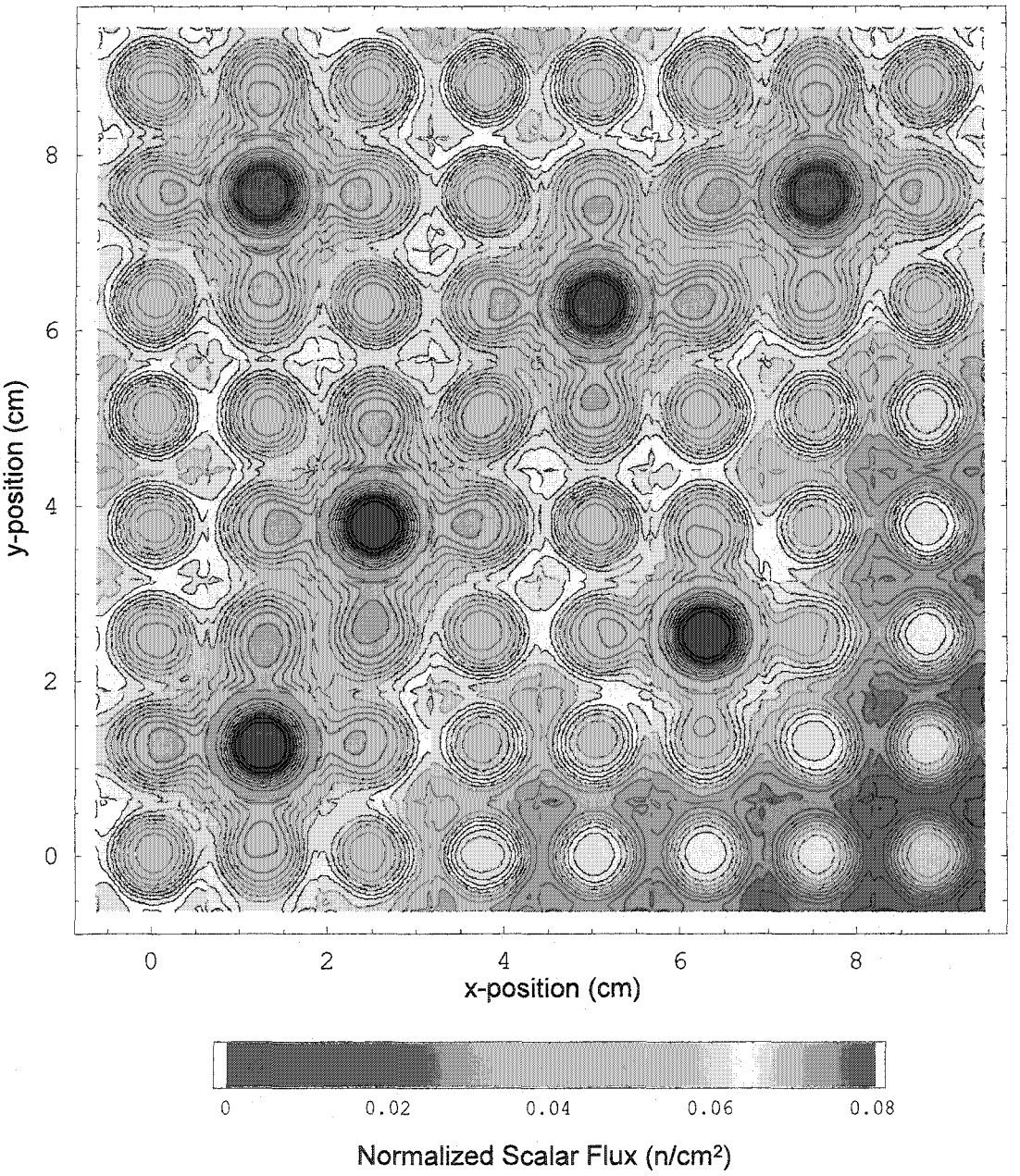

Figure 4.21. Two-dimensional density plot of the thermal flux across the face of the fuel assembly with control rods inserted. Each pin cell was approximated by a separate 9×9 order Legendre expansion. All expansion coefficients were produced using coupled track length FET estimators during a 2-million history Monte Carlo eigenvalue calculation. The resulting scalar flux values have been normalized by the number of particle histories run. The eigenvalue for the infinite system with control rods inserted was calculated to be 0.93287.

CHAPTER 5

APPLICATIONS TO RESPONSE MATRIX METHODS

The previous chapters in this dissertation have focused on presenting a very general derivation of the functional expansion technique (FET) and its mathematical properties. As a consequence, many of the numerical results presented have been limited to simply visualizing solutions from Monte Carlo simulations. It is important, however, to stress that the FET is not limited to data visualization alone. In fact, one of the most important properties of the FET is its ability to serve as a link between Monte Carlo and deterministic transport codes. One formalism for linking Monte Carlo and deterministic codes is the response matrix method (RMM).

5.1. The Response Matrix Method

The response matrix method (RMM) is a general technique that is used for simplifying and solving large linear transport or propagation problems. The method has historically been used to analyze transmission lines, wave guides, nuclear scattering, elementary particles, crystal lattice dynamics, and acoustics, along with many other physics and engineering applications[38]. The RMM operates using a "black box" approach, in which the detailed physics in large regions of the problem are condensed

into individual response matrices. Each response matrix relates the distribution and magnitude of particles or energy entering the region to the distribution and magnitude that exit the region. The RMM effectively converts linear transport problems into coarse-mesh nodal problems, in which the coupling is provided by the response matrix in each node. After the response matrices have been generated, then the global transport calculation can be extremely fast. Unfortunately, calculating the response matrices is not a simple task. For all but the most trivial problems, there exist no analytical techniques for calculating response matrices. In particle transport applications, many different numerical techniques have been tested, including diffusion theory, collision probability, and Monte Carlo methods.

5.1.1. Development of the Response Matrix Method

The response matrix method for reactor physics calculations originated with invariant imbedding, a widely-used analysis technique in physics. Invariant imbedding is a "black box" technique in which complicated physical interactions within a specified volume are replaced by a set of (typically nonlinear) response functions that relate the input conditions on the surface of the volume to the output conditions on the surface. Invariant imbedding was originally used to study the reflection and transmission of radiation through materials of varying thickness[39]. In this context, the goal of invariant imbedding is to find response equations that give the reflected and transmitted radiation fluxes due to an initial source as a function of the material thickness. The resulting response functions can be expressed either as second-order, non-linear, integro-differential equations (the invariant imbedding equations), or as functional equations that

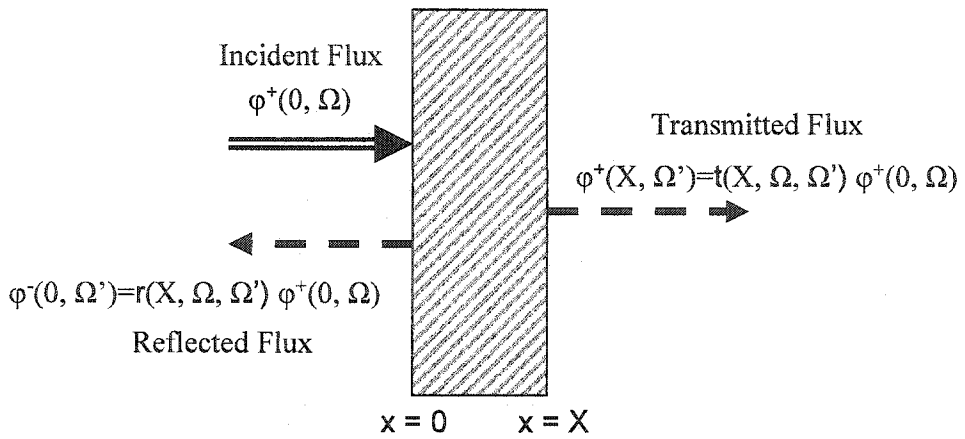

Figure 5.1. Illustration of transmission and reflection response functions for a one-dimensional slab geometry.

relate the response functions of a composite piece of material to the response functions of its constituent parts[40]. It was recognized in the 1950's that this second representation could be applicable to reactor physics calculations. Most reactor designs use a limited number of different fuel and poison types arranged in a repeating lattice. These different types of fuel and poison elements are the constituent parts that make up the composite reactor core. Determining the response functions for each type of fuel and poison element makes it possible to determine the response function for the entire core through the use of the adding relations. The article by Pfeiffer[40] gives a good review of the development of invariant imbedding in physics and the early applications to reactor physics. Unfortunately, the invariant imbedding approach is best suited for one-dimensional problems, and extending the method to higher dimensions causes difficulty.

To derive the response functions in 1-D, we begin with a slab of fixed width X and an incident angular flux on the left surface, as shown in Figure 5.1. The incident angular flux $\phi^{+}(0,\Omega)$ induces a reflected angular flux $\phi^{-}(0,\Omega')$ and a transmitted angular flux $\phi^{+}(X,\Omega')$. These reflected and transmitted flux distributions can be written

as a product of a response function times the initial source distribution and the slab thickness

$$\begin{aligned}\phi^{-}(0,\Omega') &= r(X,\Omega,\Omega')\phi^{+}(0,\Omega),\\ \phi^{+}(X,\Omega') &= t(X,\Omega,\Omega')\phi^{+}(0,\Omega).\end{aligned} \tag{5.1}$$

The response functions r and t are referred to as reflection and transmission function, respectively. These functions depend on the initial incident flux distribution as well as the slab thickness X. We notice that the transmission and reflection functions are also the Green's functions for reflected and transmitted angular flux due to the initial flux distribution at $x = 0$.

The response due to an arbitrary angular flux distribution can be written as the superposition of response functions for individual neutron angles and energies. These Green's functions can also be calculated for any normalized incident distribution and in practice are computed using elements from a set of angular basis functions. Letting $\{\psi_n(\Omega)\}_{n=0}^{\infty}$ represent a complete basis for the angular domain, it is possible to express any flux distribution as a series expansion,

$$\phi(x,\Omega) = \sum_{n=0}^{\infty} \overline{\phi}_{x,n} k_n \psi_n(\Omega), \tag{5.2}$$

where $\overline{\phi}_{x,n}$ is the n^{th} expansion coefficient for the angular flux at position x. The series expansion shown in Eq. (5.2) can also be written as a scalar product between a vector containing the expansion coefficients and a vector containing the basis functions,

$$\phi(x,\Omega) = \left\langle \underline{\phi}_x, \underline{\psi} \right\rangle, \tag{5.3}$$

where

$$\underline{\phi}_x = \left(\overline{\phi}_{x,0}, \overline{\phi}_{x,1}, \overline{\phi}_{x,2}, \cdots\right)$$
$$\underline{\psi} = \left(k_0 \psi_0(\Omega, E), k_1 \psi_1(\Omega, E), k_2 \psi_2(\Omega, E), \ldots\right). \tag{5.4}$$

Notice that, for a given set of basis functions, any flux distribution can be uniquely defined by its vector of expansion coefficients. Given this fact, it is possible to rewrite Eq. (5.1) in terms of $\underline{\phi}_0$ and $\underline{\phi}_X$, the exiting flux vectors at $x = 0$ and $x = X$, respectively,

$$\underline{\phi}_0^- = \underline{\underline{\rho}}\,\underline{\phi}_0^+$$
$$\underline{\phi}_X^+ = \underline{\underline{\tau}}\,\underline{\phi}_0^+, \tag{5.5}$$

where $\underline{\underline{\rho}}$ and $\underline{\underline{\tau}}$ are response operators. These operators have the form

$$\underline{\underline{\tau}} = \begin{bmatrix} t_{00} & t_{10} & t_{20} & \cdots \\ t_{01} & t_{11} & & \\ t_{02} & & t_{22} & \\ \vdots & & & \ddots \end{bmatrix}. \tag{5.6}$$

Each element, $t_{m,n}$, of this transmission response matrix gives the number of particles that cross the surface at $x = X$ with angular distribution $k_n \psi_n(\Omega)$, due to particles entering the system at $x = 0$ with angular distribution $k_0 \psi_0(\Omega)$. It is important to note that each response matrix is uniquely determined by the material properties and thickness of an individual region in the problem. Any changes that occur within the region require the response matrix to be recalculated. The only exception occurs in 1-D, where certain doubling, halving and adding relationships can be used to generalize a response matrix for a region of arbitrary thickness[41]. In two or three dimensions, a separate response matrix is required for each face of the node. Thus, a two-dimensional node with 4 sides would require a total of 16 response matrices to couple each incident surface to every

exiting surface. Fortunately, if the node is symmetric the number of unique response matrices is less than the total number of permutations. In the case of a two-dimensional, square, homogeneous node there are only 3 unique response matrices. These three matrices account for reflection, transmission across the node, and transmission to an adjacent surface. The use of node symmetry can greatly accelerate the calculation of response matrices. In addition to using symmetry to reduce the number of response matrices per node, the efficiency of the RMM also depends on the number of nodes in the system. The RMM works best on systems that can be partitioned into large nodes of equal geometrical form.

Response matrix methods are not restricted to handling only the angular distribution of flux. The method can also be used to account for spatial, energy, and even temporal[42-45] flux distribution across a node boundary. However, each additional phase variable increases the dimensionality of the response matrices used in the method. Calculating all of the response functions required for a six- or seven-dimensional response matrix would be prohibitively expensive. In practice, most RMM studies have been limited to a 3^{rd} order series expansion in angle and a 1^{st} order expansion in space. The resulting response matrices can be calculated quite efficiently, and they have been found to provide reasonable accuracy.

A variety of different basis sets have been studied for handling expansions in angle. In 1966, Aronson and Yarmush[38] used a half-range Legendre polynomial expansion in angle and a multigroup representation in energy. The half-range (or double) Legendre expansion was found to be particularly useful for expanding the angular component of partial flux or current distributions at node boundaries. In fact, the double

Legendre (DP_N) expansion became the standard angular expansion for many of the RMM studies that followed. Although the DP_N expansion became a popular and effective choice for the angular basis set, other angular representations have been tried, such as discrete ordinates[46], piecewise isotropic[40], and discrete Legendre polynomials[47]. All of the RMM work that treated particle energy explicitly used a multigroup representation. The multigroup treatment is favored because energy spectra containing resonance peaks are very difficult to resolve with a standard set of basis functions.

Most of the RMM studies presented in the literature have focused on the angular variation of particle flux or current at node boundaries. These studies typically assume that the spatial variation along a boundary is constant. In 1981, Nakata developed a response matrix method that accounts for this spatial variation[48,49]. However, instead of using a traditional orthogonal series expansion for the spatial dependence of the current, the RMM developed by Nakata was based on a finite element expansion. This work represents the first application of the finite element method in a response matrix framework.

The response matrices are used for local calculations within a small region of the overall problem geometry. In order to obtain the global solution for the problem, these independent regions must be linked together. This linkage is accomplished by enforcing a continuity boundary condition at the region interfaces. This condition is implemented quite easily by exchanging flux moments directly between adjacent regions. The outgoing flux expansion from one node is set equal to the incident flux distribution for the neighboring node. The actual computation is very similar to a discrete ordinates (S_N) sweep. The algorithm starts at one side of the problem with a prescribed source and

calculates the transmission of that source through successive nodes in one direction. After the code has swept through all of the nodes in one direction, it sweeps in the opposite direction to account for the reflected particles. These sweeps continue until the flux solutions at each node boundary remain unchanged between iterations. Because the global calculation only involves matrix multiplications at each node, the global calculation is extremely fast. Unfortunately, the standard sweeping algorithm can encounter severe problems due to error propagation. Response matrices can produce a very good approximation to the exiting particle distribution, but the approximation will not be exact due to truncation error. As a consequence, the source term for the next node may be in error by a small amount. As the global sweep proceeds, these small errors will generally accumulate and amplify. This problem, often referred to as lateral flux spreading or refraction, was first studied by Filippone in 1973 and 1977[41,50]. The effect of this flux spreading error becomes more pronounced as the number of nodes is increased. One possible solution proposed by Mosher and Rahnema is to reorder the sweeping pattern, in order to limit the error propagation[47].

The speed and efficiency of the global RMM calculation is offset by the need to precalculate a large number of response functions. Each response function calculation involves a fixed source transport calculation in the node of interest. A variety of different analytical and numerical schemes have been used to calculate response functions. Some of the very earliest work focused on the use of analytic transport[38,40,50-55] and diffusion theory[56-61] for calculating response functions. In 1972, Weiss was able to derive a set of response matrix equations (RME) for a 1-D slab directly from diffusion theory and prove that the RME are equivalent to the standard three-point difference equations[51]. By 1975,

however, Weiss and Lindhal concluded that analytical transport derivations of response functions had met with insurmountable difficulties[58]. Instead, Weiss and Lindhal use variational principles to derive response matrix equations based on the weak form of the diffusion equation[58,62]. For several years afterwards, work focused on this variational formulation of the RMM[63,64]. In the end, however, advancements in nodal diffusion theory[65] reduced interest in the RMM. The use of advanced homogenization techniques and discontinuity factors proved simpler and faster than diffusion based RMM.

After diffusion theory was largely abandoned for calculating response functions, many researchers considered using collision probability or S_N methods instead[66-71]. Many of these attempts proved highly successful for treating large commercial reactor problems[69-71]. Over time, these collision probability based response matrix methods evolved into the Green's function methods[72] and interface current methods[73-82]. In his review article, Mohanakrishnan gives a good overview of both the response matrix and interface current methods and the relationship between the two[77].

Finally, it is most important to note that there have been a series of studies that have used Monte Carlo simulations to calculate response functions. These studies are the most relevant to the application of the FET and will be considered in detail in the next section.

5.2. Calculating Response Functions with Monte Carlo

5.2.1. Previous Work

The concept of interfacing Monte Carlo and deterministic codes by exchanging flux and/or current moments has existed for many years. As early as 1975, McDaniel suggested a hybrid method for calculating flux distributions in a reactor pin cell[69]. The method employed a collision probability calculation in the fuel/clad/gap regions of the problem, and a Monte Carlo calculation for the coolant region. The solutions from the two methods were then linked by a continuous flux boundary condition applied at the clad/water interface. In order to make this method work, McDaniel also assumed that the flux along both sides of this interface was distributed uniformly in space and isotropically in angle. By using these approximations, only the zeroth moments of the flux and current distributions needed to be exchanged between the two regions. The zeroth moments of flux and current are both easily obtainable using traditional Monte Carlo estimators. Unfortunately, the isotropic/spatially uniform assumptions are not valid in many situations, especially near pins that are strong neutron absorbers[76,83].

Also in 1975, Bernnat et. al. published a description of a hybrid method[84] similar to that of McDaniel. The method developed was specifically designed to account for neutron streaming across a central void region in German design high-temperature pebble-bed gas reactors. The method used diffusion theory to calculate the flux distribution in the annular shaped fuel region and a Monte Carlo simulation to estimate streaming across the central cavity. In order to interface the diffusive and streaming

regions, the method assumes that the flux is isotropically and uniformly distributed along the interface, just like the method by McDaniel.

In 1988, Filippone and Alcouffe developed an S_N / Monte Carlo hybrid method that did not require an isotropic flux assumption[46]. In this method, a problem was partitioned into regions that could be solved by either Monte Carlo simulation or an S_N calculation. The independent calculations in the regions were then connected by enforcing continuity of flux across the region interfaces. The method was designed to iterate between the S_N and Monte Carlo calculations. In the initial step, a discrete ordinates calculation was performed in all of the S_N regions. This calculation produced a set of angle-dependent fluxes along each of the region boundaries. These discrete-ordinate flux distributions were then used as the source definition in the Monte Carlo simulation. The initial directions of particles in the Monte Carlo simulation were sampled from the discrete ordinate directions defined in the S_N set, according to the relative flux distribution. Upon exiting the Monte Carlo region, a particle's flux contribution was scored to the nearest angular ordinate and the particle was terminated. The results from the Monte Carlo simulation were then used as a source for the next S_N calculation, and this cycle iterated until a satisfactory result is achieved.

The first, and perhaps only, effort to create a RMM based completely on Monte Carlo simulation was reported in 1988 by Wan and Martin[85]. Their Monte Carlo Response Matrix Method (MCRMM) used Monte Carlo simulations to perform the global calculation as well as to precalculate the response matrices. Instead of traditional response matrices, the MCRMM calculated response probability density functions and response track length tables for particles entering a node. During the global solution, this

data was used to sample the exiting position as well as the path length generated by a particle entering the node. This eliminated the need to track the detailed random walk through the node, and greatly accelerated the global calculation. The method was applied successfully to a variety of different reactor lattice problems.

In 1999, Moriwaki et. al published a new method for calculating response matrices using Monte Carlo simulation[86]. The method involved the calculation of 4 sub-response matrices for each node. Instead of only treating the surface-to-surface response for particles entering a cell, the sub-response matrices were developed to take into account the surface-to-volume, volume-to-volume, and volume-to-surface responses of particles. By including information about the volumetric source of particles in a node, the method could be easily extended to handle eigenvalue calculations.

Most of these previous studies that have used Monte Carlo methods to generate response matrices have assumed fixed "cosine current" distributions for the angular flux at region boundaries[69,70,84,86]. While this approximation is valid for boundaries located in highly scattering regions, it has been shown that this approximation breaks down near absorptive regions, such as near a control blade in a boiling water reactor (BWR) core[76,77].

5.2.2. Application of the FET for Calculating Response Functions

When using Monte Carlo methods to calculate response functions for a node, a separate simulation is required for each incident flux (or current) moment distribution on each face of the node. This means that a response matrix for a six sided node, where each incident angular distribution is approximated by a 3rd order polynomial, will require 18

independent Monte Carlo simulations. Each of these independent Monte Carlo simulations samples the initial angular direction of incident particles from a probability density function that represents one of the polynomial basis functions. These particles are then tracked through the node geometry until they are absorbed or leak out. A series of tallies are defined on all of the node faces to record the angular moments of the particles that leak out of the node. Thus, the Monte Carlo simulation is able to estimate the response from each incident angular particle state. Notice that, with this technique, there is no need to modify any of the particle tracking routines. The Monte Carlo simulations only need to be configured to sample from and tally the angular moments of surface crossing flux and/or current distributions.

The surface crossing FET developed in chapter 2 is ideal for tallying the angular moments of the particles leaking out of the node. In fact, the estimators derived in section 2.1 can be applied directly without additional comment. Sampling the incident angular distribution of particles from distributions that correspond to polynomial basis functions presents a more difficult problem. Most of the commonly-used polynomial basis sets are defined such that all polynomials of order greater than zero are negative over half of their domain. To sample directly from these functions would require the use of negative weighted particles.

As an alternative to negative weights, which can be extremely inefficient, the source distributions are instead sampled from linear combinations of basis functions that are positive over the entire domain. Because these linear combinations are strictly positive they can be sampled directly, usually by rejection sampling techniques.

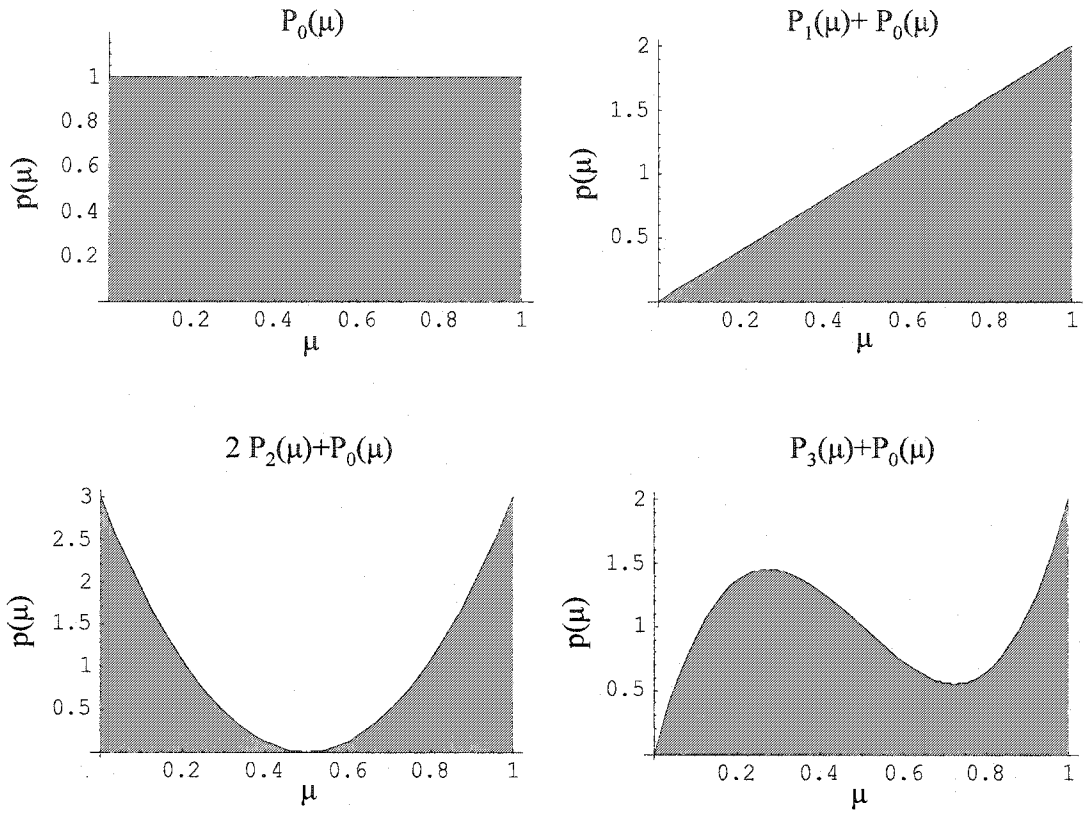

Figure 5.2. Linear combinations of Legendre polynomial basis functions used as probability density functions for sampling the angular direction of incident particles.

By linear superposition, the response due to a linear combination of basis functions is the same as the linear combination of responses due to the individual basis functions. If a linear combination is created by adding a distribution with an unknown response to a distribution known response, it is possible to infer the response due to the original distribution. The key is to find combinations of basis functions that are strictly positive. A simple algorithm can be used to construct positive combinations for basis sets that have only one element whose integral is nonzero, such as the Legendre polynomials.

Any Legendre (n > 0) basis function can be made non-negative by adding some multiple (e.g. α) of the zeroth order function. To ensure the distribution is non-negative over the entire domain the value of α must satisfy the relationship

$$\alpha \geq \left|\min\left[P_n(\mu)\right]\right|. \tag{5.7}$$

The linear combination $P_n + \alpha P_0$ is strictly positive over its domain. However, this linear combination is not a pdf because the integral of $P_n + \alpha P_0$ is equal to α instead of 1. In order to convert the combination to a true pdf it must be normalized by α. The resulting normalized pdf is given by $\alpha^{-1}P_n + P_0$.

An illustration of several linear-combination source distributions generated with this algorithm is presented in Figure 5.2. The response to a P_n source can be calculated as α times the response due to a $\alpha^{-1}P_n + P_0$ source minus the response to a P_0 source alone. Conversion from non-negative $\alpha^{-1}P_n + P_0$ source response function to a P_n response function can be done as post-processing of the simulation output.

5.3. Numerical Results

Using the surface crossing FET estimators and the sampling strategy discussed above, a modified version of MCNP4c was created to estimate transmission response functions for angular current distributions in 1-D slab geometry problems. This code was used to calculate response matrices for two benchmark problems.

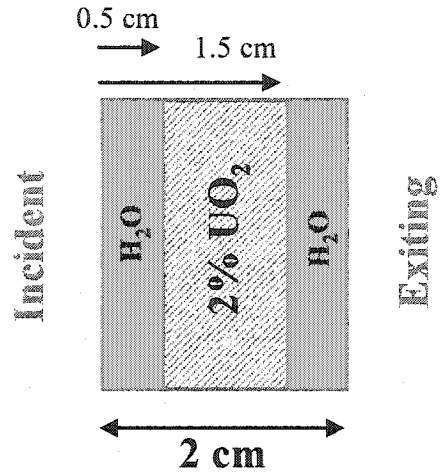

Figure 5.3. One-dimensional representation of a PWR fuel pin used for benchmark testing of the FET based Monte Carlo method for calculating response functions. The node contains a slab of 2% enriched UO_2 surrounded by water at standard temperature and pressure.

5.3.1. 1-D UO2 Fuel Pin with Coolant Channels

The first benchmark problem considered was a one-dimensional planar geometry representation of a 2% enriched UO_2 fuel pin and adjacent coolant channels, shown in Figure 5.3. Using the modified version of MCNP, a set of 12 transmission response functions was generated for this problem. The resulting response matrix, given in Table 5.1, couples 3 incident angular current moments to 4 exiting angular current moments. All response functions were generated in 1-million history simulations, assuming a uniform distribution of incident neutron energies between 100 and 500 keV.

To test the effectiveness and robustness of the response matrix for calculating exiting angular current distributions, a forward-peaked incident angular source shape was chosen that cannot be expressed exactly by a finite number of Legendre terms,

$$J^{+}(\mu) = \frac{1.317\times10^{16}\, e^{5\mu}}{\left(4.420\times10^{8} + 2.978\times10^{6}\, e^{5\mu}\right)^{2}}. \qquad (5.8)$$

Table 5.1. Transmission response matrix for 1-D PWR fuel pin with coolant channels. The response matrix relates the first 3 angular moments of the incident current distribution to the first 4 angular moments of the exiting current distribution on the opposite face of the fuel pin. All response functions were produced with 1-million history Monte Carlo simulations. The values in parentheses give the relative standard deviation for each response matrix element.

		Incident		
		$P_0(\mu)$	$P_1(\mu)$	$P_2(\mu)$
Exiting	$P_0(\mu)$	0.5187 (0.10%)	0.2458 (0.86%)	-0.0354 (5.10%)
	$P_1(\mu)$	0.2027 (0.18%)	0.1585 (1.00%)	0.0845 (1.56%)
	$P_2(\mu)$	0.0057 (5.69%)	0.0672 (2.15%)	0.1287 (0.91%)
	$P_3(\mu)$	-0.0081 (3.36%)	0.01281 (9.54%)	-0.0682 (1.45%)

The shape of this source and its P_2 approximation are shown in Figure 5.4. The L_1 norm of the difference between the exact source and its P_2 approximation is 0.0564.

Multiplying the P_2 source approximation by the response matrix for the unit cell yields a P_3 approximation to the exiting current. A 100 bin reference histogram distribution was calculated with a 1-million history analog MCNP simulation that used the exact incident current distribution specified in Eq. (5.8). A comparison between the response matrix approximation and the reference distribution, Figure 5.5, shows remarkable agreement between the two solutions. The comparison indicates that the response matrix approximation for exiting current distribution is nearly indistinguishable from the result obtained from a Monte Carlo transport simulation.

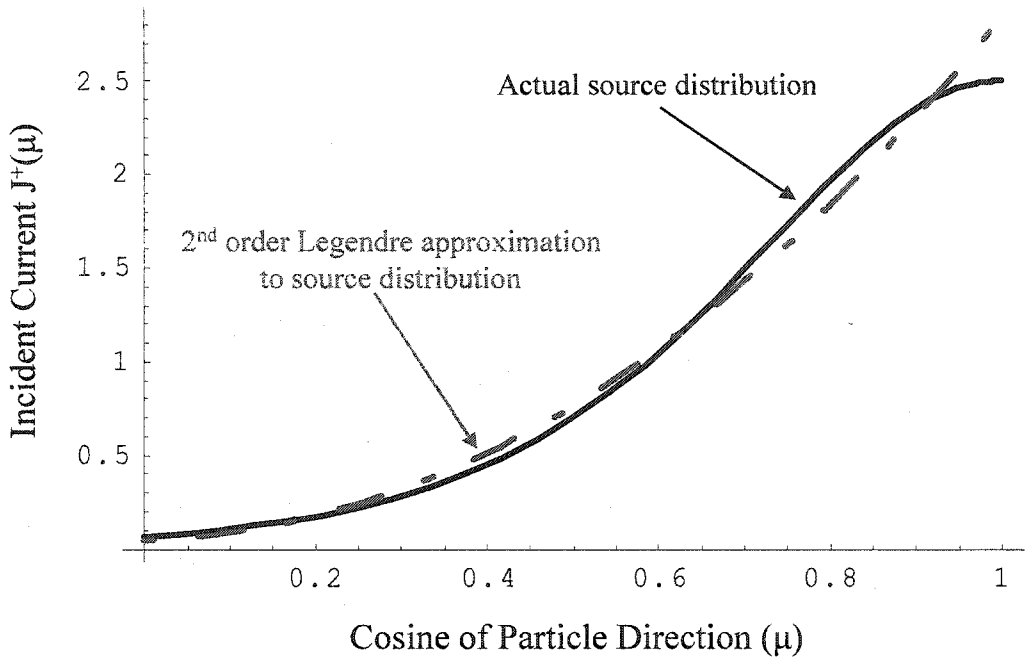

Figure 5.4. Comparison of actual angular source distribution with 2nd order Legendre approximation for the PWR fuel pin benchmark problem.

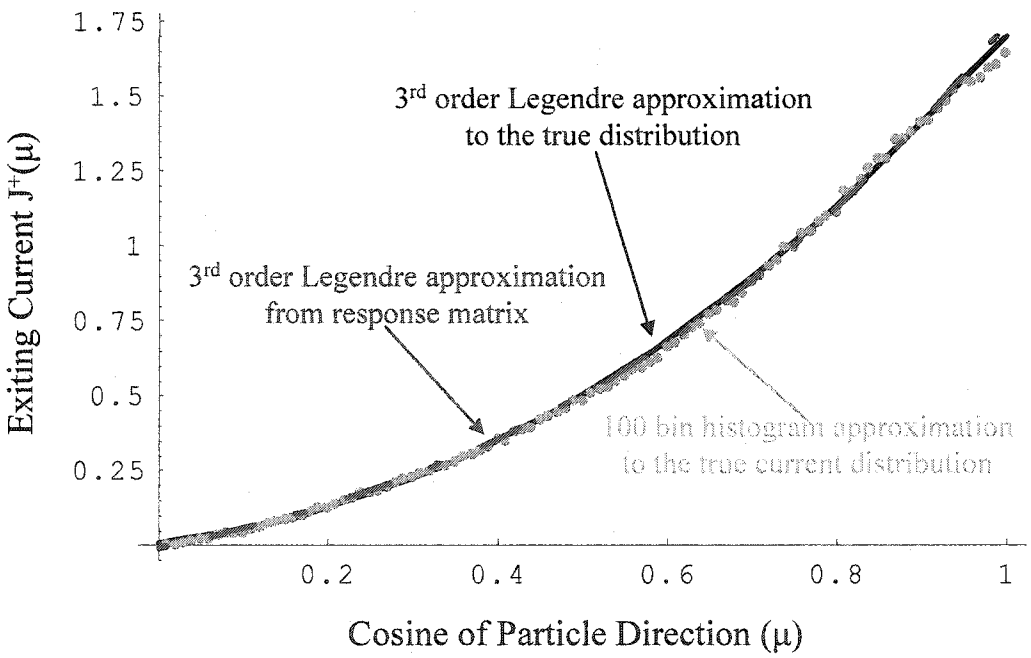

Figure 5.5. Comparison between response matrix and reference Monte Carlo solutions for the angular distribution of exiting neutron current for the PWR fuel pin benchmark problem. Both the 100-bin histogram and 3rd order Legendre reference distributions were calculated with a 1-million history Monte Carlo simulation using the exact incident source distribution. The results indicate that the response matrix solution has comparable accuracy to an actual transport calculation in the node.

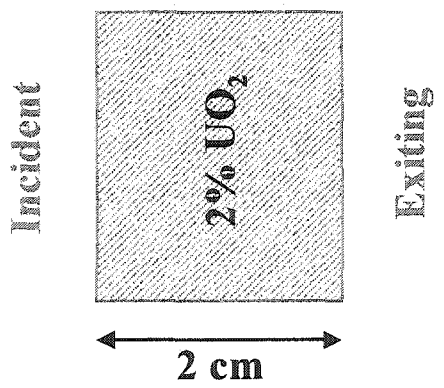

Figure 5.6. One-dimensional representation of a 2% enriched bare UO_2 slab used for benchmark testing of the FET based Monte Carlo method for calculating response functions.

5.3.2. 1-D Bare UO_2 Fuel Slab

The second benchmark test used a one-dimensional slab representation of a bare 2% enriched fuel pin, shown in Figure 5.6. The simulation conducted with this geometry was designed to test the robustness of the response functions generated with Monte Carlo. As with the first benchmark problem, a set of 12 transmission response functions were generated (3 incident moments, 4 exiting moments) with the modified version of MCNP. These response functions were estimated using 1-million history simulations, and assuming a uniform distribution of neutron energies between 100 and 500 keV. The response matrix for the bare fuel pin is given in Table 5.2.

For the first numerical test of this geometry, a highly forward-peaked angular distribution was chosen for the incident neutrons,

$$J^{+}(\mu) = \frac{1.46133\times10^{18}\, e^{10\mu}}{\left(4.01172\times10^{10} + 1.82132\times10^{6}\, e^{10\mu}\right)^{2}}. \tag{5.9}$$

Table 5.2. Transmission response matrix for 1-D bare fuel slab. The response matrix relates the first 3 angular moments of the incident current distribution to the first 4 angular moments of the exiting current distribution on the opposite face of the fuel pin. All response functions were produced with 1-million history Monte Carlo simulations. The values in parentheses give the relative standard deviation for each response matrix element.

		Incident		
		$P_0(\mu)$	$P_1(\mu)$	$P_2(\mu)$
Exiting	$P_0(\mu)$	0.5116 (0.10%)	0.2233 (0.93%)	-0.0388 (4.60%)
	$P_1(\mu)$	0.1823 (0.20%)	0.1661 (0.95%)	0.1208 (1.11%)
	$P_2(\mu)$	-0.0060 (5.33%)	0.0807 (1.76%)	0.1759 (0.66%)
	$P_3(\mu)$	-0.0066 (4.06%)	0.0103 (11.58%)	0.0867 (1.13%)

The shape of this source and its P_2 approximation are shown in Figure 5.7. Notice that the P_2 expansion is a poor representation of the actual distribution. In fact, the P_2 approximation goes negative near $\mu = 0.3$, which is an unphysical characteristic for an incident current distribution. The L_1 norm of the difference between the exact source and its P_2 approximation is 0.2780, a relatively large value.

Again, the 2nd order source approximation was multiplied by the response matrix to produce a 3rd order approximation for the angular distribution of the exiting current. A comparison between the response matrix approximation and a 100-million history reference distribution, Figure 5.8, shows remarkable agreement between the two solutions. The L_1 norm between the reference solution and response matrix solution was calculated to be 0.0734. By comparison, the L_1 norm between the reference solution and its exact P_3 approximation was found to be 0.0392. These results are especially encouraging, given the extremely poor source approximation used for the response matrix solution.

Both of these benchmark tests demonstrate that the FET based method for estimating response functions is highly effective. The response functions produced by the new algorithm are able to accurately predict the magnitude and angular distribution of neutrons exiting a pin-cell for a given source distribution entering the cell. Given the general nature of the FET and the proposed sampling algorithm there is no reason to expect that these simple 1-D angular results could not be extended to produce response functions in space, energy, and/or time.

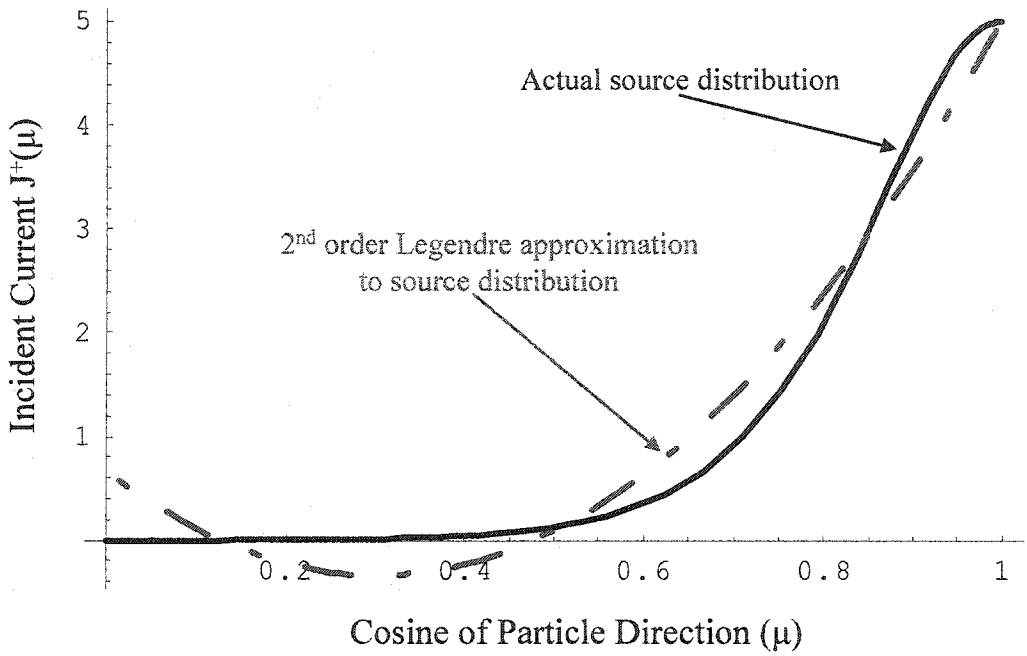

Figure 5.7. Comparison of actual angular source distribution with 2nd order Legendre approximation for the PWR fuel pin benchmark problem.

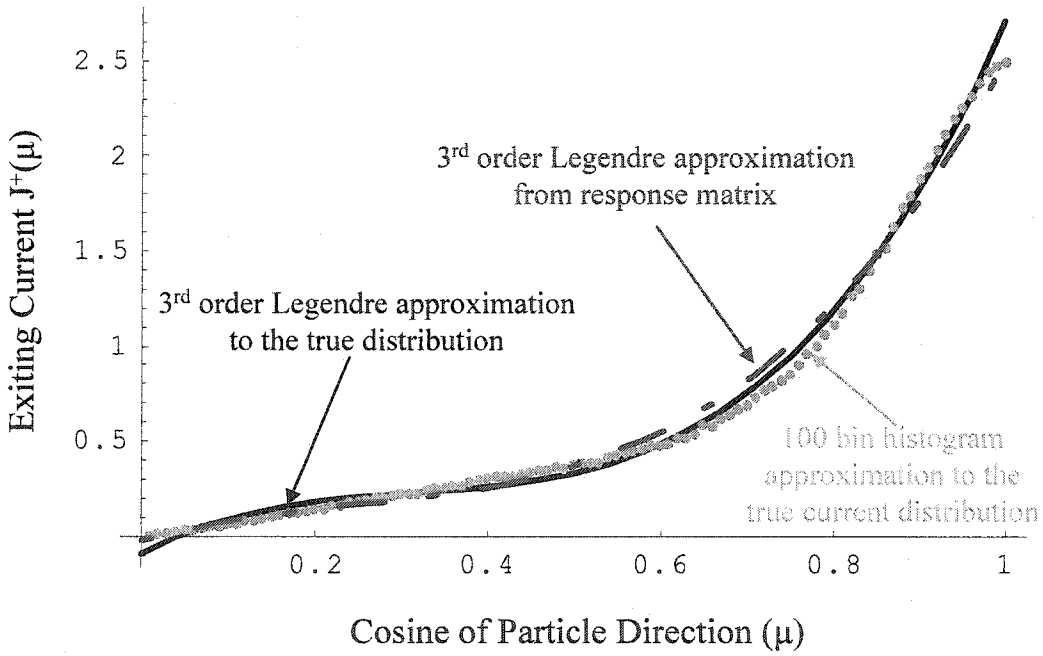

Figure 5.8. Comparison between response matrix and reference Monte Carlo solutions for the angular distribution of exiting neutron current for the bare fuel benchmark problem. Both the 100-bin histogram and 3rd order Legendre reference distributions were calculated with a 1-million history Monte Carlo simulation using the exact incident source distribution. Notice that, even with a poor initial source approximation, the response matrix is able to produce accurate exiting current distributions.

CHAPTER 6

SUMMARY & CONCLUSIONS

In this dissertation, a set of continuous Monte Carlo tallies, collectively known as functional expansion tallies, have been developed and tested for particle transport applications. This new technique uses modified versions of traditional Monte Carlo tallies to estimate the expansion coefficients of particle flux or current distributions with respect to a set of orthogonal basis functions. These estimated coefficients can then be used to reconstruct a series expansion approximation of the true distribution. In this work, new derivations for two types (discrete event and track length) of FET estimators are presented, along with detailed new analyses of the mathematical and statistical properties of these estimators. In addition, numerical results are presented that demonstrate the effectiveness of the FET for several applications of interest.

Where traditional Monte Carlo tallies can only be used to estimate integral quantities taken over a flux or current distribution, the FET produces a continuous functional approximation to the actual distribution itself. Furthermore, because the FET estimators are based on traditional Monte Carlo estimators, they require little effort to implement in existing Monte Carlo codes. Therefore, upgrading current Monte Carlo codes to include FET can quickly provide a dramatic increase in the amount of tally

information produced during a Monte Carlo simulation without extensive code development work.

For the discrete-event FET, a set of estimators for approximating the surface crossing current distribution, and its variance, were developed and implemented in a test version of MCNP. For verification and testing, this modified version of MCNP was used to estimate the time spectrum of detectable thermal neutrons in a neutron interrogation benchmark problem. The resulting functional approximations were found to agree within the limits of statistical uncertainty with a 100-bin histogram reference approximation to the true spectrum.

The results indicate that the FET is affected by two sources of error: statistical uncertainty and truncation error. The magnitudes of these errors are inversely proportional to one another and depend on the number of histories used in the simulation and the number of terms used in the functional expansion. Estimators have been developed to measure the amount of each type of error that is present in a given approximation. These estimators can also be combined to yield a cost-to-benefit metric that can determine which expansion coefficients should be included in the functional approximation. This provides a convenient method for minimizing both statistical and truncation error, thus resulting in the best possible estimate for the unknown distribution.

The properties of these two error terms were further studied by a theoretical examination of the convergence properties of the FET. A detailed analysis was performed to determine the rate at which a functional expansion converges to the true distribution as the expansion order was increased. Theoretical results demonstrate that

the convergence behavior depends primarily on the smoothness of the true distribution, but can also depend on the set of basis functions chosen for the expansion.

The initial convergence rate of the FET for a non-analytic function was shown to be algebraic, with order determined by the algebraic index of convergence of the function. For analytic functions, the initial convergence rate of the FET is exponential. Unfortunately, these convergence rates are contaminated by statistical uncertainty with order $O\left[\sqrt{M/N}\right]$, due to the stochastic nature of the Monte Carlo random walk process. For large values of the ratio M/N, the statistical uncertainty begins to dominate and diminish the accuracy of the highest order expansion coefficients. Due to these competing sources of error in the FET the analysis shows that, for a given number of histories run, there is an optimal expansion order that minimizes the sum of the truncation error and statistical error in the final approximation. This optimal expansion order is a function of the number of particle histories used in the Monte Carlo calculation. The convergence of the FET with respect to the number of particle histories remains $O\left[1/\sqrt{N}\right]$ with fixed expansion order.

For comparative purposes, a similar convergence analysis was performed for a traditional histogram tally. With increasing numbers of bins, the convergence behavior of the histogram approximation was shown to converge at a fixed rate of $O[M^{-1}]$, where M is the number of bins. As with the FET, statistical error in the histogram tally increases with order $O\left[\sqrt{M/N}\right]$, and, consequently, there exists an optimum number of histogram bins that minimizes the residual error of the approximation.

Although the FET and histogram tallies converge qualitatively in the same way, there are cases where one method can clearly outperform the other. For distributions that are at least piecewise smooth, the faster initial convergence rate of the FET can provide a better fit than a histogram approximation of the same order. However, for distributions that are only piecewise continuous (or contain very steep gradients) the histogram approximation will provide a better fit than the FET if bin boundaries can be located at or near the functional discontinuities. However, in this case, a piecewise FET approximation can outperform both a histogram tally and a global FET approximation. The judicious choice of one of these methods based on any prior knowledge of the unknown distribution can ensure that the maximum amount of information is obtained from the Monte Carlo simulation.

Numerical verification of the theoretical convergence results was conducted with a sample distribution. The empirical results agreed with the theory and demonstrated, for the sample distribution chosen, that the FET provided a better approximation to the shape of the distribution than the histogram tally.

A set of one- and two-, and three dimensional track length FET estimators was also developed for approximating the spatial expansion coefficients for flux distributions. This new technique can be used to estimate either a single global function over the entire tally region or a series of piecewise functions that, together, span the region of interest. These estimators were implemented into a modified version of MCNP4c and benchmarked against a lattice of realistic PWR type pin cells. The results of the benchmark tests show that, for all cases studied, the method provides accurate functional

estimates of the spatial flux distribution when compared to reference solutions obtained from a conventional Monte Carlo mesh tally method.

Finally, a new Monte-Carlo FET based method for calculating angular response functions for 1-D slab geometries was developed and tested on a simplified model of a PWR fuel pin. The new method can accurately predict the magnitude and angular distribution of neutrons exiting the pin-cell for a given source distribution entering the cell. Current research focuses on extending this method to multi-dimensional geometries as well as extending the concept to the sampling/tallying of shape functions in space, energy and time.

Although the concepts of functional expansion tallies were published as early as 1975, each previous implementation of the method was uniquely tailored for a specific application. This thesis demonstrates that the FET is a powerful technique that may have far more applications than previously realized. The FET is more than a data visualization tool. The technique is actually able to extract more information from Monte Carlo simulations than was previously possible with conventional tallies.

The work in this thesis presents the FET as an application-independent set of tools that can be used in conjunction with any type of Monte Carlo simulation. The estimators were generalized to apply to expansions in any combination(s) of phase variables, and in any number of dimensions. Consideration was also given to the practical implementation of the method. This included outlining many of the issues surrounding implementation in an existing code, as well as developing numerical schemes that can increase the computational efficiency of the method itself.

Although the FET offers many benefits, it is not without limitations. End-users of the method must always bear in mind that the technique produces a truncated approximation to the true solution. Therefore, using an expansion with too few terms may produce an approximation that cannot resolve important features of the distribution. Furthermore, for the basis sets considered, there is no guarantee that a functional approximation will be positive everywhere, even though physics requires the true transport solution to be positive. While many critics stress these issues, it must be noted that even deterministic methods based on series expansions are not guaranteed to be positive everywhere. Furthermore, the results in this thesis have shown the FET to be extremely robust. Even in cases where the functional approximation becomes negative, these errors are localized and do not appear to significantly degrade the overall approximation. Nevertheless, in order to address these concerns about the FET, several informal metrics and rules of thumb were developed to help ensure appropriate and consistent application of the technique. These metrics were specifically developed to help end-users optimize the method without having to devote a large amount of time to learning the details of approximation theory.

While this dissertation provides both a practical and theoretical development of the FET, there are many applications and generalizations of the method that remain to be studied. For example, all of the numerical examples and convergence derivations in this work assumed the use of polynomial basis sets. There are, however, many applications where finite element or rational basis sets may provide better approximations. Research is also currently underway into the use of the FET for Monte Carlo eigenvalue calculations. Traditional methods mimic source iteration by using a "fission bank" to

store neutron birth sites between generations. It is thought that storing a functional approximation of the fission source distribution rather than individual event locations may help to accelerate the source convergence. Perhaps the biggest opportunity for the FET, however, is in the development of future hybrid Monte Carlo/deterministic methods. The FET provides a perfect method for interfacing with P_n, S_n, or possibly sub-grid methods by exchanging flux or current moments.

BIBLIOGRAPHY

1 S. A. Dupree and S. K. Fraley, *A Monte Carlo Primer--A Practical Approach to Radiation Transport*, Plenum, New York. (2002).

2 J. J. Duderstadt and L. J. Hamilton, *Nuclear Reactor Analysis*, John Wiley & Sons, New York. (1976).

3 M. L. Adams and E. W. Larsen, "Fast Iterative Methods for Discrete-Ordinates Particle Transport Calculations," *Prog. Nucl. Energy*, **40**, pp. 3-159 (2002).

4 J. Spanier and E. M. Gelbard, *Monte Carlo Principles and Neutron Transport Problems*, Addison-Wesley, Reading. (1969).

5 E. D. Cashwell and C. J. Everett, *A Practical Manual on the Monte Carlo Method for Random Walk Problems*, Pergamon Press, New York. (1959).

6 L. L. Carter and E. D. Cashwell, *Particle-Transport Simulation with the Monte Carlo Method*, Technical Information Center, Energy Research and Development Administration, Oak Ridge. (1975).

7 A. Papoulis, *Probability, Random Variables, and Stochastic Processes*, Third ed, McGraw-Hill, New York. (1991).

8 L. Devroye, *Non-Uniform Random Variate Generation*, Springer-Verlag, New York. (1986).

9 J. F. Briesmeister, *MCNP - A General Monte Carlo N-Particle Transport Code*, LA-13709-M, Los Alamos National Laboratory, Los Alamos (2000).

10 S. Nakamura, *Computational Methods in Engineering and Science with Applications to Fluid Dynamics and Nuclear Systems*, Krieger Publishing, Malabar, FL. (1986).

11 J. M. Hammersley and D. C. Handscomb, *Monte Carlo Methods*, John Wiley & Sons, New York. (1964).

12 R. E. Walpole and R. H. Myers, *Probability and Statistics for Engineers and Scientists*, Fifth ed, Prentice Hall, Englewood Cliffs. (1993).

13 J. Spanier, "Two Pairs of Families of Estimators for Transport Problems," *SIAM J. Appl. Math*, **14**, pp. 702-713 (1966).

14 J. Stewart, *Calculus--Early Transcendentals*, Second ed, Brooks/Cole Publishing, Pacific Grove. (1991).

15 A. Dubi, in *CRC Handbook of Nuclear Reactors Calculations*, edited by Yigal Ronen (CRC Press, Boca Raton, 1986), Vol. 2, pp. 1-86.

16 S. Glasstone and M. C. Edlund, *The Elements of Nuclear Reactor Theory*, D. Van Nostrand Company Inc., Princeton. (1952).

17 S. O. Rice, in *Selected Papers on Noise and Stochastic Processes*, edited by Nelson Wax (Dover Publications, New York, 1944), pp. 133-183.

18 W. L. Chadsey, C. W. Wilson, and V. W. Pine, "X-Ray Photoemission Calculations," *IEEE Trans. Nucl. Sci*, **22**, pp. 2345-2350 (1975).

19 B. L. Beers and V. W. Pine, "Functional Expansion Technique for Monte Carlo Electron Transport Calculations," *IEEE Trans. Nucl. Sci*, **23**, pp. 1850-1856 (1976).

20 A. Noel and H. S. Wio, "A New Series-Expansion Approach in Monte Carlo: Application to Neutron Shielding," *Ann. Nucl. Energy*, **11**, pp. 225-227 (1984).

21 J. Spanier, "Monte Carlo Methods for Flux Expansion Solutions of Transport Problems," *Nucl. Sci. Eng.*, **133**, pp. 73-79 (1999).

22 T. E. Booth, "Monte Carlo Estimates of Transport Solutions to the Isotropic Slab Problem," *Nucl. Sci. Eng.*, **130**, pp. 374-385 (1998).

23 H. Lichtenstein and J. Favorite, *Exponential Monte Carlo Convergence of a Three-Dimensional Discrete Ordinates Solution*, LA-UR-99-5963, Los Alamos National Laboratory, Los Alamos, N.M. (2003).

24 D. Legrady and E. J. Hoogenboom, "Monte Carlo Midway Forward-Adjoint Coupling with Legendre Polynomials for Borehole Logging Applications," *Proceeding of Physor 2004-The Physics of Fuel Cycles and Advanced Nuclear Systems: Global Developments*, Chicago, Illinois, April 25-29, CD-ROM, (2004)

25 D. Legrady and E. J. Hoogenboom, "Visualization of Space-Dependency of Responses of Monte Carlo Calculations Using Legendre Polynomials," *Proceeding of Physor 2004-The Physics of Fuel Cycles and Advanced Nuclear Systems: Global Developments*, Chicago, Illinois, April 25-29, CD-ROM, (2004)

26 B. T. Rearden, "Perturbation Theory Eigenvalue Sensitivity Analysis with Monte Carlo Techniques," *Nucl. Sci. Eng.*, **146**, pp. 367-382 (2004).

27 D. P. Griesheimer and W. R. Martin, "Estimating the Global Scalar Flux Distribution with Orthogonal Function Expansion," *Trans. Am. Nucl. Soc.*, **89**, pp. 462-464 (2003).

28 D. P. Griesheimer and W. R. Martin, "Monte-Carlo Based Angular Flux Response Functions," *Trans. Am. Nucl. Soc.*, **89**, (2003).

29 D. P. Griesheimer and W. R. Martin, "Two Dimensional Functional Expansion Tallies for Monte Carlo Simulations," *Proceeding of Physor 2004-The Physics of Fuel Cycles and Advanced Nuclear Systems: Global Developments*, Chicago, Illinois, April 25-29, CD-ROM, (2004)

30 D. P. Griesheimer, W. R. Martin, and J. P. Holloway, "Estimation of Flux Distributions with Monte Carlo Functional Expansion Tallies," *Proceeding of Tenth International Conference on Radiation Shielding (ICRS-10)*, Madeira, Portugal, pp. (2004).

31 J. P. Boyd, *Chebyshev & Fourier Spectral Methods*, Springer-Verlag, New York. (1989).

32 G. B. Folland, *Fourier Analysis and its Applications*, Brooks/Cole, Detroit. (1992).

33 T. W. Körner, *Fourier Analysis*, Cambridge University Press, New York. (1988).

34 C. M. Bender and S. A. Orszag, *Advanced Mathematical Methods for Scientists and Engineers*, McGraw-Hill, New York. (1978).

35 I. S. Sokolnikoff and R. M. Redheffer, *Mathematics of Physics and Modern Engineering*, McGraw-Hill, New York. (1958).

36 B. Sz.-Nagy, *Introduction to Real Functions and Orthogonal Expansions*, Oxford University Press, New York. (1965).

37 A. Leonard, C. T. McDaniel, and W. P. Petrick, "Integral Transport Calculation of Spatial Gadolinium Depletion," *Trans. Am. Nucl. Soc.*, **19**, pp. 406-407 (1974).

38 R. Aronson and D. L. Yarmush, "Transfer-Matrix Method for Gamma-Ray and Neutron Penetration," *Journal of Mathematical Physics*, **7**, pp. 221-237 (1966).

39 G. G. Stokes, "On the Intensity of the Light Reflected from or Transmitted Through a Pile of Plates," *Proc. Roy. Soc.*, **11**, pp. 545 (1869).

40 W. Pfeiffer and J. L. Shapiro, "Reflection and Transmission Functions in Reactor Physics," *Nucl. Sci. Eng.*, **38**, pp. 253-264 (1969).

41 W. L. Filippone, "Improved Formulations of the Response Matrix Doubling Equations," *Nucl. Sci. Eng.*, **62**, pp. 69-91 (1977).

42 T. E. Albert and M. J. Bodoia, "Hybrid Method for Spatial Dynamic Analysis: An Invariant Imbedding Approach," *Trans. Am. Nucl. Soc.*, **14**, pp. 232-233 (1971).

43 J. M. Sicilian and A. Leonard, "A Response-Matrix Method for Space-Dependent Nuclear Reactor Kinetics Calculations," *Trans. Am. Nucl. Soc.*, **17**, pp. 252 (1973).

44 J. M. Sicilian, "Response Matrices in Space-Time Reactor Dynamics," *Nucl. Sci. Eng.*, **56**, pp. 291-300 (1975).

45 J. M. Sicilian and R. J. Pryor, "Trascal, a Two-Dimensional, Multigroup, Response Matrix Kinetics Code," *Proceeding of Computational Methods in Nuclear Engineering*, Charleston, April, pp. 103-122, (1975).

46 W. L. Filippone and R. E. Alcouffe, "S-N Monte Carlo response matrix hybrid method.," *Nucl. Sci. Eng.*, **100**, pp. 209-217 (1988).

47 S. W. Mosher and F. Rahnema, "An Intra-Nodal Flux Expansion for a Heterogeneous Coarse Mesh Discrete Ordinate Method," *Proceeding of Nuclear Mathematical and Computational Sciences: A Century in Review, A Century Anew*, Gatlinburg, TN, April 6-11, CD-ROM, (2003)

48 H. Nakata, *The Finite Element Response Matrix Method for Coarse Mesh Reactor Analysis*, Ph.D. Dissertation, University of Michigan, Ann Arbor. (1981).

49 H. Nakata and W. R. Martin, "Finite Element Response Matrix Method," *Nucl. Sci. Eng.*, **85**, pp. 289-305 (1983).

50 W. L. Filippone, "Two-Dimensional Neutron Transport Calculations Using the Response Matrix Method," *Nucl. Sci. Eng.*, **52**, pp. 23-34 (1973).

51 Z. Weiss, "Nodal Equations Dervied from Invariant Imbedding Theory," *Nucl. Sci. Eng.*, **48**, pp. 235-247 (1972).

52 E. A. Villarino and R. J. J. Stamm'ler, "The Heterogeneous Response Method in Slab Geometry," *Ann. Nucl. Energy*, **11**, pp. 429-440 (1984).

53 W. F. Miller, "Nonlinear Response Matrix Methods for Radiative Transfer," *Proceeding of American Nuclear Society, Mathematics and Computation*, Paris, pp. 361-375, (1987).

54 S.-O. Lindahl, "Reciprocity Relations in Response Matrix Theory," *Nucl. Sci. Eng.*, **53**, pp. 475-478 (1974).

55 L. L. Briggs and E. E. Lewis, "A Comparison of Constrained Finite Elements and Response Matrices as One-Dimensional Transport Approximations," *Nucl. Sci. Eng.*, **63**, pp. 225-235 (1977).

56 T. Takeda and K. Azekura, "Improved Response Matrix Method and its Verification by One-Dimensional Analysis on Fast Reactors," *Journal of Nuclear Science and Technology*, **13**, pp. 408-412 (1976).

57 T. Takeda, K. Azekura, and T. Ohnishi, "Improved Response Matrix Method for Calculating Neutron Flux Distributions," *Nucl. Sci. Eng.*, **62**, pp. 709-715 (1977).

58 Z. Weiss and S.-O. Lindahl, "High-Order Response Matrix Equations in Two-Dimensional Geometry," *Nucl. Sci. Eng.*, **58**, pp. 166-181 (1975).

59 Z. J. Weiss and R. J. J. Stamm'ler, "Nodal Coupling of Heterogeneous Pin Cells," *Trans. Am. Nucl. Soc.*, **26**, pp. 223-224 (1977).

60 N. Guessous and M. Akhmouch, "Higher Order Analytical Nodal Methods in Response-Matrix Formulation for the Multigroup Neutron Diffusion Equations," *Ann. Nucl. Energy*, **29**, pp. 1765-1778 (2002).

61 Y. Gotoh, "Response Matrix of Symmetric Nodes with Absorber Rods," *Ann. Nucl. Energy*, **14**, pp. 451-454 (1987).

62 Z. Weiss, "Some Basic Properties of the Response Matrix Equations," *Nucl. Sci. Eng.*, **63**, pp. 457-492 (1977).

63 L. A. Olvey and E. E. Lewis, "Accuracy Comparisons for Variational R, T, and T-Inverse Response Matrix Formulations," *Ann. Nucl. Energy*, **14**, pp. 203-209 (1987).

64 E. E. Lewis and W. F. Miller, *Computational Methods of Neutron Transport*, John Wiley & Sons, New York. (1984).

65 R. D. Lawrence, "Progress in Nodal Methods for the Solution of the Neutron Diffusion and Transport Equations," *Prog. Nucl. Energy*, **17**, pp. 271-301 (1986).

66 R. J. Pryor, "Recent Developments in the Response Matrix Method," *Proceeding of Advanced Reactors: Physics, Design and Economics*, Atlanta, September, pp. 169-181, (1974).

67 A. Leonard, "Collision Probabilities and Response Matrices: An Overview," *Proceeding of Computational Methods in Nuclear Engineering*, Charleston, April, pp. III-15 - III-30, (1975).

68 H. Haggblom and A. Ahlin, "Transmission Probability Method of Integral Neutron Transport Calculation for Two-Dimensional Rectangular Cells," *Nucl. Sci. Eng.*, **56**, pp. 411-422 (1975).

69 C. T. McDaniel, "A Two Dimensional Few Group Response Matrix Calculation Method for Flux and Reactivity," *Proceeding of Computational Methods in Nuclear Engineering*, Charleston, April, pp. V-111 - V-134, (1975).

70 R. J. Pryor and W. E. Graves, "Response Matrix Method for Treating Reactor Calculations," *Proceeding of ANS Topical Meeting on Reactor Calculations*, Ann Arbor, April, pp. 179-186, (1973).

71 H. S. Bailey, "Response Matrix Analysis for Fast Reactors," *Proceeding of ANS Topical Meeting on Reactor Calculations*, Ann Arbor, April, pp. 187-194, (1973).

72 R. D. Lawrence and J. J. Dorning, "Nodal Green's Function Method or Multidimensional Neutron Diffusion Calculations," *Nucl. Sci. Eng.*, **76**, pp. 218-231 (1980).

73 K. L. Thomsen, "Investigation of interface-current solution techniques for coupled heterogeneous cells," *Nucl. Sci. Eng.*, **119**, pp. 164-174 (1995).

74 R. Sanchez, "A Transport Multicell Method for Two-Dimensional Lattices of Hexagonal Cells," *Nucl. Sci. Eng.*, **92**, pp. 247-254 (1986).

75 R. Sanchez, "Approximate Solutions of the Two-Dimensional Integral Transport Equation by Collision Probability Methods," *Nucl. Sci. Eng.*, **64**, pp. 384-404 (1977).

76 P. Mohanakrishnan, "Choice of Angular Current Approximations for Solving Neutron Transport Problems in 2-D by Interface Current Technique," *Ann. Nucl. Energy*, **9**, pp. 261-274 (1982).

77 P. Mohanakrishnan, "Angular Current Approximations in Neutron Transport Calculations Using Interface Currents - A Review," *Prog. Nucl. Energy*, **7**, pp. 1-10 (1981).

78 G. Marleau and A. Hebert, "Interface Current Method for Cluster Geometry," *Nucl. Sci. Eng.*, **92**, pp. 240-246 (1986).

79 P. D. Krishnani and K. R. Srinivasan, "A method for Solving Integral Transport Equation for Pressurized Heavy Water Reactor Cluster Geometry," *Nucl. Sci. Eng.*, **78**, pp. 97-103 (1981).

80 P. D. Krishnani, "Analysis of 2-D LWR Benchmarks with an Interface Current Method for Solving the Integral Transport Equation," *Ann. Nucl. Energy*, **14**, pp. 463-472 (1987).

81 P. D. Krishnani, "Interface Current Method for PHWR Cluster Geometry with Anisotropy in the Angular Flux at Interfaces," *Ann. Nucl. Energy*, **9**, pp. 287-296 (1982).

82 P. Kohut, "Interface-flux nodal transport method.," *Ann. Nucl. Energy*, **18**, pp. 609-615 (1991).

83 R. J. Pryor, "Response Matrix Method and the Cosine Currents Approximation," *Trans. Am. Nucl. Soc.*, **17**, pp. 262 (1973).

84 W. Bernnat, W. Klumpp, and P. Holder, "Treatment of Big Cavities in Diffusion Calculations by Monte Carlo Response Matrices.," *Atomkernenergie*, **26**, pp. 153-157 (1975).

85 T.-C. Wan and W. R. Martin, "The Monte-Carlo Response Matrix Method," *Trans. Am. Nucl. Soc.*, **55**, pp. 359 (1987).

86 M. Moriwaki, K. Ishii, H. Maruyama et al., "A New Direct Calculation Method of Response Matrices Using a Monte Carlo Calculation," *Journal of Nuclear Science and Technology*, **36**, pp. 877-887 (1999).